Driven pile

Disturbed soil

Sheet pile wall

Effect of Proximity of Sheet Pile Walls on the Apparent Capacity of Driven Displacement Piles

Effect of Proximity of Sheet Pile Walls on the Apparent Capacity of Driven Displacement Piles: Final Report

August 2018

DISCLAIMER

The opinions, findings, and conclusions expressed in this publication are those of the authors and not necessarily those of the State of Florida Department of Transportation.

SI (MODERN METRIC) CONVERSION FACTORS (FROM FHWA)

APPROXIMATE CONVERSIONS TO SI UNITS

SYMBOL	WHEN YOU KNOW	MULTIPLY BY	TO FIND	SYMBOL
LENGTH				
in	inches	25.4	millimeters	mm
ft	feet	0.305	meters	m
yd	yards	0.914	meters	m
mi	miles	1.61	kilometers	km

SYMBOL	WHEN YOU KNOW	MULTIPLY BY	TO FIND	SYMBOL
AREA				
in²	square inches	645.2	square millimeters	mm²
ft²	square feet	0.093	square meters	m²
yd²	square yard	0.836	square meters	m²
mi²	square miles	2.59	square kilometers	km²

SYMBOL	WHEN YOU KNOW	MULTIPLY BY	TO FIND	SYMBOL
VOLUME				
fl oz	fluid ounces	29.57	milliliters	mL
ft³	cubic feet	0.028	cubic meters	m³
yd³	cubic yards	0.765	cubic meters	m³
NOTE: volumes greater than 1,000 L shall be shown in m³				

SYMBOL	WHEN YOU KNOW	MULTIPLY BY	TO FIND	SYMBOL
MASS				
oz	ounces	28.35	grams	g
lb	pounds	0.454	kilograms	kg
T	short tons (2,000 lb)	0.907	megagrams (or "metric ton")	Mg (or "t")

SYMBOL	WHEN YOU KNOW	MULTIPLY BY	TO FIND	SYMBOL
TEMPERATURE (exact degrees)				
°F	Fahrenheit	5 (F-32)/9 or (F-32)/1.8	Celsius	°C

SYMBOL	WHEN YOU KNOW	MULTIPLY BY	TO FIND	SYMBOL
ILLUMINATION				
fc	foot-candles	10.76	lux	lx
fl	foot-Lamberts	3.426	candela/m²	cd/m²

SYMBOL	WHEN YOU KNOW	MULTIPLY BY	TO FIND	SYMBOL
FORCE and PRESSURE or STRESS				
lbf	pound force	4.45	newtons	N
kips	kips	4,448.22	newtons	N
lbf/in²	pound force per square inch	6.89	kilopascals	kPa
ksi	kips per square inch	6,894.76	kilopascals	kPa
tsf	tons (short) per square foot	95.67	kilopascals	kPa
pcf	pound force per cubic foot	156.967	newtons per cubic meter	N/m³

APPROXIMATE CONVERSIONS TO SI UNITS

SYMBOL	WHEN YOU KNOW	MULTIPLY BY	TO FIND	SYMBOL
LENGTH				
mm	millimeters	0.039	inches	in
m	meters	3.28	feet	ft
m	meters	1.09	yards	yd
km	kilometers	0.621	miles	mi

SYMBOL	WHEN YOU KNOW	MULTIPLY BY	TO FIND	SYMBOL
AREA				
mm²	square millimeters	0.0016	square inches	in²
m²	square meters	10.764	square feet	ft²
m²	square meters	1.195	square yards	yd²
ha	hectares	2.47	acres	ac
km²	square kilometers	0.386	square miles	mi²

SYMBOL	WHEN YOU KNOW	MULTIPLY BY	TO FIND	SYMBOL
VOLUME				
mL	milliliters	0.034	fluid ounces	fl oz
L	liters	0.264	gallons	gal
m³	cubic meters	35.314	cubic feet	ft³
m³	cubic meters	1.307	cubic yards	yd³

SYMBOL	WHEN YOU KNOW	MULTIPLY BY	TO FIND	SYMBOL
MASS				
g	grams	0.035	ounces	oz
kg	kilograms	2.202	pounds	lb
Mg (or "t")	megagrams (or "metric ton")	1.103	short tons (2,000 lb)	T

SYMBOL	WHEN YOU KNOW	MULTIPLY BY	TO FIND	SYMBOL
TEMPERATURE (exact degrees)				
°C	Celsius	1.8C+32	Fahrenheit	°F

SYMBOL	WHEN YOU KNOW	MULTIPLY BY	TO FIND	SYMBOL
ILLUMINATION				
lx	lux	0.0929	foot-candles	fc
cd/m²	candela/m²	0.2919	foot-Lamberts	fl

SYMBOL	WHEN YOU KNOW	MULTIPLY BY	TO FIND	SYMBOL
FORCE and PRESSURE or STRESS				
N	newtons	0.225	pound force	lbf
N	newtons	0.000224809	kips	kips
kPa	kilopascals	0.145	pound force per square inch	lbf/in²
kPa	kilopascals	0.000145	kips per square inch	ksi
kPa	kilopascals	0.000145038	kips per square inch	ksi
N/m³	newtons per cubic meter	0.0104526	pound force per cubic foot	pcf

*SI is the symbol for International System of Units. Appropriate rounding should be made to comply with Sec. 4 of ASTM E380. (Revised March 2003)

TECHNICAL REPORT DOCUMENTATION PAGE

1. Report No.	2. Government Accession No.	3. Recipient's Catalog No.	
4. Title and Subtitle Effect of Proximity of Sheet Pile Walls on the Apparent Capacity of Driven Displacement Piles		5. Report Date August 2018	
		6. Performing Organization Code	
7. Author(s) Chung, J., McVay, M., Davidson, M., Taghavi, A., Mishra, N., Taylor, A., Nguyen, T.		8. Performing Organization Report No.	
9. Performing Organization Name and Address University of Florida 1949 Stadium Rd. Room 365 P.O. Box 116580 Gainesville, FL 32611		10. Work Unit No. (TRAIS)	
		11. Contract or Grant No. BDV31-977-26	
12. Sponsoring Agency Name and Address Florida Department of Transportation 605 Suwannee Street, MS 30 Tallahassee, FL 32399		13. Type of Report and Date Final Report July/2014-August/2018	
		14. Sponsoring Agency Code	
15. Supplementary Notes			

16. Abstract

The present research investigated the effects that installation and removal of sheet pile walls (SPW) have on driven piles founded in granular soils. The efforts completed as part of the present study have involved both physical testing and numerical simulation of standardized laboratory tests on granular materials. Further, physical centrifuge tests have been conducted to provide benchmark measurements of soil stresses; changes in soil stresses during installation and/or removal of structural objects; and, pile skin-friction and end bearing forces across multiple SPW-soil-pile test scenarios. Also, numerical modeling efforts, simulation results, and comparisons between physical measurements taken from selected centrifuge tests and computed results from simulations of (1) Pile driving into sand; (2) SPW installation followed by pile driving into sand; and, (3) SPW installation, pile driving, and subsequent SPW removal have been done and are reported as Task 3.1 and Task 3.2. As Task 5 of this project, geometric parameters with regards to the complex pile-soil-sheet pile wall system were identified and rigorous parametric study has been performed. Two geometric parameters, namely, (1) relative horizontal offset distance between the pile and SPW and (2) ratio of SPW embedment depth to pile embedment length, are identified as the configurational factors controlling the effects of installation and subsequent removal of SPW on overall response of pile-soil-SPW foundation systems. Based on the results of a parametric study, design recommendations are made to be used by geotechnical and structural engineers to obtain a robust estimate of changes in design loads pertaining to varying configurations of pile-soil-SPW system.

17. Key Words Bearing capacity; Dislocation (Geology); Pile driving; Resistance (Mechanics); Sheet pile walls; Soil mechanics		18. Distribution Statement No restrictions.		
19. Security Classif. (of this report) Unclassified		20. Security Classif. (of this page) Unclassified	21. No. of Pages 167	22. Price

ACKNOWLEDGEMENTS

EXECUTIVE SUMMARY

In recent years, technological advances have been made in relation to pile foundations, and as a result, it is now recognized that the process of pile construction or installation in the ground can cause major changes in the stress state and density conditions of soil in the vicinity of the pile. Such recognition signifies the value of basic research, which has enabled geotechnical engineers to depart from the traditional approach of employing empirical constants to modify theoretical predictions, where corresponding design predictions did not allow engineers to reliably account for residual stresses induced during pile installation or sheet pile wall construction. Examples of the common, empirical approach include an averaging of empirical coefficients in Hanna (1963) through translation of undrained shear strength of stiff clays into 'average' adhesion values for bored piles; Meyerhof's (1959, 1960) estimation of the extent of zones of increased soil density and shear strength near pile tips; and, Kishida's (1967) linear interpolation of internal friction angles within an empirically calculated zone in the vicinity of driven piles. Despite the abundance of empirical methods (which were obtained from observational experiments and in situ testing), numerous uncertainties remain regarding the soil densification (or loosening) and its influence on geostress states of pile-soil systems. This is especially the case when construction practice includes the use of sheet pile walls (SPW), e.g., in supporting off-shore structures or in pile foundation construction.

Phenomena associated with use of SPW have also been observed when groups of piles are driven into the ground. The ultimate load capacity of the group may be either greater or less than the sum of the capacities of the individual piles, depending on whether or not the soil undergoes compaction (or, alternatively, loosening) during pile driving. For scenarios where driving-induced soil compaction occurs, piles driven in the vicinity of SPW or adjacent piles can develop greater load capacities relative to those piles driven in virgin ground. The phenomenon that individual pile stress states are dependent upon the proximity of other pre-driven structural members is further complicated for those scenarios where pile driving into dense soil causes loosening rather than compaction. Subsequent to installation of driven piles, removal (pull-out) of any nearby SPW may well further alter the pile-soil stress states, due to soil disturbances that occur during extraction of the SPW. Such disturbances can lead to reductions in frictional resistance at pile-soil interfaces and, thus, overestimation of pile design capacities.

Most of the early research carried out on the phenomenological behavior of soils under the action of shear stresses was primarily restricted to the study of residual loads (or residual compression and tension) in relation to peak strength conditions (and failure criteria). Despite this long-standing finding, little success has been achieved in the rigorous prediction of residual stress states, partly because (1) the analysis of pile installation in soil is a large strain problem, which involves predominant constitutive and kinematic nonlinearities and (2) penetration of an object into particulate materials is a boundary-value problem, where the continuum hypothesis is not valid. Consequently, design practice concerning pile installation has been based on general engineering and mechanics principles, previous design experience, and engineering judgment. Given the limitations associated with extant pile-driving analysis tools, several cycles of design, fabrication, and load testing may typically be required to arrive at reliable, safe foundation designs. Furthermore, design optimization—which requires that the sensitivity of foundation response to

changes in key design parameters be evaluated—can be costly if physical testing is the sole assessment-mechanism available.

In the study documented in this report, steps were taken toward an alternative methodology, wherein a main portion of the assessment can be performed using computational simulation (combined discrete and finite element analysis). Use of simulation can result in more rapid analysis, improved reliability of foundation design, and reduced development costs. Small-scale physical testing (e.g., geotechnical centrifuge tests) was utilized to validate and qualify the integrity of the computational model. Far fewer cycles of development and testing are required if simulation results can be relied upon to identify both design parameters that improve design robustness and to quantify design load reduction that may degrade foundation performance. Evaluating the zone of influence of SPW is of particular interest in the current study. Given the setup time and costs involved in physical testing of pile driving, conducting a strictly physical experiment-based parametric study to evaluate the influence of SPW would be cost prohibitive. Thus, the present study described in the remainder of this final report deals with the development and use of a *prototype* computation model through rigorous verification of laboratory-scale experimentation and a parametric study using a calibrated computational to evaluate the influence of in situ pile-SPW systems on the pile design capacity.

TABLE OF CONTENTS

LIST OF FIGURES

xvi

LIST OF TABLES

Chapter 1
INTRODUCTION

1.1 Introduction

The fundamental objective of this project was to clarify the principal mechanisms behind pile driving that induce changes in soil microstructure of granular soils. Three-dimensional combined discrete and finite element analysis was carried out to investigate and evaluate the particulate nature of soil systems subjected to penetration by hardened objects through simulation of the mechanical interaction between penetrator (e.g., SPW or pile) and soils, as well as sequentially combined driven pile and SPW systems. Taking into account the proximity of SPW, the study employed explicit modeling of soil particle-structure dynamic interactions and residual stress zone of influence resulting from both pile driving and pulling out behavior. Further, the proposed study enabled quantification of particle-to-particle contact forces in soil densification (or loosening). Primary motivations to use the proposed combined numerical procedures to this boundary value problem are (1) to capture the intrinsic features of geo-materials (geostatic stress states; dilatancy; and, stress dependencies of kinematic response to the complex phenomena associated with SPW pre-installation (and post-removal) and pile driving and (2) to simulate lock-in stress through inter-particulate contacts and associated densification of soil clusters by nonconservative forces acting on particle boundaries in the microstructures. In contrast to the conventional continuum-hypothesis-based numerical methods, e.g., Finite Difference Method, Finite Element Method, Smooth Particle Hydrodynamics (SPH), or hybrid Lagrangian-SPH Method, the numerical approach proposed herein is capable of simulating (1) realistic in situ stress state initialization of preloading conditions; and, (2) effective stress developed during and after SPW installation. As a result, the effects of pile driving at control volumes were assessed via fully-coupled particle-structure interactions relevant to particulate clusters of granular soils at the micro-structure scale (e.g., parameterized interparticle contact behaviors at mesoscopic scale).

1.2 Background and Motivation

There are occasions in which a temporary sheet pile wall or cofferdam is driven prior to the installation of displacement piles. If the location of a sheet pile wall is relatively close and the penetration is of certain depth, it will affect the capacity of the piles to be driven. An additional "temporary" resistance is induced due to additional lateral stresses that are generated as a result of trying to drive a displacement pile next to a rigid element (sheet pile wall). This has been evidenced in the field when piles next to sheet piles penetrate less than expected and at higher blow counts than observed in test piles that were driven away from or without the presence of a sheet pile. A similar phenomenon is observed when trying to drive piles close together: they become progressively more difficult to install as a result of the soil displacement of the adjacent piles.

However, when the sheet pile is extracted after the piles are driven, there will be some relaxation, and the pile will experience some loss of capacity. The pile will lose side friction and bearing (if the tip of the pile is close or above the tip of the sheet pile). The duration of the vibrations imposed during the extraction of the sheet pile may increase this loss of capacity. If the proximity of the temporary sheet pile is not considered during design or during driving of the piles, an inspector may accept piles with an apparent higher capacity than the piles will have after the sheet pile is

extracted. If the pile has no way of being tested after the sheet pile is removed, the project personnel have no way of verifying the final capacity of the piles. This is typically the case when the pile cap is constructed before the sheet pile is removed, and as a consequence piles may end up with a nominal bearing capacity lower than the intended one.

It has been recognized for a long time that driven piles densify the sand around the pile. For example "Pile Foundation Analysis and Design", Poulus, 1990, Chapter 2, makes reference to this phenomenon and cites findings and publications from others that indicate sandy soils around the pile densify after driving. Currently, there is not a reference or an accepted methodology that designers can use to determine the additional resistance that these piles may experience during installation. It is accepted that this phenomenon occurs but a consistent approach to quantify this effect is needed.

The objectives of this project are to:

•   Quantify the increase in foundation resistance (axial stiffness) due to the proximity of the temporary sheet pile.
•   Quantify the influence of sheet pile distance and sheet pile depth on the increase in pile load capacity.
•   Quantify the loss of capacity due to sheet pile extraction.
•   Determine distances beyond which the sheet pile wall does not influence the driving resistance of the pile.
•   Develop practical recommendations for designers to account for the effect of the sheet pile on the pile capacity.

Therefore, the goal of this study is to quantify those dynamic soil-structure interaction which hold greatest significance in the assessment of pile design capacity by: 1) Tabulating numerical predictions of pile-SPW system response (generated as part of parametric study for the geometric parameters of SPW (i.e., distance and embedment depth in relation to the location of driven pile); and then, 2) Identifying trends in the tabulations of the response quantities. Those geometric parameters that retain significance (i.e., give indications of meaningful input-response trends) when processed in this way are directly packaged (via graphs) into graphical design-oriented tools for use by geotechnical engineers.

1.3 Scope

The scope of the remainder of this report is as follows:
- In Ch. 2, the experimental methodology for centrifuge modeling is overviewed. The centrifuge and testing apparatus is described and the experimental procedure is given in detail.
- In Ch. 3, the numerical procedures employed in this project are reviewed. The technical details of the combined Discrete Element – Finite Element modeling approach are explored, and specifics regarding boundary conditions and specific testing scenarios are described.

- In Ch. 4, the results of a comprehensive parametric study are reviewed, with respect to the relative horizontal offset and relative embedment depth of the pile and sheet-pile walls in the numerical simulations.
- In Ch. 5, recommendations for design practice are given based on the results of the parametric study. Loading recommendations are provided accounting for the relative horizontal offset and embedment depths of the structural components, and a procedure for the use of the provided graphical tools is outlined.
- In Ch. 6, the research contributions of this project are reviewed alongside a concluding discussion and final recommendations.
- A list of cited references is provided.

CHAPTER 2
EXPERIMENTAL RESEARCH: CENTRIFUGE MODELING

The overall objective of the current research is to study the effect of driven sheet pile walls (SPWs) on the resistance of subsequently driven piles in a granular medium by utilizing a combination of geotechnical centrifuge testing and novel computational methods. In order to fulfill the overall study objective, it is required to develop a calibrated and validated numerical model that could simulate soil behavior, structures behavior, and the interaction between soil and structures. The chapter documents the completion of Task 4, experimental investigation, which involves the development of three scenarios, as follows:

(1) Scenario 1: A pile is driven into the soil and it is then subjected to incremental quasi-static axial loads and simultaneously the load-deformation behavior, along with changes in geostatic stresses, are quantified;

(2) Scenario 2: A sheet pile is driven into a granular soil deposit and a pile is subsequently driven in close proximity of a SPW. The pile is then subjected to incremental quasi-static axial loads to quantify the load-deformation behavior and corresponding changes in geostatic stress;

(3) Scenario 3: Upon completion of sequential SPW, followed by pile installation, the SPW is extracted from the ground. The pile is then subjected to incremental quasi-static axial load and both the load-deformation behavior and geostatic stress states are quantified.

Of great importance are centrifuge tests in calibrating and validating the numerical models, based on three scenarios. The results of comparisons between numerical results (Task 3) and centrifuge testing results (Task 4) will be presented in the subsequent chapter.

2.1 Overview of Geotechnical Centrifuge Testing

Centrifuge testing allows the investigation of system-level, complex problems that would otherwise only be possible by full-scale testing. An important aspect to be considered in testing reduced-scale centrifuge models is their similitude with field-scale prototypes. Because the strength, stiffness, deformation, and volume change in soils is stress-dependent, the key objective of a centrifuge model is to keep the stresses identical to that of a prototype. The geotechnical centrifuge used in this study is shown in Fig. 2.1. Centrifuge testing includes several key steps. After constructing the reduced-scale centrifuge model, it sits inside a basket located at one end of the centrifuge arm with its long dimension parallel to the direction of arm. Adjustable counterweights on the other end balance the weight on the model side (Fig. 2.1). The container gradually rotates 90º from a horizontal stationary position as the centrifuge is spun-up. This step takes about 15-20 minutes and allows for a gradual transition of stresses. After reaching the target centrifugal acceleration, the model is tested.
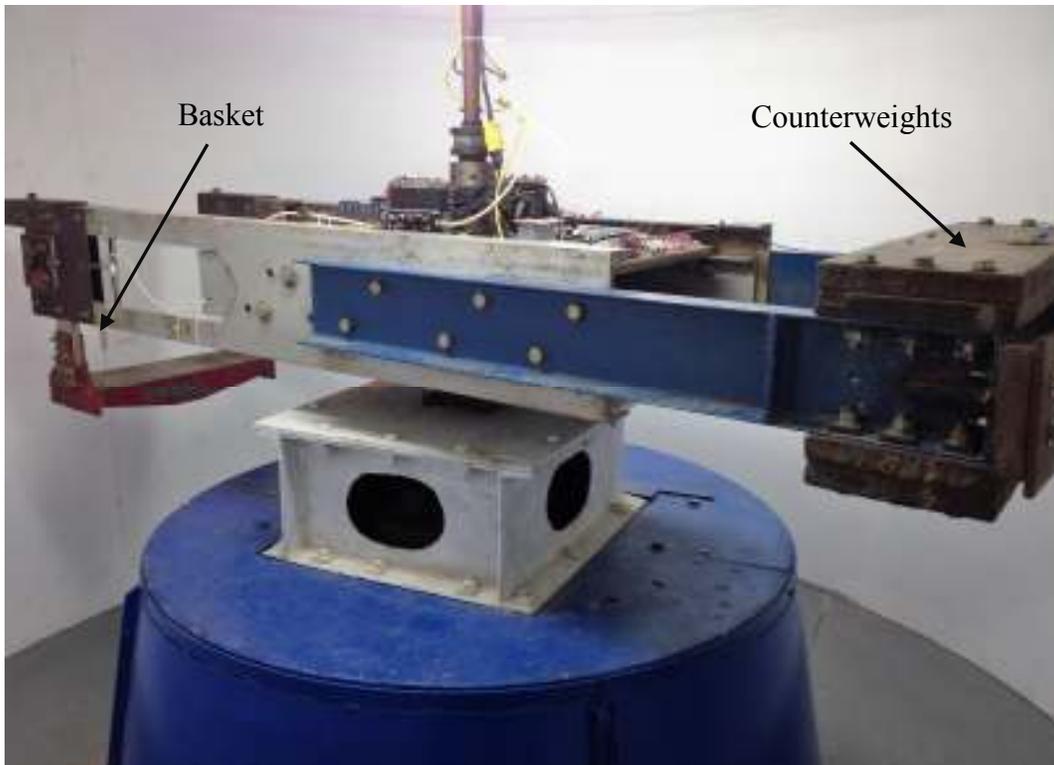
Figure 2.2.1 Geotechnical centrifuge at the University of Florida, Gainesville

2.1.1 Scaling Laws

In centrifuge modeling, the scale factor for length may be expressed as L* = 1/N. L* is the ratio of length in the model to length in the prototype. The scaling laws for centrifuge model tests can be found in Schofield (1981), Kutter (1992), and Garnier et al. (2007). A list of the main scaling factors used to convert the measured data to prototype-scale units is provided in Table 2.1.

Table 2.1 Centrifuge scaling factors

Quantity	Symbol	Scale Factor
Gravity	g	N
Length	l	N^{-1}
Volume	v	N^{-3}
Mass	m	N^{-3}
Force	F	N^{-2}
Stress	σ	1
Strength	s	1
Moduli	E	1
Time (dynamic)	t_{dyn}	N^{-1}
Time (diffusion)	t_{dif}	N^{-2}

2.1.2 Advantages of Centrifuge Testing

Analyzing a geo-structure such as a pile in the vicinity of a sheet pile wall as a system is a highly complex undertaking; however, with advances in computer hardware, mechanics, and computational techniques, huge leaps in our ability to digitally simulate these systems have been made. In fact, our ability to computationally model civil infrastructure has outstripped our ability to physically model these complex systems. Physical models are, however, necessary to validate computational simulations as well as understand failure mechanisms of complex structures. Creating full-scale physical models (e.g. instrumenting a real structure as it is built) is very costly and time consuming. Furthermore, field conditions such as subsurface soil profiles are often unknown, it is difficult to take a real structure to the failure state, and only limited loading conditions can be studied. Small-scale centrifuge models can solve all of these problems and make it possible to study geotechnical systems under variety of conditions. A geotechnical centrifuge makes it possible to accurately model deep deposits with realistic stress conditions; control the repeatability of test results; directly observe failure mechanism; apply a wide range of dynamic or quasi-static loads; validate numerical and empirical models, and use in consulting (Mitchell, 1991). The centrifuge tests are also time and cost effective compared to full-scale tests.

2.1.3 Limitations of Centrifuge Testing

Similar to other geo-structural modeling techniques, centrifuge modeling has its own inherent limitations. Loss of prototype detail is associated with modeling large prototype geo-structures which utilizes large scale factors (e.g. $N=10^4$). For example, in studying the interaction of a fault with a shallow foundation or an embedded structure in deep deposits of granular media, a thin film of cohesive layer, though could affect the behavior of the structure, might be overseen or difficult to consider in centrifuge modeling.

Scale effects can become important when trying to directly model a real prototype event. For example, in investigating the bearing capacity of a foundation resting on a granular media, it is important to choose a reasonable scale ratio between the dimensions of the foundation and grain sizes. Scale effects become, however, less important if the centrifuge test results are aimed to be used in understanding the mechanisms involved in the studied problem or validating a numerical model.

Boundary effects are associated with centrifuge containers specially in studying seismic problems. A well-designed container can, however, reasonably satisfy the concerns regarding the boundary effects created by artificial boundaries of a model container. The important boundary effects in a model container include (1) distortion of the overall stress field and soil rocking relative to the base plane as a result of frictionless smooth end walls; (2) strain dissimilarity and soil deformation restriction as a result of a rigid end wall; (3) generation and propagation of unwanted P waves as a result of rigid end walls and their interaction with the model soil; (4) destroying K_0 conditions due to the deflection of side walls; and (5) frictional support to the edges of the model with relatively close boundaries. The first three effects might be of concern in dynamic problems. Many of these boundary effects can be minimized in specially designed model containers such as a flexible shear beam (FSB) container (Kutter, 1995) for seismic problems or a smoothed wall rigid container (Santamarina and Goodings, 1989) for static problems.

Another centrifuge modeling aspect to be considered in modeling axially loaded pile foundations in granular material is the scale effects. McDowell and Bolton (2000) recommended the pile width to the median grain size (B/D_{50}) be greater than 20 to study the behavior of axially loaded piles in centrifuge testing. Fuglsang and Ovesen (1987) recommended a B/D_{50} ratio greater than 30 for studying the response of a general model structure in centrifuge testing.

2.2 University of Florida Centrifuge and Model Container

The centrifuge model tests in this study were carried out at a centrifuge acceleration of 32 g in a rigid container. The maximum payload for the University of Florida centrifuge is 12.5 g-ton and the available basket area is approximately 3.7 ft^2. The beam radius is 59 in (1.5 m) and the maximum centrifugal acceleration is 80 g.

The rigid container used in our tests had internal dimensions of 22 in (length) × 8 in (width) × 18 in (height). The rigid container consisted of two aluminum solid plates fixed to two rigid Plexiglas transparent plates. This container made it possible to reduce the boundary effects and reasonably simulate the prototype event. By placing the structural models and instruments as far as possible from the boundaries, the boundary effects were further minimized.

2.3 Centrifuge Test Set-up

From this point onwards, all the results are presented in prototype scale unless otherwise stated. The soil profile in centrifuge models consisted of a normally consolidated dry sand layer. The total depth of the layer was 42.7 ft.

2.3.1 Sand Properties

To prepare the sand layer in the centrifuge model, Florida natural sand was air-pluviated to achieve a relative density of 65%. Details about air-pluviation method are provided in section 2.3.2. Laboratory tests were performed by the FDOT: States Material Office (SMO) to characterize this soil. Sieve analyses revealed that the USCS name of the soil is "SP" with coefficients of uniformity and curvature of 1.77, and 1.08, respectively. Details about sand properties are provided in Fig. 2.2. Direct Shear Tests (DSTs) were performed by SMO at a relative density of 63% and the results are provided in Fig. 2.3 for 3 different applied normal stresses of 7 psi, 14 psi, and 21 psi. Based on DSTs, the peak and residual internal friction angles were 31.7 and 29.57, respectively (see Figs. 2.4 and 2.5). Additional DST results on relative densities of 55% and 93 % are provided by SMO and presented in Appendix A.
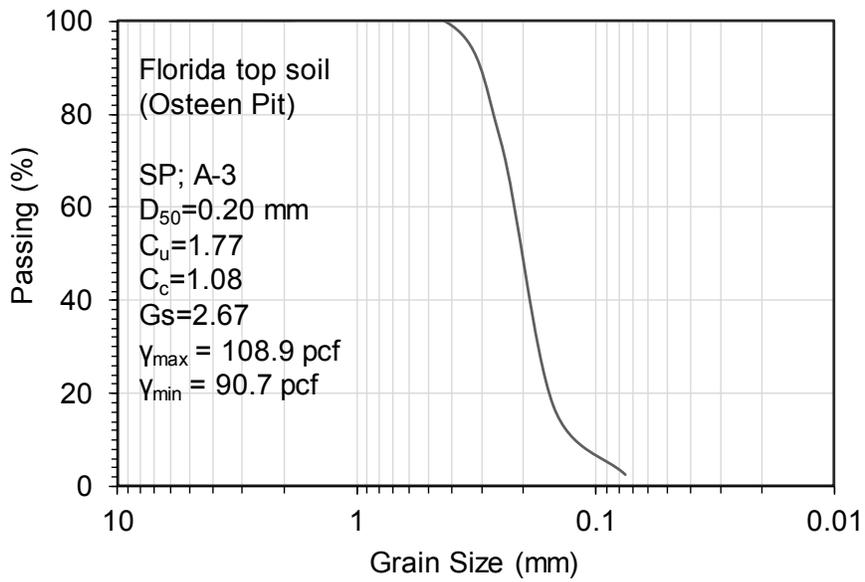
Figure 2.2 Soil gradation and properties
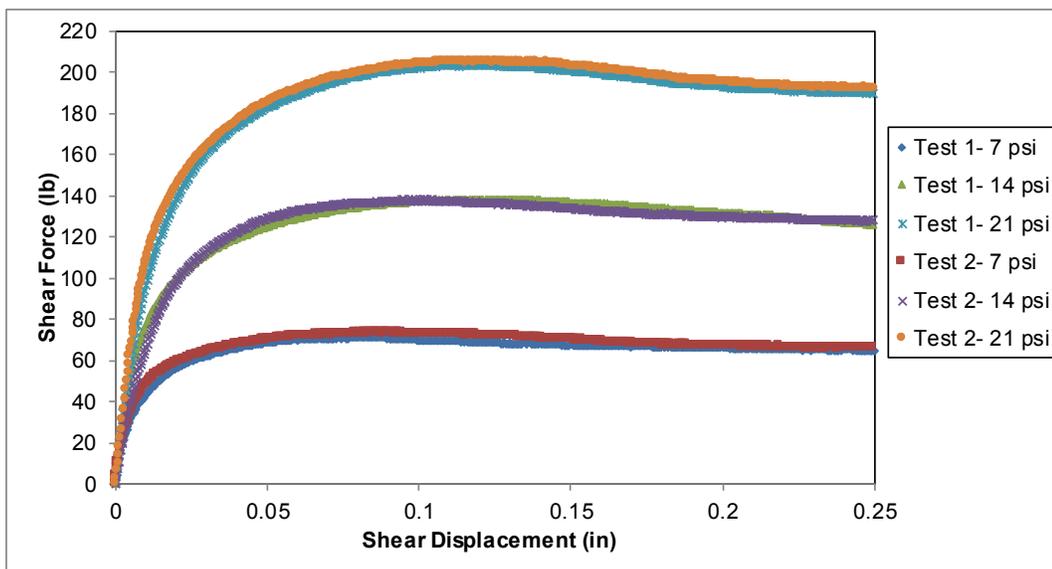
Figure 2.3 Direct shear test (DST) results at 63% relative density and normal stresses of 7 psi, 14 psi, and 21 psi
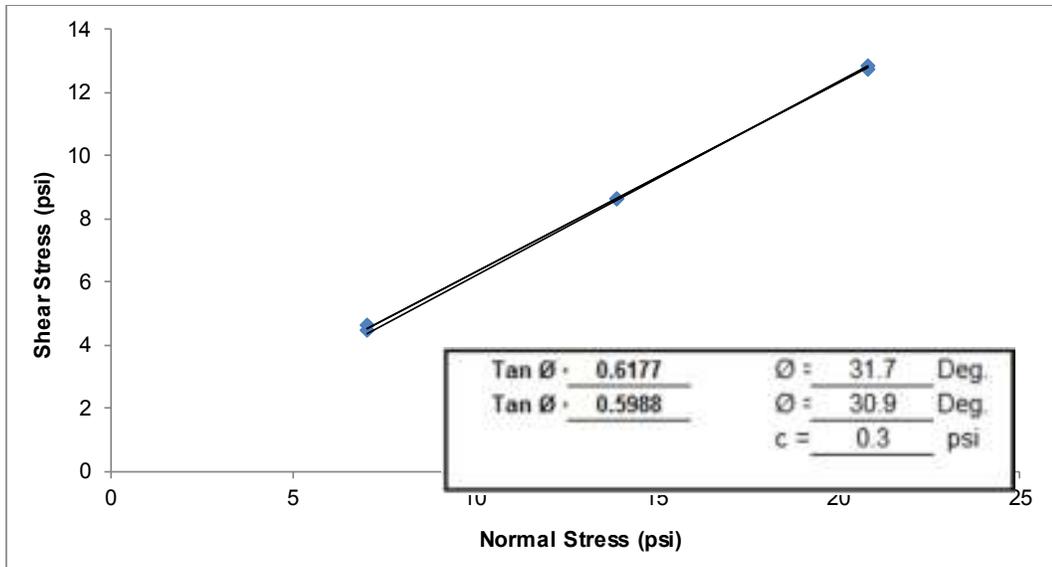
Figure 2.4 Peak internal friction angle obtained from DST at 63% relative density
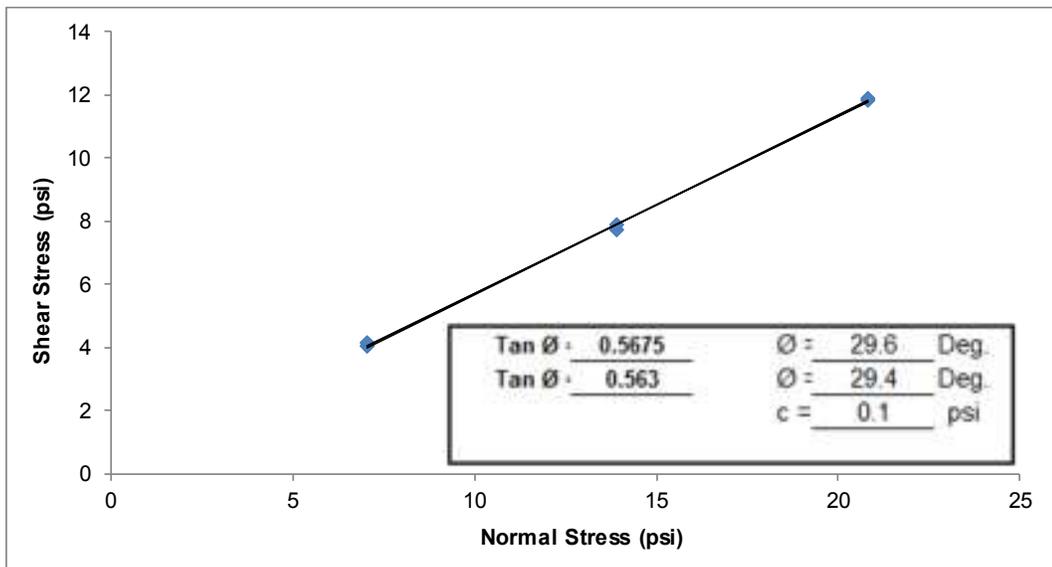
Figure 2.5 Ultimate internal friction angle obtained from DST at 63% relative density

2.3.2 Dry Pluviation of Granular Materials

To prepare a homogenous granular layer, sand grains were air-pluviated to achieve the desired relative density and a void ratio. For this purpose, a novel pluviator was designed and fabricated by Bridge Software Institute (BSI). The pluviator consisted of a hopper, a shutter, and a diffuser-sieve. By covering the entire area of the centrifuge container, the pluviator ensures a

9

homogenous distribution of grains. The sand layer density was controlled by maintaining a nearly constant drop height and rate. Sand was pluviated into the model container in successive layers, with each layer followed by leveling of the surface using a vacuum. Each lift corresponded to the elevation of a horizontal instrument array. A schematic sketch of the pluviator is shown in Fig. 2.6.
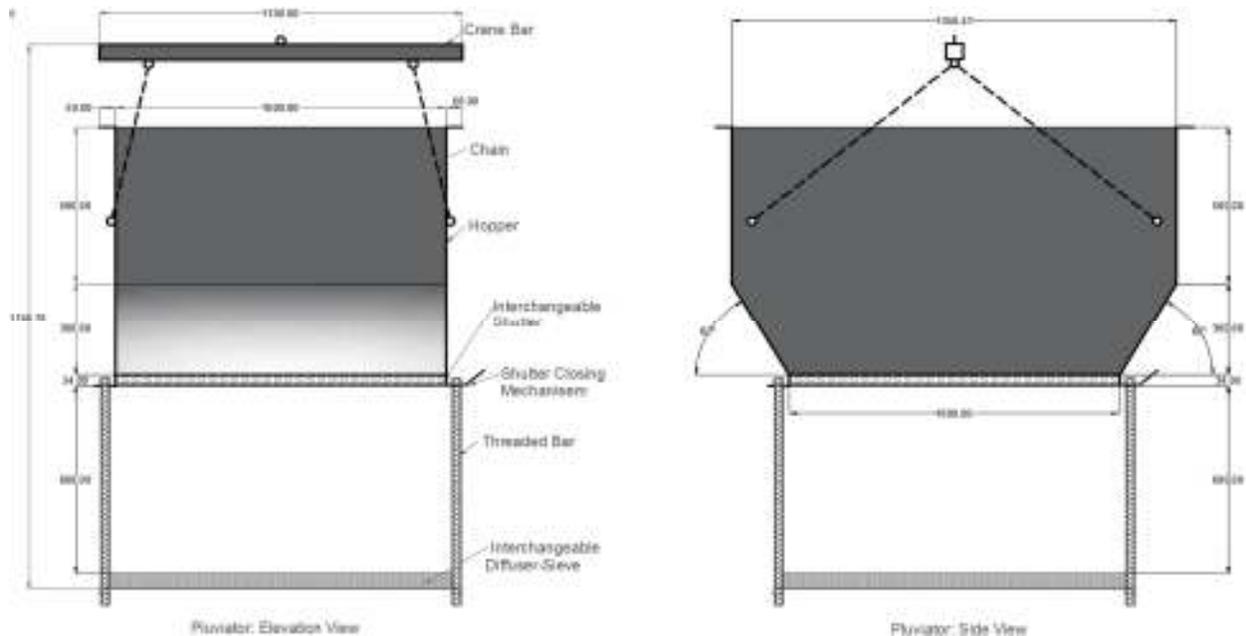
Figure 2.6 Schematic sketch of the pluviator

2.3.3 Pile Characteristics

The model pile was fabricated from a hollow aluminum tube with a square cross section. The prototype values of the axial stiffness of the aluminum square tube pile closely matched those of the FDOT square concrete piles. The outside width (B) of the pile was 2.0 ft and the wall thickness (t) was 4.0 in. The cross sectional area (A) of the pile was 320 in^2 and the second moment of area (I) was 22187 in^4. The Young's modulus (E) of aluminum was 10000 ksi. The single pile was 30.2 ft long with the lower 17.7 ft inserted into the granular profile. The pile characteristics are provide in Table 2.2 for both model and prototype scales. Using this pile and aforementioned Florida natural sand, B/D_{50} ratio of 95.25 was obtained, ensuring there are no (or negligible) scale effects in the current centrifuge model tests.

The bottom of the pile was fabricated from a solid aluminum piece having length and width of 1.5 ft and 2 ft, respectively. This solid piece served as the casing for the tip load cell. The load cell was placed in this casing so that it would be possible to measure the loads without any concerns regarding stress concentration if the load cell was touching soil grains at the pile tip.

Craig (1985) showed that the volume changes in sand during pile driving could be significant and recommended driving pile foundations in flight in centrifuge tests. McVay et al. (1994) and McVay et al. (1998) were the first who used a pneumatic system to drive the piles in

sand in flight. To keep the pile plumb initially, it was first pre-embedded in sand to a depth of 1.3 ft (0.5 inch in model scale) before spinning. In addition, two templates were used to help with driving the pile vertically in flight. The bottom template was just above the ground surface level, and the top one was spaced at 6 ft above the bottom template. Both templates were fixed to the container. The miniature pile-driving hammer has a convex elliptical shape at the tip and was positioned in the internally carved concave-shaped pile-top during hammer impact, which helped maintain vertical alignment. The hammer was attached to a top rigid square-shaped plate with displacement-controlled movements. Four symmetrically placed pneumatic cylinders produced the required air-pressure for the movement of the top plate. The air pressure of the cylinders, and therefore the applied force, could be controlled during centrifuge tests by means of a pressure gauge and regulator located in the control room.

2.3.4 Sheet Pile Wall Characteristics

Considering that a vast number of sheet pile shapes, sizes, and resulting SPW configurations are used in construction, a scaled prototype of a representative SPW was incorporated into the centrifuge testing. In particular, the SPW was constructed using a steel plate, in which the tongue-and-groove were cut to form a typical U-shaped section. The cross-section of the SPW is shown in Fig. 2.7. The SPW was 40.0 ft long with the lower 17.7 ft inserted into the granular profile. The SPW characteristics are provided in Table 2.3 for both model and prototype scales.

2.3.5 Sheet Pile Wall – Pile System

The pile being driven in the vicinity of the SPW provideed a complex geo-structural system. In this system, the distance between the pile and SPW and the relative tip elevation of pile and SPW were among the factors that would alter the behavior and interaction of the structural models with the surrounding soil. Other factors included soil properties, mechanical properties of the pile and SPW, and their installation method.

For this project, a net distance of 4.93 ft (≈ 2.5 B) was chosen for the pile and SPW, which is a typical distance for the similar cases in the field. In the first effort, the same number of miniature hammer impact loads were applied to the pile top so that the stress history would be repeatable during all tests. Having similar air pressure inside the pneumatic cylinders, we tried to apply identical forces to pile top per impact. The pile top displacement and force were being monitored during driving. As the impact loads were applied manually by moving down and up the hammer, in some cases, the pile tip ended up at a different elevation than the target depth. Therefore, in these cases, the number of hammer blows was increased.
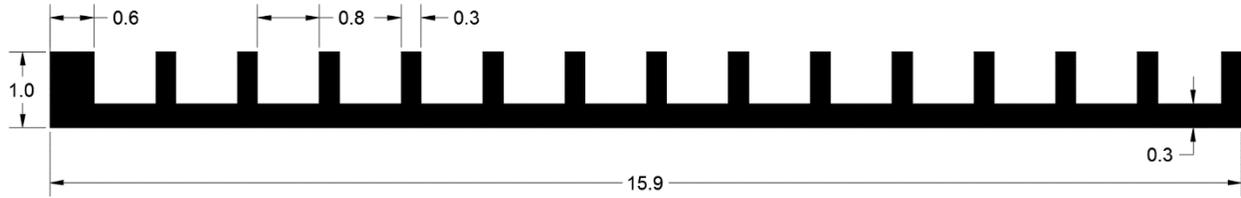
Figure 2.7 Cross-section of the SPW (dimensions in ft)

Table 2.2 Sheet pile wall characteristics

Scale	Scale factor	Length (in)	Width (in)	Wall thickness (in)	Area (in^2)	Modulus of Elasticity (ksi)	E.A (kips)	Total embedment depth (in)
Model	1.0	15.039	5.96	0.375	1.14	2.9×10^4	33147	6.652
Prototype	32.0	481.25	190.72	12	27796	2.9×10^4	8.1×10^8	212.86

2.4 Instrumentation and Data Acquisition

The model was instrumented with load cells (LCs), pressure sensors (PSs), a linear variable displacement transducers (LVDT), and a string potentiometer (SP). Two Micro-Electro-Mechanical Systems (MEMS) accelerometers were also utilized to monitor centrifugal acceleration. The instrumentation layout is shown in Fig. 2.8. The LVDT was used to measure the pile settlement during load tests. PSs were placed adjacent to the structural models and in the granular profile to record the earth pressure in geostatic and also during driving the structural models. A string potentiometer was mounted on the top loading plate to monitor the pile and the SPW settlement during driving. Two LCs at top and toe of the pile were used to record the applied loads during pile driving and in load tests. The instruments were attached to National Instruments RIO (NI RIO) channels which in turn communicate with a RIO control unit (housed in a wall mounted enclosure in the control room). This unit controlled the centrifuge system and communicates with the LabVIEW based GUI program (CICADA).
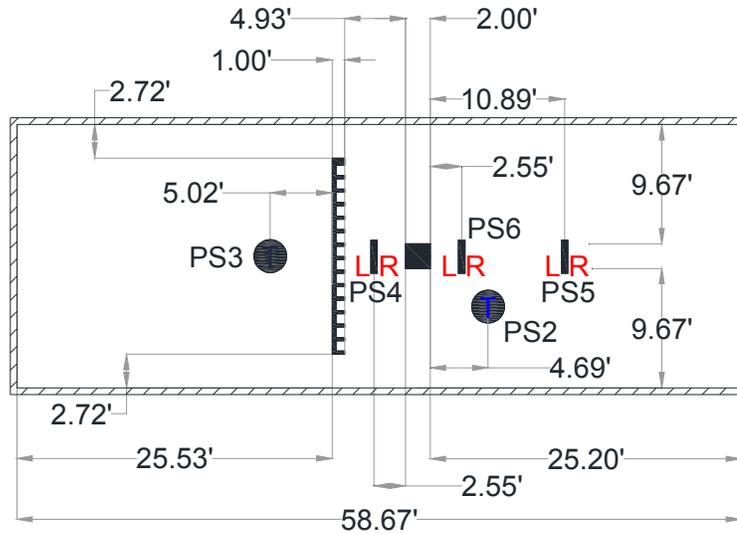
Figure 2.8 Instrumentation layout. Note that PS stands for pressure sensor. For horizontal placement of the PS4, PS5 and PS6, the two sides of each sensor are denoted by L (left side) and R (right side).

2.5 Testing Sequence

2.5.1 Equal SPW and Pile Tip Depths

Three loading scenarios were considered for the pile load testing in centrifuge tests. In the first loading scenario, the centrifuge model was spun to the target centrifugal acceleration (i.e. 32-g). The pile was then driven in-flight into sand under impact (i.e. dynamic) loading applied by a miniature hammer on top of the pile. Upon reaching the target embedment depth during pile driving, the pile was subjected to an axial quasi-static load test and load-deformation behavior was captured using top and toe load cells and LVDTs (Fig. 2.9).

In the second loading scenario, the SPW was first pushed in flight to the target depth. The pile was then driven into the same depth as the SPW. The second axial load test was then conducted at this stage (Fig. 2.10).

In the third loading scenario, similar to the second loading scenario, the SPW and pile were first driven to the same target depth. The SPW was then totally pulled out of the granular profile and consequently the third axial load test was performed on the single pile. During all three stages of the test, the changes in initial stress states was recorded using the pressure sensors installed adjacent to the structural models (Fig. 2.11).

13

2.5.2 Lower SPW Tip Depth than the Pile Tip Depth

In the second series of tests, the SPW toe was driven to 8.87 ft depth (half depth of the pile toe). These tests were conducted to study the effects of the reduced SPW confinement on the axial capacity of the adjacent pile.
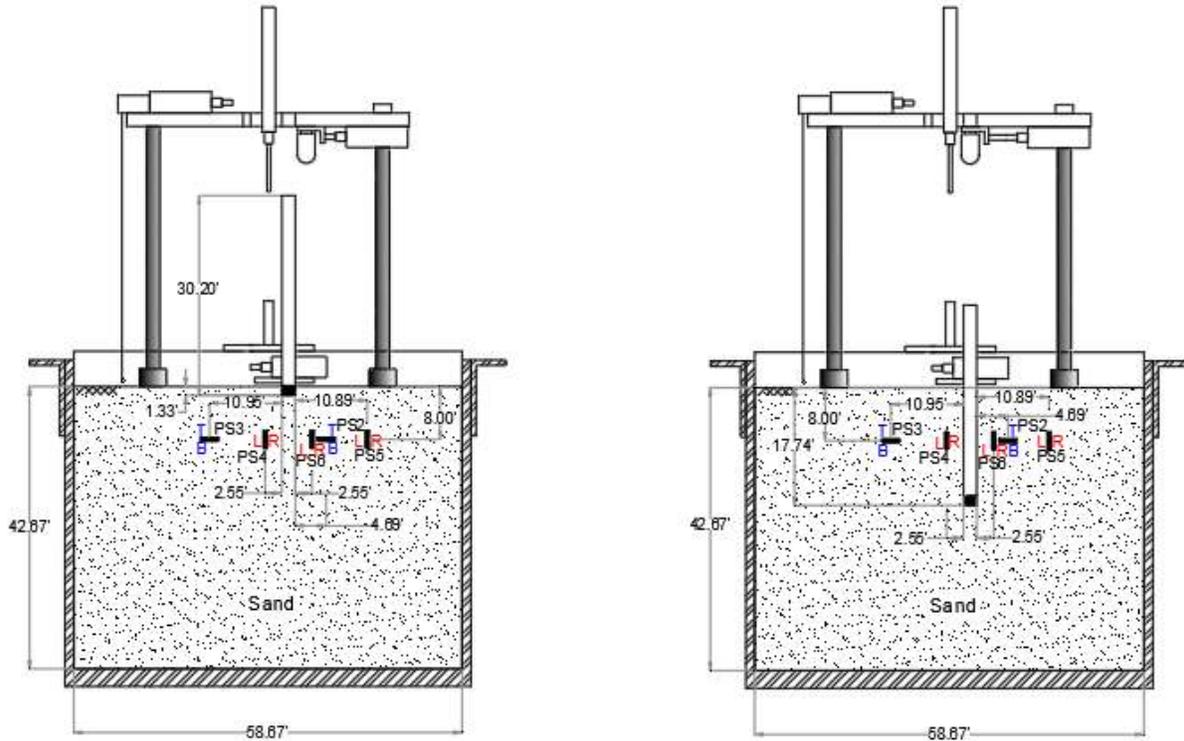
Figure 2.9 Centrifuge test setup for the first loading scenario. Note that PS stands for pressure sensor. For horizontal stress measurement of the PS4, PS5 and PS6, the two sides of each sensor are denoted by L (left side) and R (right side). For vertical stress measurement of the PS2 and PS3, the two sides of each sensor are denoted by T (top) and B (bottom).
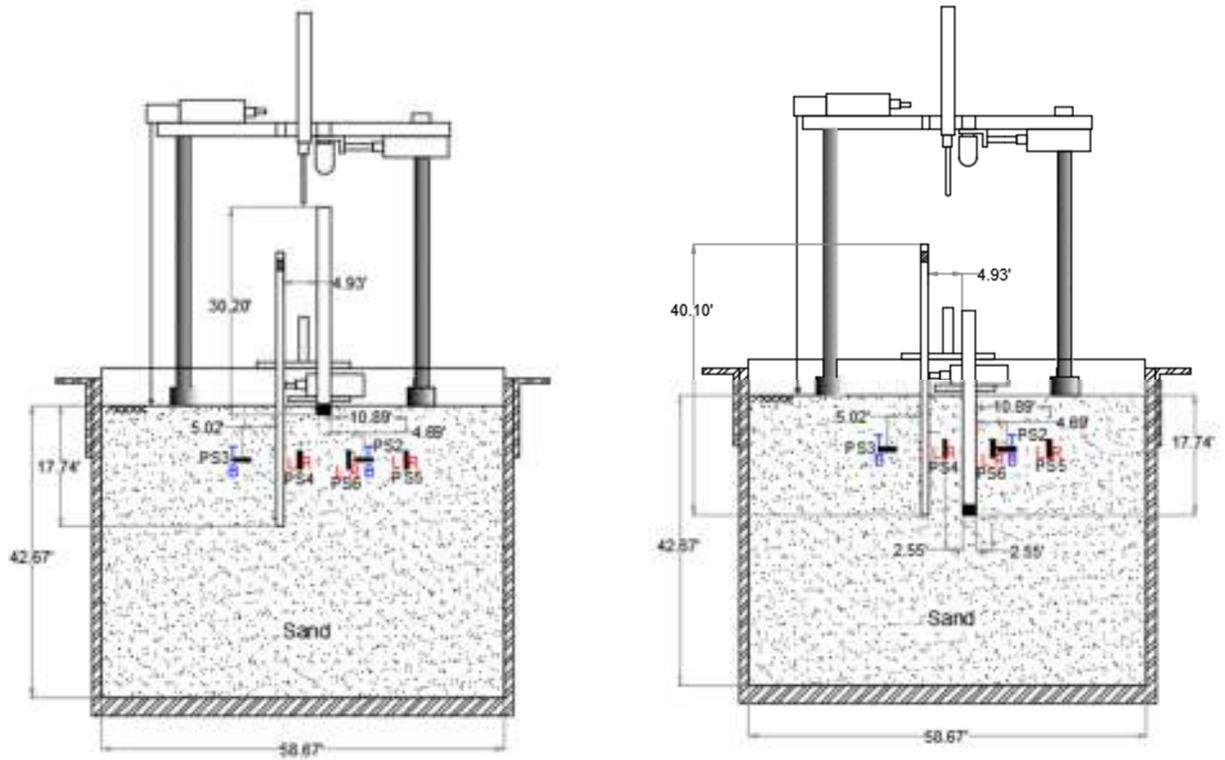
Figure 2.10 Centrifuge test setup for the second loading scenario. Note that PS stands for pressure sensor. For horizontal stress measurement of the PS4, PS5 and PS6, the two sides of each sensor are denoted by L (left side) and R (right side). For vertical stress measurement of the PS2 and PS3, the two sides of each sensor are denoted by T (top) and B (bottom).
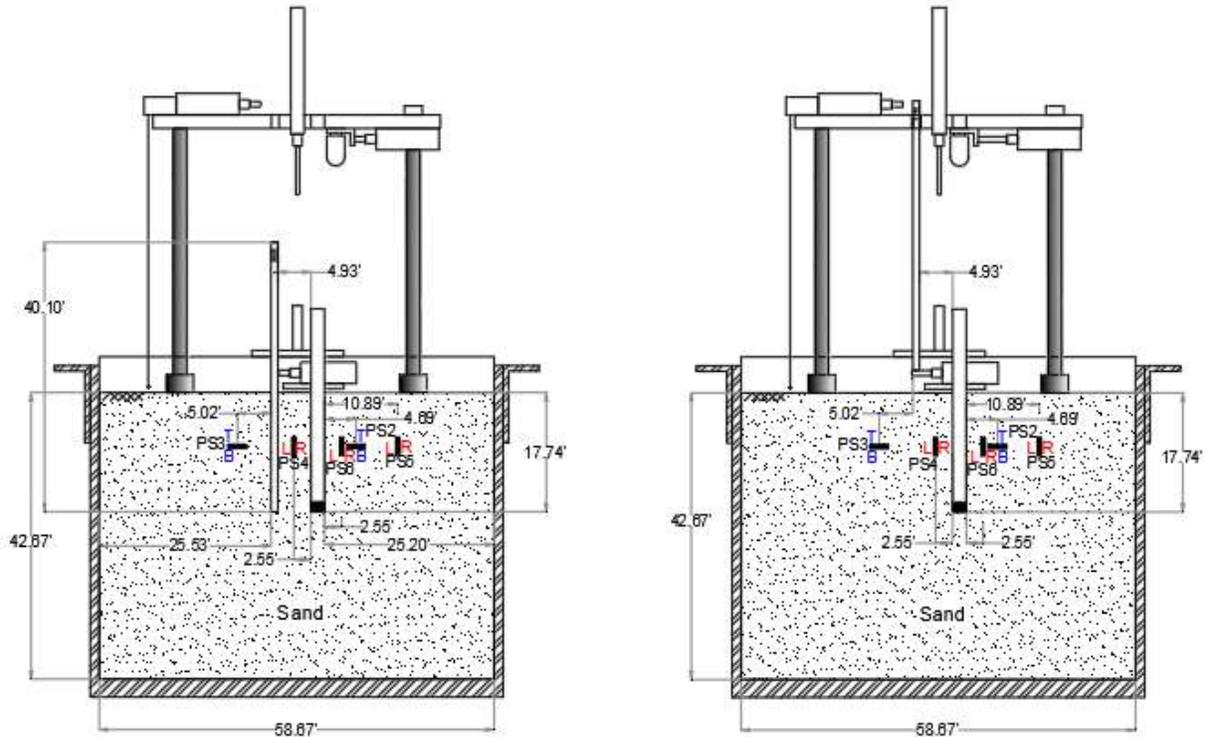
Figure 2.11 Centrifuge test setup for the third loading scenario. Note that PS stands for pressure sensor. For horizontal stress measurement of the PS4, PS5 and PS6, the two sides of each sensor are denoted by L (left side) and R (right side). For vertical stress measurement of the PS2 and PS3, the two sides of each sensor are denoted by T (top) and B (bottom).

2.6   Pile Load Testing

As described earlier, two series of load tests were performed to check the repeatability and validity of centrifuge tests. The results from different loading scenarios are compared in Figs. 2.12-2.13 for the (a) Ultimate and (b) Davisson capacities. In the case of Davisson Offset Limit Method, the load corresponding to the movement that exceeds the elastic compression of the pile by 0.15 + B/120 (in unit of inch), where B is width of the square pile. Also presented in Table 2.4 are both the Ultimate and Davisson Capacities per load scenarios.

Evident from Figs. 2.12 and 2.13, Scenario 2 has a significant effect on the pile's load settlement response. Specifically, installing the sheet pile wall followed by driving the pile and performing a load test increasing the ultimate capacity (both side and tip) of the pile compared to Scenario 1 (single pile). However, to develop the pile's ultimate capacity, it has to displace significantly more than Scenario 1. This behavior is similar to pile group vs. single pile response reported by O'Neil (2001). That is, T-Z (side) and Q-Z (tip) curves of pile become stiffer (Force/displacement) due to the nearby pre-installed SPW. In case of Scenario 3, the removal of the sheet pile wall near the pile, loosens the soil and results in a reduced stiffness as well as Davisson capacity of pile for Scenario 3 vs. 1. The reduced confinement because of the SPW removal is manifested in the stress time histories described in the following sections (e.g. see

16

section 2.8.1). After removing the SPW, horizontal soil stress drops to a value lower than that for scenario 1, causing a reduction in axial pile capacity in small displacements compared to scenario 1. In large displacements, the ultimate capacity values for scenario 1 and 3 are about the same (see Fig. 2.17).

Fig. 2.14 shows the load-displacement responses during all three scenarios on the single pile in the vicinity of the SPW driven to the half depth. Sand relative density was maintained at 65%. Comparing scenario 1 load-displacement responses from tests 2 and 3, a reasonable repeatability has been achieved (Fig. 2.15). Comparing scenario 2 tests results, decreasing the SPW embedment depth has reduced the pile capacity in test 3 compared to test 2 (Fig. 2.16). After removing the SPW in scenario 3, less pile capacity reduction has been observed in test 3 than test 2 (Fig. 2.17). Scenario 3 ultimate capacity values in displacements greater than 1.5 in are, however, about the same with that in scenario 1. Ultimate and Davisson capacity values are shown in Fig. 2.14b and reported in Table 2.5.

Table 2.3 Ultimate and Davisson Capacity for the piles in each scenario

Load Test Scenario	Ultimate Capacity (kips)	Davisson Capacity (kips)
Scenario 1 – Test 1	468	150
Scenario 1 – Test 2	547	152
Scenario 2 – Test 1	728	182
Scenario 2 – Test 2	807	184
Scenario 3 – Test 1	509	80
Scenario 3 – Test 2	606	106
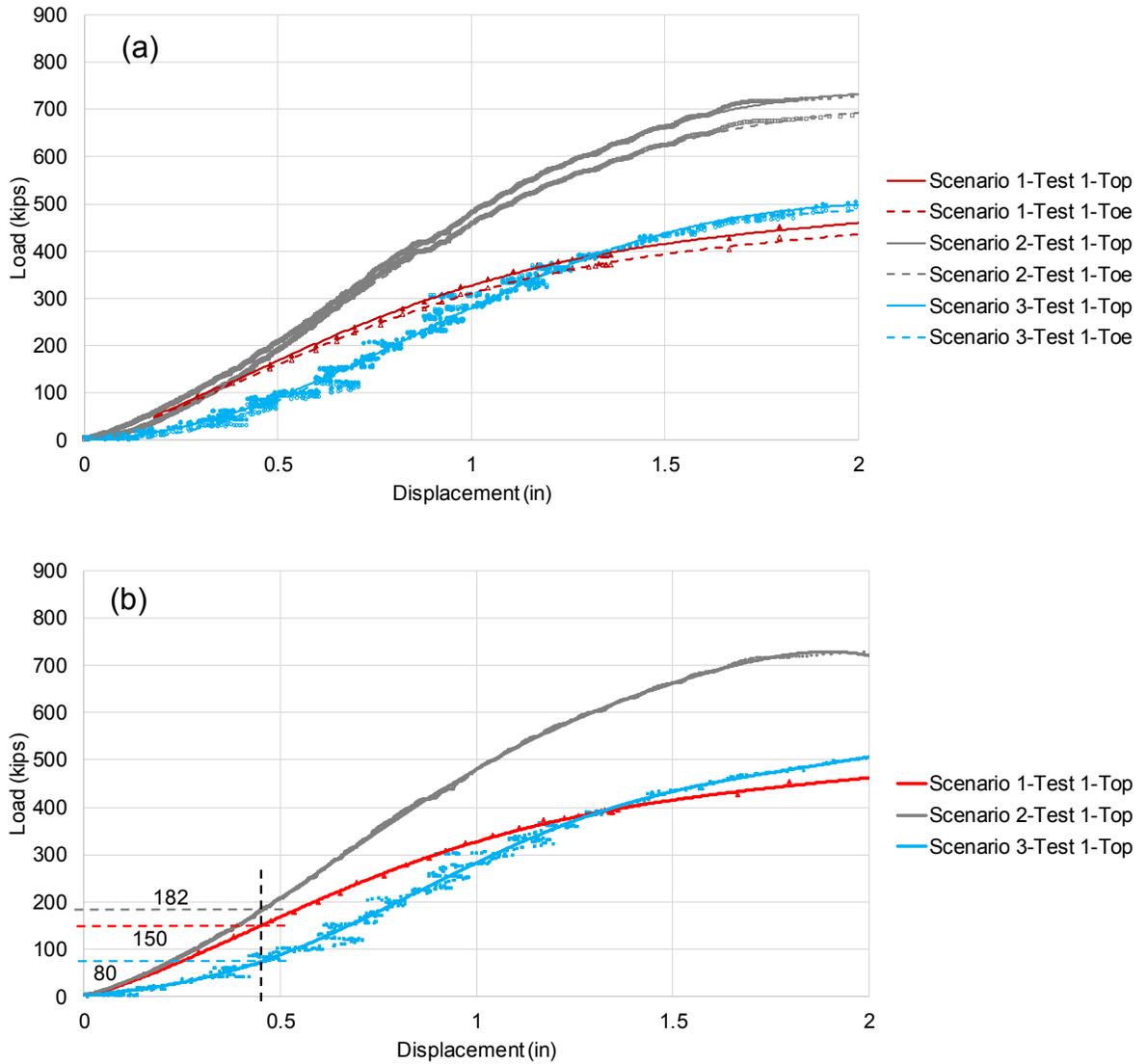
Figure 2.12 (a) Ultimate and (b) Davisson pile load-displacement response for three scenarios in sand with relative density of average 60%
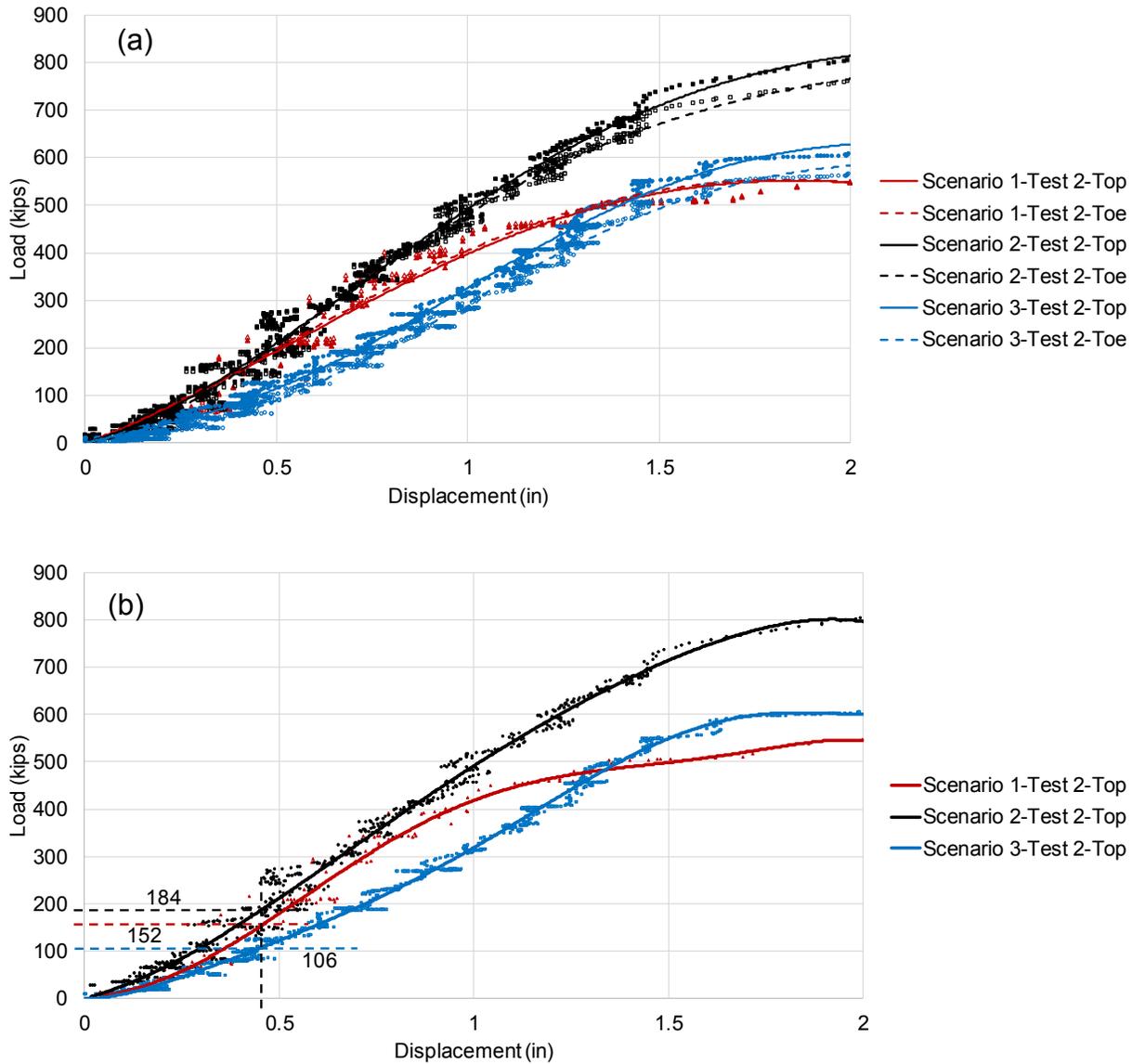
Figure 2.13 (a) Ultimate and (b) Davisson pile load-displacement response for three scenarios in sand with relative density of average 65%
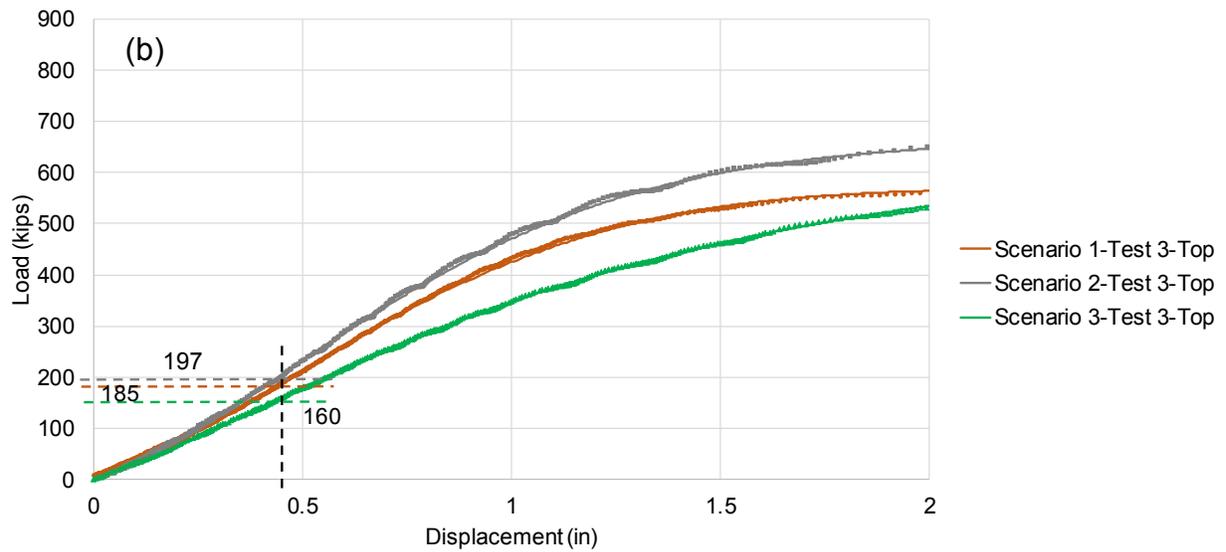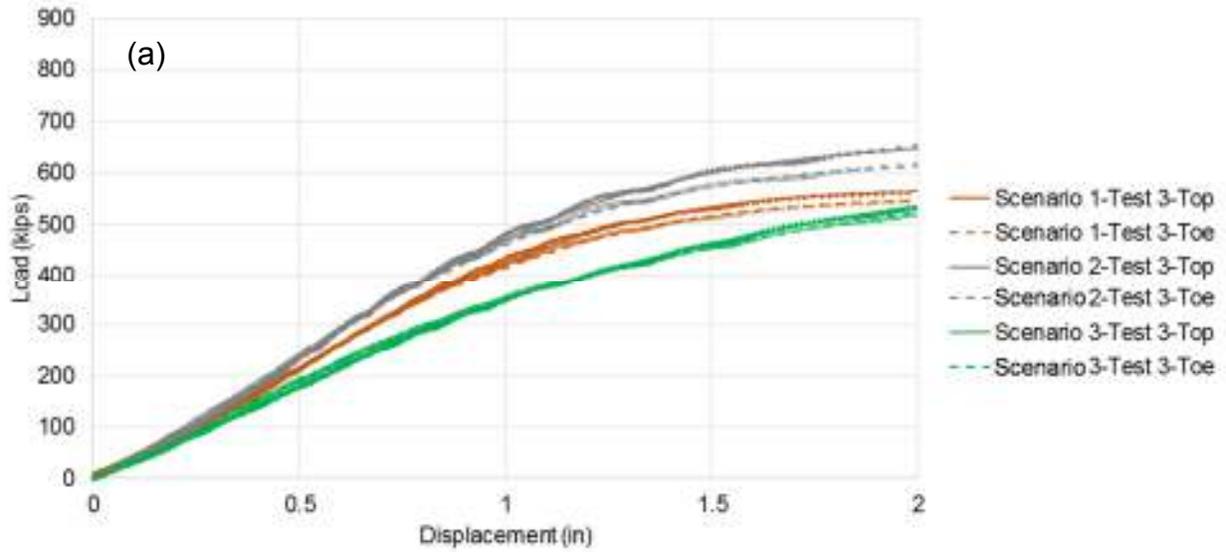
Figure 2.14 (a) Ultimate and (b) Davisson pile load-displacement response for three scenarios in sand with relative density of average 65% (SPW tip elevation is half of the pile tip elevation)

Table 2.4 Ultimate and Davisson Capacity for the piles in each scenario; SPW driving depth is half pile penetration depth

Load Test Scenario	Ultimate Capacity (kips)	Davisson Capacity (kips)
Scenario 1 – Test 3	561	197
Scenario 2 – Test 3	649	185
Scenario 3 – Test 3	534	160

20
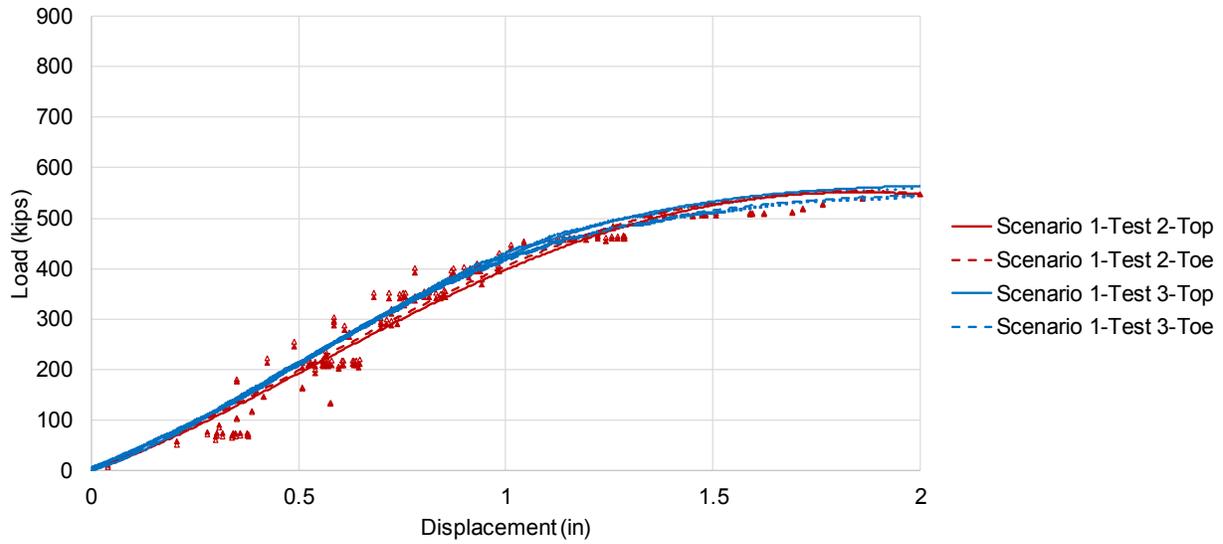
Figure 2.15 Repeatability of scenario 1 test results
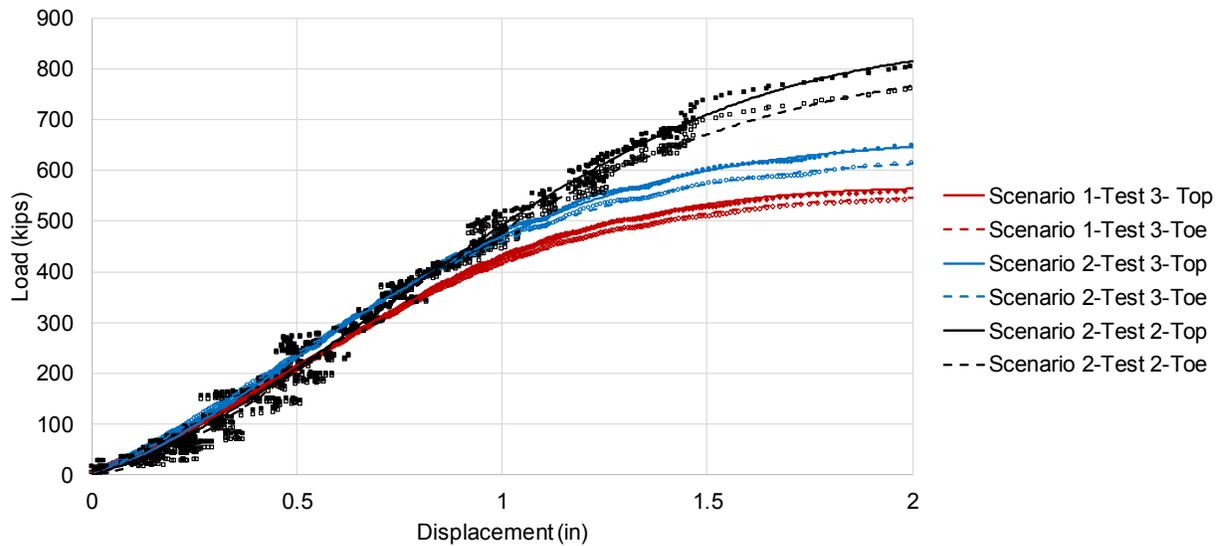
Figure 2.16 Scenario 2 load test results for the cases where the SPW tip depth is same as the pile tip depth (test 2) and the SPW tip depth is half of the pile tip depth (test 3). Responses are also compared with scenario 1 load test results. Sand relative density is 65%.
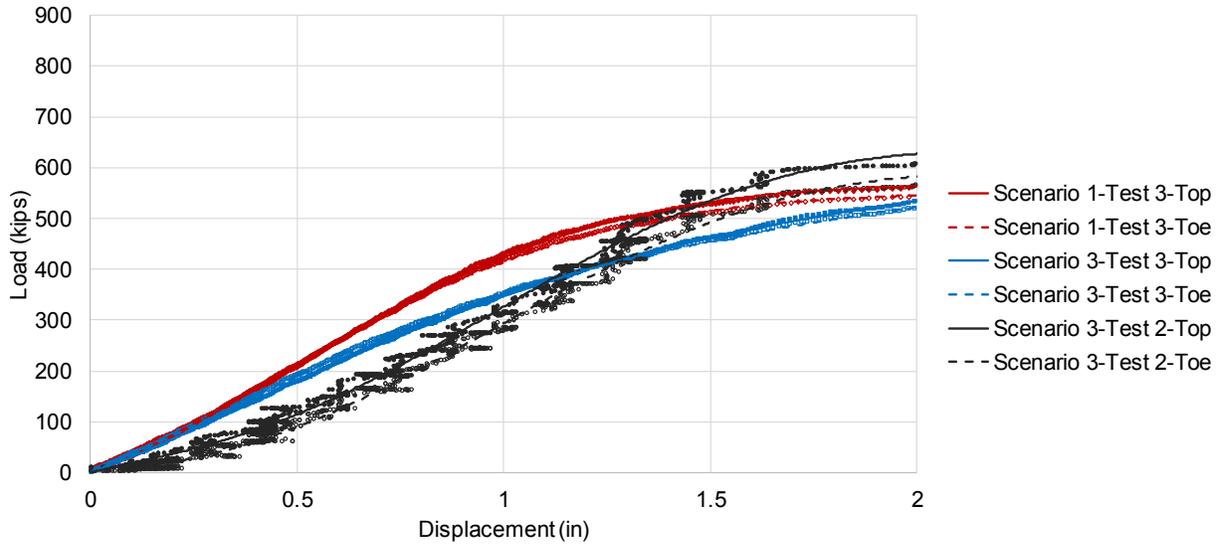
Figure 2.17 Scenario 3 load test results for the cases where the SPW tip depth is same as the pile tip depth (test 2) and the SPW tip depth is half of the pile tip depth (test 3). Responses are also compared with scenario 1 load test results. Sand relative density is 65%.

2.7 Vertical Stress – Time Histories

2.7.1 Equal SPW and Pile Tip Depths

Stress time histories should be interpreted considering the tip elevation of structural objects (i.e. pile or SPW) with respect to the pressure sensor elevation. All pressure sensors were buried in 8 ft depth in the soil profile. As stated earlier, the pile was driven to the target depth by five impact loads (i.e. five blow counts). In a few cases, however, a couple more impacts were needed to drive the pile to the target depth. This was because pile driving was performed in-flight by a displacement-controlled procedure and moving the pile driving hammer manually downward and then upward. The pile tip elevation at the end of each impact load was about -5.0 ft, -8.0 ft, -10.5 ft, -13.5 ft, and -17.7 ft, respectively.

The PS2 pressure sensor was located at a 2.3 B distance at the right side of the pile to record the changes in vertical stress during the centrifuge tests (see Figs. 2.8 - 2.11). As shown in Figs. 2.18 - 2.22a, during pile driving in all centrifuge tests, when the hammer impacted the pile top, a spike in the vertical stress was observed. This was followed by a sudden decrease in the vertical stress due to the passage of stress waves and pile rebound. After the first impact the vertical stress was decreased compared to the geostatic stress, which could be due to the pile moving sand grains from its near-field region to the sides, causing a reduction in overburden stress and increase in horizontal stresses, which is seen in Figs. 2.26 – 2.33. A positive cumulative vertical stress was observed after the second, third, and fourth impacts as a results of sand densification during pile driving when pile tip was same or lower than the pressure sensor elevation. In most pile driving cases, however, the cumulative vertical stress decreased after the fifth impact load. The decreasing trend in vertical stress was seen in the quasi-static top-down load tests in all loading scenarios. This was because in pile load testing, the stress state of near-field soil gets closer or even reaches

its failure criteria in normal stress because shear stress space causes a reduction in vertical stress (Fig. 2.22b). Evident from the stress time histories described in the following sections, both vertical and horizontal stresses decrease during the load tests, causing the Mohr circle to get closer to the Mohr failure envelope.

The SPW was driven to -17.7 ft elevation in Scenarios 2 and 3, the same elevation where the pile was driven afterward. The piston of the cylinder installed on top of the top plate was extended to the slot in top of the SPW to freely hang and then drive it to the target depth in flight by rapidly moving the top plate downward in a displacement-controlled procedure. The rapid downward movement of the SPW helped to simulate dynamic driving conditions in the field. During SPW driving in scenario 2 and 3, a spike followed by a decrease in vertical stress was observed. Similar to the pile driving, this was because of the applied impact once the SPW touched the ground surface for the first time, and then, passage of stress waves caused a sudden reduction. Further driving the SPW into deeper elevations densified the sand and increased the cumulative vertical stress during driving.

The SPW removal from the soil in scenario 3 was done in two steps. In the first and second steps, the SPW was withdrawn 9.5 ft and 8.2 ft, respectively. A sudden increase in vertical stress at the beginning of both steps was observed due to the soil stress wave. However, after the passage of the stress waves and once the SPW-soil system reached an equilibrium state, the vertical stress was decreased.

2.7.2 Lower SPW Tip Depth than the Pile Tip Depth

Figs. 2.23-2.25 present vertical stress time histories for the cases where the SPW tip was located at the half depth (8.87 ft), compared to the pile tip depth (17.74 ft). Similar trends and stress amplitudes have been observed compared to the cases where the SPW and the pile tips were at the same depth. This is mainly because in both cases, the SPW penetrates beyond the location of the PS2 pressure sensor (located at 8-ft depth), producing similar vertical stresses.
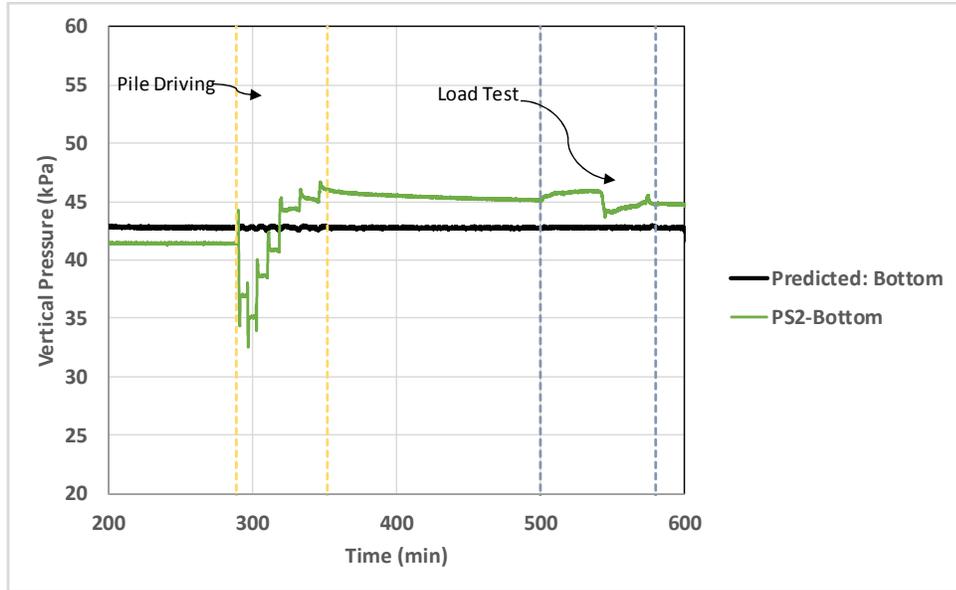
Figure 2.18 Vertical stress time history recorded by PS2 at 2.3B, right side of the pile: Scenario 1

Figure 2.19 Vertical stress time history recorded by PS2 at 2.3B, right side of the pile: Scenario 2 – Test 1

Figure 2.20 Vertical stress time history recorded by PS2 at 2.3B, right side of the pile: Scenario 2
– Test 2

Figure 2.21 Vertical stress time history recorded by PS2 at 2.3B, right side of the pile: Scenario 3
– Test 1

25
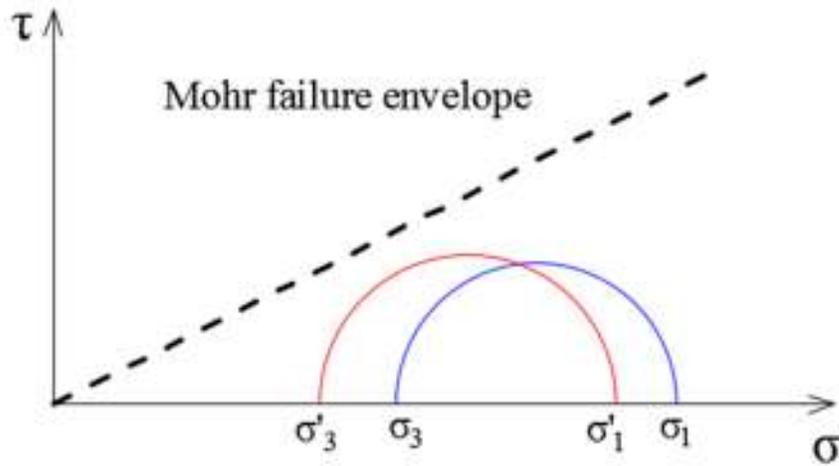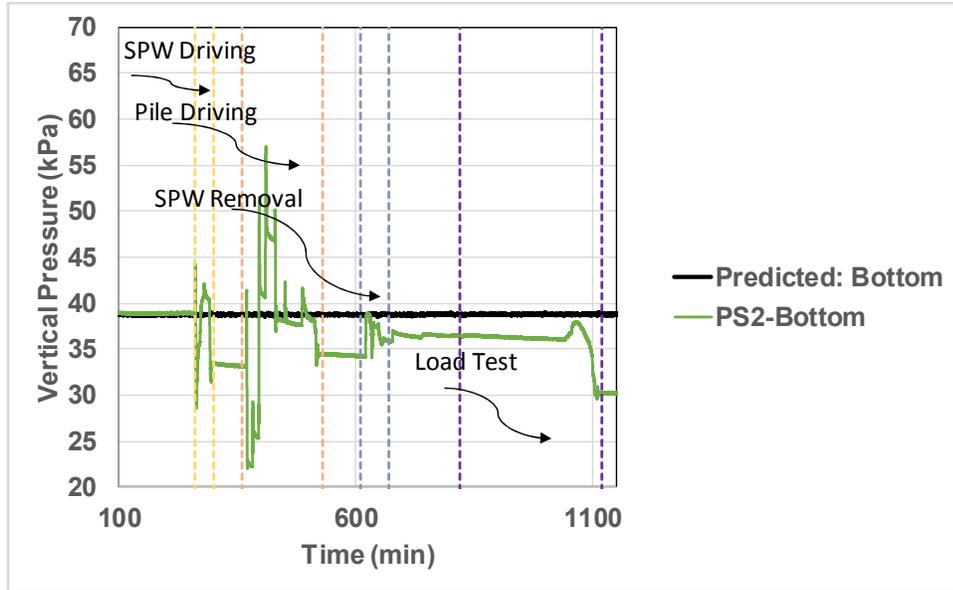
Figure 2.22 (a) Vertical stress time history recorded by PS2 at 2.3B, right side of the pile in Scenario 3 – Test 2 (top); (b) a schematic sketch of Mohr's circles during load tests (bottom).

Figure 2.23 Vertical stress time history recorded by PS2 at 2.3B, right side of the pile: Scenario 1 – Test 3 (SPW tip elevation is half of the pile tip elevation)

Figure 2.24 Vertical stress time history recorded by PS2 at 2.3B, right side of the pile: Scenario 2 – Test 3 (SPW tip elevation is half of the pile tip elevation)

27

Figure 2.25 Vertical stress time history recorded by PS2 at 2.3B, right side of the pile: Scenario 3 – Test 3 (SPW tip elevation is half of the pile tip elevation)

2.8 Horizontal Stress Time Histories in Far-Field

2.8.1 Equal SPW and Pile Tip Depths

The PS5 pressure sensor was buried at a 5.5 B distance from the right side of the pile to measure horizontal stresses in far-field (see Figs. 2.8 - 2.11). As shown in Figs. 2.26 - 2.30, consistent trends in far-field horizontal stress time histories were observed during all centrifuge tests. During pile driving, a horizontal stress spike was observed when the pile impacted the ground. This was followed by a sudden decrease in stress as the stress waves passed and pile rebounded. It seems pile driving reduces sand relative density in far-field causing a cumulative reduction in the horizontal stress. A decreasing trend in far-field horizontal stress was seen in quasi-static top-down load tests in all loading scenarios.

During SPW driving in scenario 2 and 3, the horizontal stress has been significantly increased in far-field by 122% - 135% compared to the geostatic horizontal stress conditions. This may be attributed to soil densification and the size of sheet pile vs. pile. As described earlier, the difference in the horizontal stress increase between different centrifuge tests is due to the manual SPW driving system, where the time of applied impact for SPW driving might slightly differ from one test to another. Once the SPW tip passed the sensor elevation and the SPW-soil system came into equilibrium, a 18% - 28 % reduction in the cumulative horizontal stress was observed.

During SPW removal in scenario 3, an increase in horizontal stress from the two step removal (stress wave) was observed. This increase was followed by a subsequent and cumulative decrease in horizontal stress in far-field. As stated earlier, in scenario 3, the total cumulative horizontal stress reduction was due to both pile driving and SPW removal, where at the end of SPW removal,

the horizontal stress in far-field was only about 37% (compared to 122% - 135% increase after driving the SPW) more than the geostatic horizontal stress at the beginning of the test.

2.8.2 Lower SPW Tip Depth than the Pile Tip Depth

Figs. 2.31-2.33 show the far-field horizontal stress time histories for the cases where the SPW tip was located at the half depth (8.87 ft) compared to the pile tip depth (17.74 ft). Similar trends have been observed compared to the cases where the SPW and the pile tips were at the same depth. However, as this time the SPW has produced lower confinement due to its lower embedment, the horizontal stress increase after SPW driving (in both scenario 2 and 3) in test 3 is less than that in test 2. As a result, in scenario 2, the bearing capacity in test 3 is less than test 2 (see Figs. 2.13 and 2.14).
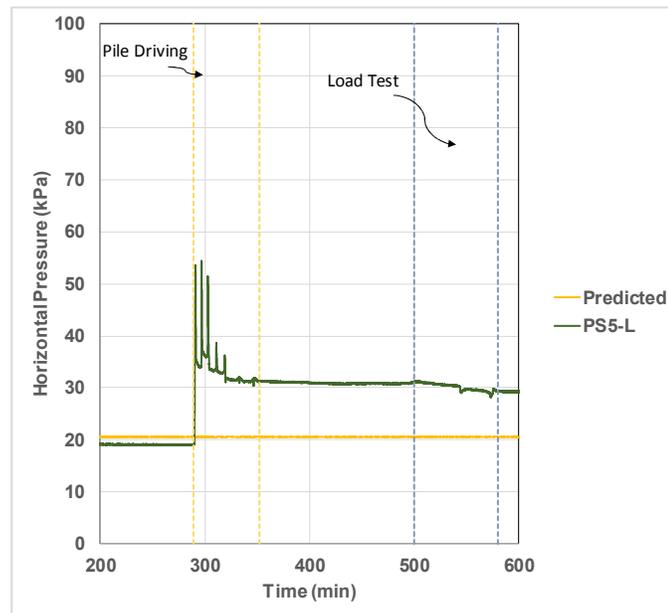
Figure 2.26 Horizontal stress time history recorded by PS5 at 5.5B, right side of the pile: Scenario 1
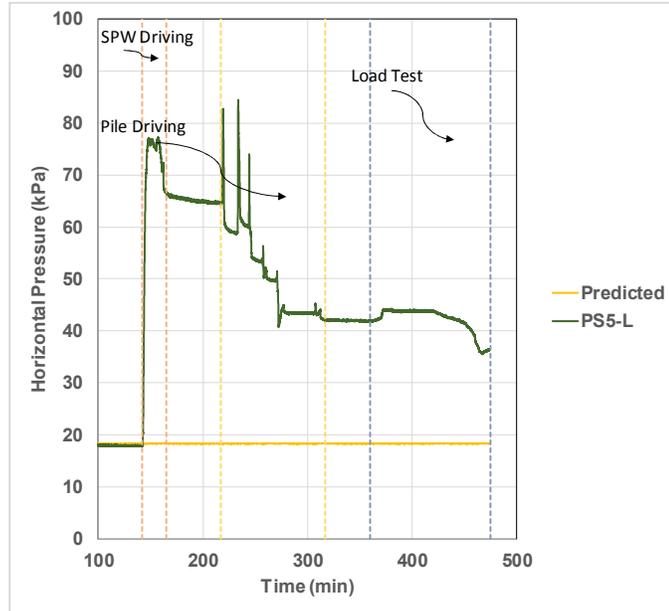
Figure 2.27 Horizontal stress time history recorded by PS5 at 5.5B, right side of the pile:
Scenario 2 – Test 1
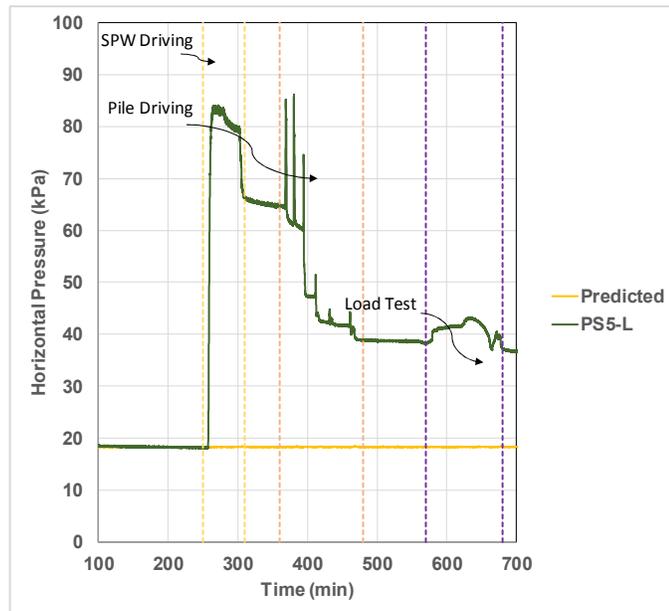
Figure 2.28 Horizontal stress time history recorded by PS5 at 5.5B, right side of the pile:
Scenario 2 – Test 2
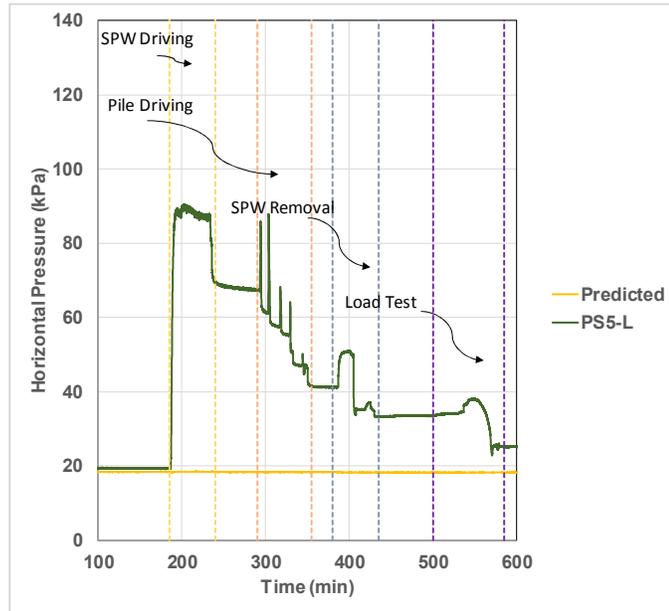
Figure 2.29 Horizontal stress time history recorded by PS5 at 5.5B, right side of the pile:
Scenario 3 – Test 1
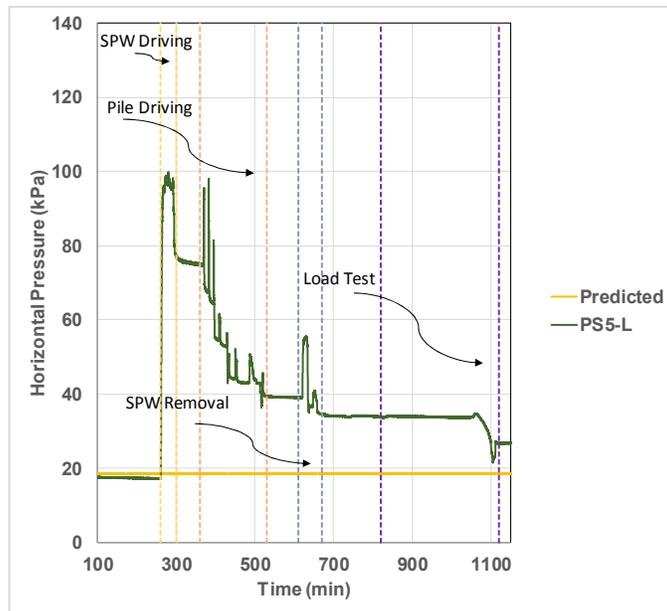
Figure 2.30 Horizontal stress time history recorded by PS5 at 5.5B, right side of the pile:
Scenario 3 – Test 2
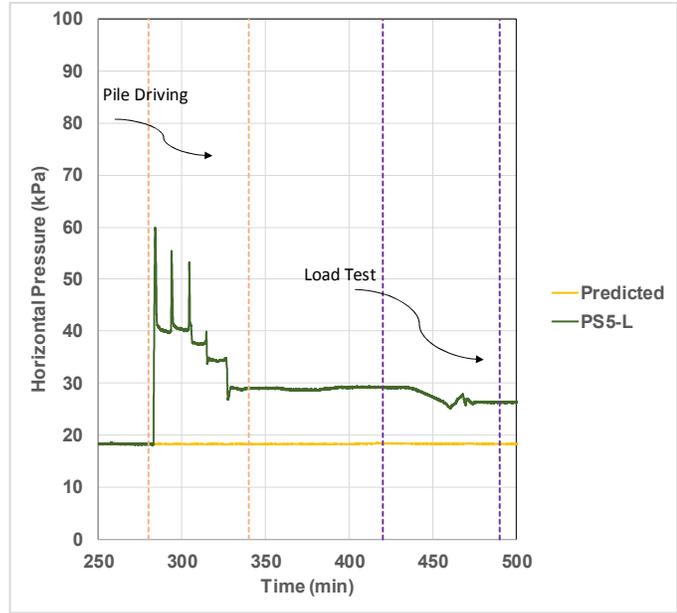
Figure 2.31 Horizontal stress time history recorded by PS5 at 5.5B, right side of the pile:
Scenario 1 – Test 3 (SPW tip depth is half of the pile tip depth)
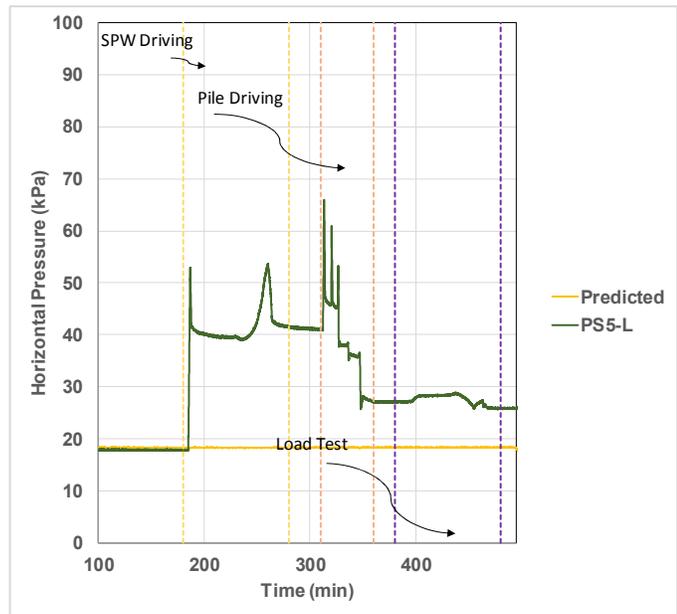
Figure 2.32 Horizontal stress time history recorded by PS5 at 5.5B, right side of the pile:
Scenario 2 – Test 3 (SPW tip depth is half of the pile tip depth)
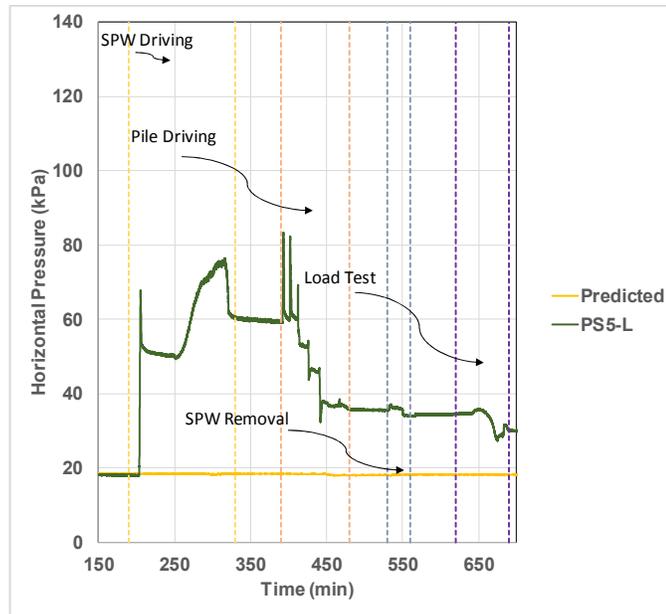
Figure 2.33 Horizontal stress time history recorded by PS5 at 5.5B, right side of the pile: Scenario 3 – Test 3 (SPW tip depth is half of the pile tip depth)

2.9 Horizontal Stress Time Histories between the Pile and the SPW

2.9.1 Equal SPW and Pile Tip Depths

The PS4 pressure sensor was buried at a 1.25 B distance from the pile to the SPW to measure horizontal stresses between objects using its two sides (i.e., PS4-L and PS4-R) with PS4-L facing the SPW (see Figs. 2.8-2.11). As shown in Figs. 2.34-2.38, consistent trends in horizontal stress time histories between the pile and the SPW were observed during all centrifuge tests. During pile driving, a horizontal stress spike was observed when the pile impacted the ground. This was followed by a sudden decrease in soil stresses as the stress waves passed and pile rebounded. It seems that the pile driving increased sand relative density between the pile and the SPW during the first impact load where the pile tip elevation was higher than the pressure sensor elevation. This caused a cumulative increase in the horizontal stress as the sand grains pushed against the sensor. Due to the higher confinement, the increase in the horizontal stress between the pile and the SPW due to the pile impact was higher than the increase recorded by the PS6 sensor in the near-field at the right side of the pile (as shown in Figs. 2.42-2.46). It seems that as the pile was driven further, it carried sand grains from the region where the pressure sensor was located, causing a reduction in the relative density and consequently in horizontal stress so that the horizontal stresses became comparable to the geostatic horizontal stresses before the tests (i.e., before driving the structural models). The horizontal stress between the pile and the SPW in quasi-static top-down load tests in Scenarios 2 and 3 tests was equal to the geostatic stresses at the beginning of the tests.

During SPW driving in Scenarios 2 and 3, the horizontal stress significantly increased between the pile and SPW. This increase was much higher than that recorded by the PS6 sensor (as shown in

Figs. 2.42 – 2.46). After driving the SPW to its target depth, the horizontal stresses were 140% - 155% higher than those in geostatic conditions. As described earlier, the difference in the horizontal stress increase between different centrifuge tests is due to the manual SPW driving system, where the time of applied impact for SPW driving might slightly differ from one test to another.

During SPW removal in Scenario 3, a relative increase in horizontal stress due dynamic two steps removal was observed. This increase was followed by a subsequent decrease. As stated earlier, in Scenario 3, the total cumulative horizontal stress reduction was due to SPW removal, where at the end of the SPW removal, the horizontal stresses between the pile and the SPW were similar to the geostatic horizontal stresses at the beginning of the test.

2.9.2 Lower SPW Tip Depth than the Pile Tip Depth

Figs. 2.39-2.41 depict the horizontal stress time histories between the pile and the SPW for the cases where the SPW tip was located at the half depth (8.87 ft) compared to the pile tip depth (17.74 ft). Similar trends have been observed compared to the cases where the SPW and the pile tips were at the same elevation. However, this time the SPW has produced lower confinement due to its lower embedment depth (in both scenario 2 and 3). Consequently, after SPW installation and during pile driving, horizontal stresses are lower in test 3 than that test 2. As a result, in scenario 2, the bearing capacity in test 3 is less than test 2 (see Figs. 2.13 and 2.14). Moreover, in scenario 3, less reduction in bearing capacity has been occurred in test 3 than test 2.
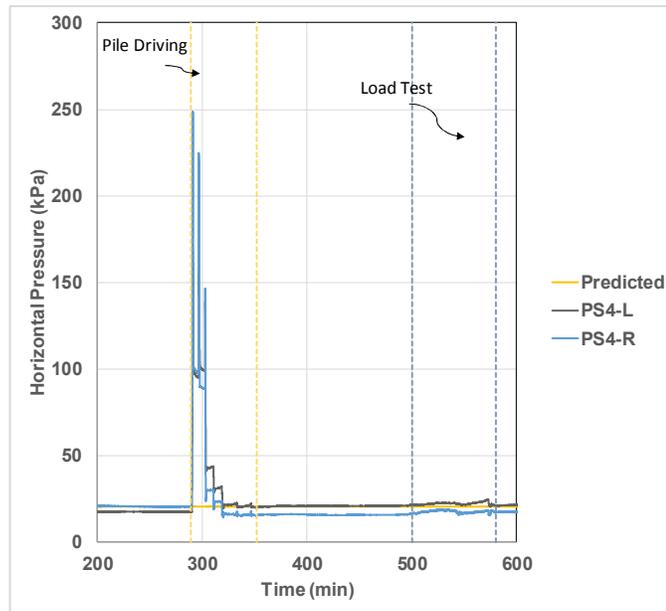
Figure 2.34 Horizontal stress time history recorded by PS4 at 1.25B, right side of the pile: Scenario 1
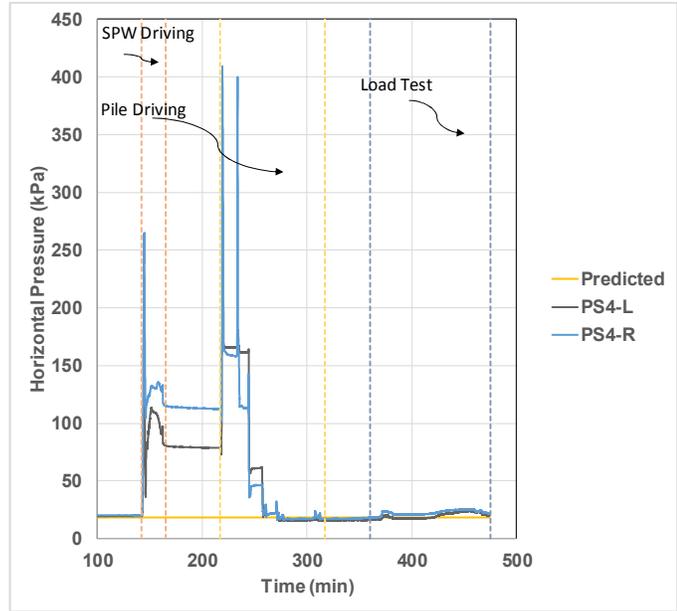
Figure 2.35 Horizontal stress time history recorded by PS4 at 1.25B, right side of the pile: Scenario 2 – Test 1
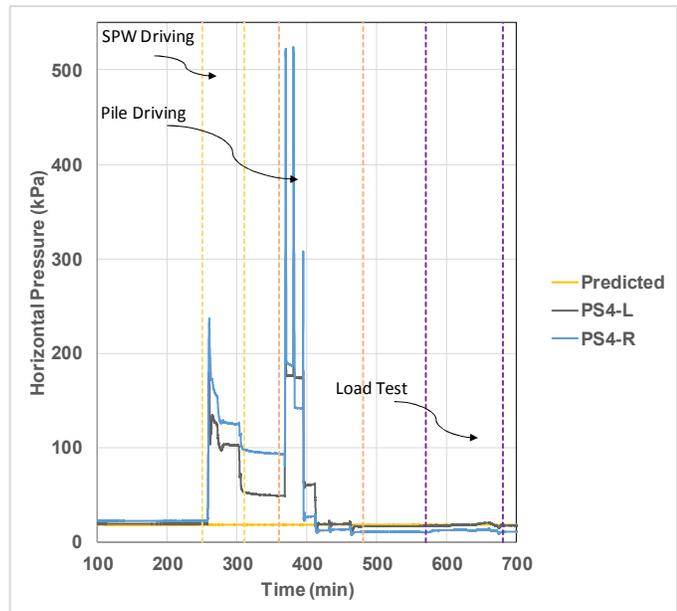
Figure 2.36 Horizontal stress time history recorded by PS4 at 1.25B, right side of the pile: Scenario 2 – Test 2

35
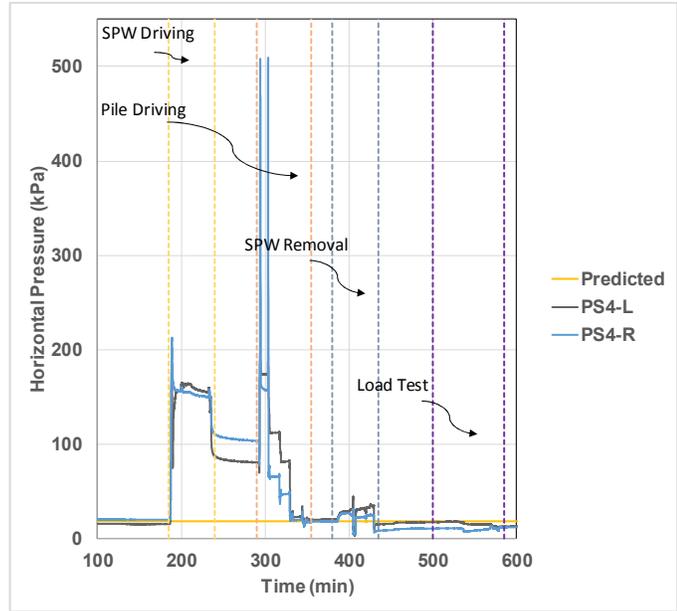
Figure 2.37 Horizontal stress time history recorded by PS4 at 1.25B, right side of the pile: Scenario 3 – Test 1
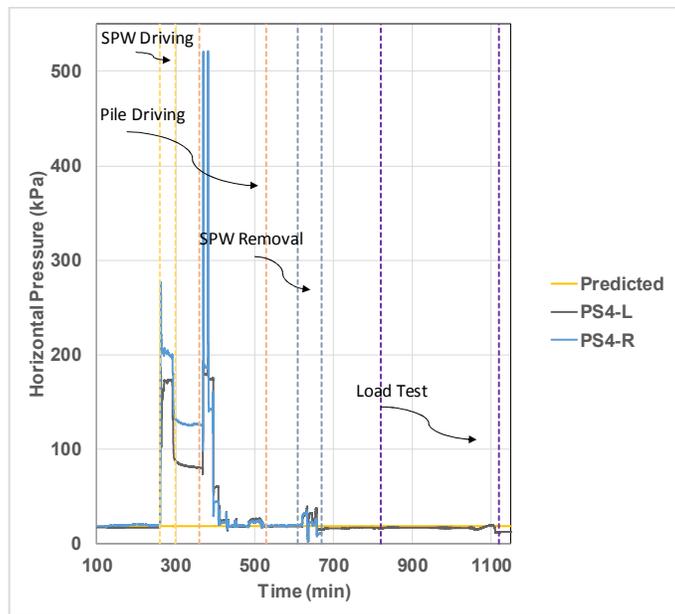
Figure 2.38 Horizontal stress time history recorded by PS4 at 1.25B, right side of the pile: Scenario 3 – Test 2
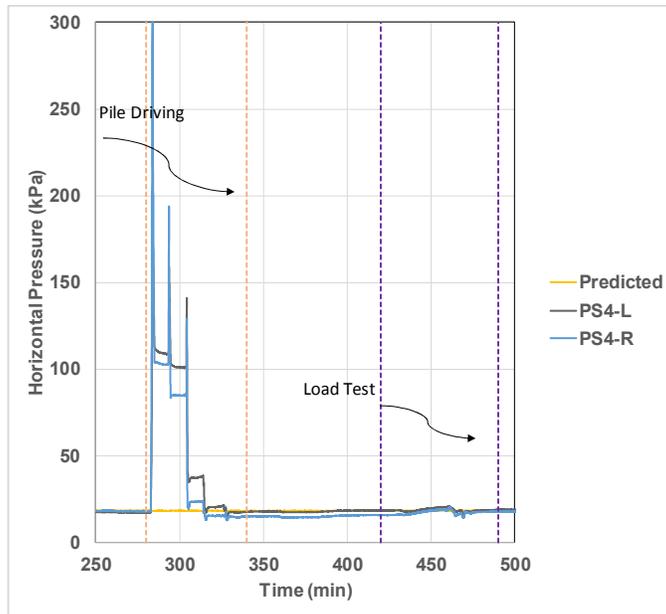
Figure 2.39 Horizontal stress time history recorded by PS4 at 1.25B, right side of the pile: Scenario 1 – Test 3 (SPW tip depth is half of the pile tip depth)
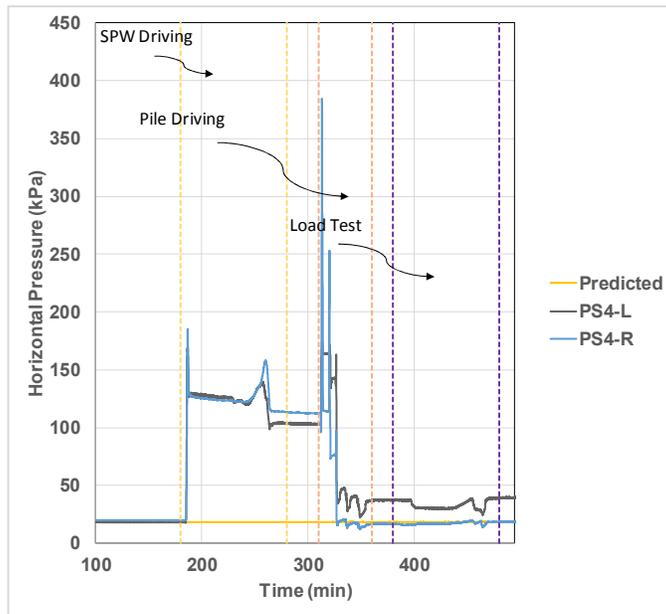
Figure 2.40 Horizontal stress time history recorded by PS4 at 1.25B, right side of the pile: Scenario 2 – Test 3 (SPW tip depth is half of the pile tip depth)
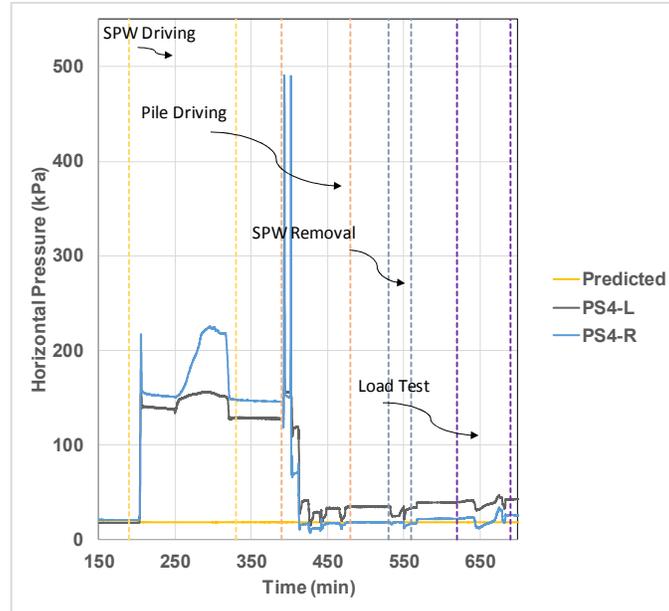
Figure 2.41 Horizontal stress time history recorded by PS4 at 1.25B, right side of the pile:
Scenario 3 – Test 3 (SPW tip depth is half of the pile tip depth)

2.10   Horizontal Stress Time Histories in Near Field

2.10.1 Equal SPW and Pile Tip Depths

The PS6 pressure sensor was buried at a 1.25 B distance from the right side of the pile to measure horizontal stresses in near-field using its two sides (i.e. PS6-L and PS6-R) with PS6-L facing the pile (see Figs. 2.8 - 2.11). As shown in Figs. 2.42 - 2.46, consistent trends in near-field horizontal stress time histories were observed during all centrifuge tests. During pile driving, a horizontal stress spike was observed when the pile impacted the ground. This was followed by a sudden decrease in stress as the dynamic stress waves passed and pile rebounded. It seems pile driving increased sand relative density in near-field during first and second impact loads where the pile tip elevation was equal or higher than the pressure sensor causing a cumulative increase in horizontal stress as the sand grains push against the sensor. As the pile was driven further, it carried sand grains from the region the pressure sensor was located causing a reduction in relative density and consequently in horizontal stress. While a relatively decreasing trend in near-field horizontal stress was seen in quasi-static top-down load tests in scenario 2 tests, an opposite trend was seen in scenario 3 tests.

During SPW driving in scenario 2 and 3, the horizontal stress significantly increased in near-field by 145% - 161% compared to the geostatic conditions. Again, this increase can be attributed to size (volume) of SPW and soil displaced. Also, as described earlier, the difference in the horizontal stress increase between different centrifuge tests is due to the manual SPW driving system, where the time of applied impact for SPW driving might slightly differ from one test to another. Once

the SPW tip passed the sensor elevation and the SPW-soil system came into equilibrium, a 33% - 64 % reduction in the cumulative horizontal stress was observed.

During SPW removal in scenario 3, an increase in horizontal stress at both two steps of removal was observed. This increase was followed by a subsequent decrease where the cumulative decrease in horizontal stress in near-field was rather remained unchanged. As stated earlier, in scenario 3, the total cumulative horizontal stress reduction was due to both pile driving and SPW removal, where at the end of SPW removal, the horizontal stress in near-field was less than 60% (compared to 145% - 161% increase after driving the SPW) more than the geostatic stress at the beginning of the test.

2.10.2 Lower SPW Tip Depth than the Pile Tip Depth

Figs. 2.44-2.49 show the horizontal stress time histories in the near-field at the right side of the pile for the cases where the SPW tip was located at the half depth (8.87 ft) compared to the pile tip depth (17.74 ft). Similar trends have been observed compared to the cases where the SPW and the pile tips were at the same elevation. However, as this time the SPW has produced lower confinement due to its lower embedment depth, in scenario 2 and 3, the horizontal stress increase after SPW driving (during pile driving) in test 3 is relatively less than that in test 2. As a result, in scenario 2, the bearing capacity in test 3 is less than test 2 (see Figs. 2.13 and 2.14). Moreover, in scenario 3, less reduction in the bearing capacity has been occurred in test 3 than test 2.
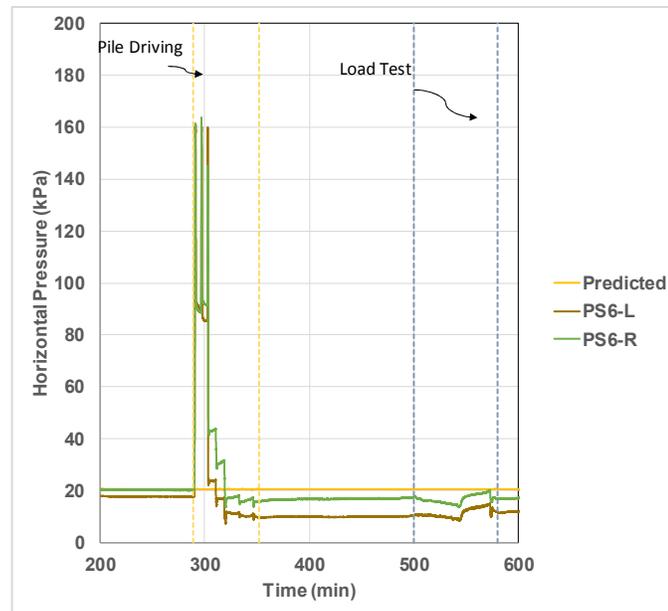
Figure 2.42 Horizontal stress time history recorded by PS6 at 1.25B, right side of the pile: Scenario 1
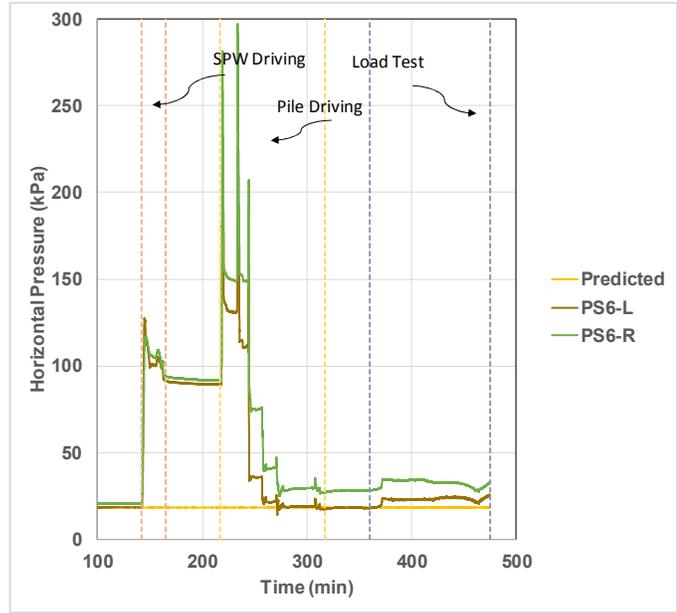
Figure 2.43 Horizontal stress time history recorded by PS6 at 1.25B, right side of the pile:
Scenario 2 – Test 1
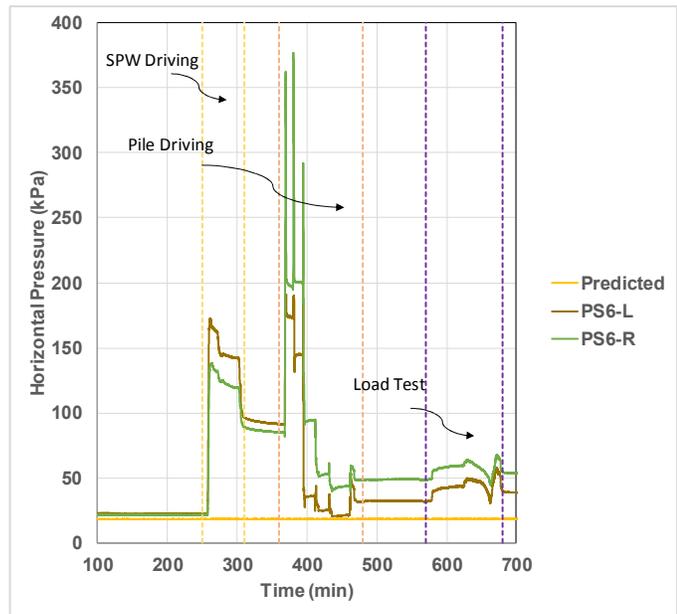
Figure 2.44 Horizontal stress time history recorded by PS6 at 1.25B, right side of the pile:
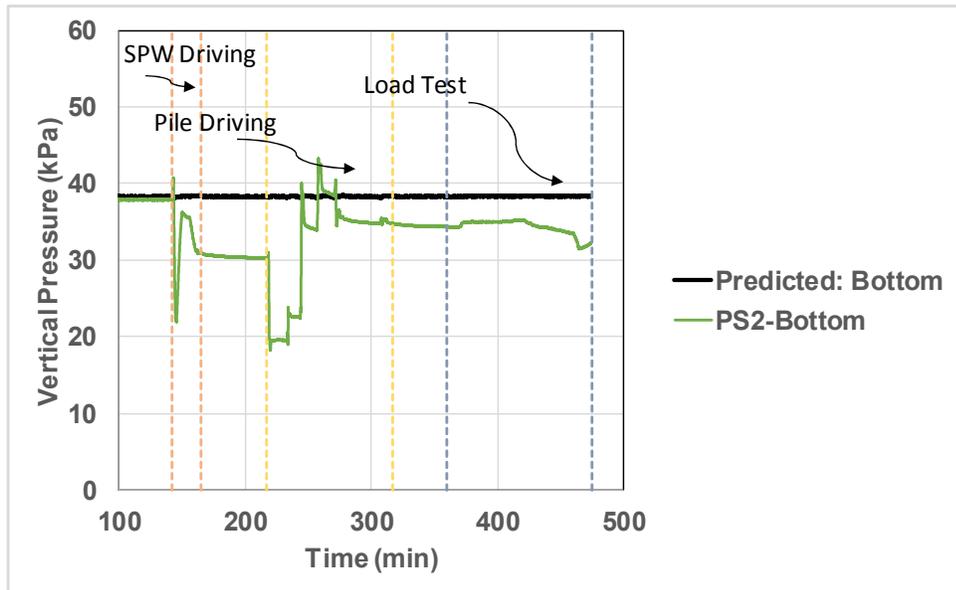Scenario 2 – Test 2
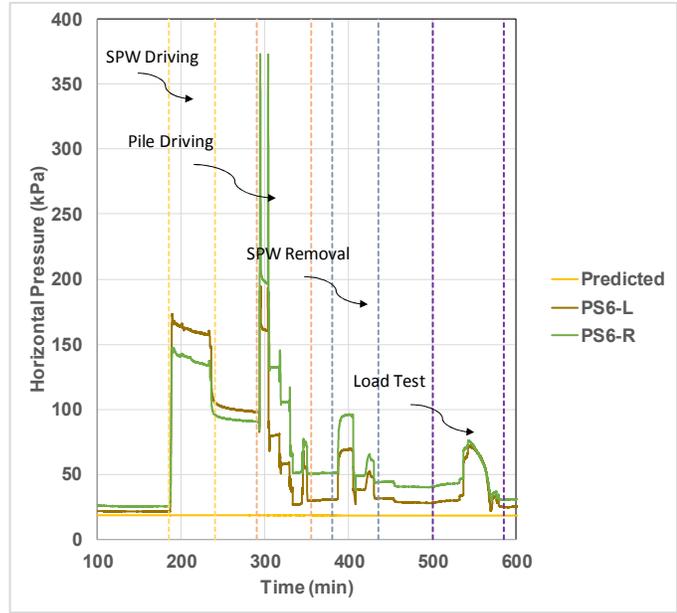
Figure 2.45 Horizontal stress time history recorded by PS6 at 1.25B, right side of the pile: Scenario 3 – Test 1
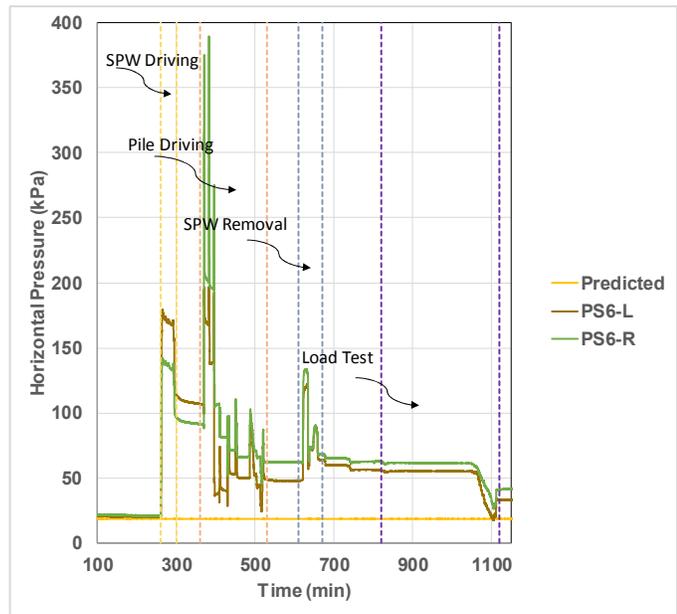
Figure 2.46 Horizontal stress time history recorded by PS6 at 1.25B, right side of the pile: Scenario 3 – Test 1
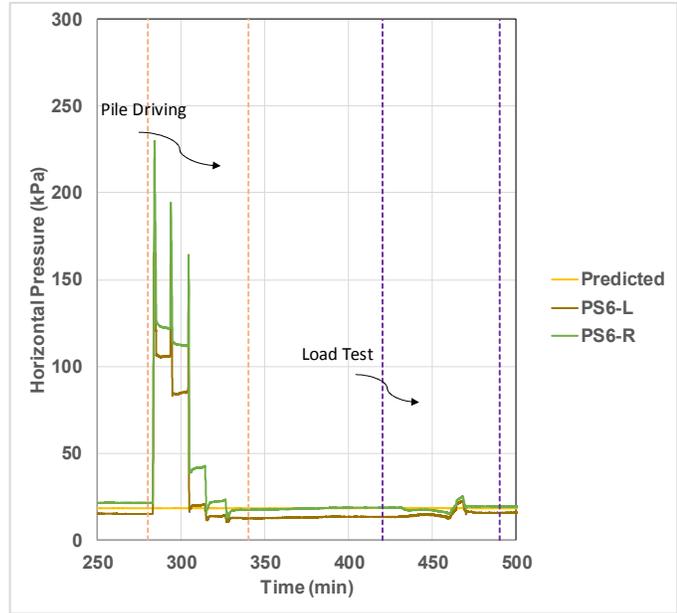
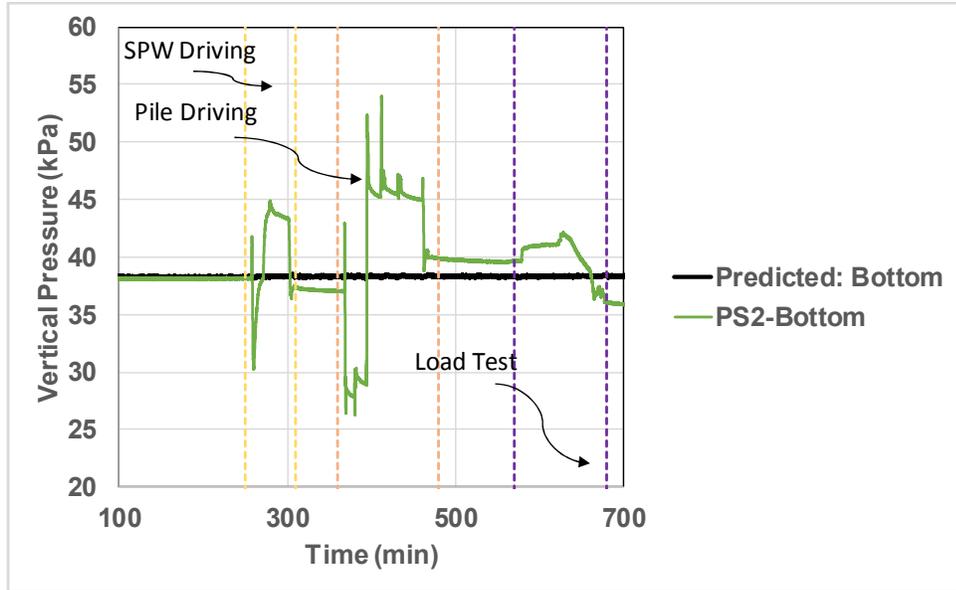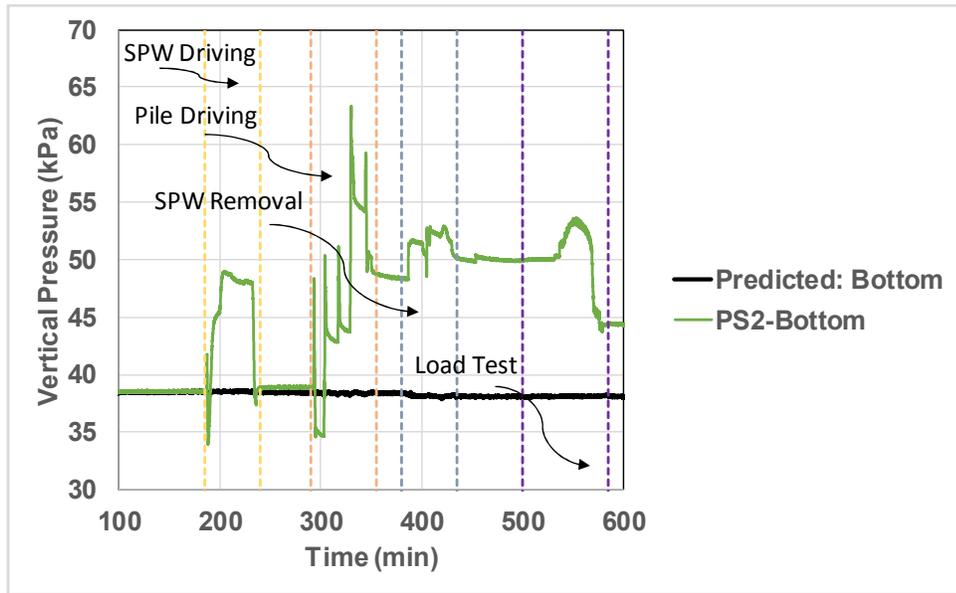Figure 2.47 Horizontal stress time history recorded by PS6 at 1.25B, right side of the pile: Scenario 1 – Test 3 (SPW tip depth is half of the pile tip depth)
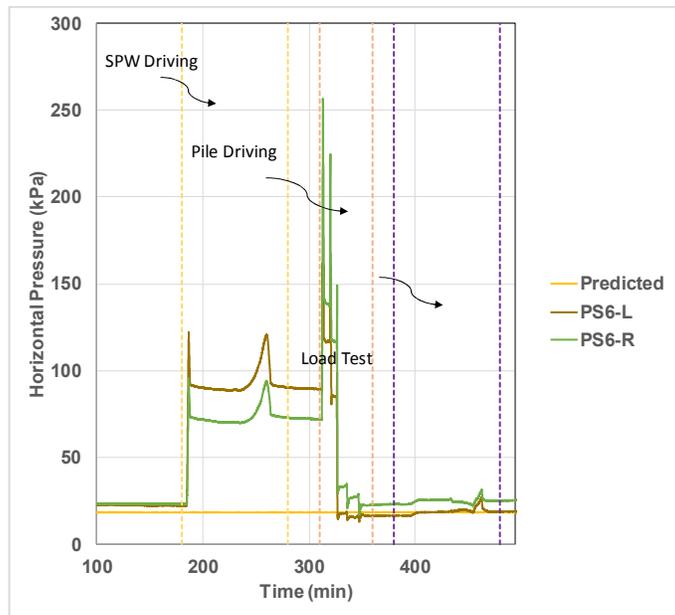
Figure 2.48 Horizontal stress time history recorded by PS6 at 1.25B, right side of the pile: Scenario 2 – Test 3 (SPW tip depth is half of the pile tip depth)
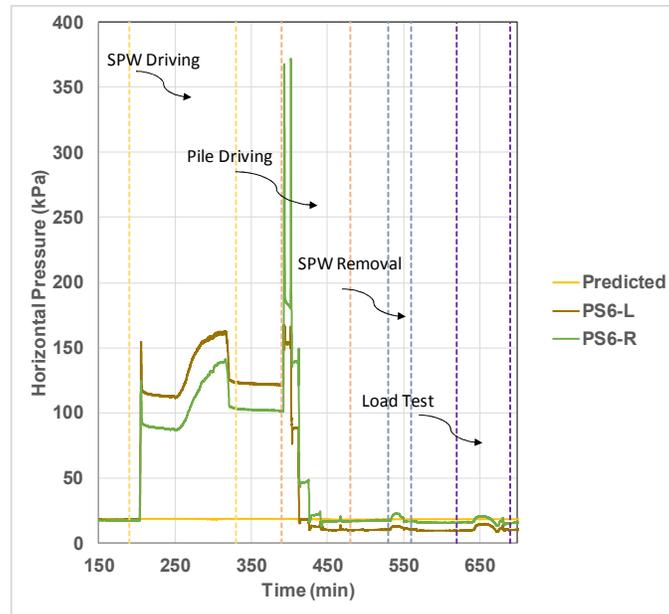
Figure 2.49 Horizontal stress time history recorded by PS6 at 1.25B, right side of the pile:
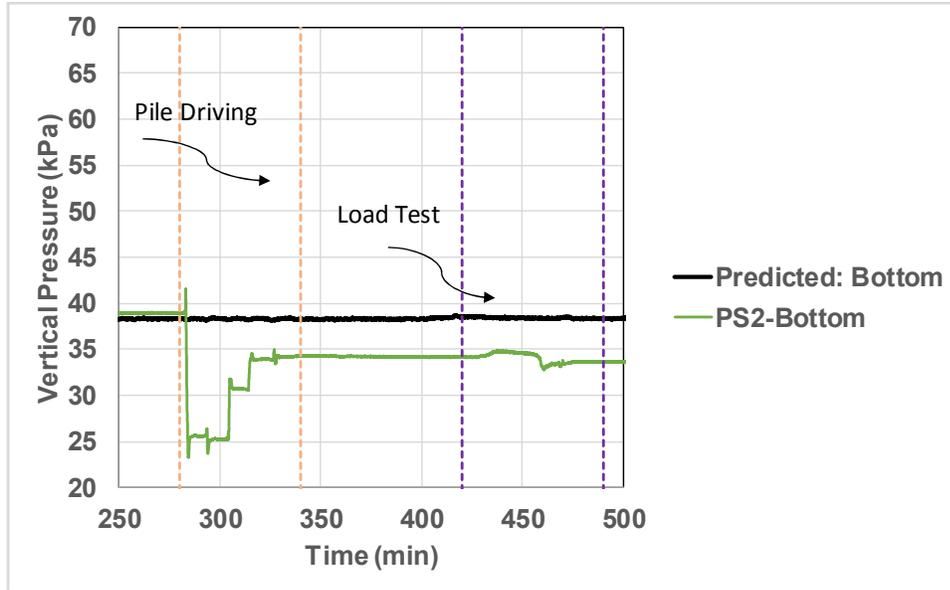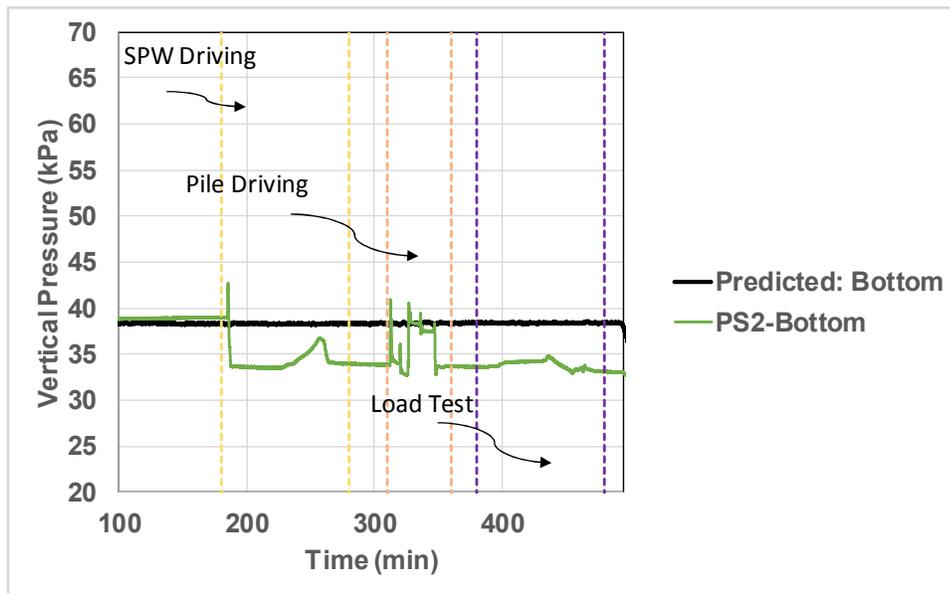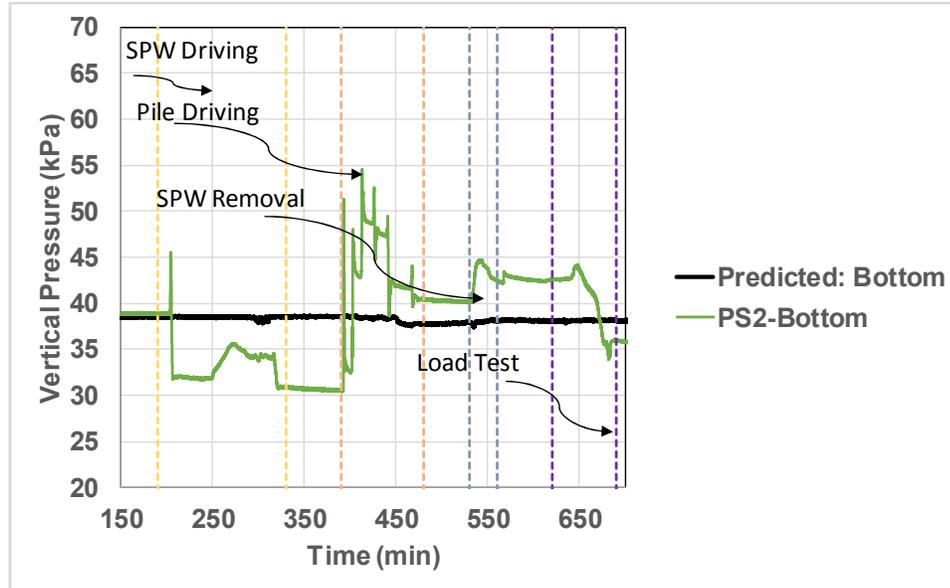Scenario 3 – Test 3 (SPW tip depth is half of the pile tip depth)

CHAPTER 3
COMPUTATIONAL RESEARCH: COMBINED DISCRETE ELEMENT - FINITE ELEMENT MODELING

3.1 Overview of Numerical Modeling Methodology

The current study is undertaken to investigate changes to pile resistance when piles are installed in the presence (and removal) of nearby SPWs. The overall study involves multiple physical test programs (standardized laboratory tests, centrifuge tests) and parallel computational efforts. In this Task 3.1 report, numerical modeling and computational efforts are focused upon for large-scale assemblies and interactions between piles, SPWs, and granular soil bodies. Selected results from recently completed (physical) scaled-centrifuge tests involving driving of piles and installations of SPWs are drawn upon to establish benchmarks for the numerical work documented herein.

The computational efforts of this study bring together two well-known analysis methods: the finite element method (FEM) and the discrete element method (DEM). As detailed in the Task 2 report, the FEM is suitable for modeling of structural objects (piles, SPWs), whereas the DEM is necessary to model the discontinuous nature of granular soil. By adopting the combined DEM-FEM approach to simulating major disturbances of granular soil bodies during SPW installation and pile driving processes, arbitrarily large deformations and stress-state changes of the numerical model portions representing the granular soil can be captured. Therefore, physical (centrifuge-test) measurements of geostatic stress, changes in stress during introduction of structural objects, changes in soil-stress subsequent to installation and driving processes can all be compared to the established benchmark (physical) measurements.

Three scenarios are of interest for Task 3: (1) Driving of a pile into granular soil, followed by pile top-down loading; (2) Driving of a SPW and then driving of a pile within close proximity, ending with top-down loading of the pile; and, (3) Driving of a SPW, driving of a pile within close proximity, removal of a SPW, ending with top-down loading of the pile. Accordingly, the primary objective of the chapter is to demonstrate feasibility of the combined DEM-FEM approach in computing pile driving responses that show reasonable agreement with physical measurements of pile load-deformation relationships and soil stresses for Scenario 1 vs. Scenario 2 and Scenario 1 vs. scenario 3.

For the three scenarios considered in Task 3, computations of geostatic stress states, changes in soil-stresses during installation and driving, and driven pile load-deformation are cataloged and compared to benchmark measurements taken from physical scaled-centrifuge tests (see Chapter 2 for physical test details). Stress quantities and load-deformation relationships arise from the substantial disturbance and redistribution of soil surrounding the embedded structural objects. To permit computations of such phenomena, models consisting of discrete spherical elements (DSEs) and solid finite elements (FEs) are utilized in combined DEM-FEM simulations to represent soil (sand) and structural (pile, SPW) components, respectively. Given the complex evolution of soil motions and stress-state changes associated with these two scenarios, simulations that demonstrate reasonable agreement with physical measurements require comprehensive exploration of relevant parameters for both the soil and structural model components. Accordingly, a major component of Task 3 is conducting and documenting the results of parametric explorations for salient model parameters, with emphases on DSE parameters (e.g., friction, contact stiffness). Presented in this

report are computed results from the parametric study, along with identification of calibrated model parameters that bring about agreement with the physical test measurements.

3.1.1 Grain-scale Properties of Discrete Elements

The mean diameter of natural sand used in the centrifuge tests was 0.2 mm. In prototype scale, the actual sand is modeled by scaling the sand particle dimension with respect to a volume-averaging method. As the mechanical properties of Florida natural sand at grain-scale are unknown, the input parameters of granules measured at smaller scales are utilized to model sand. Subsequently, macroscale parameters are calibrated to match the shear resistance (internal friction angle) measured for the sand.

First, we incorporate microscopic surface characteristics of granular materials in the rheological model of "rough" discrete spheres to simulate interparticle contact behaviors in the pile-SPW-soil systems. It is well known that grain surfaces possess some roughness, consisting of deviations from their nominal flatness. It can be difficult to solve the rough surface contact problem from the actual geometry (often referred to as a deterministic methodology) because the profiles of surfaces are highly heterogeneous (Fig. 3.1). In more recent physical measurements on grain-to-grain contact force-displacement tests, namely, micro-indentation tests (i.e., uniaxial compression tests on two individual granules in contact), contact displacement exhibits variation with respect to applied normal loads. Further, the normal contact stiffness deviates from the classical Hertz solution by a few orders of magnitude. This is because 1) the variation of contact asperity profiles affects development of contact forces and corresponding intragrain deformation (i.e., at the rate of which particles will kinematically interact with neighboring particles in contact); and 2) an apparent contact area (Archard 1957, Langroudi et al.2010) is much larger than a point-contact solution by Hertz (1882).

A well-known closed-form solution (Greenwood and Williamson 1966) has been developed for use in the analysis to improve the discrete element modeling of fractal rough surface contact. To characterize surface properties of the sample materials, statistical mean surface profiles (Bhushan 2001) derive from power spectral density functions of asperity (Nayak 1971) for height distribution, density, and mean radius. Based on the concept of stacked asperities presented by Archard (as illustrated in Fig. 3.1c), an apparent (nominal) contact area is incrementally evaluated at closing distances between the rough surfaces per statistical surface parameters obtained from the SEM data analysis. Accordingly, average contact pressures over a nominal contact area are calculated per increment of gap closure (i.e., separation distance between two non-conforming contact surfaces). A detailed analytical procedure (for which a summary is given in the appendix) is being prepared for possible publication in the Journal of Granular Matter.
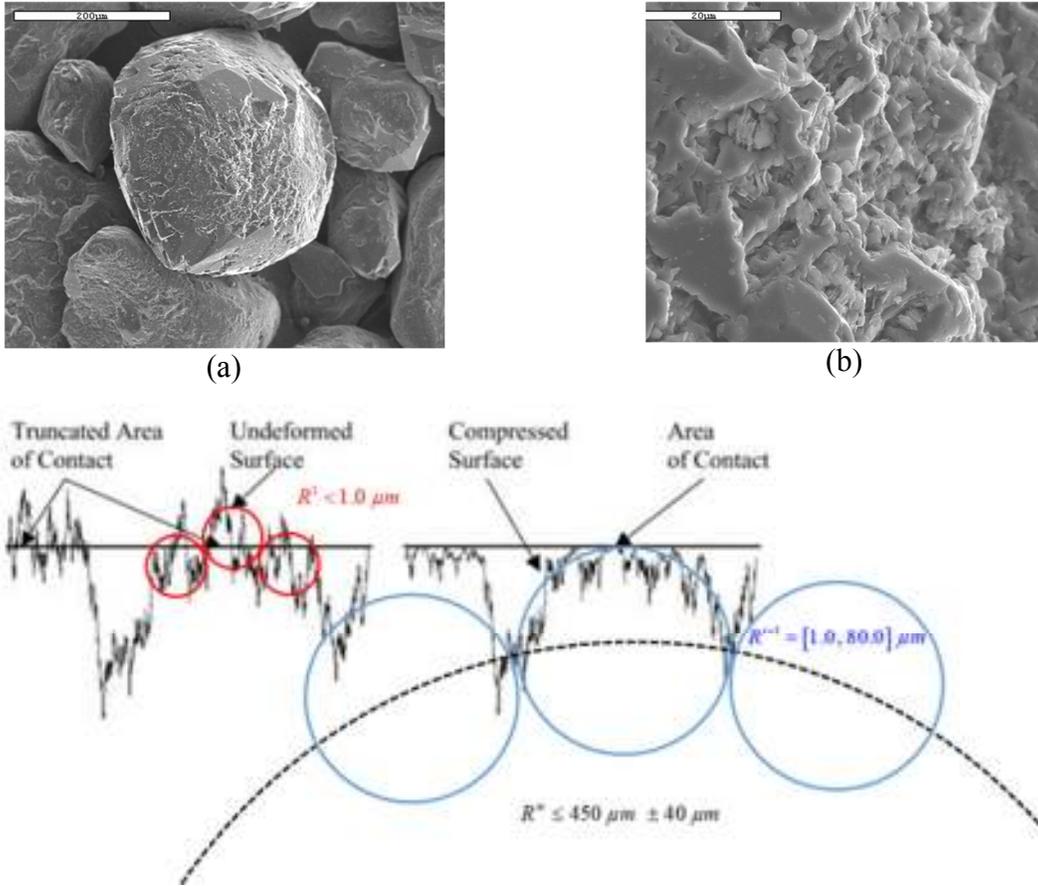
Figure 3.1 Scanning Electron Microscopy (SEM) images at low (a) and high (b) resolutions of Nevada sand and (c) schematic of contact surface roughness illustrated by a fractal structure of Archard's stacked hemispheres

In centrifuge test scenarios, the dimension of the numerical granular assembly is a cylinder with diameter of approximately 10.5 ft, and height of approximately 29.5 ft. A significant number of particles (approximately 4 billion elements) will be required to fill this domain if the DSE particle size is modeled to that of natural Florida sand. In this case, the computational cost for modeling such a large number of particles will be infeasible. Also, a scaling law from centrifuge test to numerical model is applicable, which is the result of the gravitational acceleration ratio between these two tests. For practical modeling purposes, the diameter of DSEs is selected as 0.97 in (24.75 mm) to be an optimal size for DEM simulations. This gives the ratio of the pile width to the DSE diameter to approximately 25 (a scale ratio analogous to the work by Butlanska et al. (2014)).

In the following, we estimate an equivalent elastic modulus for use with respect to the uniform diameter of DSEs in consideration of grain surface roughness and resulting relatively soft contact stiffness (due to yielding of microscopic asperities in micron). The results are obtained assuming a linear elastic response in grain contacts (a particle size distribution given in Fig. 2.2 with $d_{50} \approx 0.2\,mm$) contact level, which is completely determined by two elastic constants: normal and tangential contact stiffnesses. An intrinsic difficulty in the case of granular materials originates

from the fact that the variables at the grain scale and the macro (laboratory sample) scale are of different nature. The fundamental difference is that, at the macroscale, the bulk behavior is described by tensorial variables (stress and strain tensors), but, at the grain scale, the material behavior is written using vectorial variables (contact forces, grain displacement and rotation). Various methods have been established for scaling up from the grain scale to the macroscale. We will not present the details of the average operators in this report. The main objective of the following is to demonstrate a procedure in obtaining a reasonable constitutive relation at the scale of a representative discrete spherical volume from the information on the material behavior at grain level. A much detailed description of Hertz-Mindlin contact theory is given in Task 2 Report, and thus, is omitted. In essence, the model can be written in incremental form of contact forces:

$$\Delta F_n = \left(\frac{3d}{2}\right)^{1/2} \left(\frac{G}{1-v}\right)^{2/3} (F_n)^{1/3} (\delta_n)$$

$$\Delta F_t = \frac{2(1-v)}{2-v} \left(\frac{3d}{2}\right)^{1/3} \left(\frac{G}{1-v}\right)^{2/3} \left(F_n - \frac{F_t}{\mu}\right)^{1/3} (\delta_t)$$

where F denotes contact force with subscripts n and t referring to the local normal and tangential direction, respectively; d is grain diameter; G and v are the shear modulus and Poisson's ratio, respectively, for the sand particle constitutive relationship; δ is contact displacement, and μ is interparticle friction coefficient. The DEM approach in the rheological model for an isotropic material is leads to

$$E_{eff} = E_o \frac{1-v}{2(2-v)(1-\mu)+\mu^2(1-4v/5)} \rightarrow E_{eff} \equiv fn(E_o, v, \mu)$$

where E_o denotes a reduced elastic modulus for the effect of surface roughness in grain-scale contact stiffness; v denotes Poisson's ratio, and a collection (unit volume or mesoscale size) of sand grains produces effective modulus E_{eff} (for an agglomerate as shown in Fig. 3.2): for example, E_o is empirically evaluated using microindentation tests on silica granules with mean diameter of 0.85 mm (given in the appendix). Resulting values are in the range of 70~90 ksi (520~650 MPa). Grain (sliding) friction coefficient is also estimated per a limited number of microscratch tests: $\mu = 0.4 \sim 0.7$. Poisson's ratio of 0.3 is obtained for silica grain from the literature of the Task 2 report, respectively. These values give a low bound of $E_{eff} \approx 25$ ksi (170 MPa). Considering an asymptotic limit of number density in cubic and tetrahedral packings to be between 6 and 12, we have $v_{eff} \approx 0.22 \sim 0.44$ per $v_{eff} = N_o \frac{v}{10-6v} \rightarrow v_{eff} \equiv fn(N_o, v)$. In the highest close random packing of DEM simulations (in this study), we estimate $v_{eff} \approx 0.25 \sim 0.27$ using a numerical tolerance (equal to an asperity radius ~ 0.1 mm at the lowest frequency level which is the mean radius of the sand grain). Resulting bulk modulus is approximately in the range of 17.5 ksi (120 MPa).
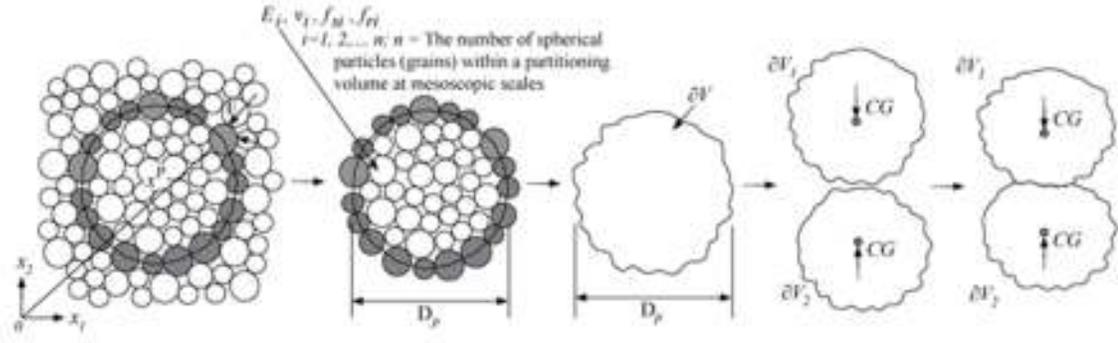
Figure 3.2 A definition of mesoscopic DSE with E_{eff} and v_{eff}, representing an assembly of subparticles inside a discrete spherical volume with diameter D_p

A more comprehensive view of effective shear behavior (at the agglomerate scale) can be seen in semi-empirical estimation of elastic constants based on semi-empirical measurements on effective elastic modulus in comparison to macroscale test data obtained from the literature. A notable consistency of the volume-averaged elastic constant(s) over a selected (upscaled) discrete element volume (with diameter of 0.97 in) shows that the void ratio dependence of the sand appears to be within a range of the DEM parameters. For example, using a semi-empirical equation of the small-strain, constant fabric shear stiffness of a statistically isotropic random packing under isotropic confining stress is given by Chang et al. (1991):

$$G_{eff} = \frac{(5-4v)}{5(2-v)}\left[\frac{\sqrt{3}\cdot cn}{\sqrt{2}\pi(1-v)(1+e)}\right]^{2/3} E_o^{2/3}(\sigma')^{1/3}$$

where cn and e are the coordination number (an average number of contacts) and void ratio of the granular medium; E_o is a reduced modulus for use in the effective tangential contact stiffness per surface roughness on grains, and σ' is confining stress. The coordination number can be replaced by a measurable physical quantity such as porosity n or void ratio $e=n/(1-n)$, using well-established correlations (Smith et al., 1929; Field 1963; German 1989; Chang et al., 1991; Sundaram 1991). Rothenburg and Bathurst (1989) estimated the ratio of normal contact force F_n to average normal contact force F_{navgS} to vary between 0.6 and 0.75 for $0.5 \le e \le 0.7$. Further, Santamarina (2001) provides a lower-bound constraint on cn and e such that $cn \ge \pi(1+e)$. Incorporating an empirical relation given by Smith et al. (1929): $cn = 13.28 - 8e$ into the above equation, we estimate the effective shear modulus:

$$G_{eff} = 0.43\frac{(5-4v)}{(2-v)}\left[\frac{1.7-e}{(1-v)(1+e)}\right]^{2/3} E_o^{2/3}(\sigma')^{1/3}$$

Per given $E_o = 70\,\text{ksi}$ (520 MPa) and $e = 0.65$, we estimate G_{eff} to be equal to 11 ksi (75 MPa) at $\sigma' = 0.1\,\text{MPa}$ and 14 ksi (95 MPa) at $\sigma' = 0.2\,\text{MPa}$. Note that we will use a range of average values

48

of the effective modulus in DEM simulations per K_o measured in the centrifuge soil model and simulated (re-produced) by DEM gravitational pluviation techniques. Therefore, due to uncertainty associated with quantification of the macroscale yield stress in the direct shear test results, the effective modulus is treated as a model parameter in DEM simulations. Thus, a range of the calculated values of effective shear modulus for the representative discrete spherical volume is tested for comparability to empirical measurements of the shear modulus in cyclic tests on soil sample scale found in the literature (Fig. 3.3). In turn, similitude relationships in elasticity between the DEM agglomerate and the soil samples (Iwasaki et al. 1978) increase confidence in the model parameters used in simulating the bulk shear behavior of the granular soil at the SPW-pile-soil system scale. Alternatively stated, the DEM model parameters used in this study are collectively capable of reasonably simulating the dependence of mesoscale shear modulus on (1) porosity of cohesionless sand in a range of 0.4, (2) confining stress, and (3) features of macro shear modulus (e.g., given in Fig. 3.3).
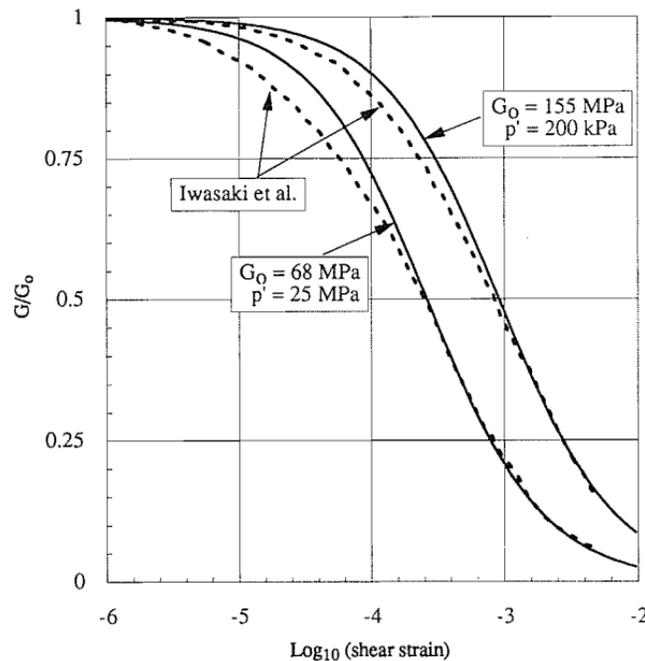
Figure 3.3 Comparison of measured shear modulus with shear strain level at mean normal stresses (denoted as p') : The plots of G/G_0 versus shear strain where G_0 is the "elastic" shear modulus. In practice, G_0 is defined as the measured value at a shear strain where no further increase in shear modulus is observed. Theoretical curves are compared with cyclic test data of Iwasaki et al. (1978) (after Fahey (1992))

3.1.2 Numerical Model Components and Simulation Sequence

A cylindrical triaxial compression test chamber of dimensions 12 in x 24 in was created for investigating bulk shear behavior of DSE assemblies. A larger triaxial chamber was modeled so that a range of discrete element diameters in monosphere assemblies can be assessed. The discrete element mesh was directly extracted from a larger discrete element mesh, which in turn,

49

was pluviated to simulate pile driving and top-down load tests. A control volume of 12 in x 24 in was extracted near the mid-depth of the larger assembly, directly from beneath the location of the pile. In other words, the control volume was extracted with consideration of the path of the pile (Fig. 3.4).
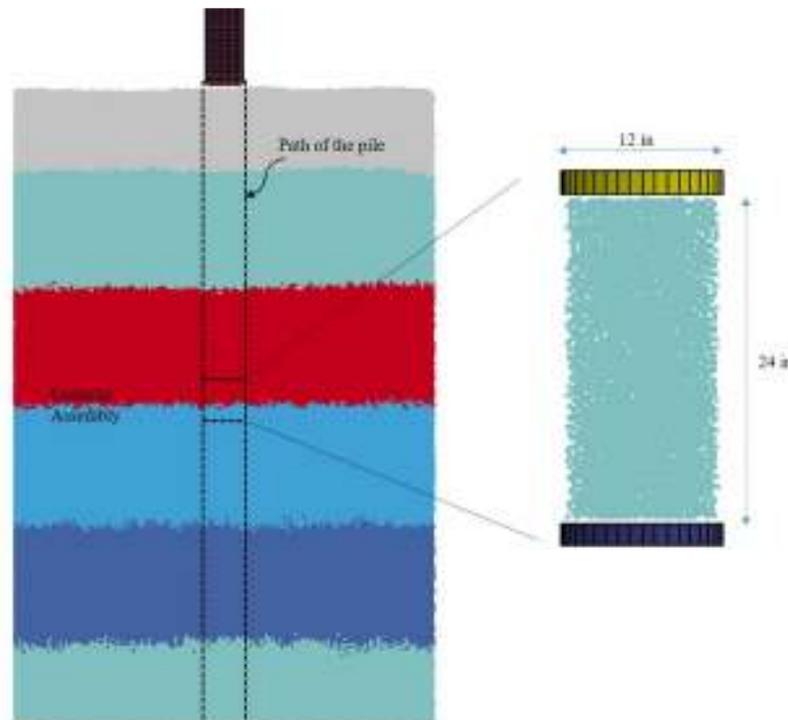
Figure 3.4 Control volume extracted from granular assembly for triaxial compression test simulations. Note that the cylindrical volume is sampled along the centroid. The pile width is two times larger than the diameter of the cylinder.

Components of the combined DEM-FEM numerical model for simulating triaxial compression testing are given below (Fig. 3.5). Included in the schematic of Fig. 3.5 are mechanical confining pressures applied to the cylindrical wall portions and axial loading (which is applied during the shearing stage). The overall modeling approach, simulation staging, and model validation was detailed as part of the Task 2 deliverable report.
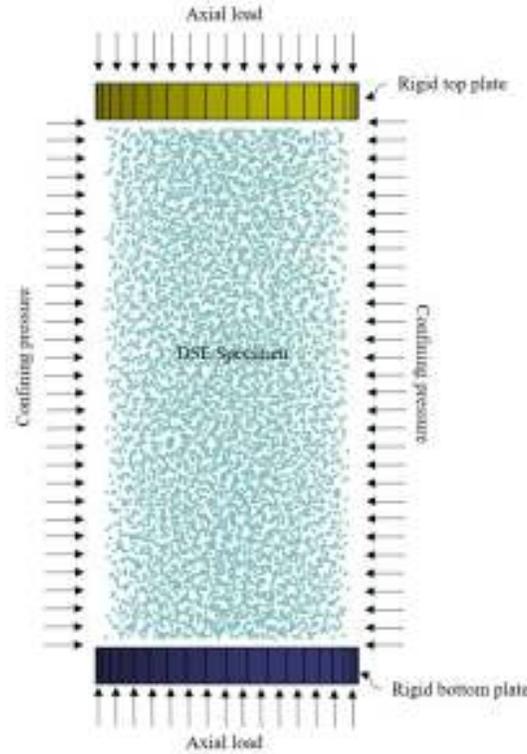
Figure 3.5 Components of the combined DEM-FEM model for simulating triaxial compression tests on granular materials

3.1.3 Summary of Simulation Results

The formulation and modeling components for DSE, previously detailed in the Task 2 report, are utilized in the current Task 3.1 report. All the input parameters used to model sand for cases with best match to the measured internal friction angle are given below (Table 3.1). The numerical pile driving and top-down load test scenarios are simulated using these input parameters for DSEs. Young's modulus and coefficient of sliding and rolling friction are not included in Table 3.1. These latter two parameters are treated as variables, and investigated as part of a parametric study discussed, discussed in Sec. 3.4 and Sec. 3.5.

Table 3.1 Input parameters for DSEs used in triaxial compression test simulations

Parameter	Value	Units
Radius	0.97 (24.75)	in (mm)
Volume	3.875 (63506)	in^3 (mm^3)
Mass density	165.5 (2651)	lb/ft^3 (kg/m^3)
Poisson's ratio	0.27	--
Normal damping coefficient	0.7	--
Tangential damping coefficient	0.4	--
Ratio of normal to tangential contact stiffness	0.8	--

51

Triaxial compression test simulations are performed at three different confining pressures: 5.8 psi (40 kPa); 10.15 psi (70 kPa); and 14.5 psi (100 kPa). The Mohr failure envelope for one of the simulations is given in Fig. 3.6 and a detailed summary of the collective triaxial compression test simulation results is given in Table 3.2. As can be seen from Table 3.2, the measured internal friction angle for Florida natural sand can well be simulated by using DSEs with the given input parameters.
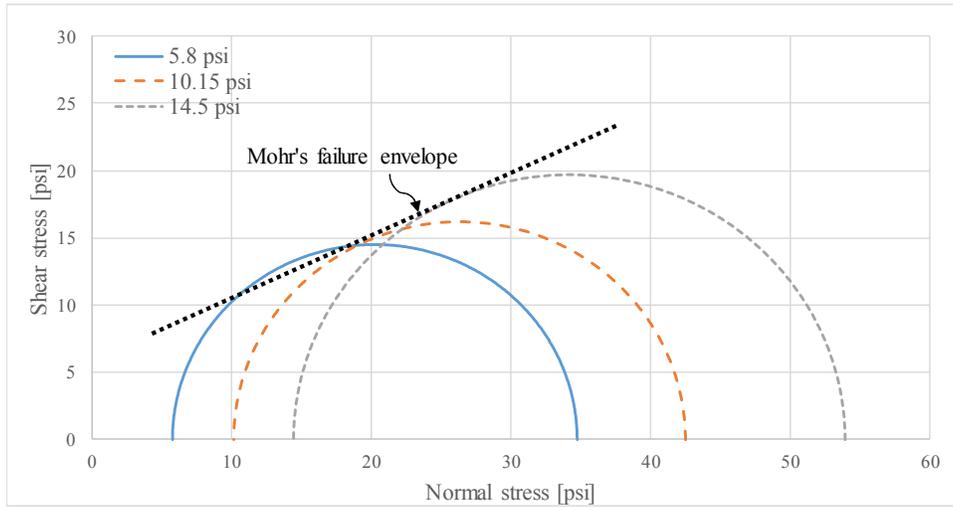
Figure 3.6 Mohr failure envelope for triaxial compression test Simulation 1

Table 3.2 Summary of triaxial compression test simulation results

Simulation:	1	2	3	4	5	6	7	8
Elastic properties:								
Mass density (lb/ft^3)	165.5	165.5	165.5	165.5	165.5	165.5	165.5	165.5
Bulk modulus (ksi)	10.52	10.52	15.77	15.77	17.87	17.87	21.02	21.02
Poisson's ratio	0.27	0.27	0.27	0.27	0.27	0.27	0.27	0.27
Rheological model parameters:								
Normal damping	0.7	0.7	0.7	0.7	0.7	0.7	0.7	0.7
Tangential damping	0.4	0.4	0.4	0.4	0.4	0.4	0.4	0.4
Sliding friction coefficient	0.6	1.0	0.6	1.0	0.6	1.0	0.6	1.0
Rolling friction coefficient	0.06	0.1	0.06	0.1	0.06	0.1	0.06	0.1
Normal stiffness factor	1.0	1.0	1.0	1.0	1.0	1.0	1.0	1.0
Tangential stiffness ratio	0.8	0.8	0.8	0.8	0.8	0.8	0.8	0.8
Shear behavior under triaxial compression testing:								
At 5.8 psi confinement:								
Peak shear strength (psi)	29	32.625	30.6	33.5	33.2	35.1	36.4	37.56
At 10.15 psi confinement:								
Peak shear strength (psi)	32.33	35.38	34.22	36.98	36.10	40.02	39.88	41.47
At 14.5 psi confinement:								
Peak shear strength (psi)	39.44	43.5	39	44.95	44.52	48	47.27	49.45
Peak internal angle of friction (º)	28.5	30.86	29.8	31.3	31.2	31.94	31.79	32.23

3.2   Boundary Condition Modeling

Boundary conditions constitute one of the fundamental aspects of modeling physical systems. Considering that only a finite subdomain of soil can be directly represented in any numerical model, simulation of pile driving using the combined DEM-FEM approach necessitates careful considerations for boundary condition modeling. For example, the extents of granular assemblies considered herein must be permitted to discretely deform in 3D at the model boundaries while absorbing propagating stress waves. This requirement poses additional challenges to that of, for example, deformation along a continuum in 2D (Zhao and Liu 2003, Mandal and Maity, 2016). However, non-reflecting boundary conditions (Lysmer and Kuhlemeyer 1969) are necessary for mimicking behaviors that would be observed in the real world since (physically) the 3D discontinuous soil medium continues outward from the pile and/or SPW installation locations. Phenomena such as motions of DSEs making up the model boundaries, the propensity for developing confinement stresses, absorption and reflection of stress waves that reach the boundary, and overall energy dissipation must be captured by the boundary condition components.

Local non-reflecting boundary conditions (LNRBCs) make up a special class of boundary condition modeling approaches (Givoli 1991) and are integral to computing motions and stresses of granular assemblies using the DEM, where again, only portions of the granular media of interest can by modeled within practical hardware and software limitations. LNRBCs can be defined as energy-absorbing boundary conditions with limited constraints placed on boundary elements. In this capacity, LNRBCs contribute to system stability and restraint at levels that fall somewhere between those of fixed boundary conditions and free boundary conditions.

3.2.1 Overview

Utilization of LNRBCs is of particular benefit for modeling scenarios where soil media are to be disturbed by the introduction of structural objects (e.g., installation of piles into a sandy medium). For such applications, the boundaries of numerical models must absorb incident stress waves, but must not reflect (or at least, minimally reflect) stress waves. As a consequence of absorbing the energy of incident stress waves, no appreciable stress wave reflection should propagate—from the system boundaries—back into the system assembly. Such non-reflecting characteristics allow for systems fitted with LNRBCs to (approximately) mimic behaviors that would be observed when considering assemblies with infinite domains, where stress waves propagate, and ultimately dissipate, as the volume which the stress wave encompasses continually increases. In the following, a methodology is presented for quantifying and applying displacement-based LNRBCs to cylindrical assemblies of monospheres (Fig. 3.7).
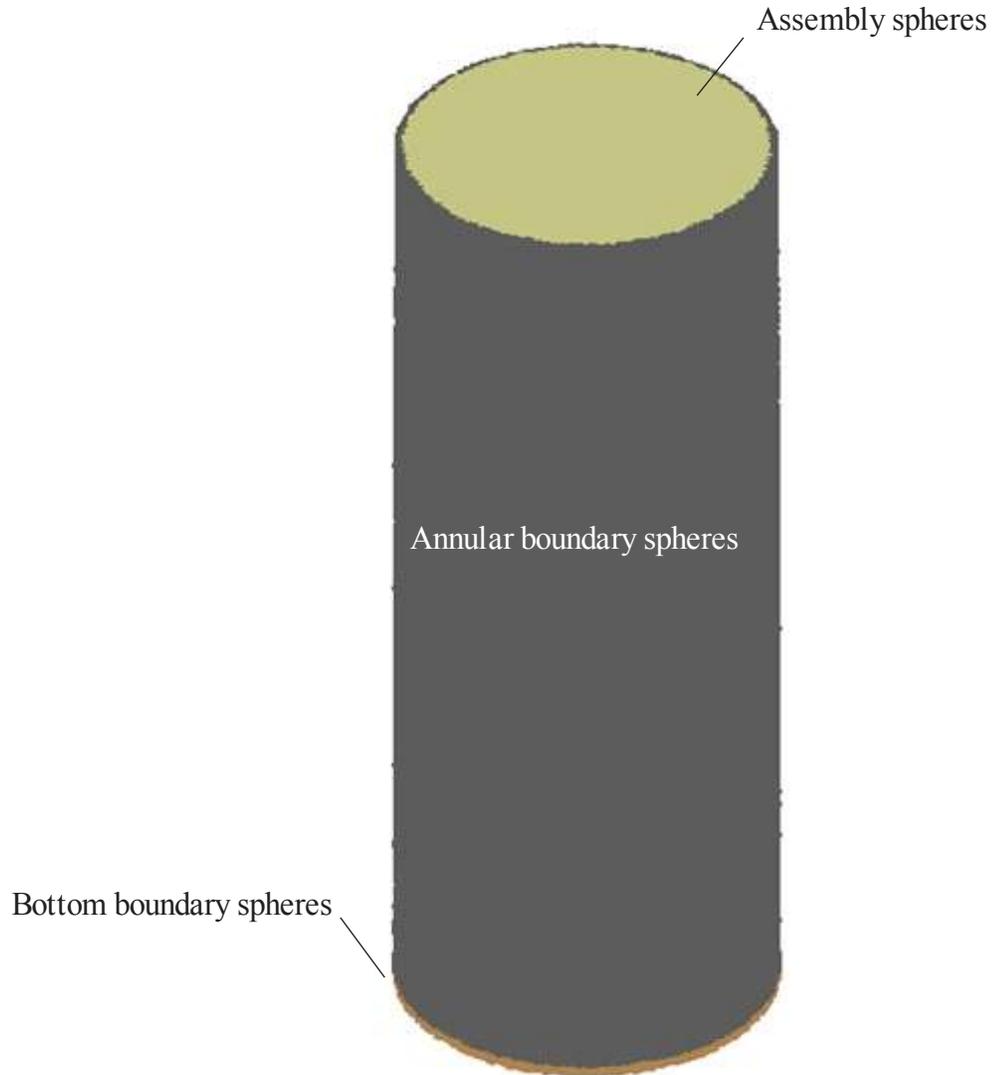
Figure 3.7 Isometric view of cylindrical DEM assembly

The displacement-based approach makes use of springs and dampers (i.e., a viscous-spring boundary, Jingbo and Yandong 1998) attached to DSEs located at the assembly boundaries (Fig. 3.8). Three components are utilized in forming LNRBCs for the current study: linear elastic springs, linear-viscous dampers, and confining pressures. Selected springs are initialized with compressive offsets such that confining effects are achieved. Importantly, the initial spring offsets—in the ensemble—produce force per unit area to satisfy a desired distribution of confining pressures.
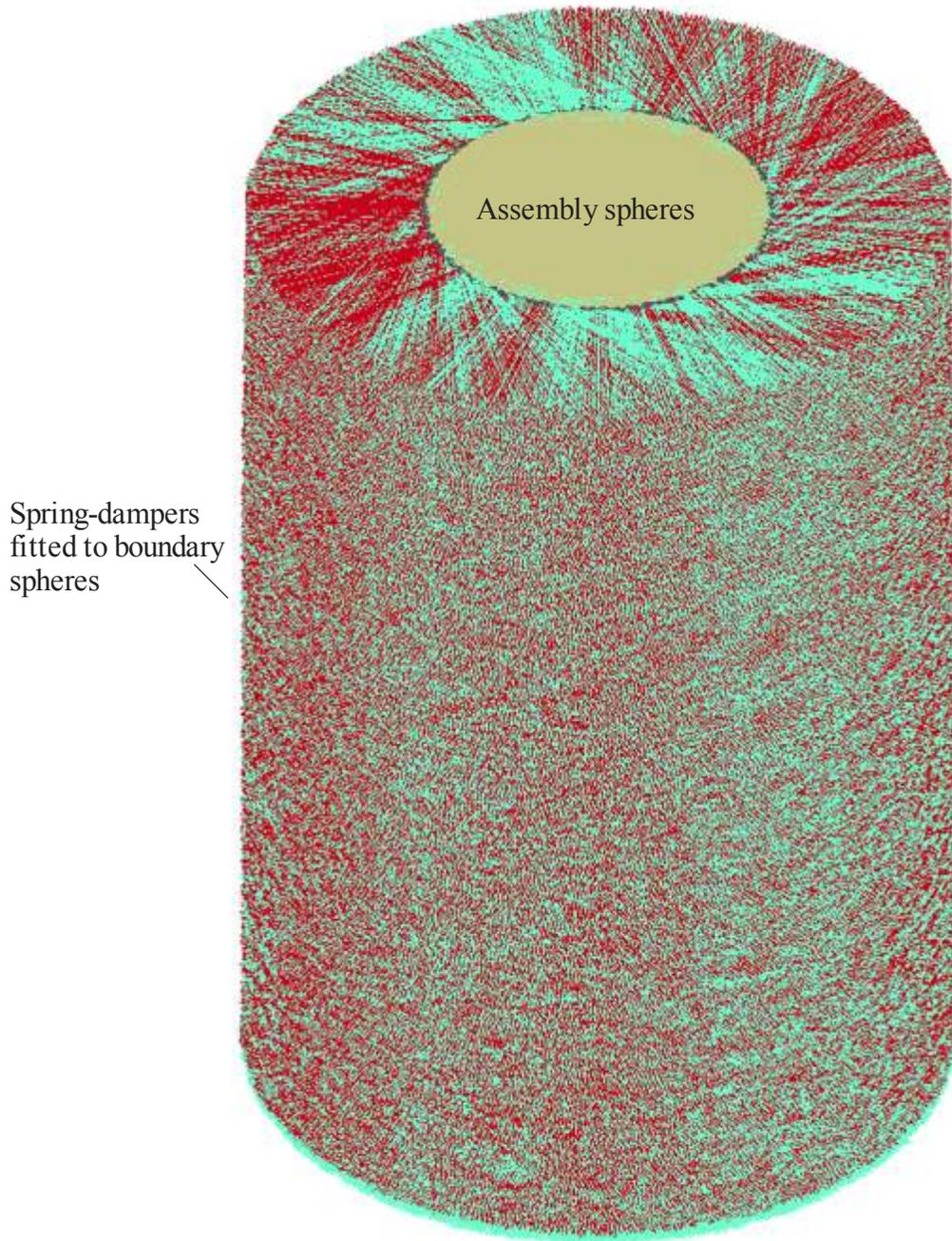
Figure 3.8 Isometric view of cylindrical DEM assembly fitted with LNRBC springs and dampers

3.2.2 Mechanism for Assembly Confinement

In this study, cylindrical assemblies fitted with LNRBCs are intended to exhibit pre-existing geostatic stresses. Further, the boundary condition modeling must allow confinement stresses to persist. To be effective, boundary spheres must promote assembly stability (i.e., must be able to maintain a mechanically stable state when the assembly is subjected to gravitational acceleration). Lastly, boundary spheres must promote absorption of incident stress waves.

Spring components of LNRBCs are intended to act as primary enforcers of assembly confinement. Further, the boundary springs are defined to strike a balance between: 1) Mimicry of the presence (and normal contact stiffness) of assembled discrete spherical elements (DSEs) located beyond the actual model domain; and, 2) Sufficient flexibility so not to over-constrain boundary motions (which would in turn lead to stress wave reflection). Stated alternatively, the springs must be capable of maintaining geostatic stresses in the cylindrical assemblies, but must not introduce non-physical over-constraint of the assembly spheres.

Recall that an annular region is defined (with non-zero radial thickness), and all spheres that fall within the annulus are designated as boundary spheres. For those spheres located near to the annular boundary region, incident stress waves are anticipated to be dominated by particle motions that are predominantly horizontal (e.g., a particle with velocity *v*, as shown in Fig. 3.9) but may hold both radial and circumferential vector components. Therefore, three unique spring-damper pairs are affixed to designated annular boundary spheres, and oriented such that one spring-damper pair lies in each of the radial, vertical, and tangential (circumferential) directions (Fig. 3.9, note that the spring-damper components in the tangential direction are not shown).

Initial offsets are supplied to the radial-direction spring, where the initial compressive offset produces a horizontal (radial) confining force. The confining force magnitude is defined such that the radial confining stress for any unit area along the annular boundary approximately equals the horizontal stress that would be observed for the assembly under a mechanically stable state. Alternatively stated, the initial compressive spring offset acts to maintain horizontal geostatic stresses present within the cylindrical assembly. As a means of further promoting mechanical stability, springs oriented in the vertical direction are supplied an initial compressive offset such that the associated prestressing force equals the body-force of the boundary sphere. In contrast, the tangential (circumferential) springs are not assigned an initial offset.
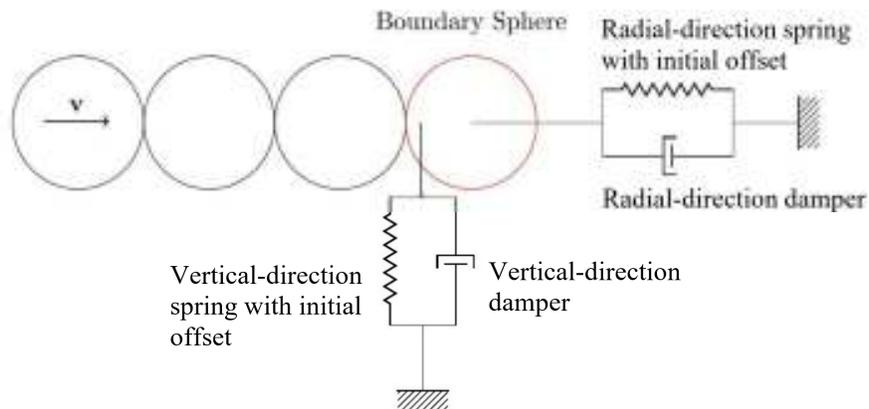
Figure 3.9 Displacement-based LNRBC configuration for annular boundary spheres of cylindrical assemblies (circumferential components not shown)

For spheres located along the bottom boundary (see Fig. 3.10), the direction of incident stress wave propagation is anticipated to be predominantly in the vertical direction. Accordingly, emphasis is placed on ensuring confinement and mechanical stability of the assembly in the vertical direction. As shown in Fig. 3.9, one spring-damper is oriented in the vertical direction,

while the other two spring-dampers are oriented in the radial and tangential (circumferential) directions (note that the tangential-direction spring-damper is not shown in Fig. 3.10). Here, the initial compressive spring offset supplied to the vertical spring is defined such that—on a unit area basis—the vertical stress produced by the spring prestressing forces approximately equals the (geostatic) vertical stress at the assembly bottom.
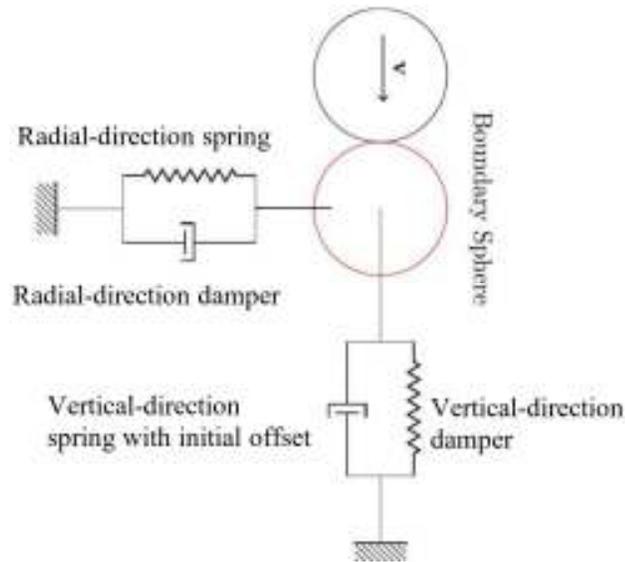
Figure 3.10 Displacement-based LNRBC configuration for bottom boundary spheres of cylindrical assemblies (circumferential components not shown)

3.2.3 Mechanism for Energy Dissipation

Absorption of incident stress waves along the assembly boundary can be primarily attributed to the dampers affixed to each boundary sphere. Care is taken in assigning damping coefficients to that are representative of the natural frequencies of vibration of the constituent spheres for translational motions. When the coefficients of restitution for normal direction and tangential direction contact interactions correspond to damping levels of 70% and 40%, respectively, then: 1) Attenuation of "overshoot" phenomena is achieved for normal-direction contact interactions; and, 2) Compatibility is achieved among vibration frequencies in the normal and tangential directions. Damping coefficients supplied to the dampers affixed to annular boundary spheres are such that damping at 70% of critical is achieved for translation in the radial direction, while damping at 40% of critical is achieved for translations in the vertical and tangential (circumferential) directions. For bottom-boundary spheres, dampers oriented in vertical direction are configured to achieve 70% of critical damping, while dampers oriented in the orthogonal directions (radial, tangential) are configured at 40% of critical damping.

3.2.4 Pushing the limit of DEM

Ideally, three unique spring and damper definitions would be supplied for each boundary sphere. For assemblies containing several million elements, between one and three million entities

must be defined to satisfy unique LNRBC components at each sphere. However, in association with use of general purpose multi-physics simulation software LS-DYNA (LSTC 2017), software limitations are encountered when attempting to view or simulate assemblies possessing millions of LNRBC components. Necessarily, the LNRBC is discretized to overcome these software limitations. For example, the vertical portion of cylindrical assemblies is subdivided (Fig. 3.11), and all radial spring definitions (stiffness, initial offset) within a subdivision are identical. Likewise, all vertical spring definitions within a subdivision are identical, as are all tangential (circumferential) spring definitions. The number of vertical subdivisions (n_v) has been taken as 500 for the models considered below.
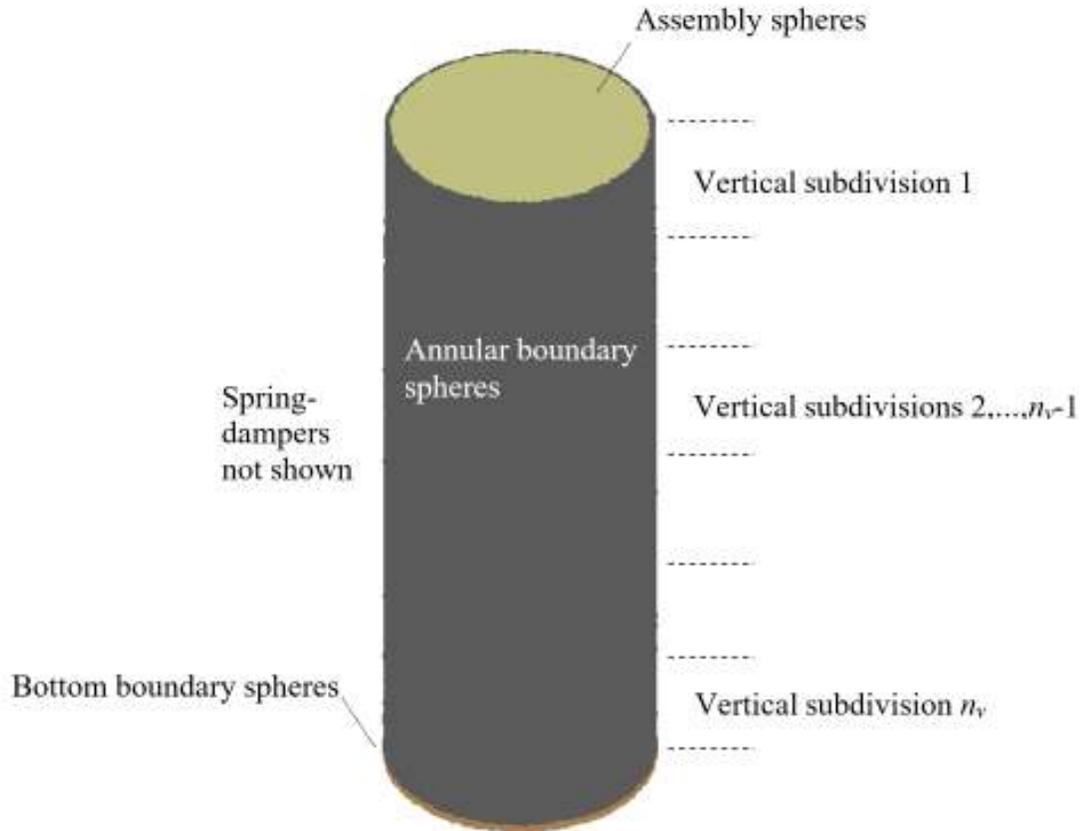
Figure 3.11 Isometric view of cylindrical DEM assembly with indication of vertical subdivisions (n_v) for fitting with unique normal-direction springs

Each DSE designated as a boundary sphere possesses a unique radial position relative to the vertical-centroidal axis of the DSE assembly. However, if unique LNRBC radial components were to be supplied to each boundary sphere in the numerical (LS-DYNA) model, then several million unique LNRBC model components would be added. The software LS-DYNA, however, is limited to unique component counts on the order of 1E+04. Therefore, as an additional measure to model radial LNRBC components while not exceeding software limitations, the domain is again discretized. Here, the discretization occurs in a radial manner, where the DSE assembly is divided into sectors. Specifically, the boundary spheres are subdivided radially into 360 subdivisions

(where n_r = 360 subdivisions, as shown in Fig. 3.12). Boundary spheres that fall within a given radial subdivision are fitted with dampers of equal-valued damping capabilities in the radial direction. For a given radial-direction damper, the associated vertical and tangential (circumferential) dampers satisfy the 0.7/0.4 ratio discussed in Ch. 2 of the Task 2 deliverable report.
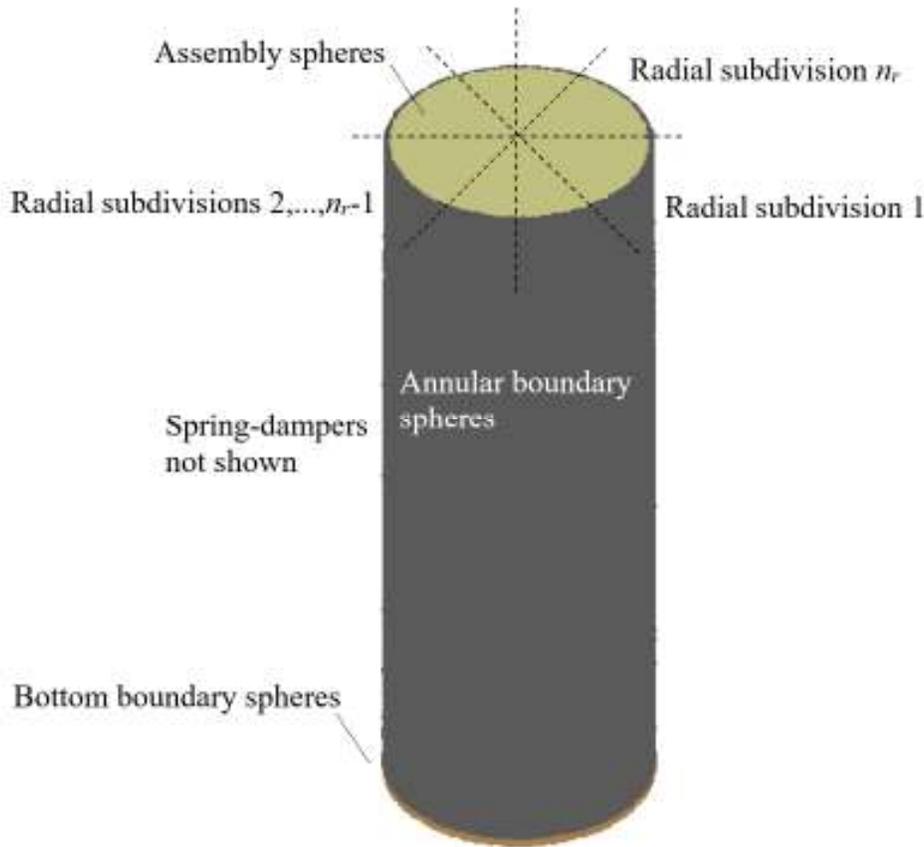
Figure 3.12 Isometric view of DEM assembly with indication of radial subdivisions (n_r) for fitting with unique normal-direction damping

3.3 Numerical Modeling of Test Scenario 1

A significant portion of the research efforts toward completing Task 3.1 have been devoted to generating numerical models capable of simulating the physical centrifuge test scenario 1. Due to limitations on software memory allocation and hardware processing speeds, overall dimensions of system-scale numerical models cannot be identical to those of the centrifuge test. In order to reduce the influence of modeling within a limited domain, the local non-reflecting boundary condition described in previous section is applied in simulating granular assemblies associated with the physical centrifuge testing.

In Sec. 3.3, the detailed setup for the numerical model of the granular assembly and pile is described. Furthermore, a parametric study is performed for model calibration. The stress in the packing during pile driving, and the load-deformation relationship during top-down load test phase

are used as critical results for model validation. A representative model for test scenario 1 is selected in the end of this section.

3.3.1 Model Components and Simulation Sequence

In addition to boundary condition modeling, the required components for numerical modeling of test scenario 1 include the granular assembly (comprised of DSEs) and a finite element pile (having the same properties as the pile object used in the centrifuge test). A schematic of the numerical model for scenario 1 is given in Fig. 3.13.
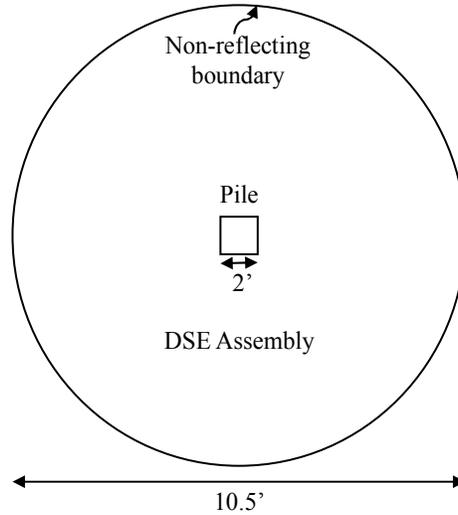
Figure 3.13 Schematic of scenario 1 test setup (refer to Fig. 3.11 for details of non-reflecting boundary)

Regarding the mechanical behavior of DSEs, the parameters given in Table 3.3 are defined in LS-DYNA (LSTC 2017),

Table 3.3 Basic parameters of the discrete element sphere

Characteristics	Value
Diameter (in)	0.97 (24.75)
Poisson's Ratio	0.27
Normal Damping Coefficient	0.7
Tangential Damping Coefficient	0.4
Normal Stiffness Ratio	1.0
Tangential Stiffness Ratio	0.8
Mass Density (pcf)	~ 168.6
Friction Coefficient with Pile	0.5

The Young's modulus and intergranular friction coefficient are not included in the parameter definitions above, because the influence of these parameters is assessed later as part of a parametric study (the results of which include selection of representative parameter values).

60

When performing the parametric study, the variation of Young's modulus and intergranular friction coefficient leads to different void ratio of packing. In order to maintain mass conservation between numerical packing and the granular assembly used in centrifuge, which has unit weight of about 105 pcf, mass densities are assigned to DSEs to preserve physically representative bulk density values across different packings. Therefore, the mass density assigned to the DSEs is not a constant value. One such value is listed in the parameter definition in Table 3.3.

After all the basic parameters are defined for the numerical model, the DSEs are positioned within a rigid cylindrical container. A packing settlement simulation is then conducted to bring about a mechanically stable state under gravitational acceleration. This is the granular assembly obtained for further model preparation and pile driving simulation. To verify that the packing possesses comparable geostatic stresses with respect to the granular bodies of the centrifuge tests, the geostatic stresses of the packing and the ratio of horizontal stress to vertical stress are analyzed. Quantitative results produced as part of the packing settlement simulations (e.g., geostatic stress profiles) are presented later.

With a stabilized numerical packing being obtained, the next step is the selection of a layer of boundary spheres. As mentioned in Sec. 3.2, springs and dampers in three directions are attached to the selected boundary spheres, and spring-damper properties are specified so as to promote local non-reflecting boundary conditions. In this simulation, a layer of approximately 4 inches of DSEs are chosen, as indicated in Fig. 3.14. Refer to Fig. 3.11 for the isometric view of cylindrical DEM assembly fitted with LNRBC springs and dampers.
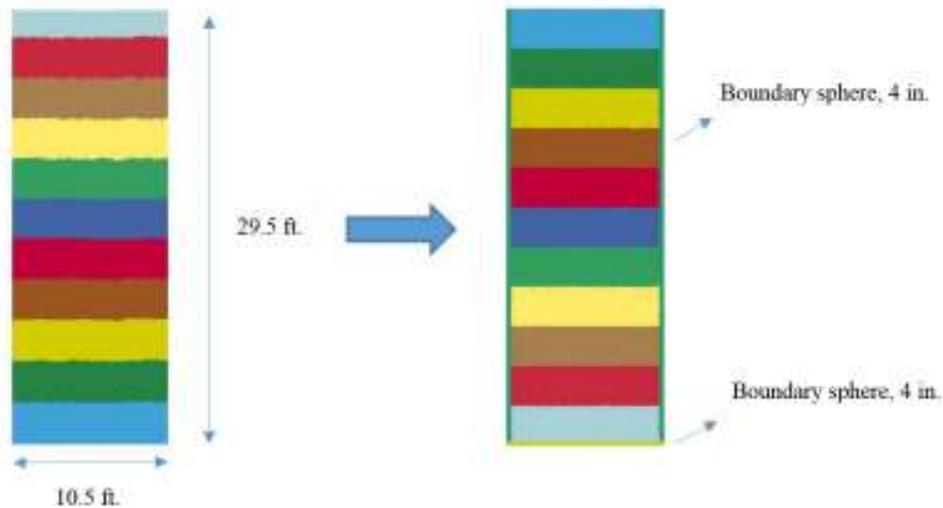
Figure 3.14 Numerical packing and selection of boundary spheres

The pile model consists of 8-node solid elements, with the geometry being defined to mimic the pile used in centrifuge test. Additionally, the pile constitutive properties (for contact force generation) are defined so as to match those of the physical pile object. The dimension and configuration of the pile FEM model is shown in Fig. 3.15.
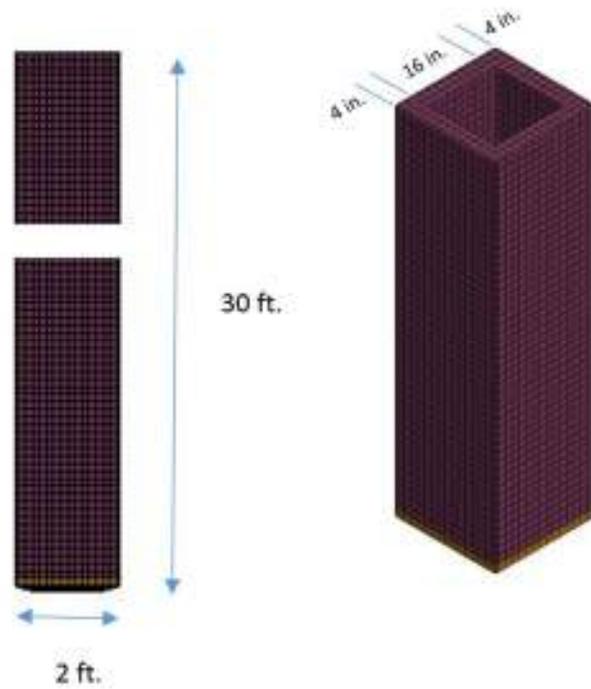
Figure 3.15 Geometry and solid element mesh of FEM pile

The pile driving sequence is simulated as per averaged pile tip displacement per blow in centrifuge tests, as indicated in Fig. 3.16.
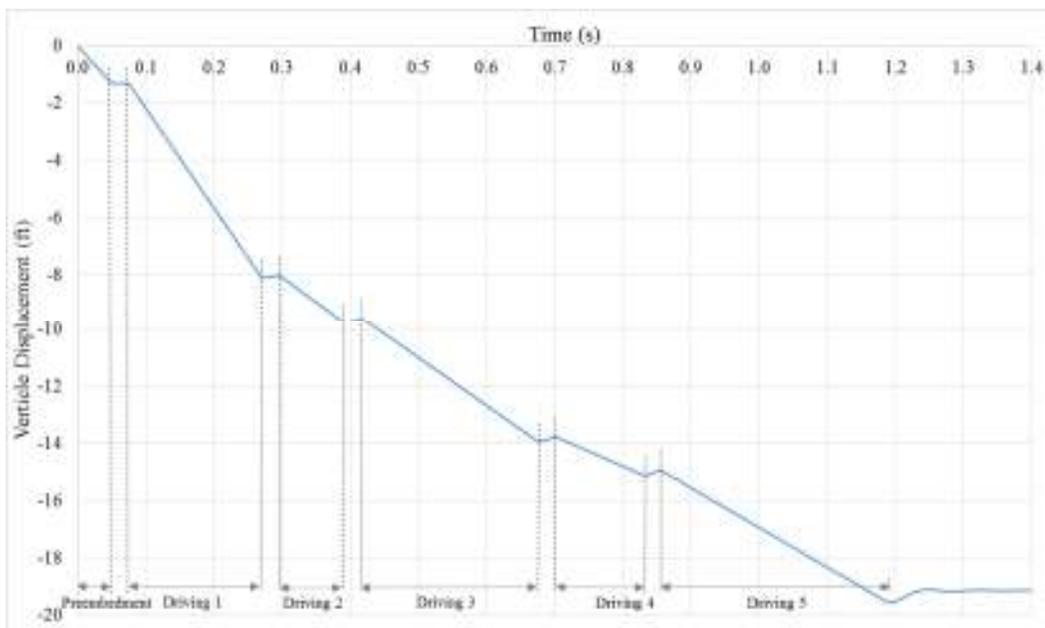
Figure 3.16 Pile driving sequence in numerical model for Scenario 1

After pile driving sequence, the packing was settled until dynamic effects from the pile driving phase had dissipated. Subsequently, the top-down loading was applied to the pile. During

the whole procedure, the resistance of the granular packing to the pile and the stress of packing was monitored for comparison with (physically measured) centrifuge test data.

3.3.2 Parametric Study

A parametric study was conducted to establish quantitative effects of bulk modulus and intergranular friction coefficient of DSEs on granular assembly stresses and pile-resistance. Four values of bulk modulus and two values of intergranular friction coefficient were used to build the matrix of input parameters. The range of parameter values investigated for bulk modulus and intergranular friction are listed in Table 3.4.

Table 3.4 Simulation number and corresponding input parameters for parametric study

Simulation No.	Bulk Modulus ksi(MPa)	Intergranular Friction Coefficient (Sliding, Rolling)
1(S1)	10.52(72.5)	0.6 0.06
2(S1)	10.52(72.5)	1.0, 0.10
3(S1)	15.77(108.7)	0.6, 0.06
4(S1)	15.77(108.7)	1.0, 0.10
5(S1)	17.87(123.2)	0.6, 0.06
6(S1)	17.87(123.2)	1.0, 0.10
7(S1)	21.02(144.9)	0.6, 0.06
8(S1)	21.02(144.9)	1.0, 0.10

For each listing in Table 3.4, a mechanically stable packing was generated with satisfaction of benchmark geostatic stresses, and a pile was introduced into the DSE assembly per Fig. 3.13. As the final stage of the scenario 1 simulations, top-down loading was applied to the pile. Selected stress and load-resistance results were extracted from the simulations and compared to physical measurements from the centrifuge testing.

3.3.3 Simulation of Geostatic Stresses

For all system-scale simulations, geostatic stresses were monitored to ensure that valid initial (pre-driving) states were achieved for the DSE assemblies considered. Also, in order to show that the internal friction angle of the numerical packing was within a reasonable range, the ratio between horizontal stress and vertical stress was also calculated. The results are given in Fig. 3.17.

(a)   (b)
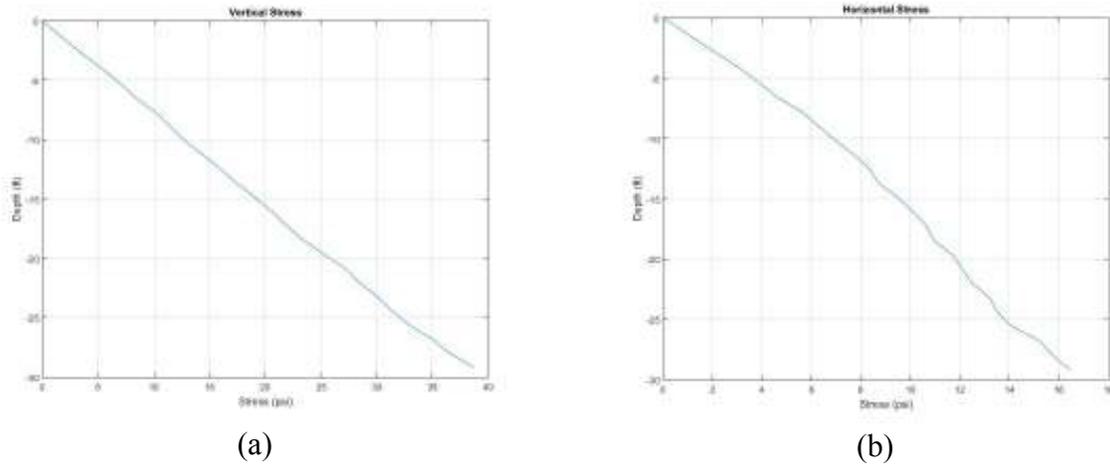
Figure 3.17 Geostatic stresses for DEM assemblies: (a) Vertical stress profile; (b) Horizontal stress profile

As shown in Fig. 3.17, the geostatic stresses increase linearly with respect to the depth of measured location. The stress profiles are consistent with those of a physical granular assembly with unit weight of (approximately) 105 pcf.
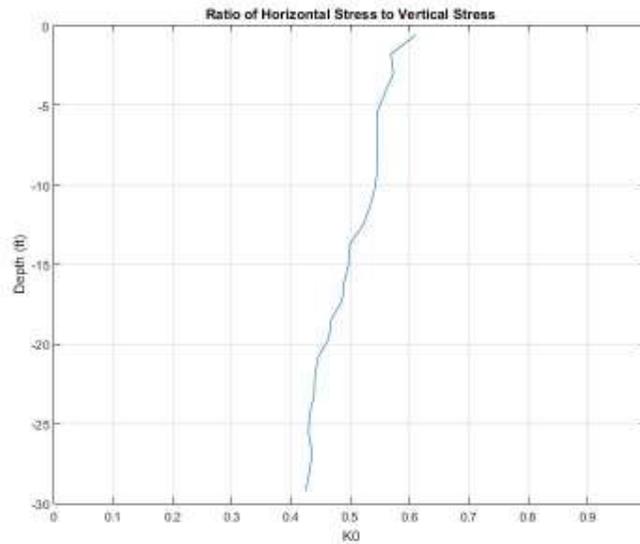
Figure 3.18 The ratio of horizontal stress to vertical stress of numerical packing

From Fig. 3.18, the ratio between horizontal stress and vertical stress varies slightly from top to bottom of the packing. This packing is fairly homogeneous according to the analysis of this parameter. In addition, the mean value of this ratio is around 0.5, which matches with the measurement of the packing used in the (physical) centrifuge test.

3.3.4 Measured vs Computed Stresses During Pile Driving

During physical centrifuge testing, several pressure sensors are distributed throughout the granular body. Positions of relevant pressure sensors are given in Section 2.5 and detailed in the Task 4 report. Per the orientation of pressure sensors, the normal stress in the particular direction is measured.

In the numerical models, the stresses of pressure sensors are simulated. More specifically, by selecting an appropriate control volume at the location of a given pressure sensor, the representative stress is calculated and compared with the stress readings obtained during centrifuge testing. As an example, positioning of the stress sensor PS 4 in the physical test setup is given in Fig. 3.19. Pertinent to the numerical model, this sensor is located at a depth of 8 ft and pile offset of 2.55 ft. While readings from this device were taken during physical testing, volume-averaged stresses are computed and cataloged as part of the numerical simulations.
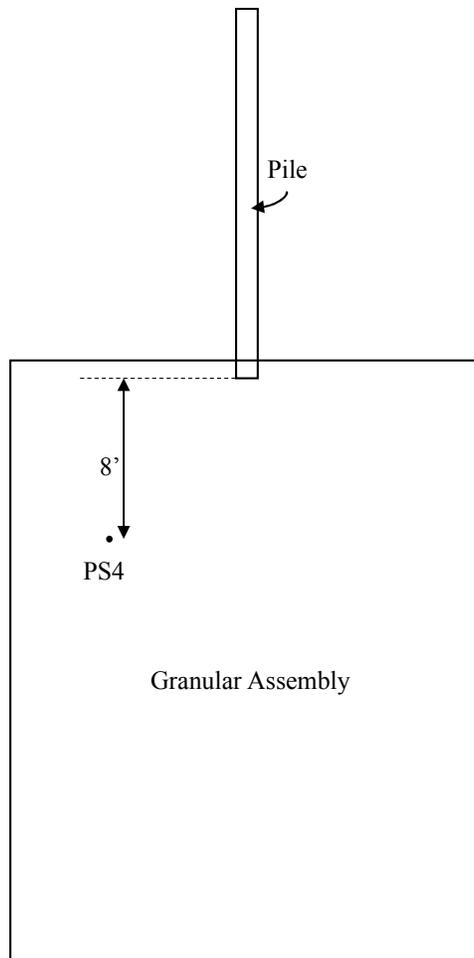
Figure 3.19 Schematic of pressure sensor PS 4 location (elevation)
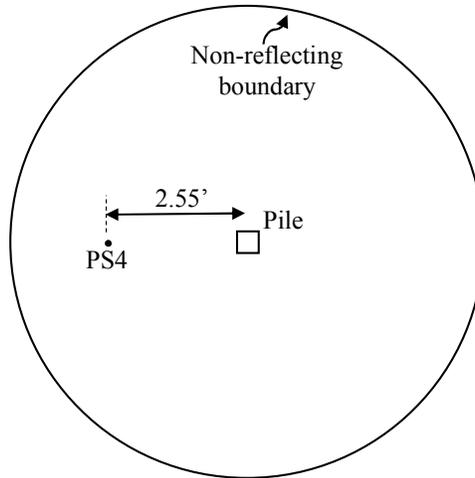
Figure 3.20 Schematic sketch of location of pressure sensor PS4 – plan view (refer to Fig. 3.11 for details of non-reflecting boundary)

Fig. 3.21 compares horizontal stresses of simulation 1, 2 (recall Table 3.4) to those stresses obtained from PS4 during centrifuge testing of scenario 1. For this branch of the parametric study, the bulk modulus of DSEs is defined as 10.52 ksi, the friction coefficient is varied as listed in Table 3.3.
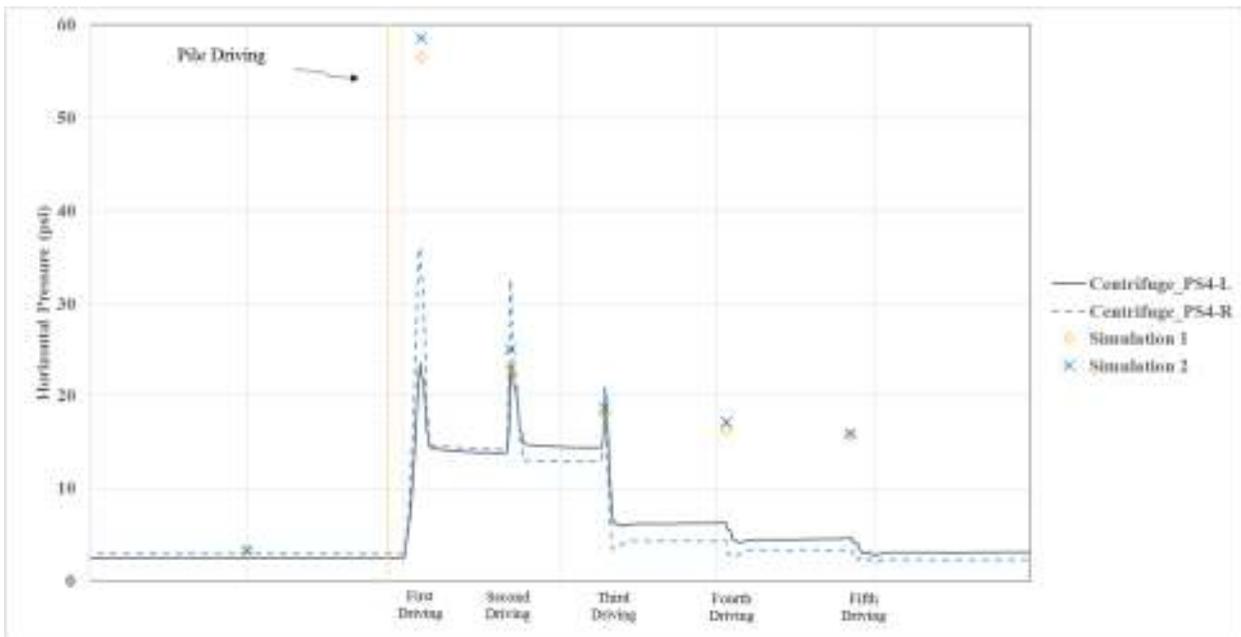
Figure 3.21 Horizontal stresses generated at the location of sensor PS4 during physical testing and for Simulations 1 and 2

Fig. 3.22 depicts horizontal stresses obtained from simulations 3, 4. For this subset of the parametric simulations, the bulk modulus of DSEs is defined as 15.77 ksi, while the friction coefficient is varied as indicated in Table 3.4.
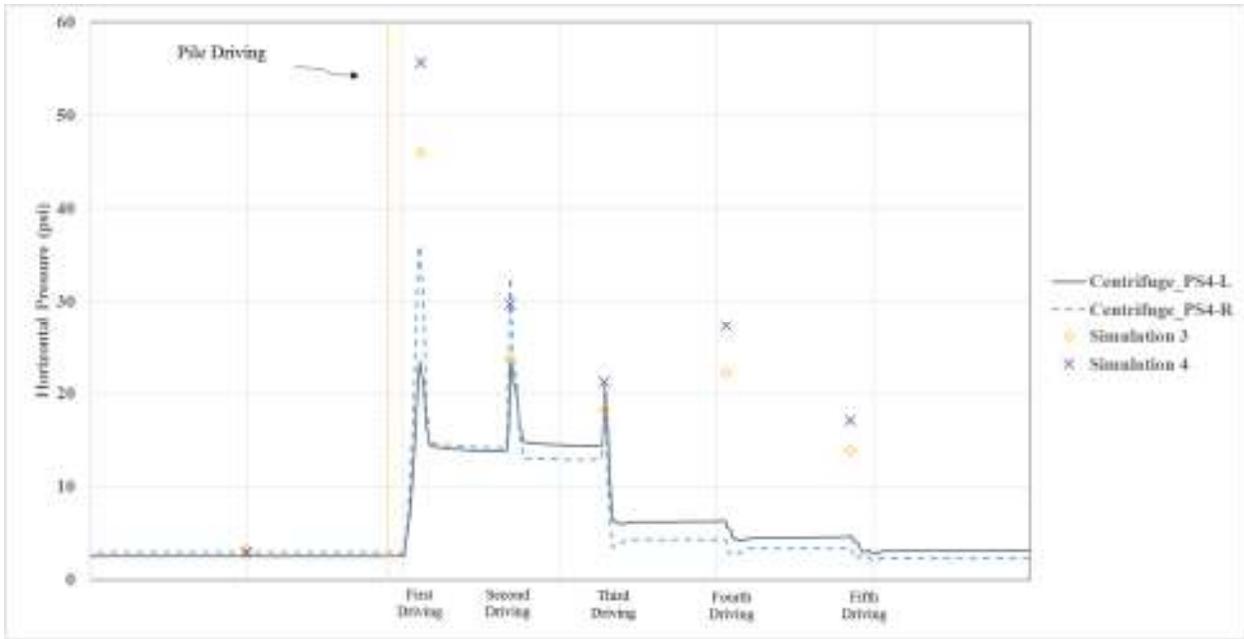
Figure 3.22 Horizontal stresses generated at the location of sensor PS4 during physical testing
and for Simulations 3 and 4

Fig. 3.23 depicts horizontal stresses obtained from simulations 5, 6. For this subset of the parametric simulations, the bulk modulus of DSEs is defined as 17.87 ksi, while the friction coefficient is varied as indicated in Table 3.4.
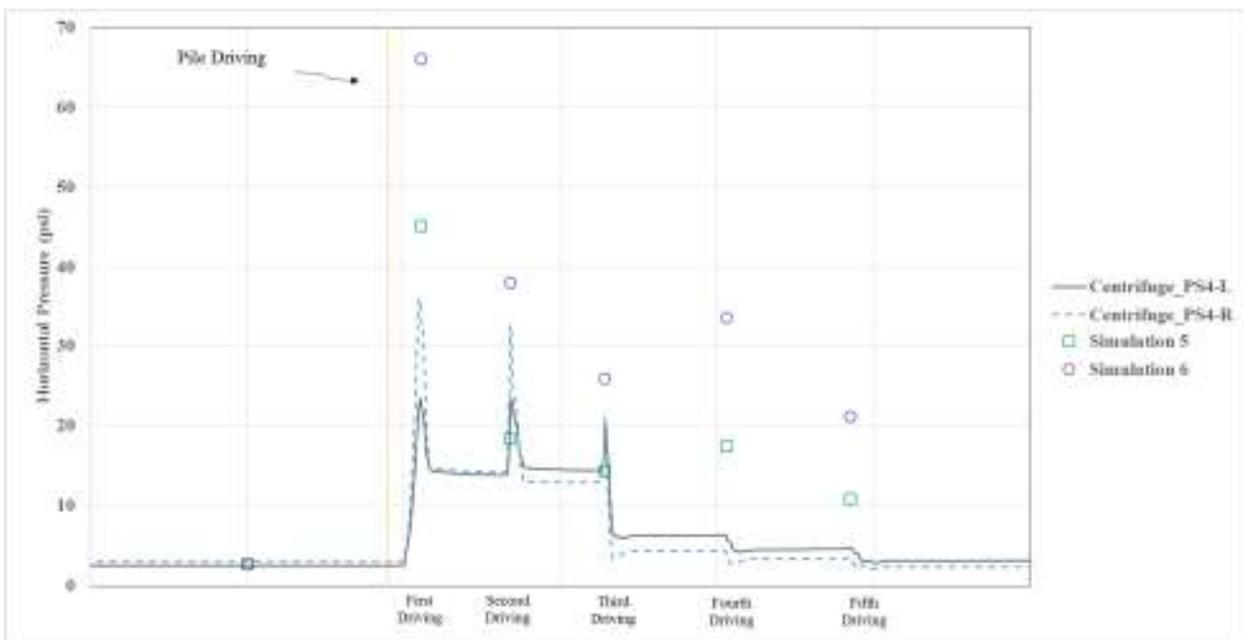
Figure 3.23 Horizontal stresses generated at the location of sensor PS4 during physical testing
and for Simulations 5 and 6
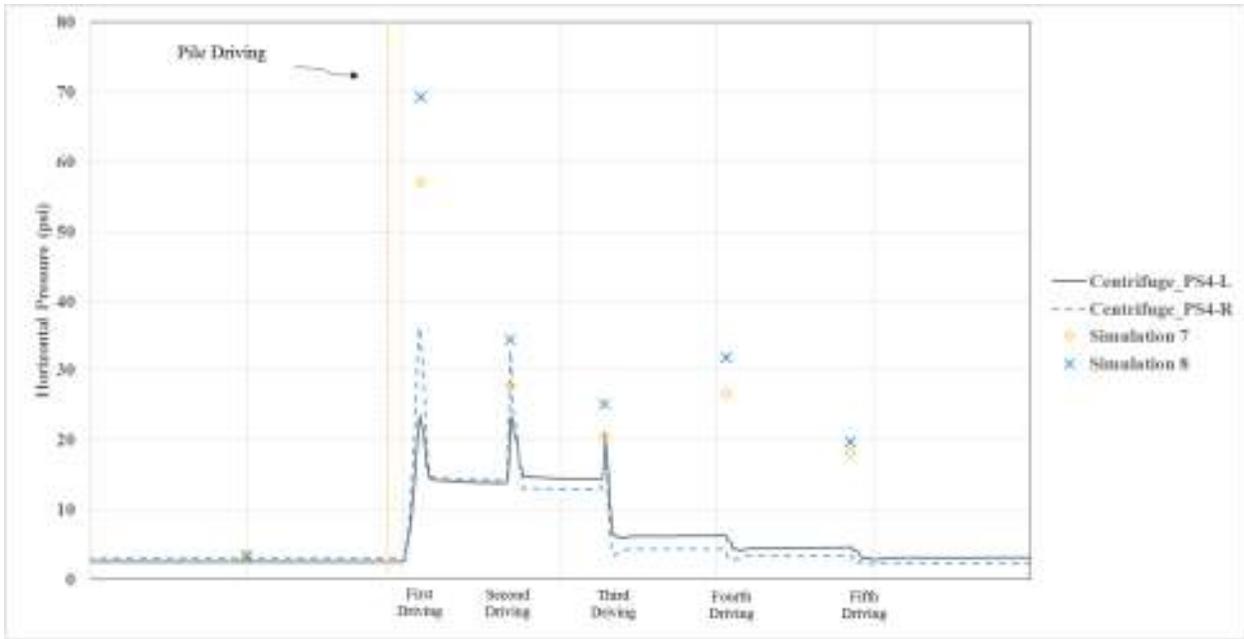
Figure 3.24 Horizontal stresses generated at the location of sensor PS4 during physical testing and for Simulations 7 and 8

Among the simulations conducted, the best match to physical stress measurements at the location corresponding to sensor PS4 are associated with simulation 6 and 7. The upper and lower bound measured data from simulation 6 and 7 are plotted in Fig. 3.25.
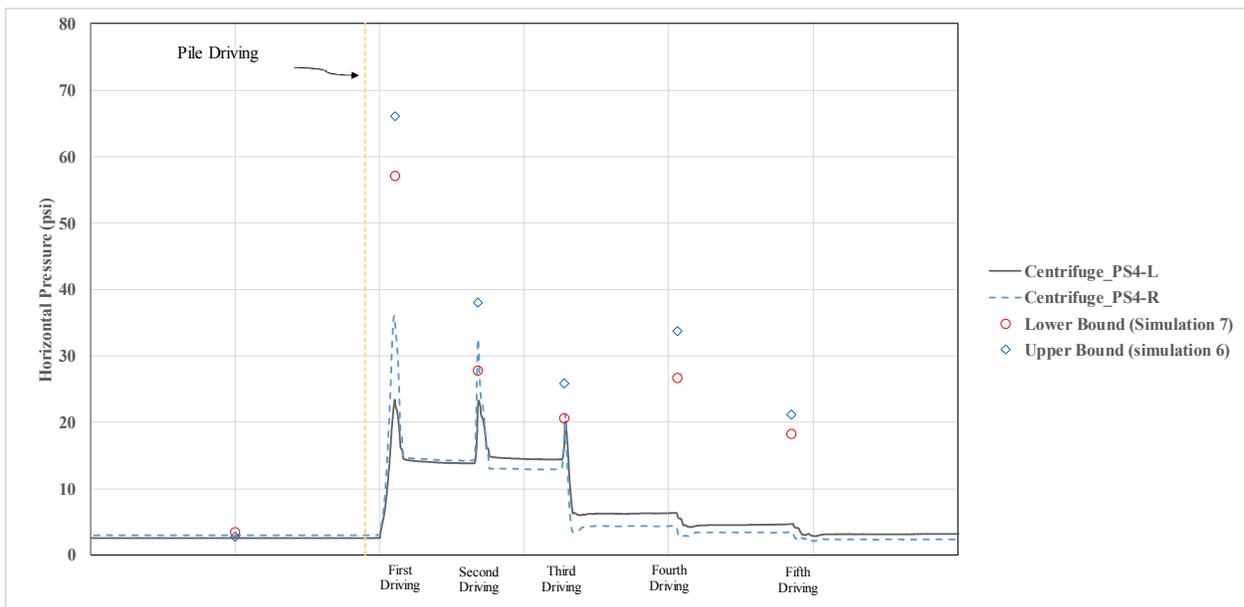
Figure 3.25 Horizontal stresses generated at the location of sensor PS4 during physical testing compared to upper and lower bound stresses for Simulations 6 and 7

Stresses around the fixed points in space are predicted at consistently higher levels during dynamic loading steps relative to stresses measured in the centrifuge tests. In essence, these stresses are the result of the dynamic stress equilibrium between two consecutive sampling locations in time; stress waves propagate through the fixed point in space at an incident time. The dimensions of the centrifuge test series are based on a scale factor of 32 with respect to the prototype scale. In fact, the loading rate was not controllable in the centrifuge tests. It fluctuates between durations of 25 ms and 100 ms at 32-g. Using the prototype loading duration (e.g., 100 ms; Holscher et al. 2012) as a representative value, the loading duration of the DEM simulation is calibrated with respect to a time-history of dynamic resistance measured in the pile (embedded load cells) during the centrifuge pile driving sequence. To make a qualitative comparison between the measured and predicted results, a best-matched set of loading durations is simulated on an iterative basis in order to re-produce amplitudes of dynamic (pile) resistance at each dynamic loading step. In turn, the loading steps fall in the range of 100 and 300 ms at the prototype scale, as shown in Fig. 3.16. Thus, all stresses are plotted in a sequence of blows (normalized driving durations in the frequency domain). In this way, we can maintain a meaningful comparison among possible peak amplitudes of stress waves as they propagate throughout the medium.

To measure the prototype stress wave propagation in the centrifuge test correctly, stress generation, attenuation and wave propagation must be scaled properly. If the volumetric mass of sand in DSE and volume-averaged contact stiffness of DSE are comparable between the prototype and the model, wave propagation will also be scaled correctly. In other words, subject to stress levels similar to those in the prototype, the DSE assembly should be capable of generating macroscale stress waves if all parameters are "correctly scaled" (Ovesen (1981)). Though, considering possible variances in association with the effective parameters of the representative discrete spherical volume, the investigators opt to use a range of values of effective modulus to capture incipient occurrence of stress wave (velocity) at a fixed point in space during each of the loading durations.

In the normalized time domain, DEM simulations consistently predict the occurrence of peak amplitudes of the prototype stress (volume-averaged contact forces among DSEs) at each incident of pile driving (e.g., compare Fig. 3.25 to Fig. 3.16; corresponding predicted dynamic resistance of pile is given later in Fig. 2.42 of Pile Driving Simulations 5 and 7). However, in the physical tests, peak incidences in stress wave propagation may not be captured by the available transducers (or recorded in a data acquisition system), particularly for the fourth and fifth pile-driving incidents when stress wave velocity appears to exceed "excitation response" (in-out) signal frequency of the sensors. Given an estimated (spherical) wave velocity which varies between 2000 ft/s and 2500 ft/s (610~762 m/s) of the granular medium (predicted by DEM simulations) and the (initial) distance between the sensor location (PS4) and the pile driving path of 2.55 ft (0.78 m), acceleration signals require a window of processing time (frequency) to be less than 1.0 ms. But, this is a smaller window than that which can be captured at the sampling rate of the available data acquisition system. It is possible that signals interpreted for conversion to stress amplitudes may not have always been at the peak incident in space (schematically illustrated in Fig. 3.26). It is noted that an average wave velocity of 1500 ft/s (450 m/s) was measured on time signals during drop-ball centrifuge tests (steel ball with about one third of the pile mass and a drop height of a few feet at the prototype scale) on medium dense sand by Semblat et al. (1995). The measured stress data may therefore not be amenable to quantitative identification such short-lived peaks of stress. The best approach to the calibration of the DEM models, therefore, is to observe the

dynamic forces (accelerations) of the pile and check the accuracy of the predictive procedure upon establishment of a reference dynamic state. This serves to narrow phenomenological variations in the installation sequences of the pile-SPW-soil system.
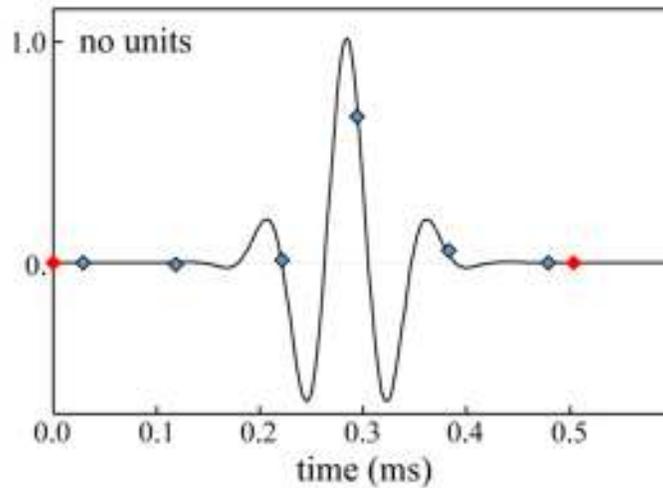
Figure 3.26 Schematic of temporal sampling variation used for time-frequency analysis of acceleration signals: the markers show when a signal is recorded for the wavelet (solid line) at two different sampling rates. The six blue markers illustrate that a sampling rate of 0.1 ms may still miss the peak incidence. The red markers indicate that a signal sampling rate at 0.5 ms may completely miss the wavelet passing through a point in space (after Semblat et al., 1995)

3.3.5 Measured vs Computed Pile Driving and Top-Down Load Test Results

Following the input parameters for parametric study described in section 3.3.2, eight simulations are built and submitted for Test Scenario 1. The pile driving and top-down load displacement relationship simulated by numerical model and measured from centrifuge test are are presented in the following.

Fig. 3.27 shows the top-down load simulation results of Simulations 1 and 2. In this batch of simulations, the effective elastic modulus of DSEs is defined as 10.52 ksi whereas the (sliding and rolling) friction coefficients vary. The detailed values are given in Table 3.5.

70
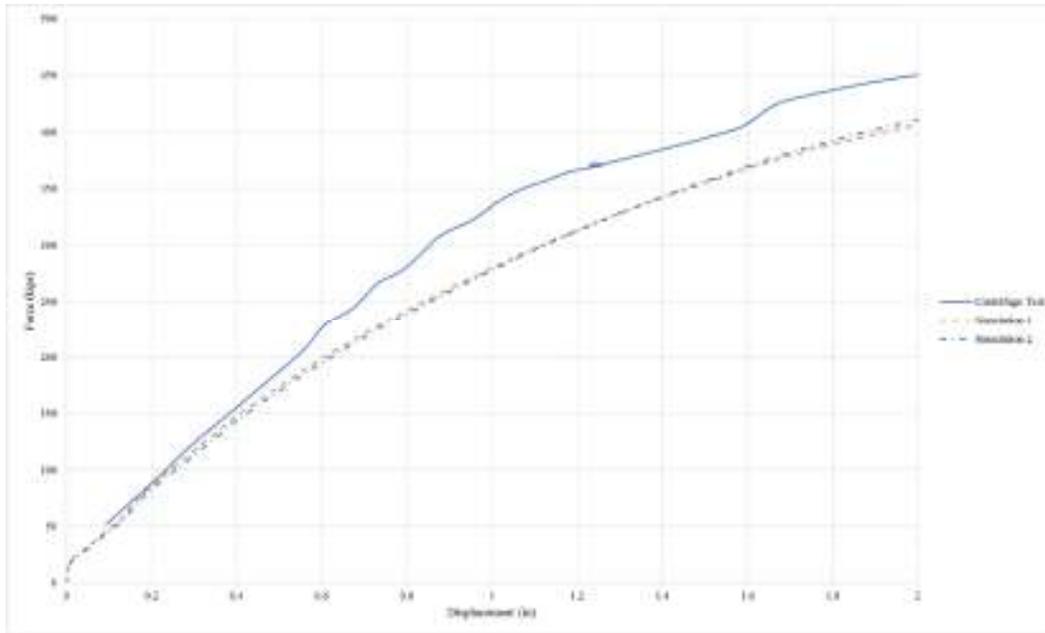
Figure 3.27 Load displacement relationship during top-down load phase for Simulations 1 and 2

Table 3.5 Ultimate and Davisson Capacity for the piles in simulations 1 and 2

Simulation Number	Ultimate Capacity (kips)	Davisson Capacity (kips)
Centrifuge Test	450	150
1(S1)	406	149
2(S1)	412	131

Fig. 3.28 shows the top-down load simulation results of simulation 3, 4. In this batch of simulations, the effective elastic modulus of DSEs is defined as 15.77 ksi whereas the friction coefficients vary. The detailed values are given in Table 3.6.
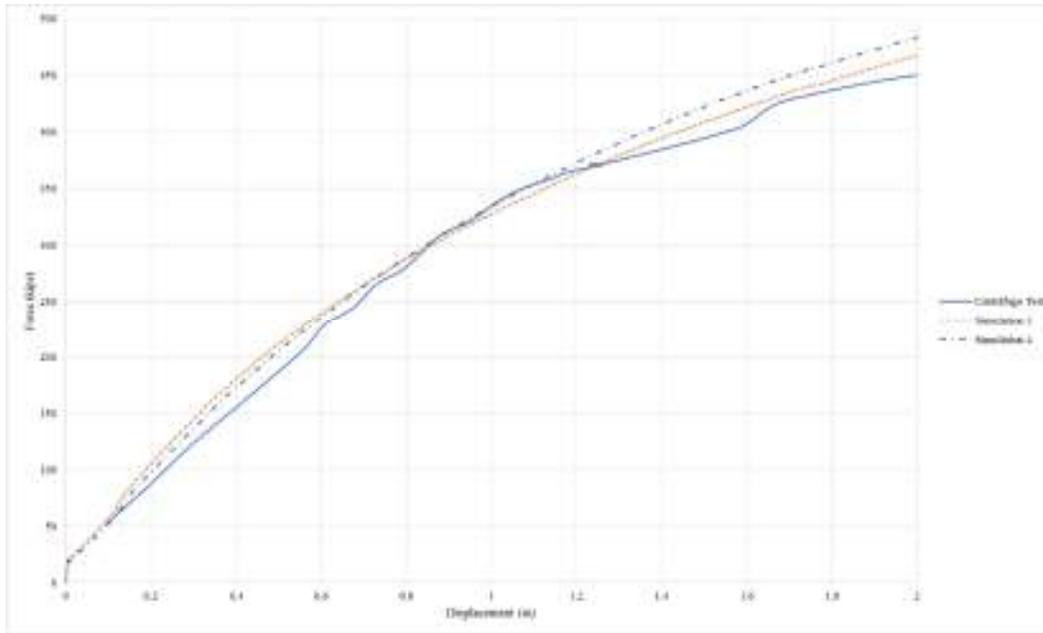
Figure 3.28 Load displacement relationship during top-down load phase for simulations 3 and 4

Table 3.6 Ultimate and Davisson Capacity for the piles in simulations 3 and 4

Simulation Number	Ultimate Capacity (kips)	Davisson Capacity (kips)
Centrifuge Test	450	150
3	468	180
4	484	173

Fig. 3.29 shows the top-down load simulation results of simulation 5, 6. In this batch of simulations, the effective elastic modulus of DSEs is defined as 17.87 ksi whereas the friction coefficients vary. The detailed values are given in Table 3.7.
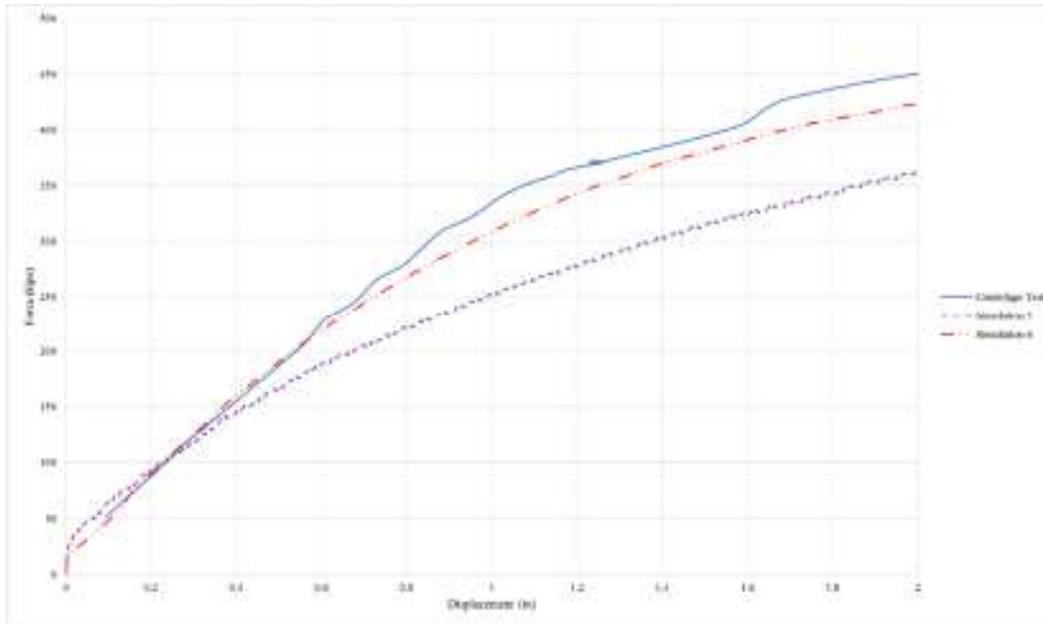
Figure 3.29 Load displacement relationship during top-down load phase for simulations 5 and 6

Table 3.7 Ultimate and Davisson Capacity for the piles in simulations 5 and 6

Simulation Number	Ultimate Capacity (kips)	Davisson Capacity (kips)
Centrifuge Test	450	150
5	321	145.2
6	424	161

Fig. 3.30 shows the top-down load simulation results of simulation 7, 8. In this batch of simulations, the effective elastic modulus of DSEs is defined as 21.02 ksi whereas the friction coefficients vary. The detailed values are given in Table 3.8.
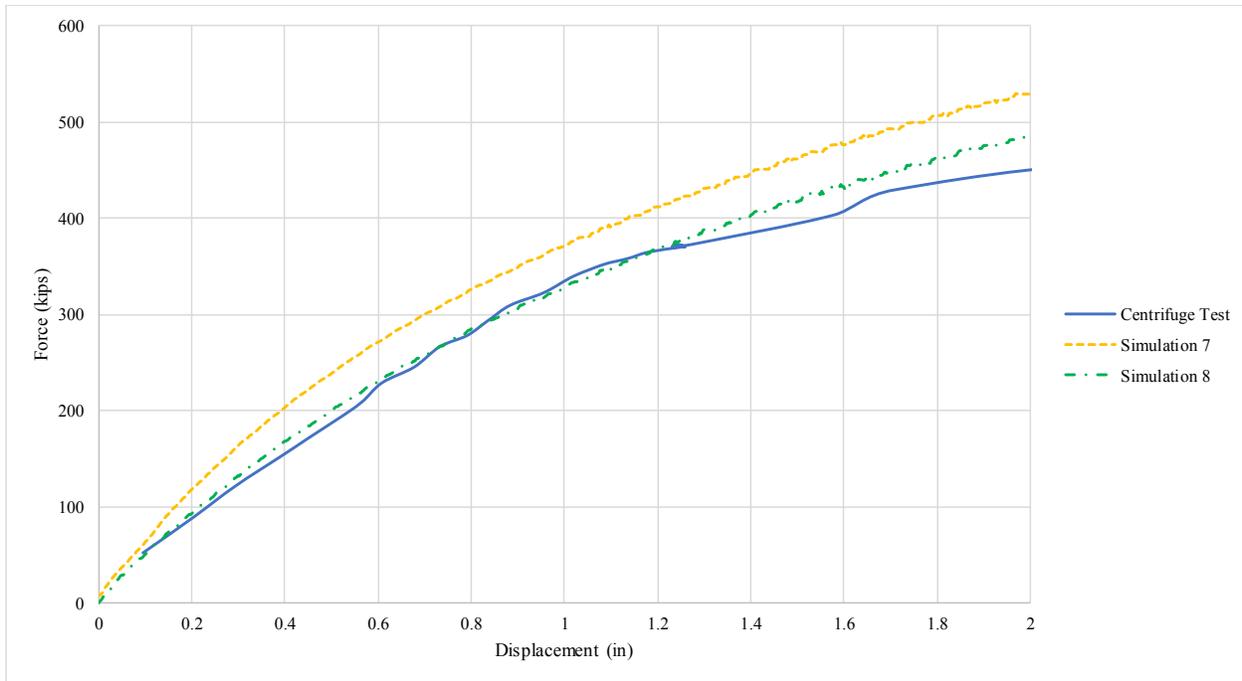
Figure 3.30 Load displacement relationship during top-down load phase for simulations 7 and 8

Table 3.8 Ultimate and Davisson Capacity for the piles in simulations 7 and 8

Simulation Number	Ultimate Capacity (kips)	Davisson Capacity (kips)
Centrifuge Test	450	150
7	529	202
8	485	196

The load-displacement time history during pile driving is plotted for the numerical simulations that show good agreement with measured driving history in Fig. 3.31. From Fig. 3.27 to Fig. 3.30, the top-down load test results of the centrifuge test (Test Scenario 1) is reasonably bounded by simulations 6 and 7. The load-displacement curve of top-down load test simulation for these bounding cases are given in Fig. 3.32. Corresponding input parameters are listed in Table 3.9.

74
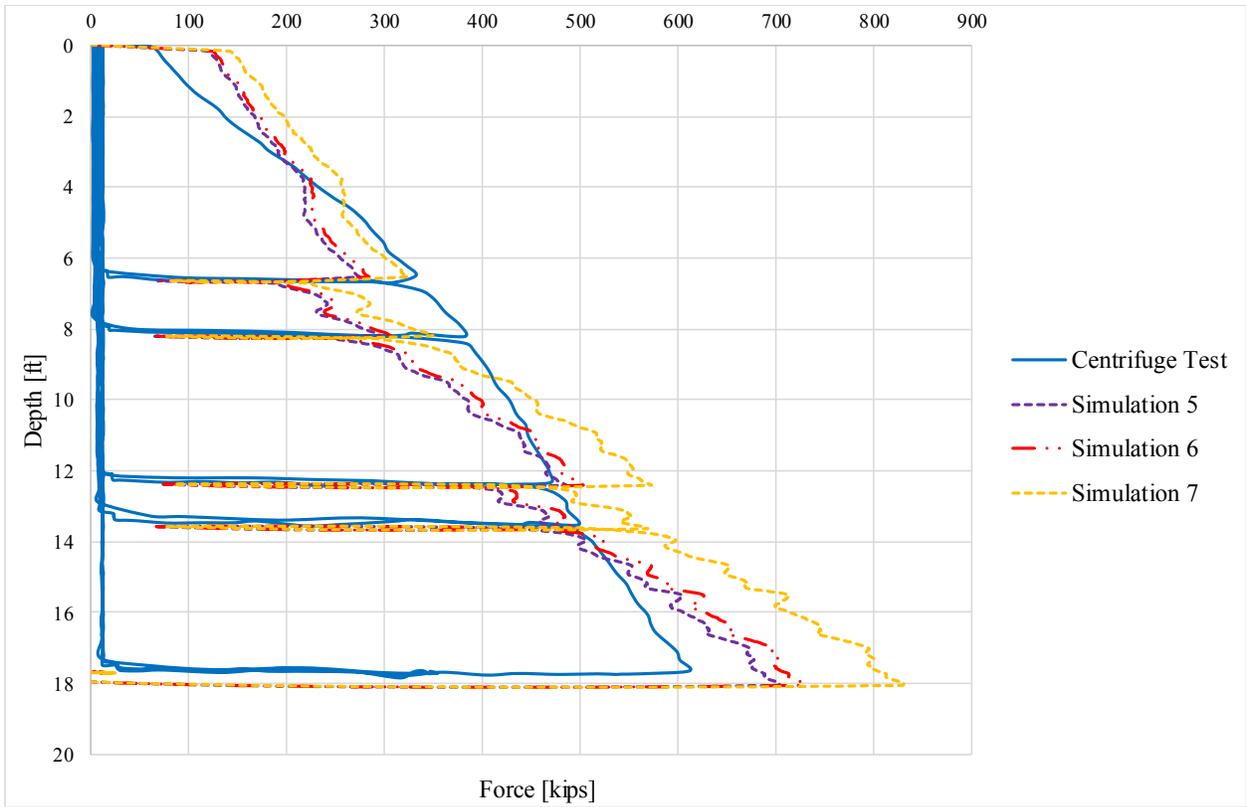
Figure 3.31 Comparison of dynamic load resistance among centrifuge and simulations 5, 6, and 7
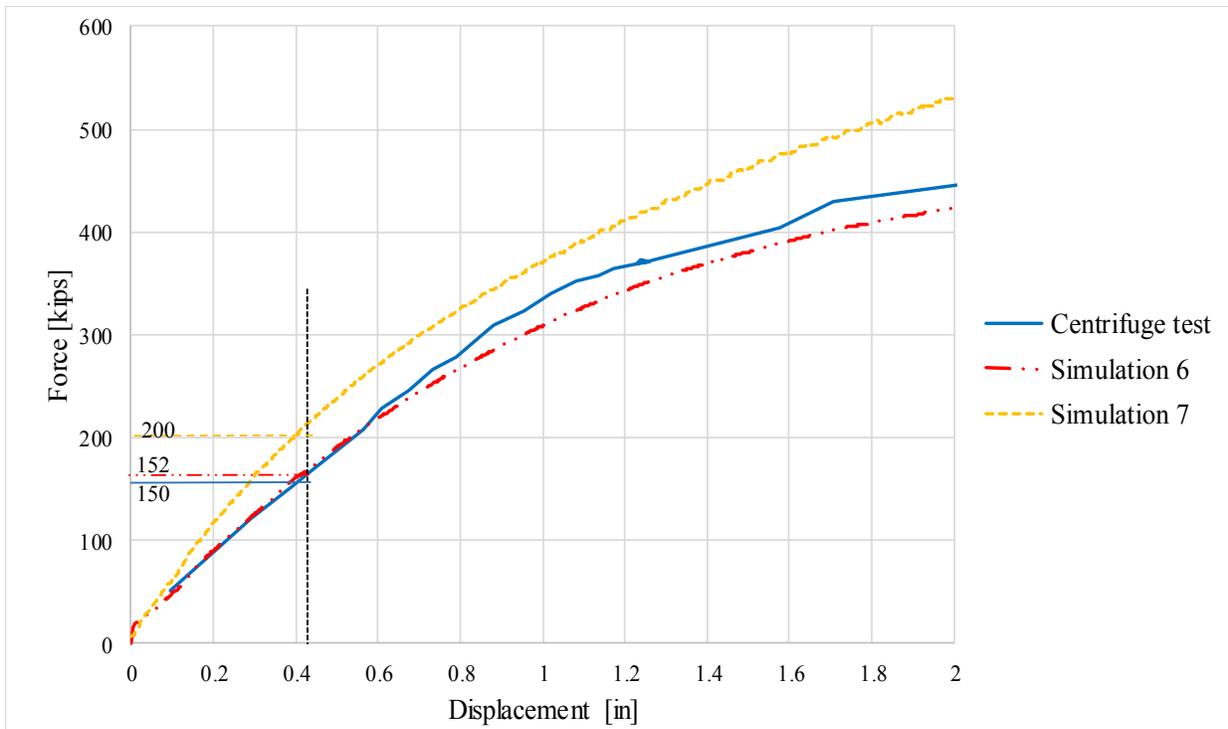
Figure 3.32 A numerical approximation of the top-down load test result under Scenario 1 condition

Table 3.9 Ultimate and Davisson Capacities for Scenario 1		
Load Test Scenario	Ultimate Capacity (UC) (kips)	Davisson Capacity (DC) (kips)
Centrifuge test	468	150
Simulation 6(S1)	425	152
Simulation 7(S1)	532	200

3.3.6 Identification of Representative Model for Test Scenario 1

Comparisons of measured (physical, centrifuge) and computed (numerical simulation) stresses and top-down load results demonstrate that the combined DEM-FEM modeling approach is capable of simulating behaviors of granular bodies as well as the resistance of structural objects inserted into said granular bodies. Even so, the following observation is made concerning the overall comparisons: stresses generated at selected locations in the numerical simulation are generally of greater magnitude than those measured during physical centrifuge testing. However, a consistent trend is observed among the change in stresses across both numerical and physical test results, particularly during pile driving. Further, pronounced stress peaks are present among both the physical and numerical results at the onset of each driving stage.

As indicated in Fig. 3.32, Simulation 6(S1) and Simulation 7(S1) successfully bound the physical measurements of pile load-displacement. Given the relatively strong level of agreement with respect to physical versus numerical records of pile load-deformation, representative numerical models are identified with emphasis on top-down load test results.

3.4 Numerical Modeling of Test Scenario 2

In this section of the report, a detailed account of numerical models used for simulating scenario 2 of centrifuge tests is given. The stresses within the assembly and the load-displacement relationship during the top-down load test are used as deciding factors for model calibration.

3.4.1 Model Components and Simulation Sequence

Most of the components of the numerical model to simulate scenario 2 are the same as those used for scenario 1 simulations (Sec. 3.3.1). The new addition to the previous test setup is the SPW. To accommodate SPW driving in the granular assembly at a prescribed distance from the pile and the boundary, a much larger granular assembly is required as compared to scenario 1 (where only the pile was introduced into the DSE assembly). This exponentially increases the number of elements required to mesh the entire volume for conducting system-scale simulations. Owing to the computational cost associated with running discrete element models, it becomes unfeasible to use such a small discrete element (as used in scenario 1) to mesh such a large volume. Hence, based on the dimension requirements for scenario 2, a scaling factor was determined and the granular mesh used for scenario 1 was scaled up by that factor to create the larger domain while maintaining feasibility of practical simulation runtimes. A schematic for the scenario 2 setup and determination of the scale factor is given below (Fig. 3.33).
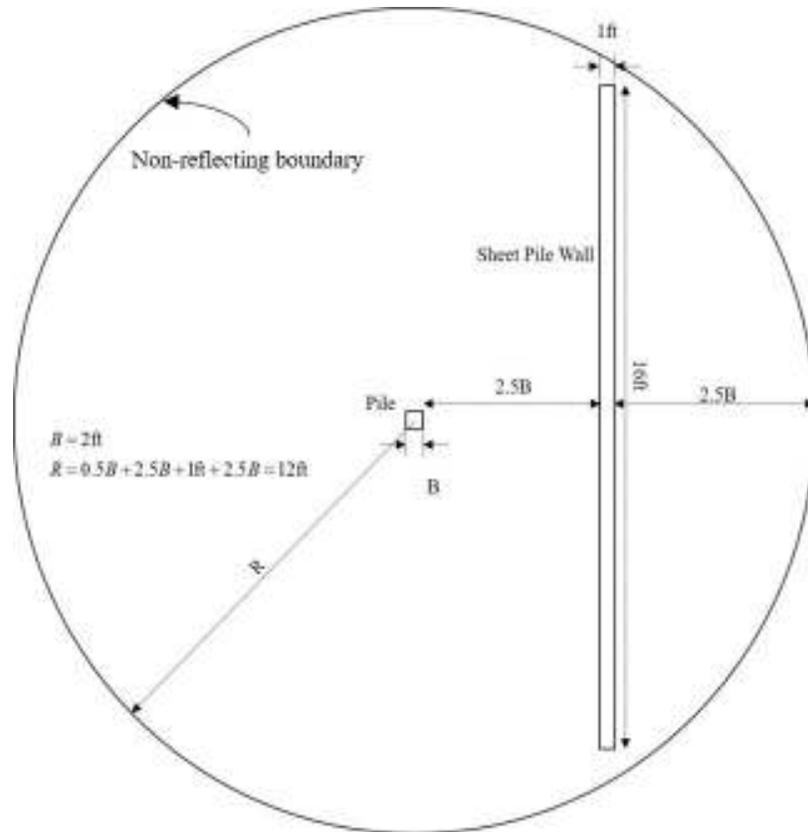
Figure 3.33 Schematic for Scenario 2 setup (refer to Fig. 2.19 for details of non-reflecting boundary)

As can be seen from Fig. 3.33, the large domain of granular assembly needs to be at least 24 ft in diameter. The diameter of granular assembly used in scenario 1 is 10.5 ft. Thus, the scale factor between larger and smaller granular assembly is 2.28. In the process of scaling up, the discrete elements are also scaled up to 0.97 in diameter. The shear resistance of a granular assembly using these discrete elements are estimated using triaxial compression test as described in Sec. 3.1. Another important aspect to consider while scaling up the granular assembly is that the depth of the packing, after scaling up, is about 68 ft. For the purpose of simulating SPW and pile driving sequence, a depth of about 30 ft is estimated to be sufficient. Thus, the bottom 38 ft of the scaled up granular assembly is removed so as not to disturb the stresses developed within the assembly under body forces. The scaled granular assembly is then fitted with the LNRBC spring and dampers described in Sec. 3.2.

A finite element SPW model is created to represent the SPW used in physical testing. The dimensions of the SPW are shown in Fig. 3.34. The SPW driving sequence is given in Fig. 3.35. Note that the DSE assembly is permitted to reach a steady state after SPW driving and prior to pile driving, and again after pile driving.
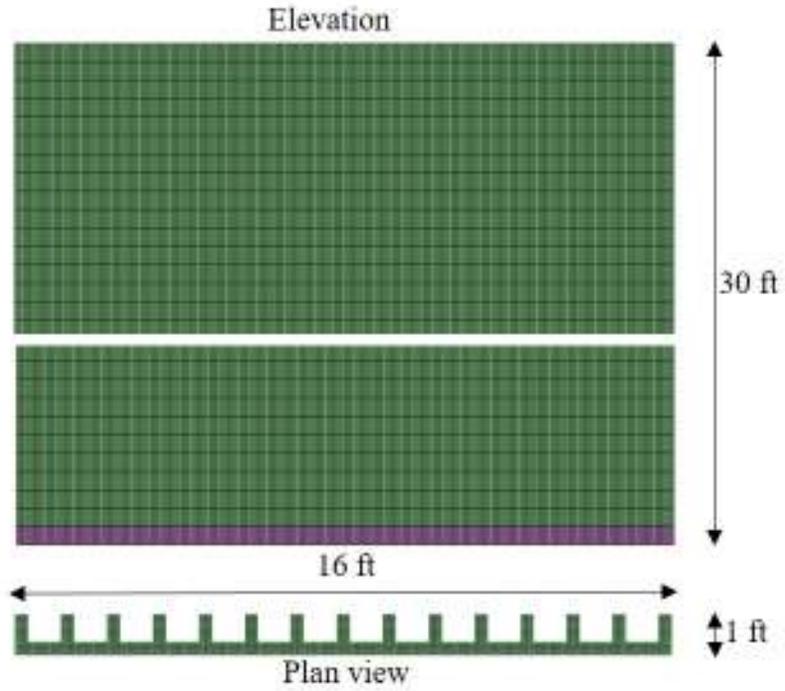
Figure 3.34 Sheet pile wall dimensions
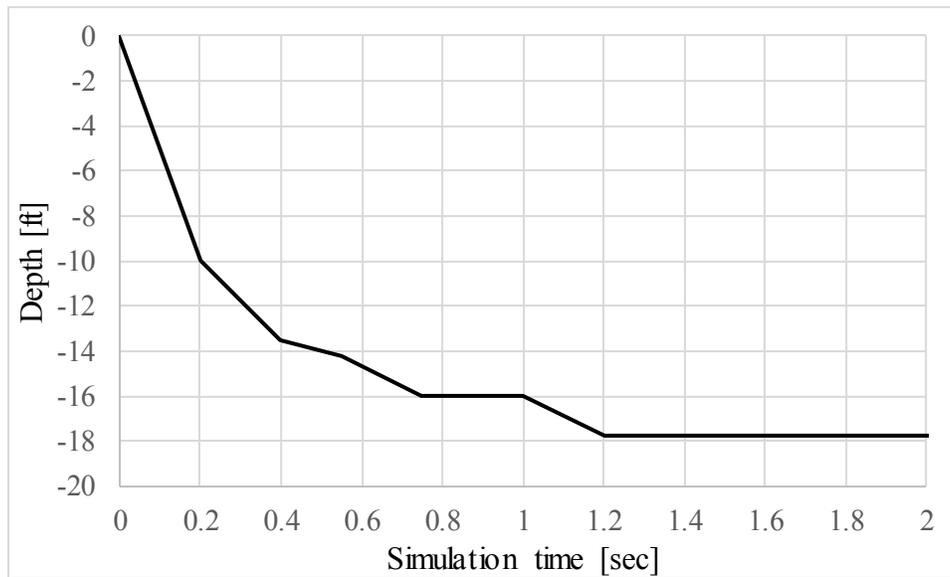
Figure 3.35 SPW driving sequence

The pile driving sequence used in scenario 2 is given below in Fig. 3.36.
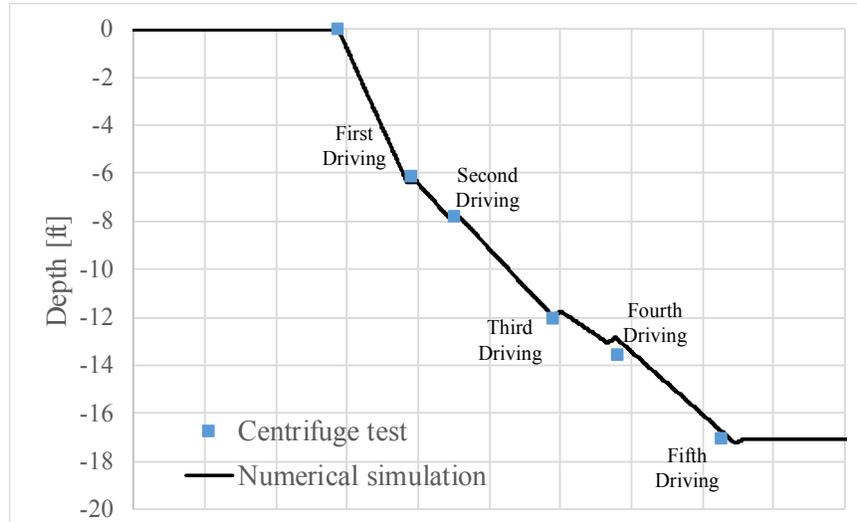
Figure 3.36 Pile driving sequence used in Scenario 2: the tic marks of the abscissa represent 0.1 sec. time intervals.

3.4.2 Parametric Study

A parametric study is performed with respect to bulk modulus (contact stiffness) and inter-granular sliding friction for discrete elements. Similar to the set of input variables used in scenario 1 test matrix, four values of bulk modulus and two values of sliding friction coefficient are selected for investigation. For higher sliding friction coefficient, only the cases that compare well with the centrifuge test are included here. The test matrix for the parametric study is given below (Table 3.10).

Table 3.10 Test matrix for parametric study for Scenario 2

Simulation	Bulk modulus ksi (MPa)	Inter-granular friction coefficient (sliding; rolling)
1 (S2)	10.52 (72.5)	0.6; 0.06
3 (S2)	15.77 (108.7)	0.6; 0.06
5 (S2)	17.87 (123.2)	0.6; 0.06
6(S2)	17.87 (123.2)	1.0; 0.1
7 (S2)	21.02 (145)	0.6; 0.06

3.4.3 Simulation of Geostatic Stresses

Geostatic stresses are analyzed to exhibit the validity of granular assembly consisting discrete elements to represent sand at rest. Geostatic stresses for one the assemblies from the test matrix are shown in Fig. 3.37 below. The coefficient of lateral earth pressure at rest is also quantified as the ratio of horizontal to vertical stresses, and is plotted with respect to depth in Fig. 3.38.
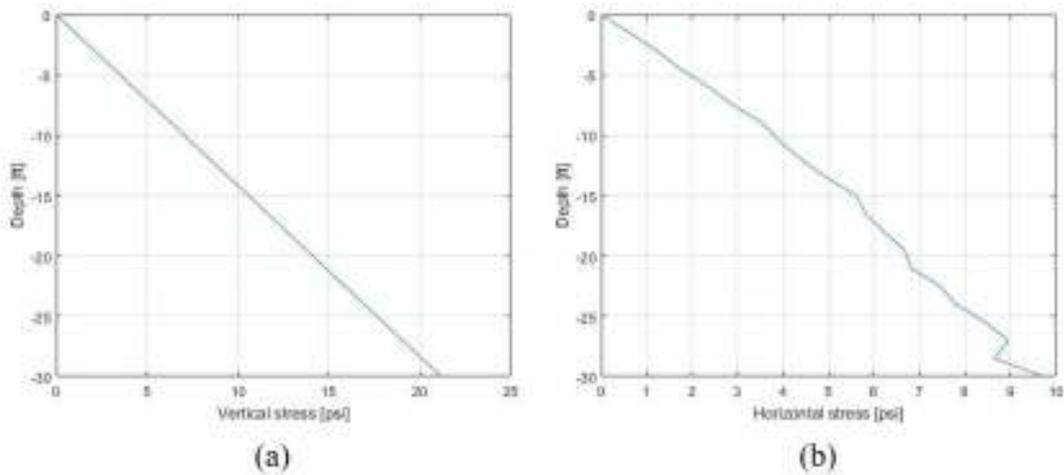
Figure 3.37 Geostatic stresses in numerical granular assembly used in Simulation 5: (a) Vertical stress; (b) Horizontal stress
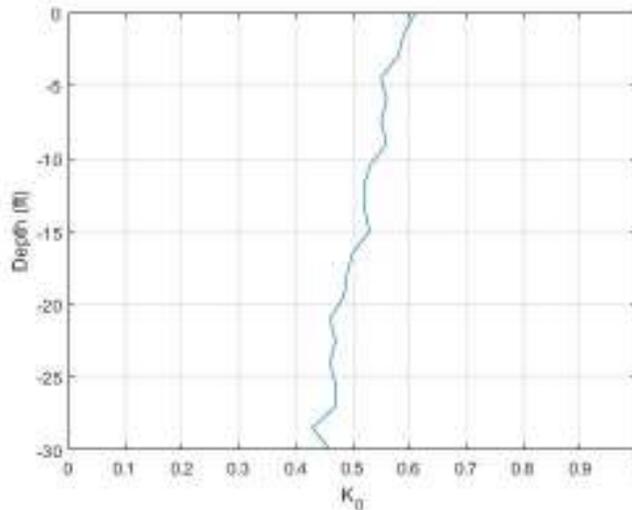
Figure 3.38 Coefficient of lateral earth pressure at rest in numerical granular assembly used in Simulation 5

As can be seen from above figures, the stress state of granular assembly bears a good resemblance with actual at rest conditions in natural sand. Namely, the stress profiles are consistent

with those of a physical granular assembly with unit weight of (approximately) 105 pcf. The average K_0 value for all the granular assemblies for scenario 2 lies in the range of 0.45 to 0.58.

3.4.4 Measured vs Computed Stresses During Sheet Pile Wall Installation

In the physical test setup, a number of pressure sensors were located within the sand mass to measure horizontal and vertical pressure throughout the various testing stages. As has been described in previous sections, the domain sizes differ between physical centrifuge test setup and numerical test setup. Hence, results from all the pressure sensors cannot be utilized to compare the stresses between physical and numerical test results. Pressure sensor locations that fall within the numerical domain are given below (Figs. 3.39 and 3.40).
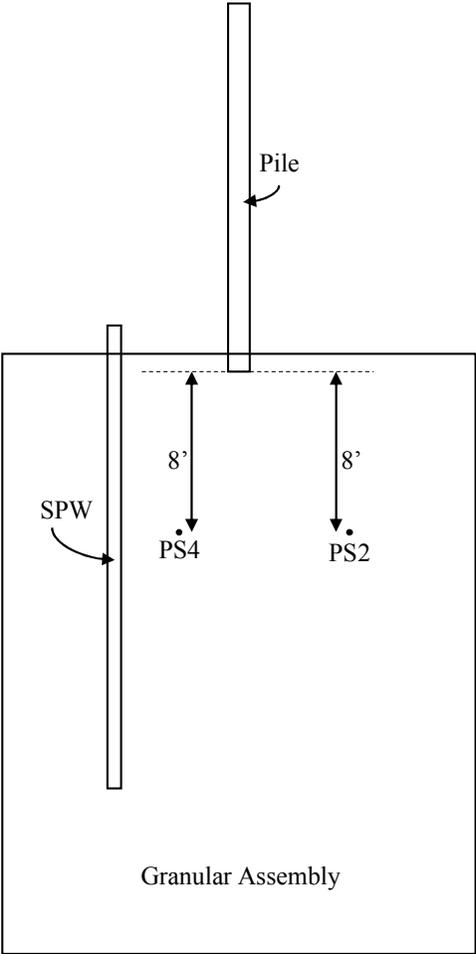
Figure 3.39 Schematic of pressure sensor locations in numerical domain (elevation)
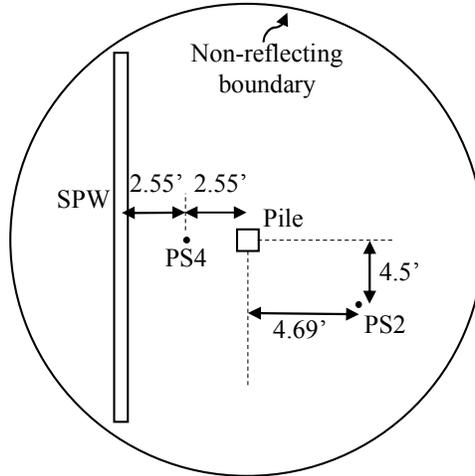
Figure 3.40 Schematic of pressure sensor locations in numerical domain – plan view (refer to Fig. 3.11 for details of non-reflecting boundary)

Vertical stress measurements from pressure sensor PS2 are plotted below (Figs. 3.41 and 3.43). Also, horizontal stress measurements from pressure sensor PS4 are plotted below (Figs. 3.42 and 3.44). During the duration of test sequence in centrifuge, there is possibility of the transducer to displace from its original location. Displacement of the sensors (relative to the initial fixed locations) are unknown during the dynamic loading sequence. For qualitative comparisons, stress amplitudes in the numerical domain are predicted in bounded frequency domains sampled in the initial locations of the transducers. This bounded approach is utilized mainly to demonstrate (1) the stress wave propagation (stress time history) in high frequency (faster loading rate), and (2) resulting stress patterns due to particle rearrangement during and after SPW installation in centrifuge testing. Again, the peak amplitudes of the stress wave do not always appear to be recorded in the data acquisition system as explained earlier.
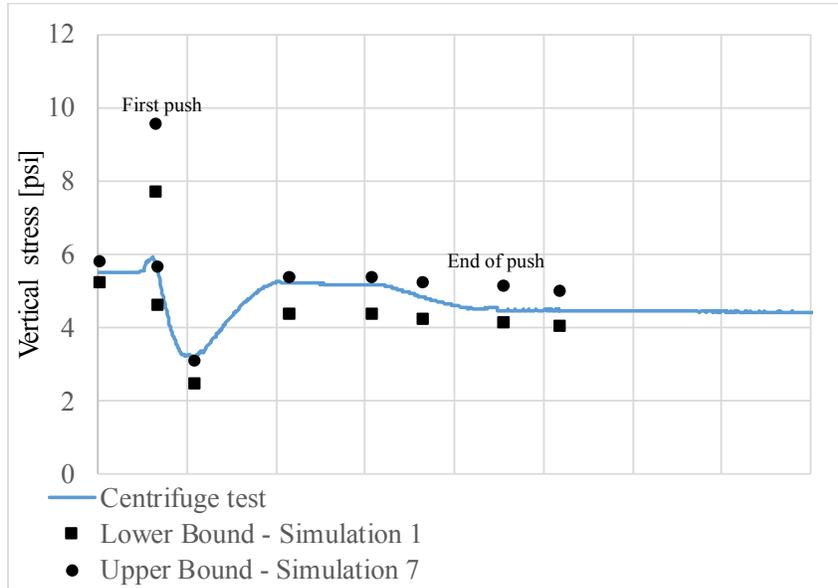
Figure 3.41 Vertical stress results (bounded) from pressure sensor PS2 during SPW installation from Simulations 1 and 7
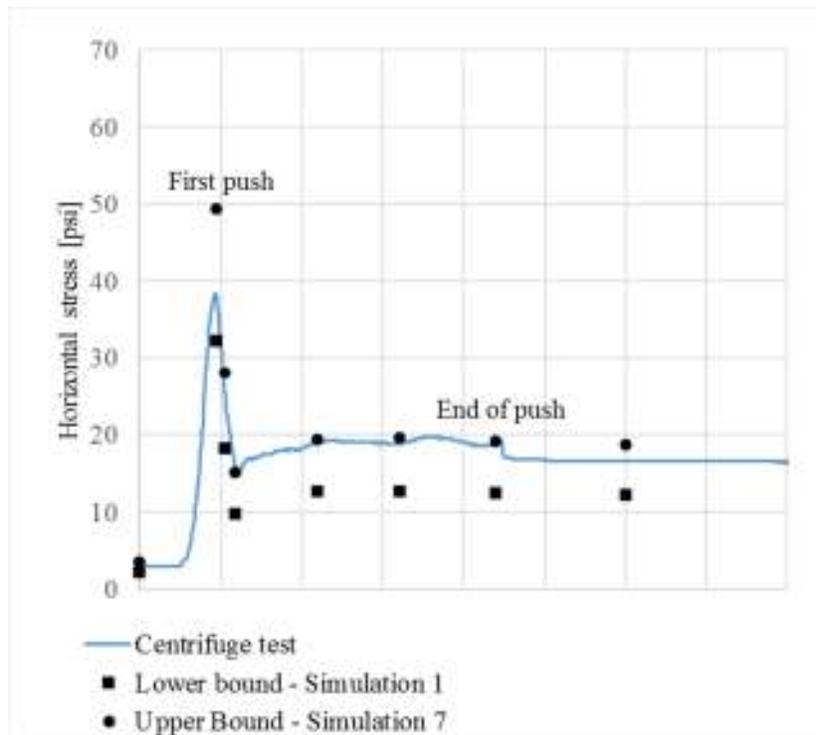
Figure 3.42 Horizontal stress results (bounded) from pressure sensor PS4 during SPW installation from Simulations 1 and 7
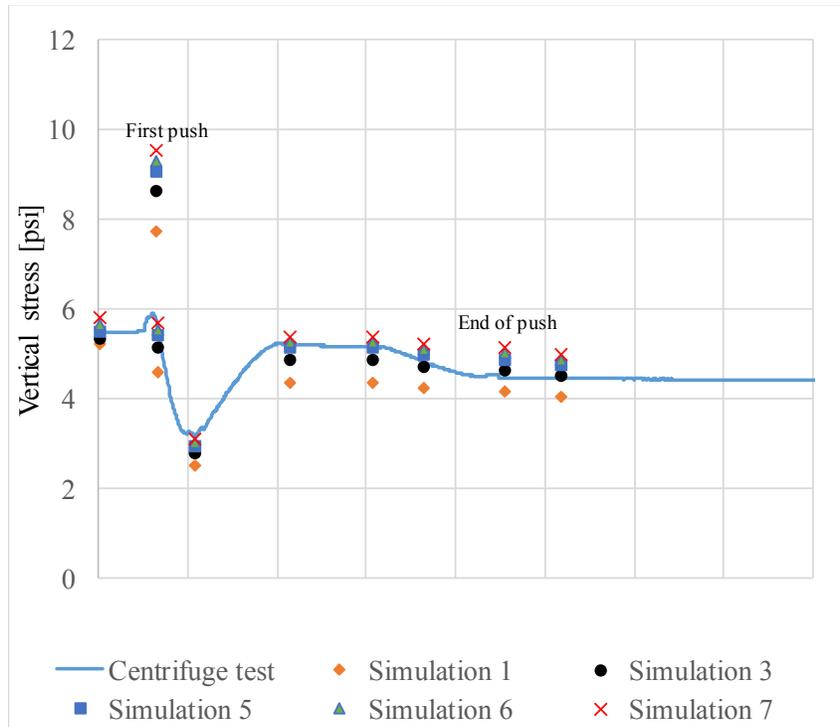
Figure 3.43 Vertical stress results from pressure sensor PS2 during SPW installation from numerical Simulations 1 through 7
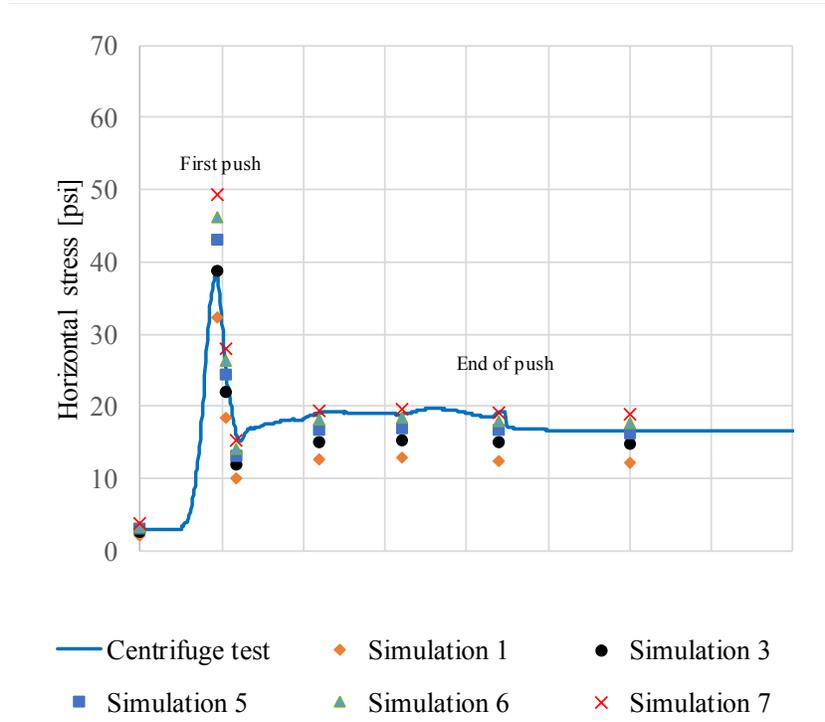
Figure 3.44 Horizontal stress results from pressure sensor PS4 during SPW installation from numerical Simulations of 1 through 7

3.4.5 Measured vs Computed Stresses During Pile Driving

Vertical and horizontal stress results from physical tests are compared with stress results from numerical simulations in a manner similar to the one described in Sec. 3.4.4.
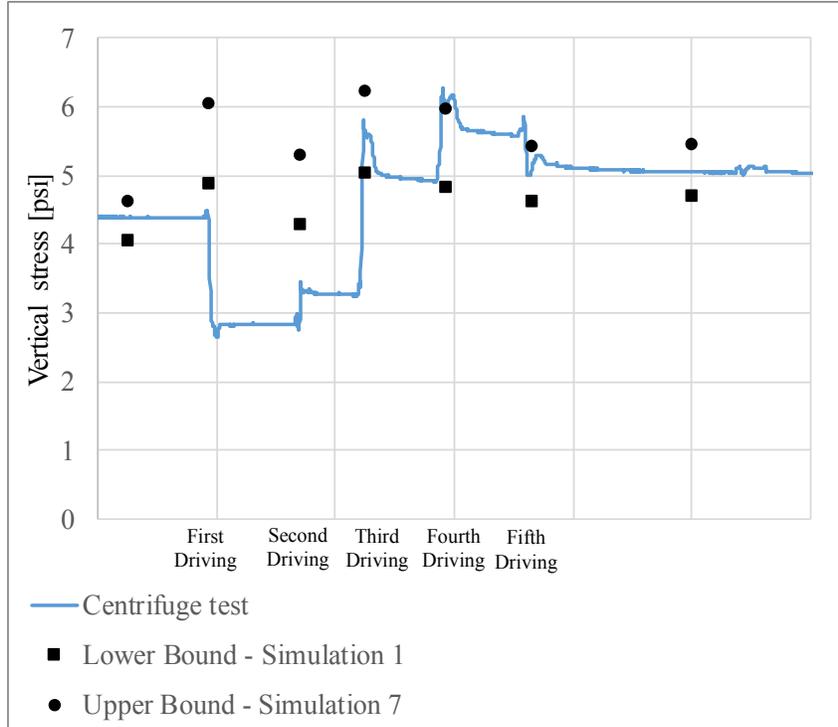
Figure 3.45 Vertical stress results (bounded) from pressure sensor PS2 during pile driving phase from Simulations 1 and 7
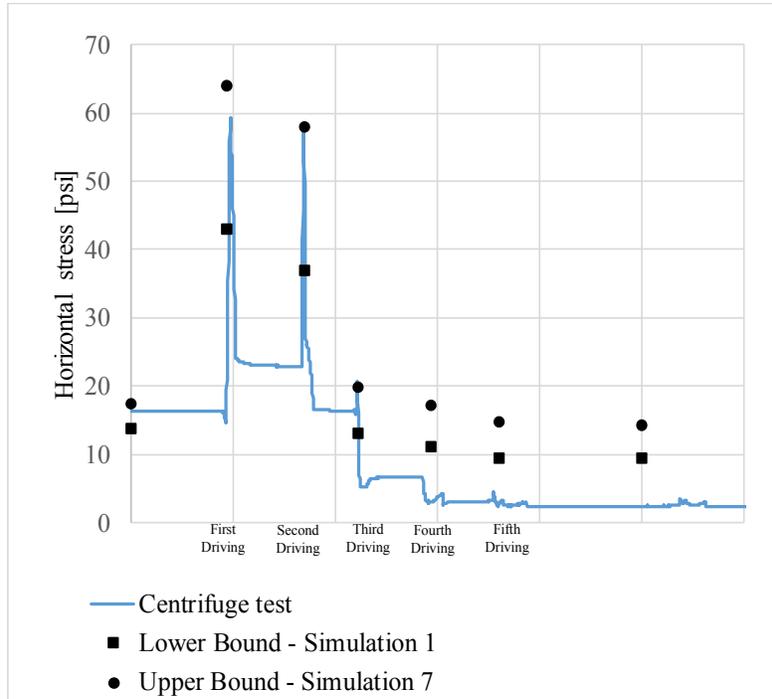
Figure 3.46 Horizontal stress results (bounded) from pressure sensor PS4 during pile driving phase from Simulations 1 and 7
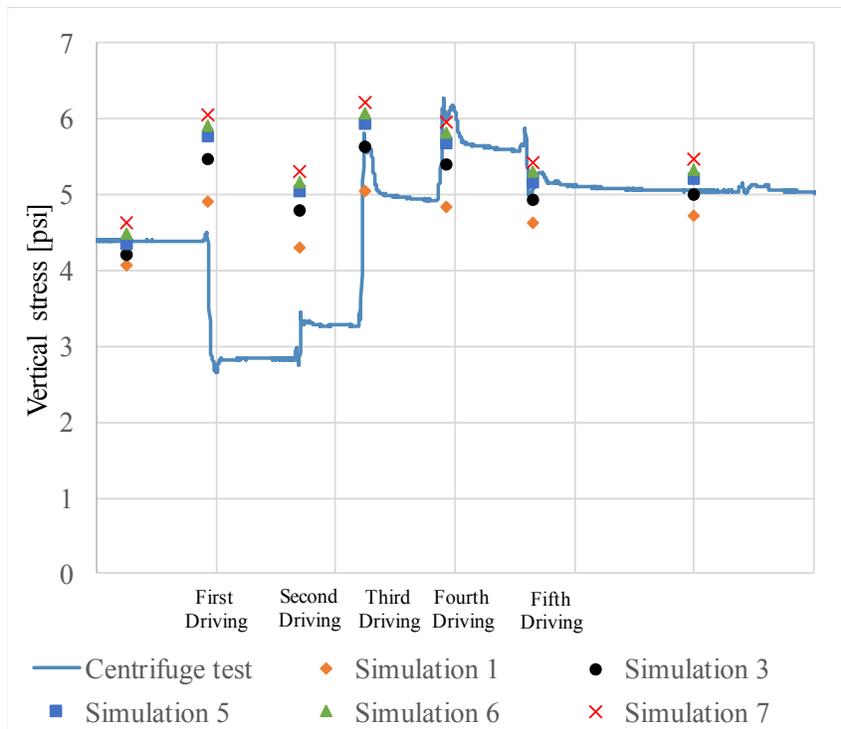
Figure 3.47 Vertical stress results from pressure sensor PS2 during pile driving phase from numerical Simulations 1 through 7
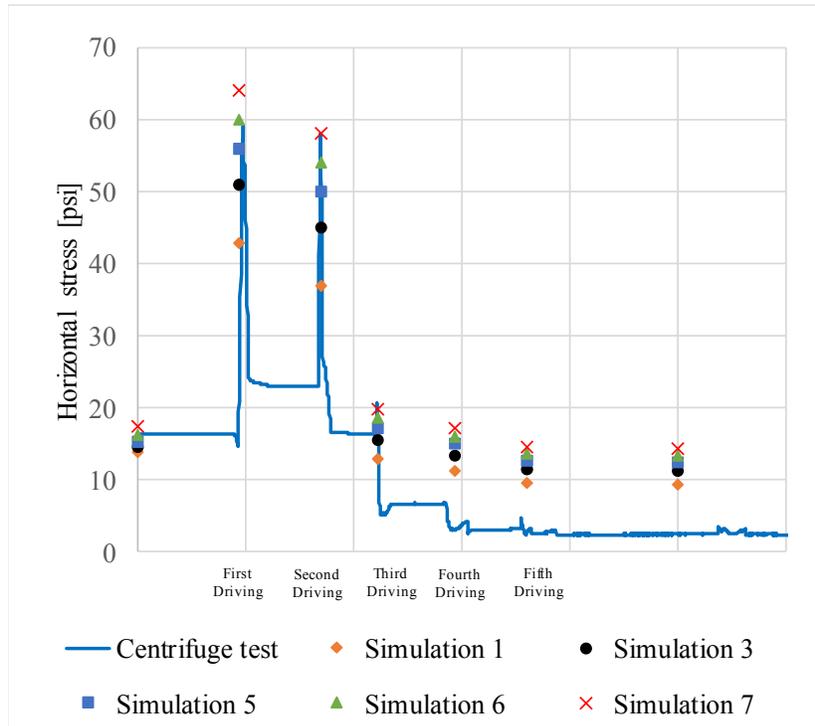
Figure 3.48 Horizontal stress results from pressure sensor PS4 during pile driving phase from numerical Simulations 1 through 7

As presented in Figs. 3.41 through 3.48, the sudden introduction of structural components have an effect on stress propagation in the granular medium. During SPW installation, horizontal stresses are predicted to be maximum 300% increase in amplitudes whereas vertical stresses increase about 100%. During subsequent pile driving phase, horizontal stresses still increase 350% as the tip of the pile approaches the SPW embedment depth. Vertical stresses minimally increase (about 20%). Dynamic phenomena induced by the reflected stresses on the SPW further increases dilative effects in locked-in confining stresses. As a result, development of greater principal stress is observed around the pile tip region during pile driving.

Given in Figs. 3.49 through 3.53 are comparative screenshots of Scenario 1 (Simulation 6(S1)) versus Scenario 2 (Simulation 6(S2)) with respect to the development of vertical stresses. The screenshots are taken at the initial condition (a steady state after SPW installation, but prior to pile driving), and subsequently, at the end of each instance of five dynamic loading steps (pile driving sequence). The SPW is pre-installed at a distance of 2B from the pile surface. For graphical illustration purposes, a different fringe-color scale is used for the stress magnitudes between the two scenarios; at the same stress scale, coloring become more or less uniform in either one of the two. The stress magnitudes that are computed per scenarios are given at each instance of five dynamic loading steps in Table 3.11 (Simulation 6(S1) and Simulation 6(S2)) and Table 3.12 (Simulation 7(S1) and Simulation 7(S2)).
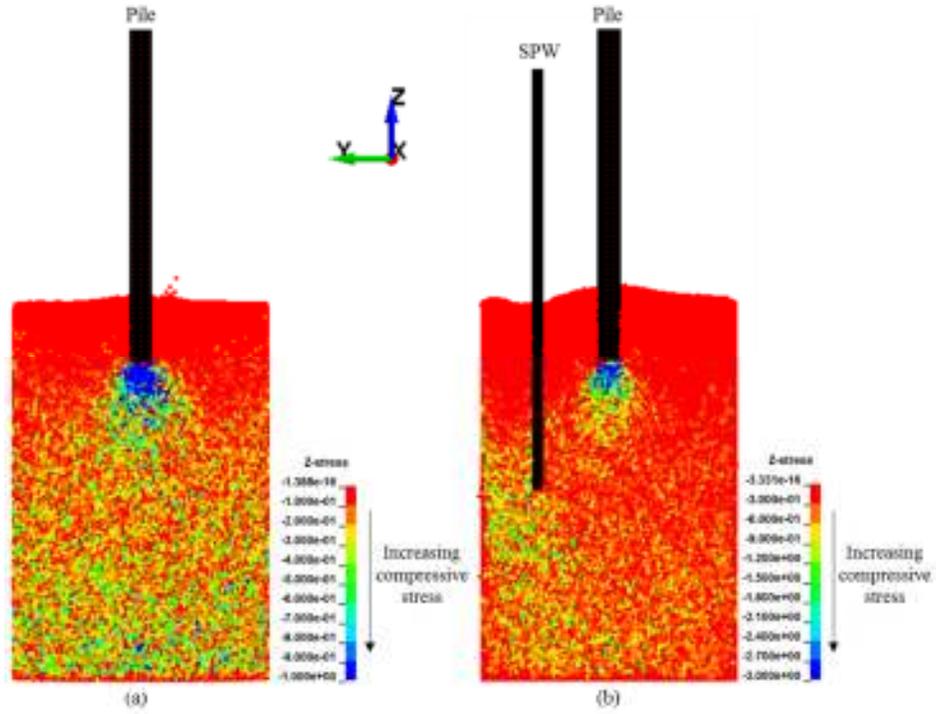
Figure 3.49 Vertical stresses generated throughout the DSE assembly during first increment of pile driving: (a) Scenario 1; (b) Scenario 2
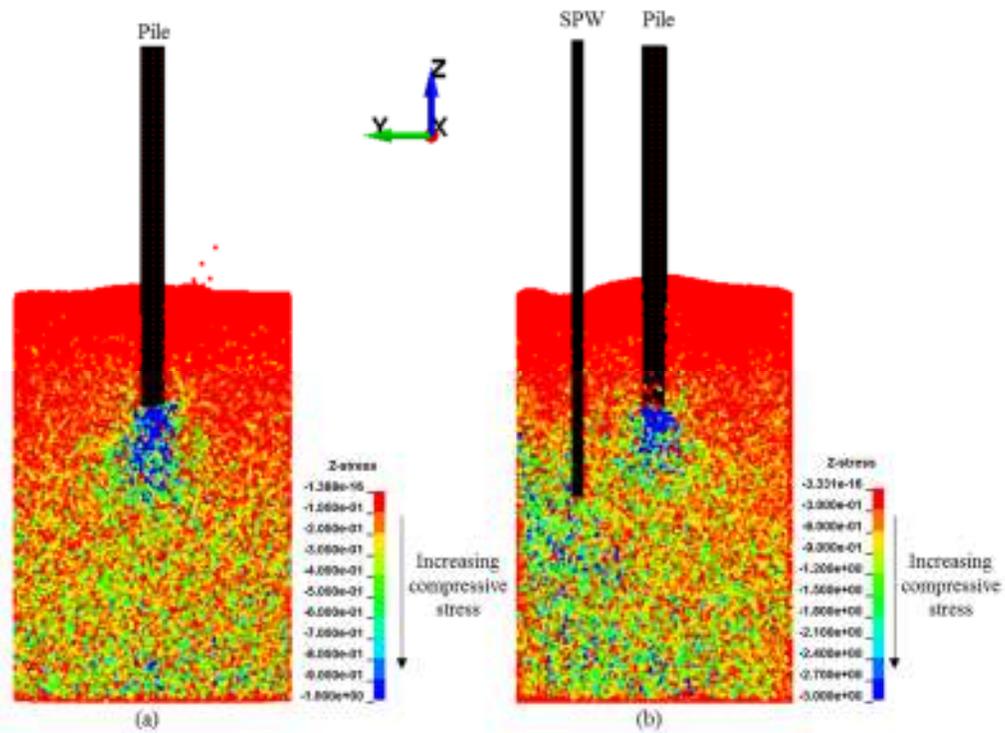
Figure 3.50 Vertical stresses generated throughout the DSE assembly during second increment of pile driving: (a) Scenario 1; (b) Scenario 2
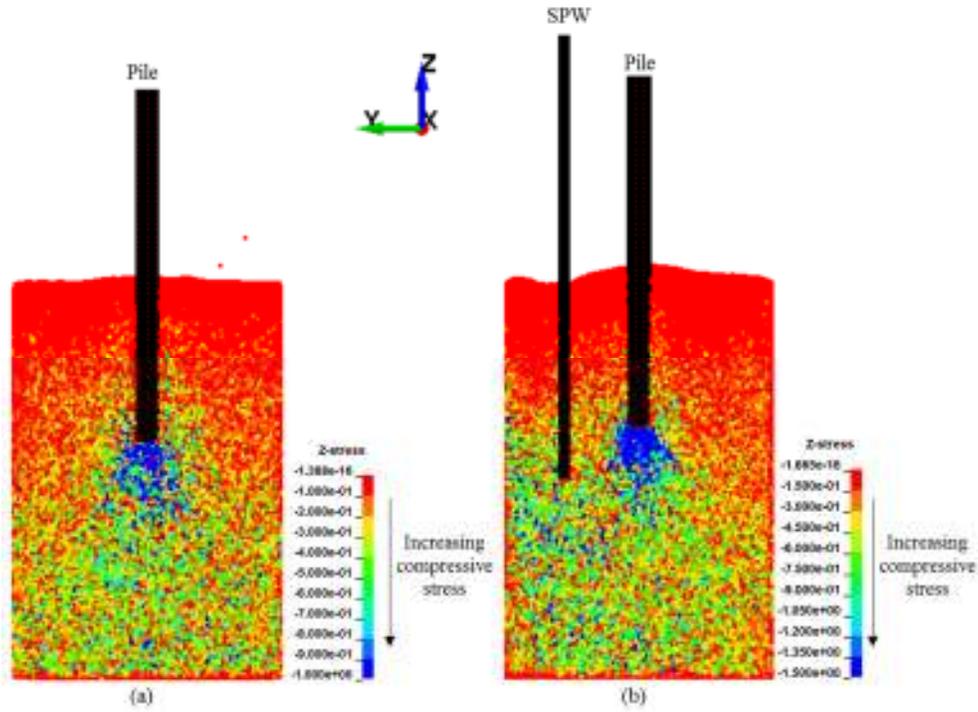
Figure 3.51 Vertical stresses generated throughout the DSE assembly during third increment of pile driving: (a) Scenario 1; (b) Scenario 2
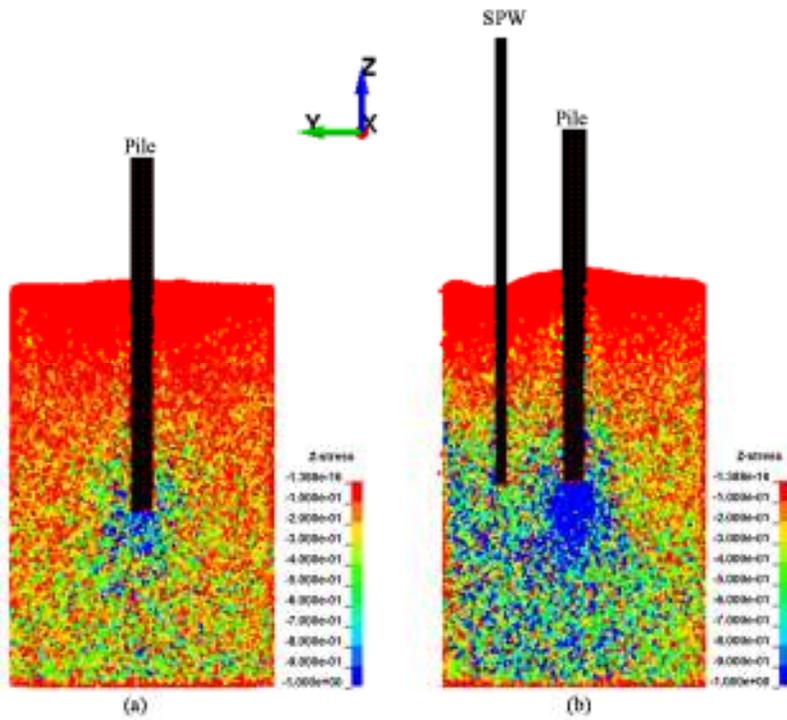
Figure 3.52 Vertical stresses generated throughout the DSE assembly during fourth increment of pile driving: (a) Scenario 1; (b) Scenario 2
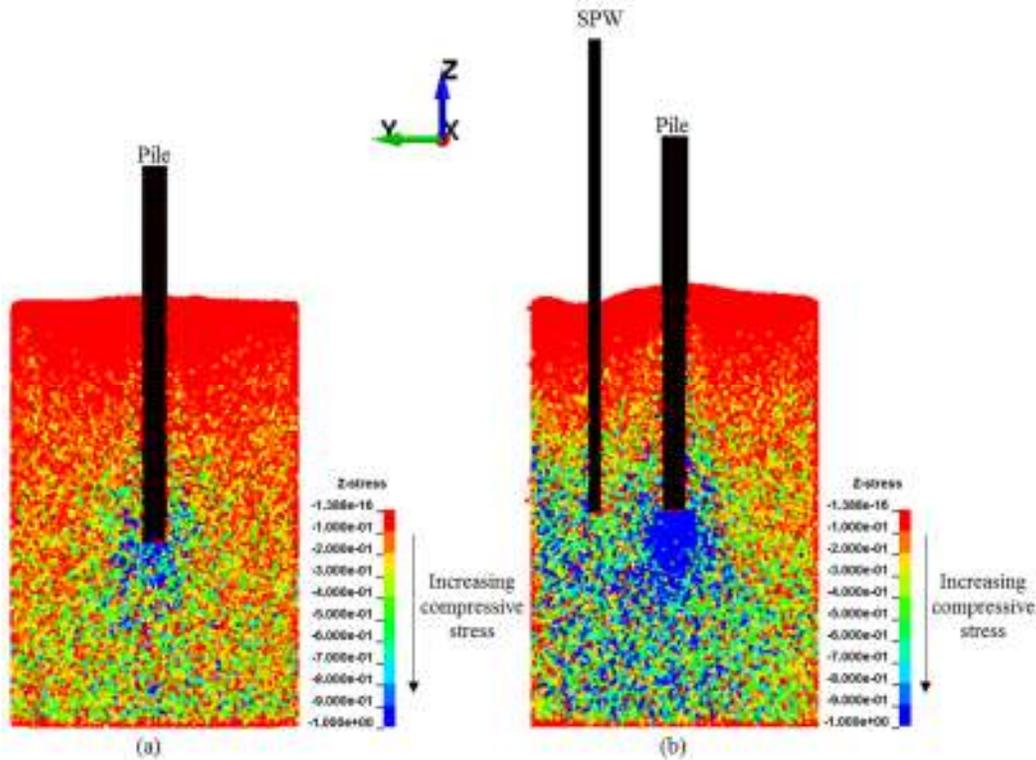
Figure 3.53 Vertical stresses generated throughout the DSE assembly during fifth increment of pile driving: (a) Scenario 1; (b) Scenario 2

Table 3.11 Comparison of maximum compressive pressures between numerical results from Scenarios 1 and 2 (Simulation 6)

Sampling frequency	Maximum horizontal stress (ksi)		Maximum vertical stress (ksi)	
	Scenario-1 Simulation 6(S1)	Scenario-2 Simulation 6(S2)	Scenario-1 Simulation 6(S1)	Scenario-2 Simulation 6(S2)
End of first driving (Fig. 2.61)	0.91	1.04	1.89	2.02
End of second driving (Fig. 2.62)	0.85	0.98	1.68	1.87
End of third driving (Fig. 2.63)	1.03	1.26	2.03	2.35
End of fourth driving (Fig. 2.64)	1.21	1.18	2.12	2.42
End of fifth driving (Fig. 2.65)	0.95	1.31	1.86	2.35

Table 3.12 Comparison of maximum compressive pressures between numerical results from Scenarios 1 and 2 (Simulation 7)

Sampling frequency	Maximum horizontal stress (ksi)		Maximum vertical stress (ksi)	
	Scenario-1 Simulation 7(S1)	Scenario-2 Simulation 7(S2)	Scenario-1 Simulation 7(S1)	Scenario-2 Simulation 7(S2)
End of first driving (Fig. 2.61)	0.97	1.10	2.07	2.16
End of second driving (Fig. 2.62)	0.89	1.05	1.83	1.97
End of third driving (Fig. 2.63)	1.21	1.24	2.19	2.50
End of fourth driving (Fig. 2.64)	1.17	1.34	2.27	2.69
End of fifth driving (Fig. 2.65)	0.98	1.36	2.03	2.47

3.4.6 Measured vs Computed Pile Driving and Top-Down Load Results

Resultant forces are measured at the toe and top of the pile throughout the test sequence. The two major phases of testing where force-displacement results are plotted are the pile driving and top-down load test. A comparison is made between numerical and physical test results. Analyzing force-displacement relationship during the above mentioned phases gives a clear picture of how granular material behaves under dynamic as well as quasi-static loading. Good agreement between force-displacement profiles from numerical and physical results ensure that discrete elements can be utilized to simulate both dynamic as well as static physical test conditions.

In Fig. 3.54, the force-displacement profiles for the numerical simulations during pile driving are plotted along with measured force-displacement profile from centrifuge test.
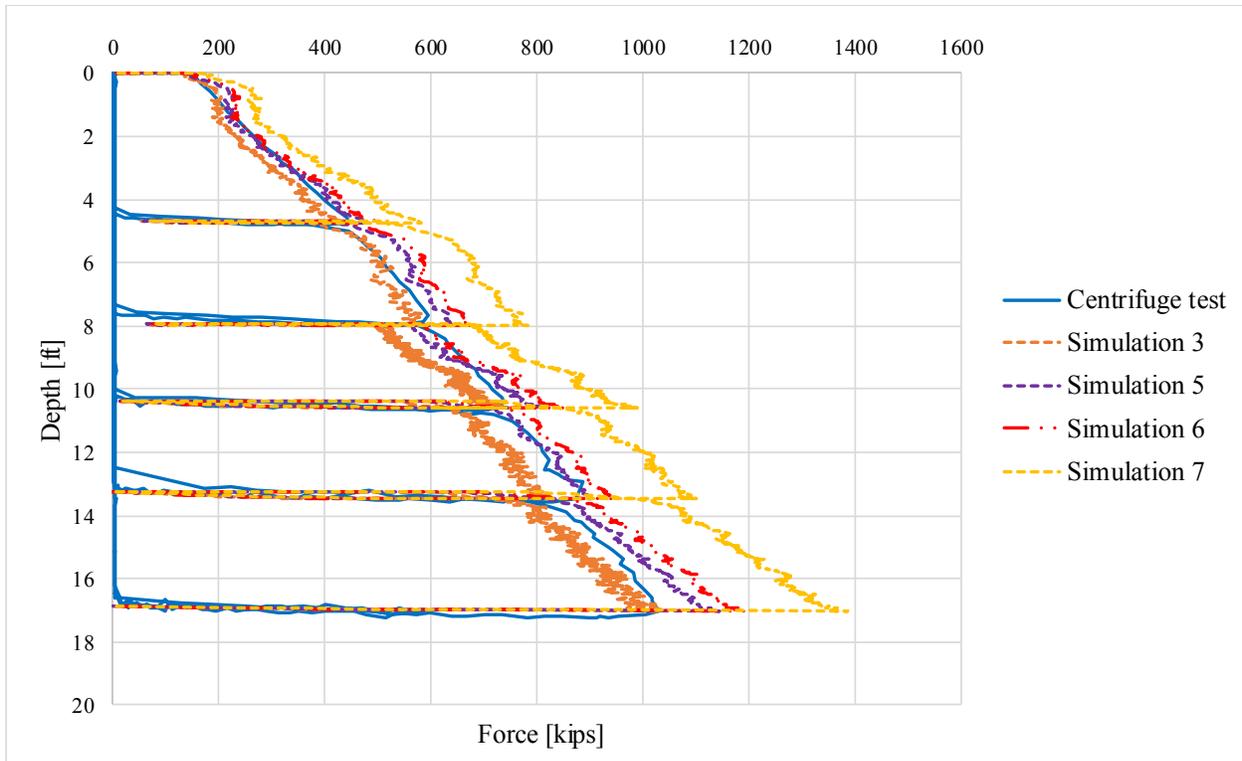
Figure 3.54 Numerical predictions of pile driving in Scenario 2 for SPW embedment depth equal to the depth of pile tip

In Fig. 3.55, the force-displacement profile during quasi-static top-down load test from all the numerical simulations of scenario 2 are plotted with the force-displacement results from centrifuge test. A wide array of force-displacement relationships are achieved from different numerical simulations which successfully envelope the physical test measurements. In Fig. 3.56, a bounded solution is presented with respect to the top down load test results obtained from the centrifuge tests.
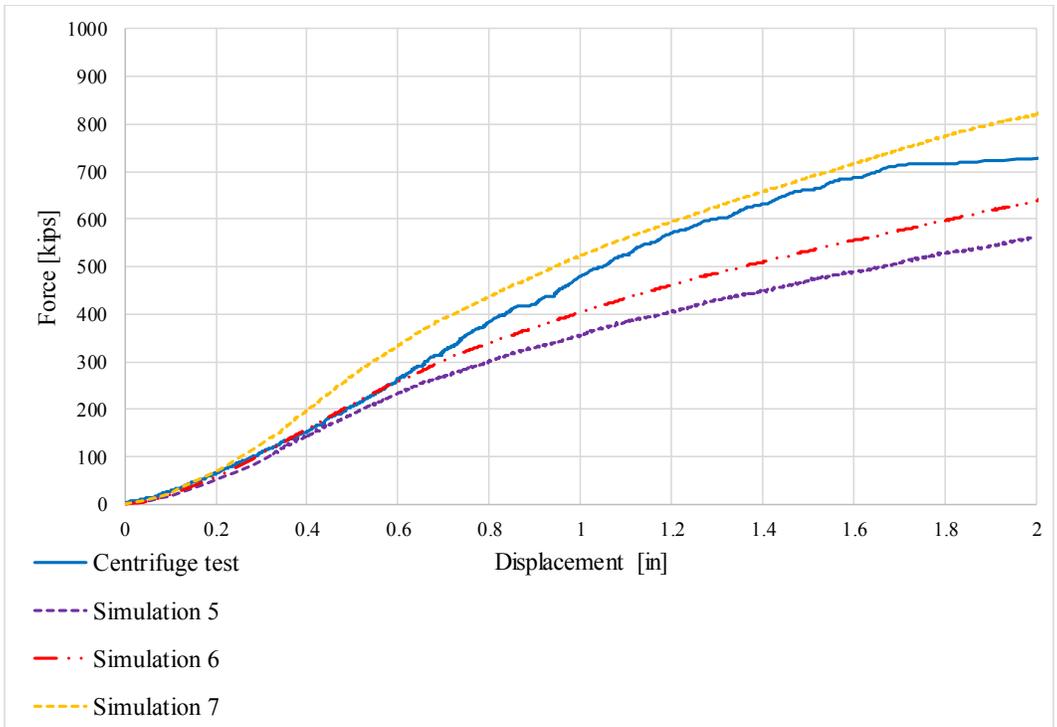
Figure 3.55 Force-displacement results during top-down load test from numerical simulations of Scenario 2
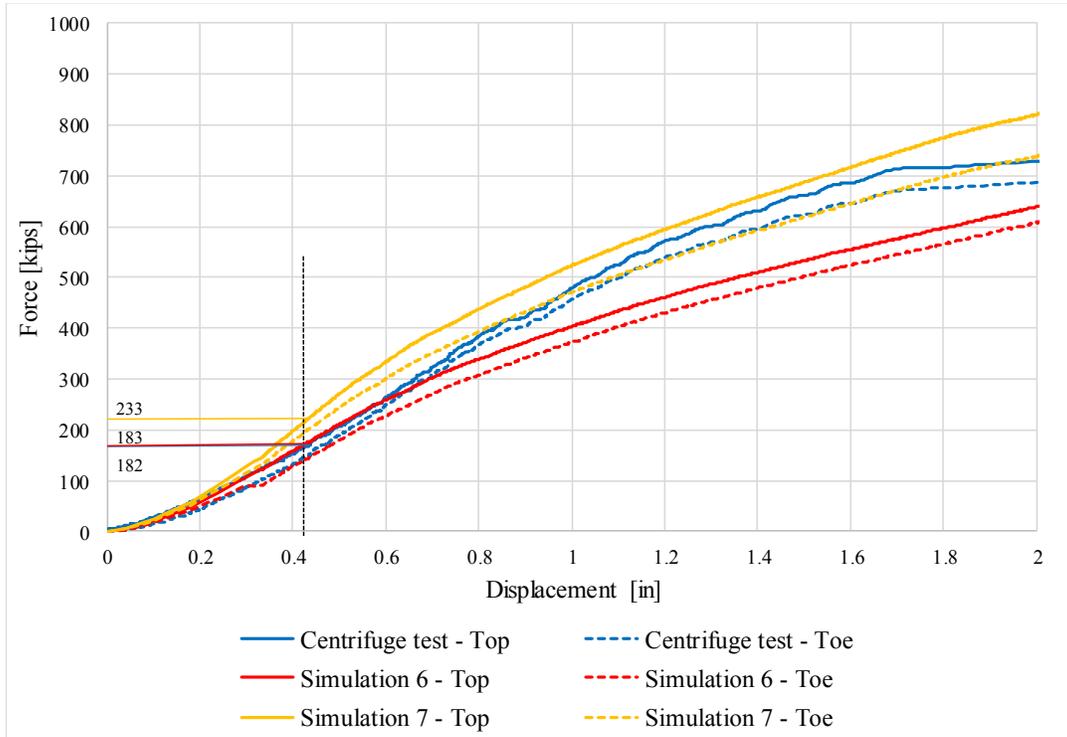
Figure 3.56 Upper- and lower-bound numerical predictions of the top-down load test result under Scenario 2 condition for SPW embedment depth equal to the depth of pile tip

As listed in Table 3.13, ultimate and Davisson capacities for numerical simulations are calculated and compared with centrifuge test results. Good agreement is present among results from Simulation 6 for stiffness assessment (serviceability criteria). The results of Simulations 6 and 7 bound the load capacity at top displacement of 2 inches.

Table 3.13 Ultimate and Davisson Capacities for Scenario 2

Load Test Scenario	Ultimate Capacity (UC) (kips)	Davisson Capacity (DC) (kips)
Centrifuge test	728	182
Simulation 6(S2)	698	183
Simulation 7(S2)	820	233

3.4.7 Representative Models for Parametric Study in Association with Task 5

Based on comparisons of results from the above sections (Secs. 3.4.1 - 3.4.6) between numerical and physical tests, it can be seen that discrete elements can be utilized to simulate the dynamic and quasi-static response of an assembly of granular material. A wide array of dynamic and static response was achieved by performing a parametric sensitivity study. From all the numerical models, the Simulation 6(S2) model gives the best prediction of dynamic (inertial) resistance in the pile during pile driving of Scenarios 1 and 2. Accordingly, Simulation 6 prediction under Scenario 1 and Scenario 2 is in good agreement with the measured Davisson capacity. At top displacement of 2 inches, Simulation 6(S2) and Simulation 7(S2) bound the ultimate pile capacity observed in the centrifuge tests. Although dynamic (inertial) resistances are over-predicted during Scenario 2 pile driving, Simulation 7 provides an upper bound to the ultimate capacities of Scenario 1 and Scenario 2. Given complexity in the loading sequences (including Scenario 3), a practical engineering remedy can be use of averaging the numerical results obtained from both Simulation 6 and Simulation 7. Therefore, the effects of the SPW installation and removal in the pile capacities would be further investigated using both Simulation 6 and Simulation 7 models per each geometric variations, i.e., SPW installation distance and depth with respect to the pile location, in association of Task 5.

3.5 Numerical Modeling of Test Scenario 3

In Scenario 3, the sheetpile wall (SPW) is first driven into the sand bed. The pile is subsequently driven to the target embedment depth by applying dynamic (impact) loading. Once the SPW-pile reaches a steady (static equilibrium) state, the SPW is pulled out incrementally. Upon removal of the SPW, the top of the pile is subjected to quasi-static (incremental) vertical loads. The top down load-displacement relationship is predicted in comparison to measured loads (per readings of top and toe load cells) and top displacement (per readings of LVDT). A detailed description of all the centrifuge test sequences is given in the Task 4 deliverable report of this project.

3.5.1 Selected Models and Simulation Sequence

Among a wide array of numerical models that are developed as a part of Scenarios 1 and 2, the Simulation 6 and Simulation 7 models provide a numerical means to bound Scenario 1 and Scenario 2. Key input parameters of the two models are given in Table 3.14.

Table 3.14 Model parameters for Simulation 6 and Simulation 7

Simulation	Bulk modulus ksi (MPa)	Inter-granular friction coefficient (sliding; rolling)
6(S3)	17.87 (123.2)	1.0; 0.1
7 (S3)	21.02 (145)	0.6; 0.06

The loading sequences of Scenario 2 are repeated for the geometry of the DSE assembly in Figure 3.33, and the dimensions of SPW and the pile in Figure 3.34 and Figure 3.35 respectively. The pile driving sequence can be found in Figure 2.48. For the simulation of incremental pull-out of SPW, the SPW removal time history measured in the centrifuge test of Scenario 3 is used as shown in Figure 3.58.
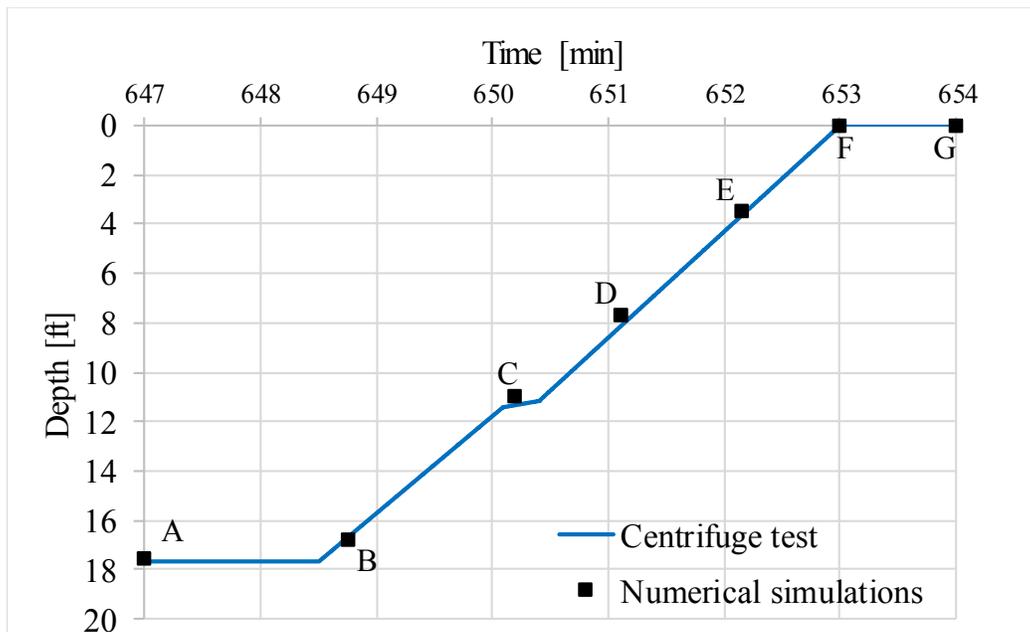
Figure 3.57 Time history of SPW tip locations during the removal process: The black markers along the displacement profile of the SPW tip represent temporal states of the FEM SPW model as it is being pulled out vertically.

3.5.2 Measured vs Computed Stresses during Sheet Pile Wall Removal

Pressure versus time was cataloged at two locations in the (numerical) granular domain, which correspond to pressure cells PS2 and PS4 in the physical centrifuge testing (recall Fig. 2.5). Readings from these pressure sensors (PS2 and PS4) are compared to the computed stresses that are volume-averaged at the fixed locations of the sensors. The volume-averaging corresponds to macroscopic stresses in the granular medium. The sampling locations of the computed stresses are given in Figure 3.39 and Figure 3.40. The geometric locations of the sensors and additional relevant discussion are provided in Section 3.3.4.

Vertical stresses at the PS2 location are plotted in Figure 3.58. Horizontal stresses at the PS4 location are plotted in Figure 3.59. To make qualitative comparisons between centrifuge test stresses and numerical simulation stresses, a normalized time scale is set based on the measured locations of the SPW tip. Designating the SPW tip position as a reference timeframe facilitates direct comparison between temporal states A through G, specified in Figure 3.57.
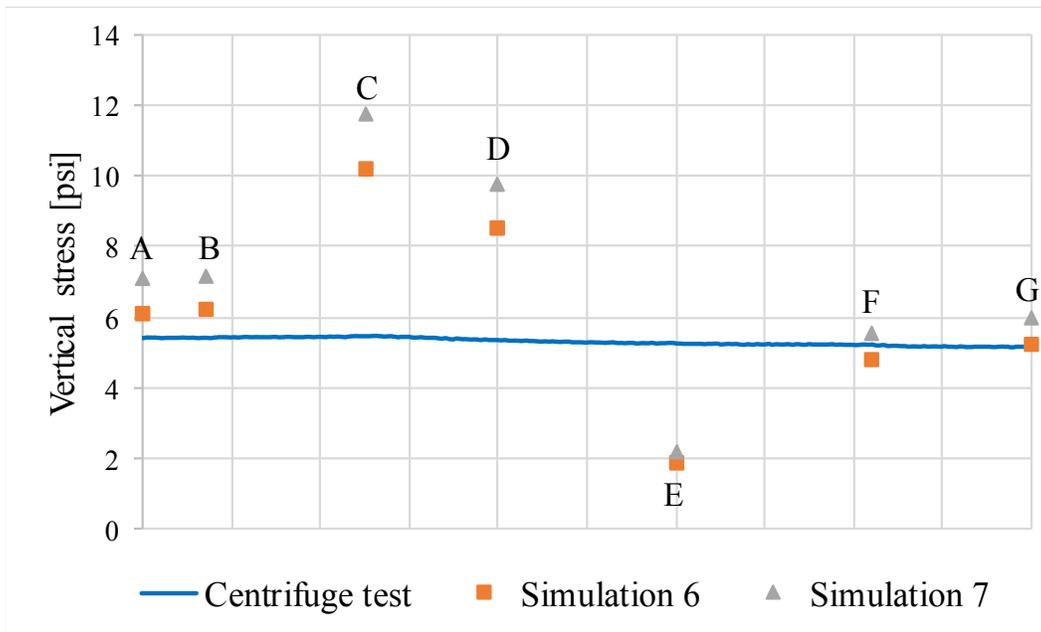
Figure 3.58 Vertical stresses from pressure sensor PS2 during removal of SPW

96
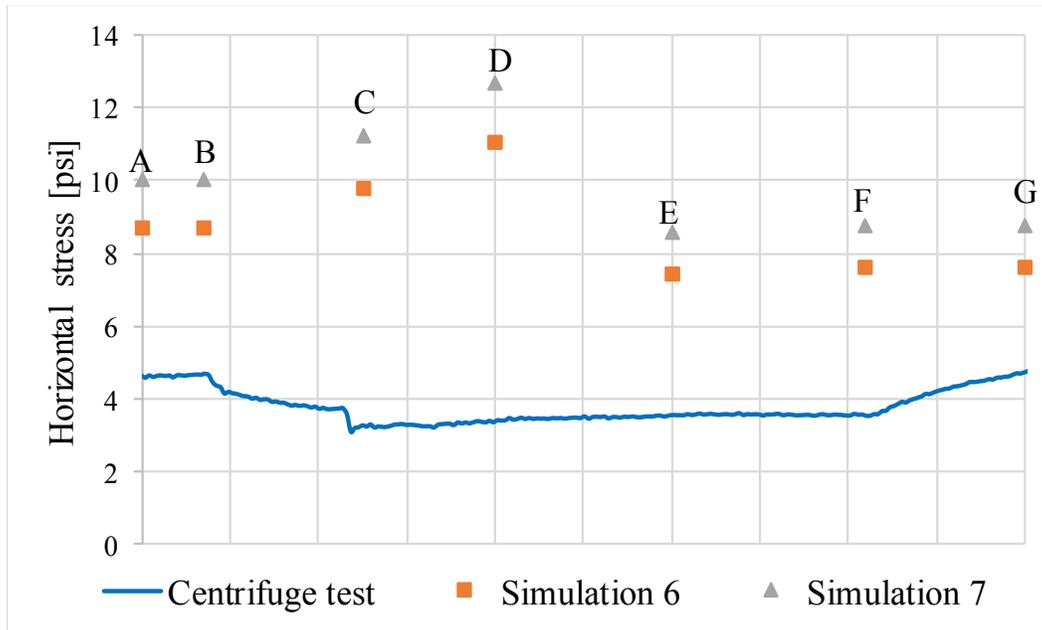
Figure 3.59 Horizontal stresses from pressure sensor PS4 during removal of SPW

As presented in Figure 3.58 and Figure 3.59, stress waves propagate due to agitation during SPW upward motions. An increase in the stresses is predicted as the SPW tip passes by the locations where PS2 and PS4 are (initially) placed. It is probable that, during physical testing, the 'floating' sensors may have been displaced due to particles' motions throughout the SPW and pile installation and subsequent SPW removal.

In Figs. 3.60 through 3.65, changes in stress states are graphically illustrated in a sequence according to the successive spatiotemporal locations of SPW tip specified as B, C, D, E, F and G in Fig. 3.57. Using Point A of Fig. 3.57 as a reference stress state (left columns of Figs. 3.60 through 3.65), the simulated stress fields during the SPW removal show asymmetric reduction of locked-in horizontal stresses. It is noted that these changes in stress magnitude are taken with respect to the points in time defined in Fig. 3.57, and that the stress magnitudes do not include initial geostatic stresses. Magnitudes of horizontal and vertical stresses are summarized for each of the incremental locations during the SPW removal in Table 3.14.

Subsequent to dynamic (tensile) loading at the interfaces between newly formed void spaces and adjacent DSEs, particle re-arrangement takes place under self-equilibrating gravity forces. The discrete elements are dragged along the moving SPW shaft. Continual collapse of granular structures near the SPW shaft leads to relieving locked-in horizontal stresses in proximity of the pile. The SPW installation and removal in the granular medium causes permanent deformations of the soil mass, rotation of the planes of principal stress, and differential volume changes in the approximate vicinity 2.5B distance. When the granular structure regains structural stability, i.e., a metastable granular-assembly, it is obvious that the SPW removal has caused a substantial loss in confining stresses along the pile shaft and passive resistances near the tip region.
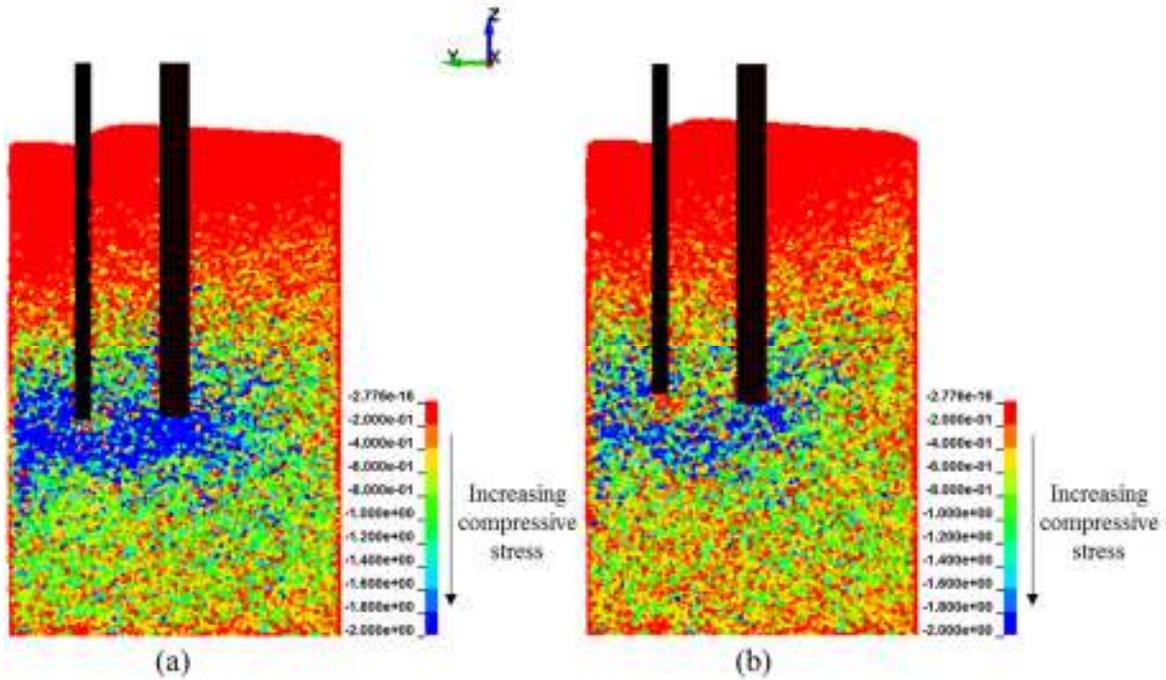
Figure 3.60 Horizontal stresses generated throughout the DSE assembly during SPW removal:
(a) Scenario 2 at equilibrium after completion of pile driving; (b) Scenario 3 at SPW tip position
B (recall Fig. 3.57)
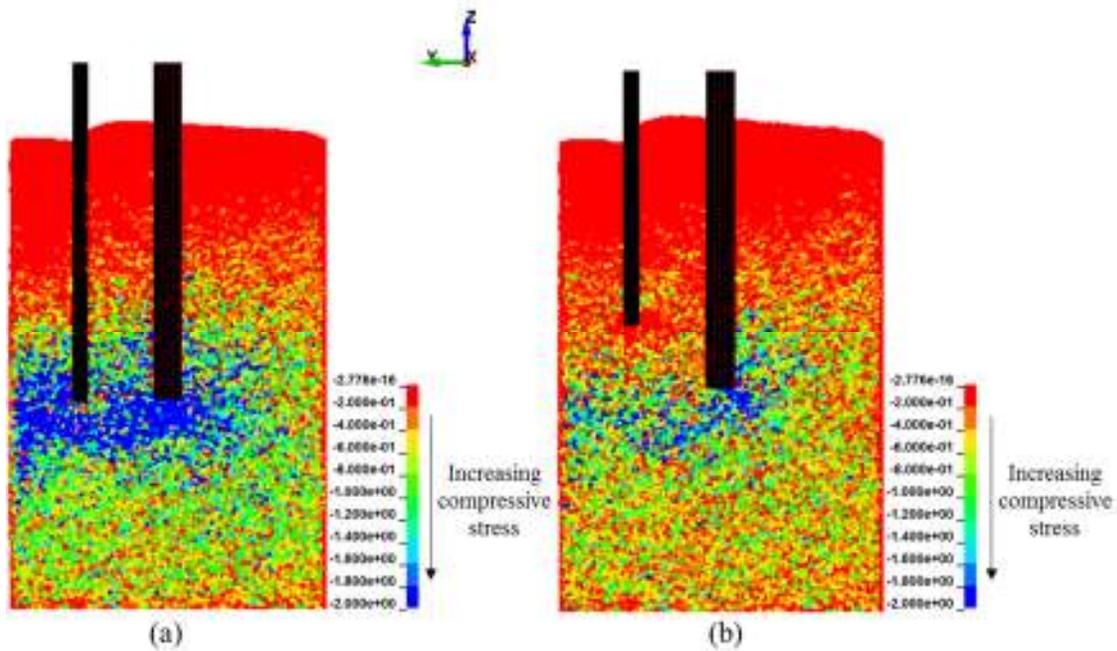
Figure 3.61 Horizontal stresses generated throughout the DSE assembly during SPW removal:
(a) Scenario 2 at equilibrium after completion of pile driving; (b) Scenario 3 at SPW tip position
C (recall Fig. 3.57)
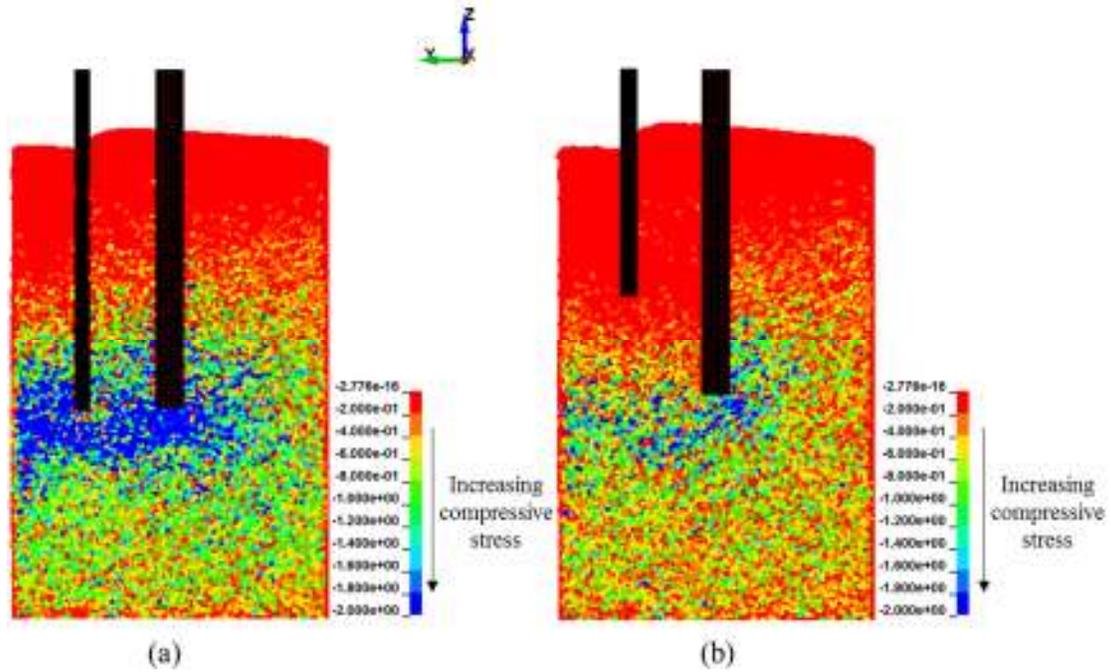
Figure 3.62 Horizontal stresses generated throughout the DSE assembly during SPW removal: (a) Scenario 2 at equilibrium after completion of pile driving; (b) Scenario 3 at SPW tip position D (recall Fig. 3.57)
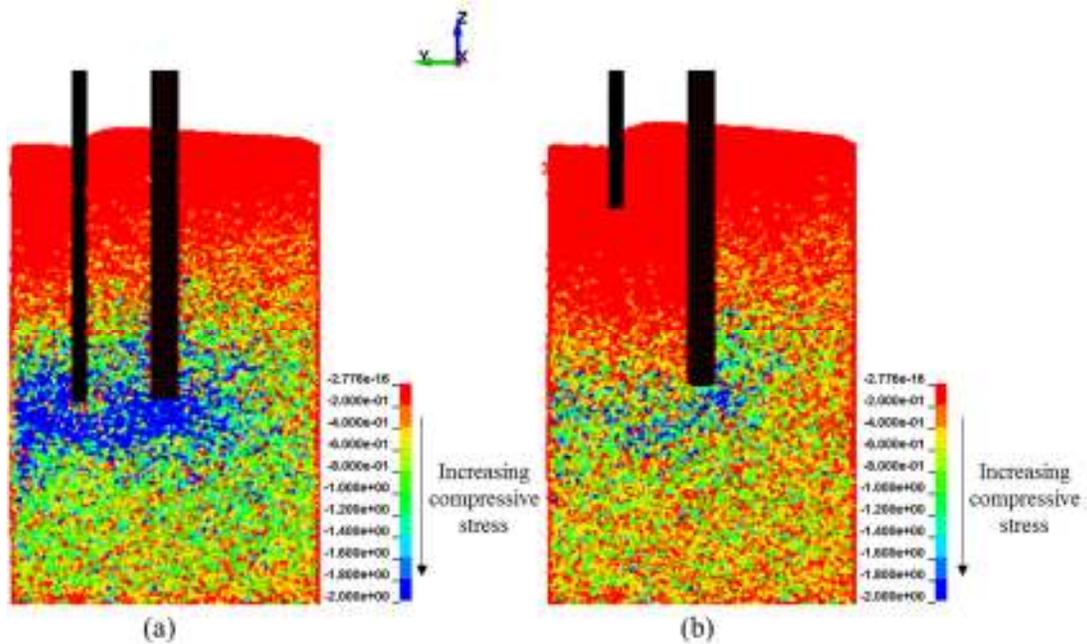
Figure 3.63 Horizontal stresses generated throughout the DSE assembly during SPW removal: (a) Scenario 2 at equilibrium after completion of pile driving; (b) Scenario 3 at SPW tip position E (recall Fig. 3.57)
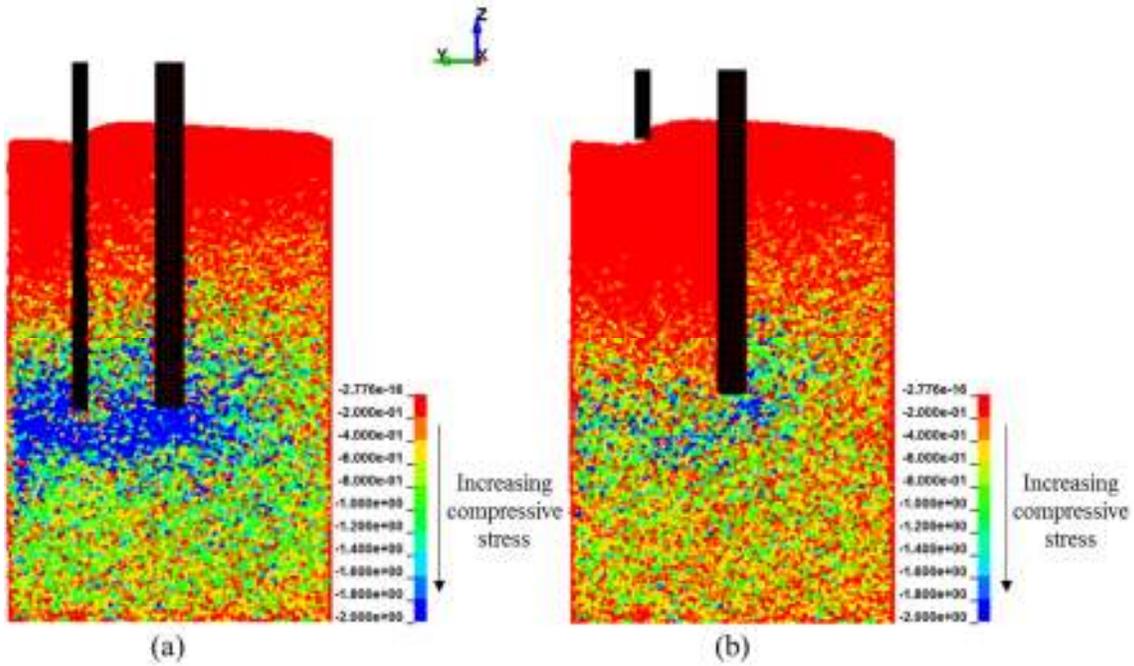
Figure 3.64 Horizontal stresses generated throughout the DSE assembly during SPW removal:
(a) Scenario 2 at equilibrium after completion of pile driving; (b) Scenario 3 at SPW tip position
F (recall Fig. 3.57)
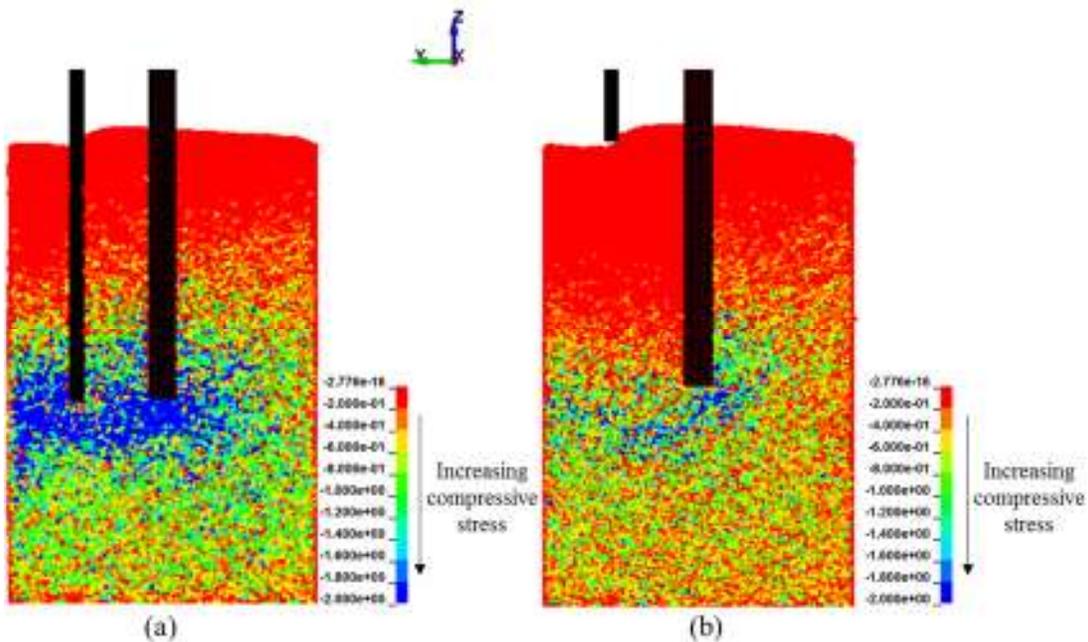
Figure 3.65 Horizontal stresses generated throughout the DSE assembly during SPW removal:
(a) Scenario 2 at equilibrium after completion of pile driving; (b) Scenario 3 at SPW tip position
G (recall Fig. 3.57)
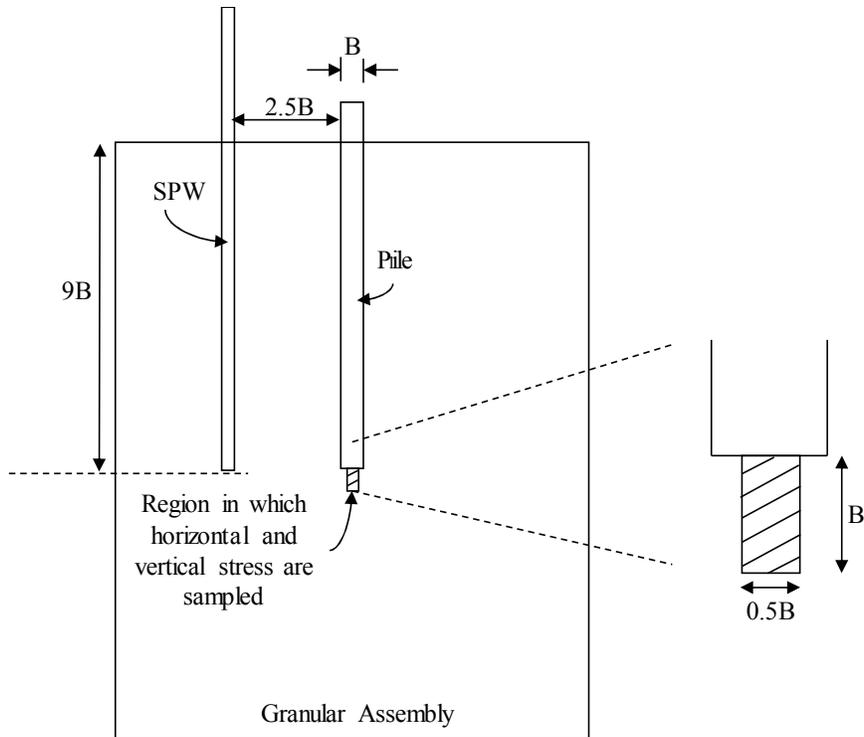
Figure 3.66 Macroscopic sampling for computation of volume-averaged stresses given in Table 3.15

Table 3.15 Comparison of compressive pressures in the vicinity of the pile tip between numerical results from Simulation 6 and Simulation 7 (refer to Figure 3.67 for the sampling location)

Points (Figure 3.1)	Simulation 6(S3)		Simulation 7(S3)	
	Horizontal stress (ksi)	Vertical stress (ksi)	Horizontal stress (ksi)	Vertical stress (ksi)
A	1.31	2.35	1.36	2.47
B	1.305	2.36	1.353	2.472
C	1.1	2.38	1.16	2.48
D	1.08	2.34	1.10	2.45
E	1.05	2.33	1.07	2.435
F	1.075	2.339	1.11	2.47
G	1.082	2.40	1.18	2.51

For quantitative analysis of the temporal variation in horizontal stresses that are graphically illustrated in Figures 3.60 through 3.65, the region between the SPW and pile is sub-divided into nine control regions (volumes) that are stacked as shown in Figure 3.67. Volume-averaged horizontal stresses are plotted at the mid depth of each discretized region (Figure 3.68 for Simulation 6(S3); and, Figure 3.69 for Simulation 7(S3)).
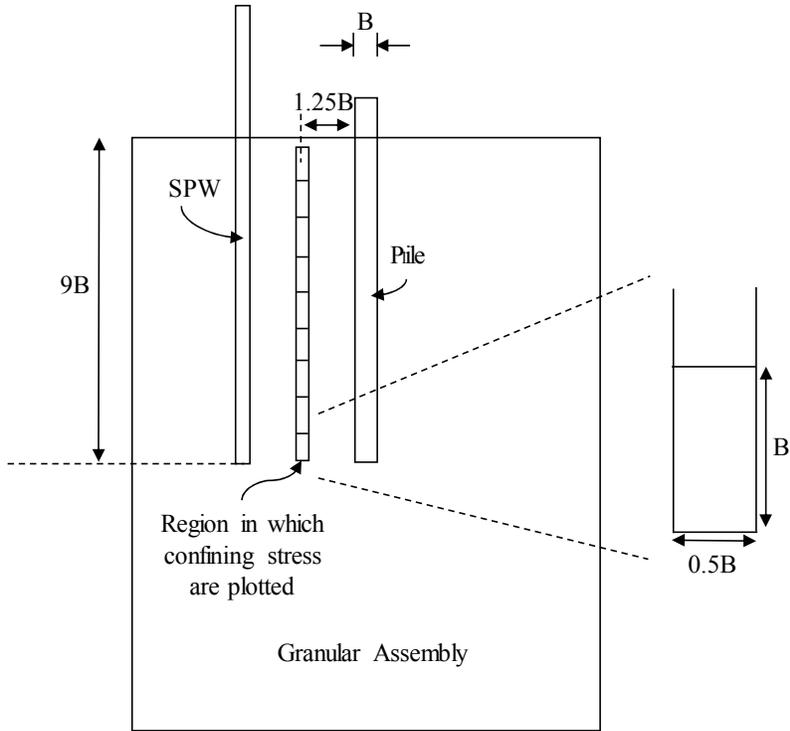
Figure 3.67 Discretization of the granular assembly for computation of volume-averaged horizontal stresses
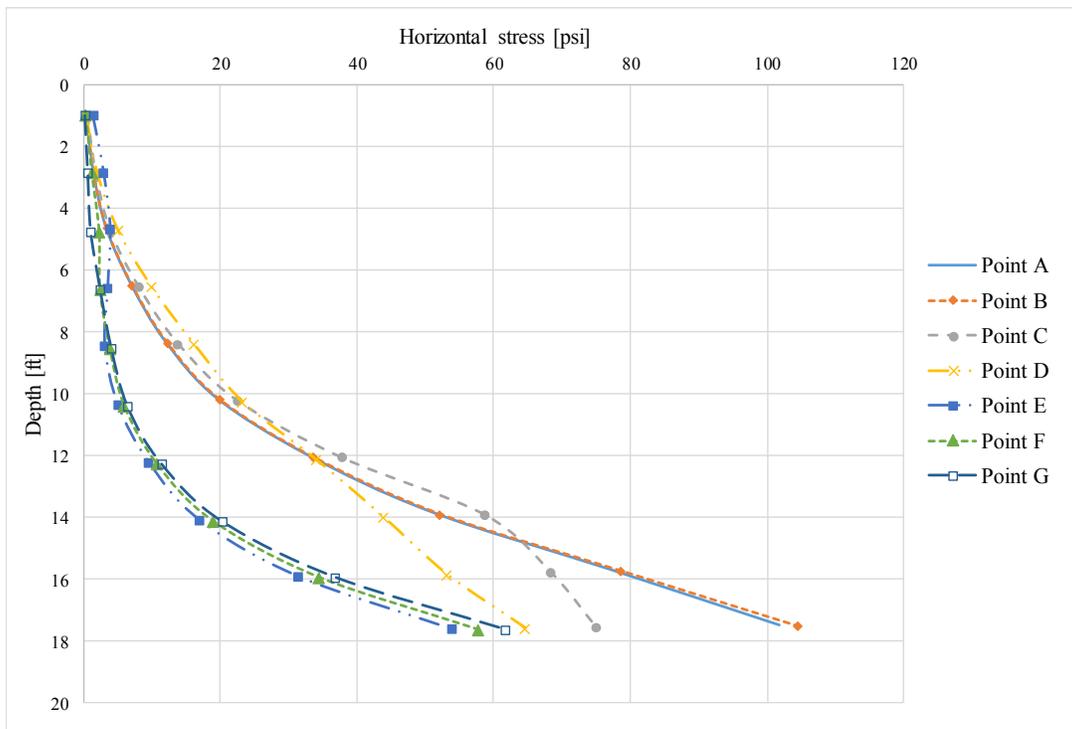
Figure 3.68 Horizontal stress profile through depth at each temporal state during SPW removal (Simulation 6(S3))
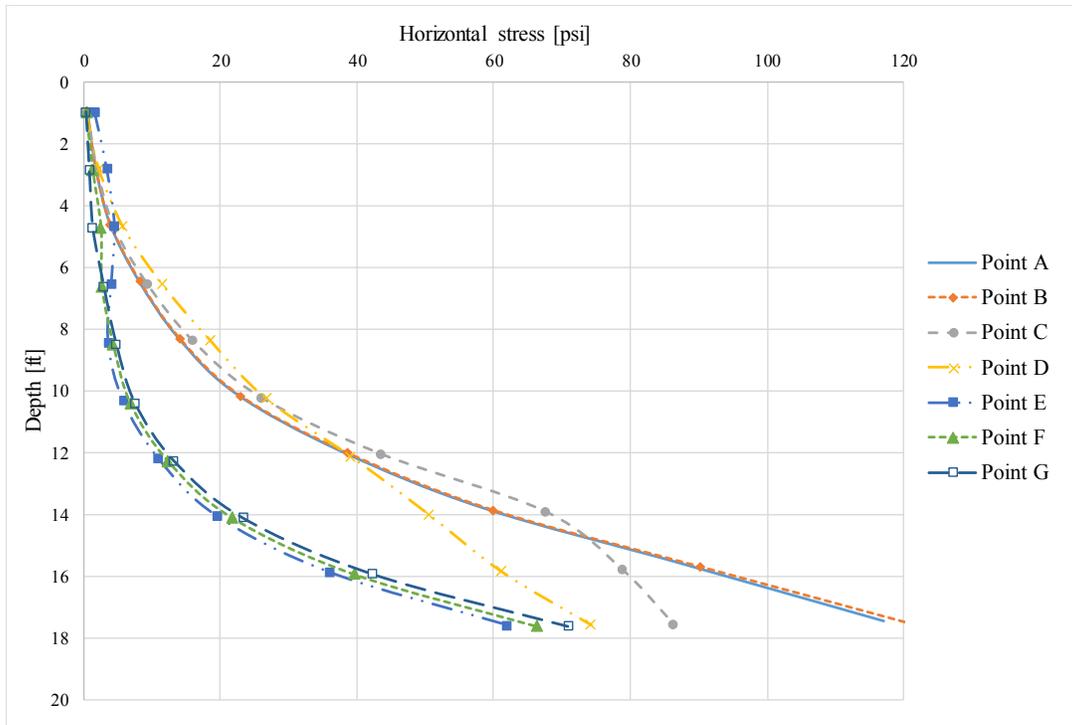
Figure 3.69 Horizontal stress profile through depth at each temporal state during SPW removal (Simulation 7(S3))

3.5.3 Measured vs Computed Pile Driving and Top-Down Load Results

In Figure 3.70, simulation results of quasi-static top-down load test are plotted in comparison to the corresponding centrifuge measurements. Numerical prediction of the ultimate and Davisson capacities are compared with the centrifuge test results in Table 3.16. Simulation 6 shows consistent agreement in Davisson capacity with respect to the centrifuge test results for both Scenario 2 and Scenario 3. However, the Simulation 7 results provide a better representation of the yielding behavior of the SPW-pile system for the development of end bearing under Scenario 3. The variation of side friction is a relatively minor factor in the reduction of pile capacity. More importantly, the SPW-pile system undergoes a substantial loss in end bearing upon removal of the SPW. The SPW installation depth is considered to be a key system design parameter in relation to the tip location of the pile.
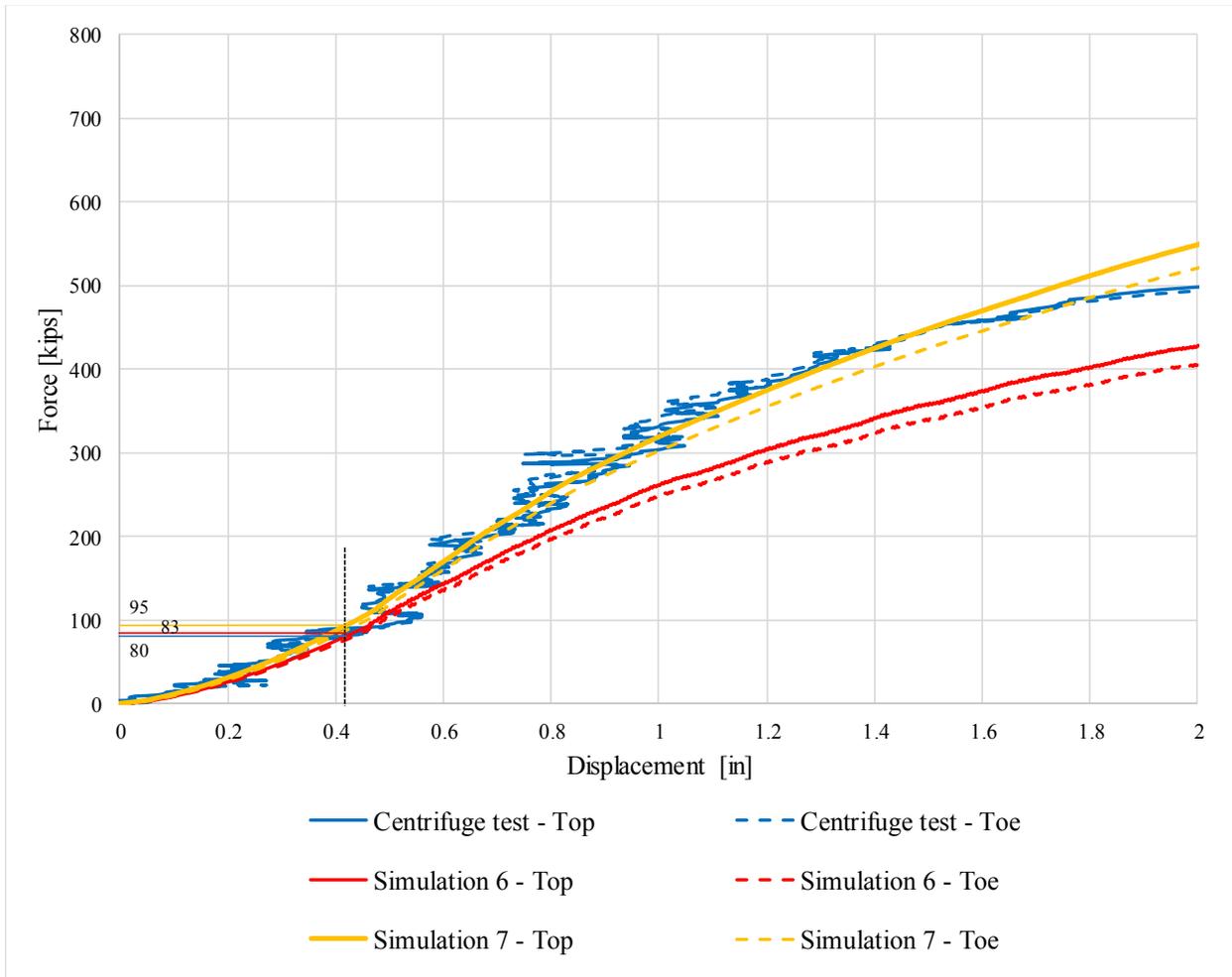
Figure 3.70 Upper- and lower-bound numerical predictions of the top-down load test result under Scenario 3 condition for SPW embedment depth equal to the depth of pile tip

Table 3.16 Ultimate and Davisson Capacities for Scenario 3

Load Test Scenario	Ultimate Capacity (UC) (kips)	Davisson Capacity (DC) (kips)
Centrifuge test	499	80
Simulation 6(S3)	428	83
Simulation 7(S3)	549	95

3.6 Summary of Bench-marked Simulation Results

In both Scenario 2 and Scenario 3, the sheetpile wall (SPW) is first driven into the sand bed. The pile is subsequently driven to the target embedment depth by applying dynamic (impact) loading. Once the SPW-pile reaches a steady (static equilibrium) state, the SPW is pulled out incrementally. Upon removal of the SPW, the top of the pile is subjected to quasi-static (incremental) vertical loads. The top down load-displacement relationship is predicted in comparison to measured loads (per readings of top and toe load cells) and top displacement (per readings of LVDT).

A comparison is made in Figures 3.71 and 3.72 for the pile top-down load tests conducted in the centrifuge under all three loading scenarios. Numerical results obtained from Simulation 6 and Simulation 7 are subsequently plotted in Figures 3.73 through 3.76. Changes in the pile capacities are tabularized in Table 3.17 and Table 3.18.
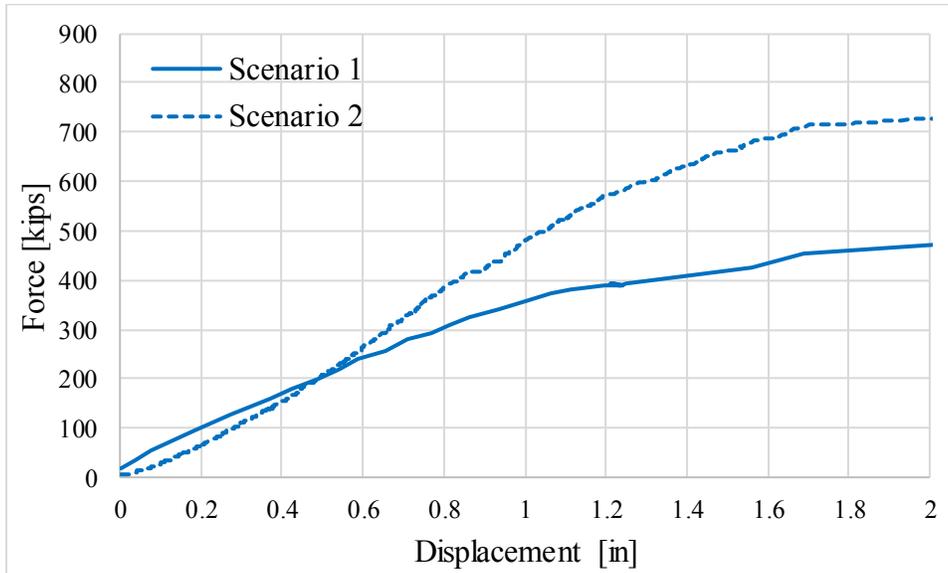
Figure 3.71 Scenarios 1 and 2 top-down load test results – physical tests
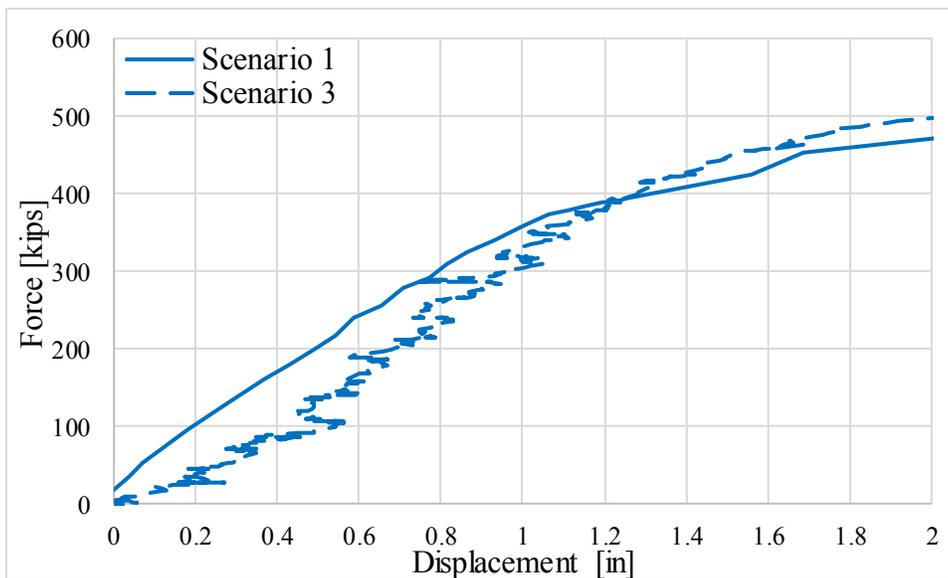
Figure 3.72 Scenarios 1 and 3 top-down load test results – physical tests
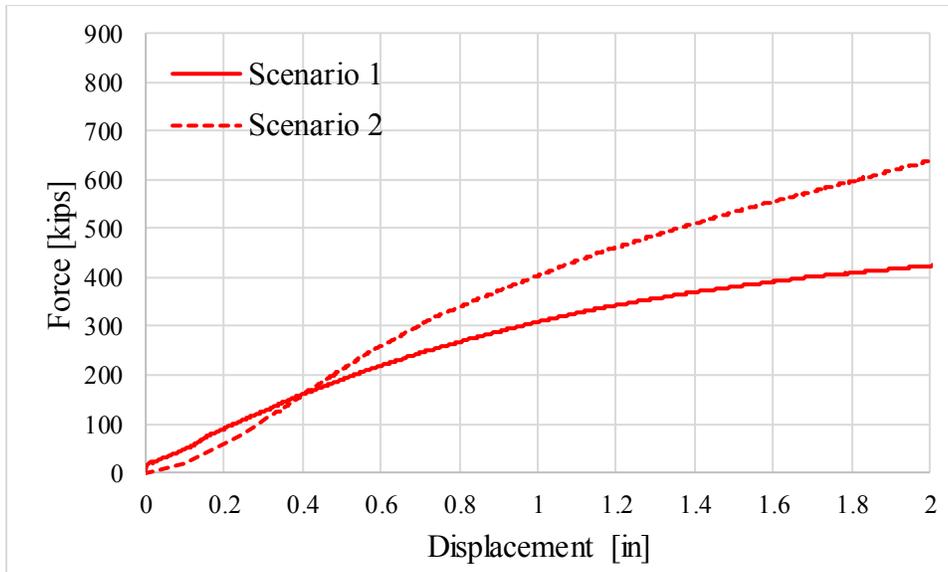
Figure 3.73 Scenarios 1 and 2 top-down load test results – Simulation 6
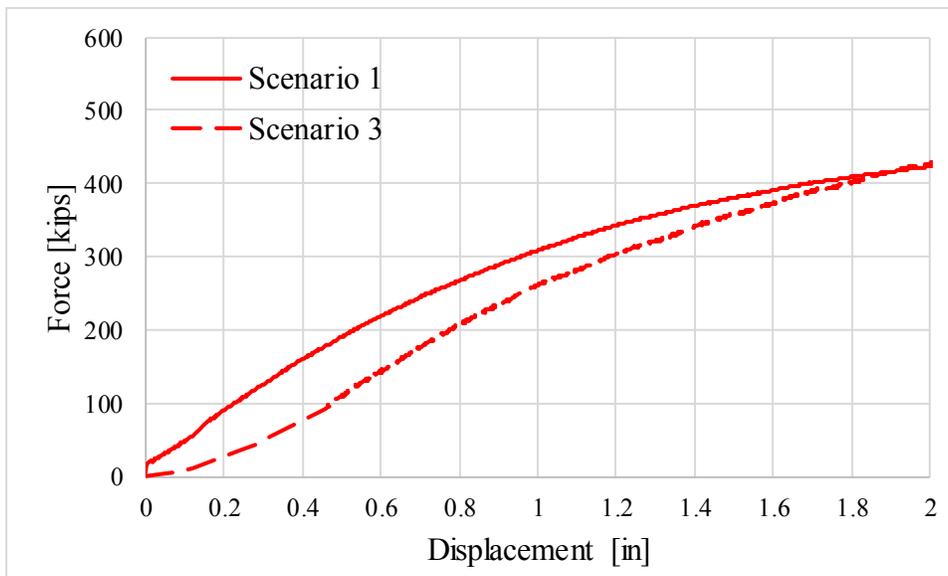
Figure 3.74 Scenarios 1 and 3 top-down load test results – Simulation 6
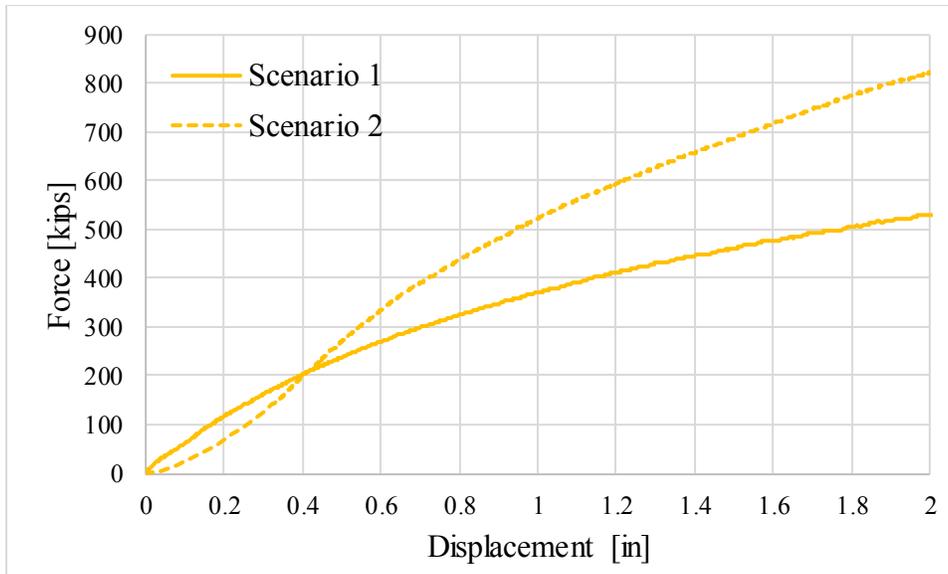
Figure 3.75 Scenarios 1 and 2 top-down load test results – Simulation 7
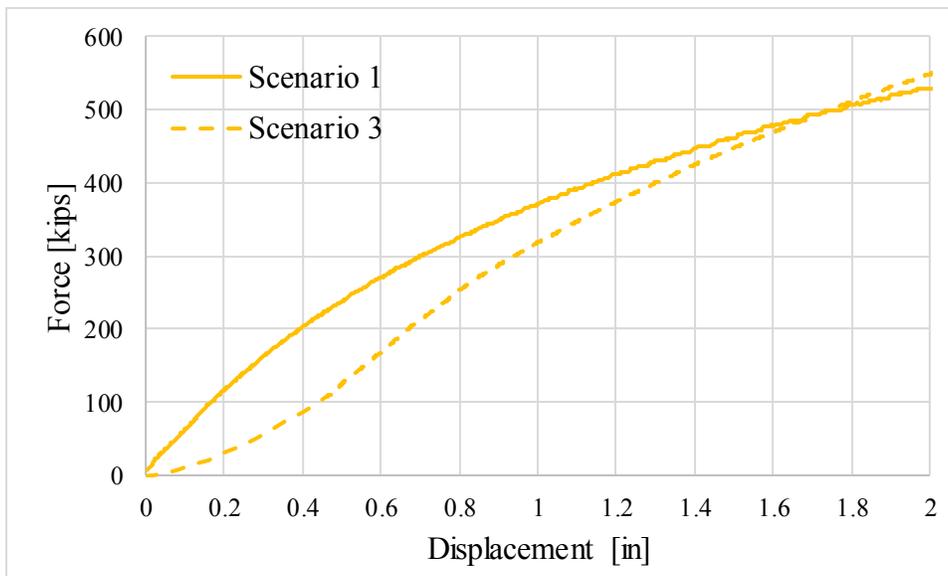
Figure 3.76 Scenarios 1 and 3 top-down load test results – Simulation 7

Table 3.17 Comparison of pile capacities between Scenario 1 and Scenario 2

Pile capacity	Loading scenario	Centrifuge test	Numerical results		
			Simulation 6	Simulation 7	Average
Davisson	1	150 kips	152 kips	200 kips	176 kips
	2	182 kips	183 kips	233 kips	208 kips
	% change	21.3 (+)	20.4 (+)	16.5 (+)	18.2 (+)
Ultimate	1	468 kips	425 kips	532 kips	478.5 kips
	2	728 kips	698 kips	820 kips	759 kips
	% change	55.5 (+)	64.24 (+)	54.14 (+)	58.62 (+)

Table 3.18 Comparison of pile capacities between Scenario 1 and Scenario 3

Pile capacity	Loading scenario	Centrifuge test	Numerical results		
			Simulation 6	Simulation 7	Average
Davisson	1	150 kips	152 kips	200 kips	176 kips
	3	80 kips	83 kips	95 kips	89 kips
	% change	46.6 (-)	45.4 (-)	52.5 (-)	49.4 (-)
Ultimate	1	468 kips	425 kips	532 kips	478.5 kips
	3	499 kips	428 kips	549 kips	488.5 kips
	% change	6.62 (+)	0.71 (+)	3.2 (+)	2.1 (+)

As observed across the set of simulation results, considerable stresses are induced ahead of the SPW and pile tips during driving (recall Table 3.15). A larger soil mass is pushed to the sides as the pile and SPW tip portions achieve greater embedment depths. As the tip of the SPW passes (upward) through the deformed zone, the chaotic particulate behavior agitates the shaft of the driven pile. The discontinuous interaction forming part of the pile-soil interface shear zone causes a decrease in shaft friction.

As the confining pressure in the pile tip region is increased in the dynamic loading sequences of Scenario 1 and Scenario 2, particle crushing may have a significant influence on the soil shear strength, and thus, the rate of dynamic loading may be expected to change the soil stress state to some extent (particle breakage is beyond the project scope). However, soil strength characteristics in terms of effective stresses increase substantially due to the transient loading events of Scenario 1 and Scenario 2. The mobilized soil strength is numerically simulated in the end bearing region by distinct intergranular frictional bonding and dilatancy effects. Accordingly, the numerical prediction of averaged soil resistances is in good agreement with observed changes in the pile capacities measured in the centrifuge test data, as shown in Table 3.17 and Table 3.18.

CHAPTER 4
PARAMETRIC STUDY OF DESIGN LOAD CAPACITIES

4.1 Overview of Task 5

In the current phase of research project, the complex geo-structural system consisting of the granular media, pile and sheet-pile wall are closely investigated to identify and isolate the effects of the geometric configuration of the said system only. In other words, the geometric configuration of the system, such as the distance between the pile and SPW and the relative embedment of SPW corresponding to the depth of the pile tip, are closely investigated to observe the effects of the identified parameter on response of granular media. This investigation is performed across both loading scenarios 2 and 3. Based on the simulation results, design recommendations are made to be used in order to obtain an approximate estimate of pile load capacity corresponding to various geometric configuration of the system.

4.1.1 Relative Horizontal Offset

First among identified geometric parameters is the relative horizontal offset between the pile and sheet pile wall (SPW). As has been concluded in task 3.2 report, the introduction of SPW in the vicinity of the pile alters the stress state within the "zone of influence" around the SPW. Depending on the location of SPW corresponding to the location of the pile, the influence zone created by installation of SPW may or may not have a significant effect on the pile capacity. To observe the effects of installation and subsequent removal of SPW on pile capacities as a function of distance between SPW and pile, the relative horizontal offset between the pile and SPW is parametrized. For the current investigation, five horizontal offsets are selected these are: 4 ft; 5 ft; 6 ft; 8 ft; and 10 ft.

4.1.2 Relative Embedment Depth

The second identified geometric parameter is the embedment depth of SPW tip relative to the embedment depth of pile tip. The zone of influence in which the stress state within granular assembly is altered is also affected by the depth up to which the SPW tip is embedded. The more the embedment depth, the larger this zone of influence is. Similar to the case of relative horizontal offset, the embedment depth of SPW tip is normalized with respect to the embedment depth of pile tip. Pile tip is embedded to a depth of approximately 17.7 ft. For the current investigation, four different embedment depths for SPW tip are selected for investigation: 4.425 ft $\left(\text{embedment depth ratio of } 0.25\right);$ 8.85 ft $\left(\text{embedment depth ratio of } 0.5\right);$ 13.275 ft $\left(\text{embedment depth ratio of } 0.75\right);$ and 17.7 ft $\left(\text{full embedment depth}\right).$

4.1.3 Simulation Matrix

Based on the above identified parameters, a test matrix for all the simulations that were performed as the part of the investigation is created. Parametric study is carried out using both the simulation 6 and simulation 7 numerical models from Task 3. However, the results in the

subsequent sections have been calculated as an average value between the two. The test matrix for all the simulations as a part of parametric study is given below (Table 4.1).

Table 4.1 Test matrix parametric study for loading Scenarios 2 and 3

Simulation	Ratio of SPW embedment depth to pile tip depth	Horizontal offset distance between pile and SPW (ft)
6	$\frac{1}{4}$	4
		5
		6
		8
		10
	$\frac{1}{2}$	4
		5
		6
		8
		10
	$\frac{3}{4}$	4
		5
		6
		8
		10
	1	4
		5
		6
		8
		10
7	$\frac{1}{4}$	4
		5
		6
		8
		10
	$\frac{1}{2}$	4
		5
		6
		8
		10
	$\frac{3}{4}$	4
		5
		6
		8
		10
	1	4
		5
		6
		8

		10

The simulation results from the parametric study are discussed in the following sections.

4.2 Parametric Study Results

Numerical simulations are carried as per the test matrix defined in the previous section. Quasi-static top-down load-displacement behavior is the main focus of this chapter as the objective of Task 5 is to provide design recommendations.

4.2.1 Top-Down Loads when Controlling for Relative Horizontal Offset

The quasi-static top-down load-displacement behavior of the SPW-pile system is investigated for geometric parameters of horizontal offset distances between pile and SPW and relative depths between pile tip and SPW toe. Results are shown in Fig. 4.1 through Fig. 4.5 under Scenario 2 conditions. A pattern emerges with respect to horizontal offset distances (HOD) between pile and SPW; the closer proximity to the pre-installed SPW, the stiffer pile axial behavior, and the deeper SPW is pre-installed the greater maximum load carrying capacity. For example, the axial resistance predicted at HOD of 4 ft is much greater than that at HOD of 10 ft. Lateral confinement substantially increases as movement of granular mass is constrained to an extent by the proximity of SPW. The SPW-pile system noticeably gains a higher load carrying capacity with a deeper installation of the SPW.
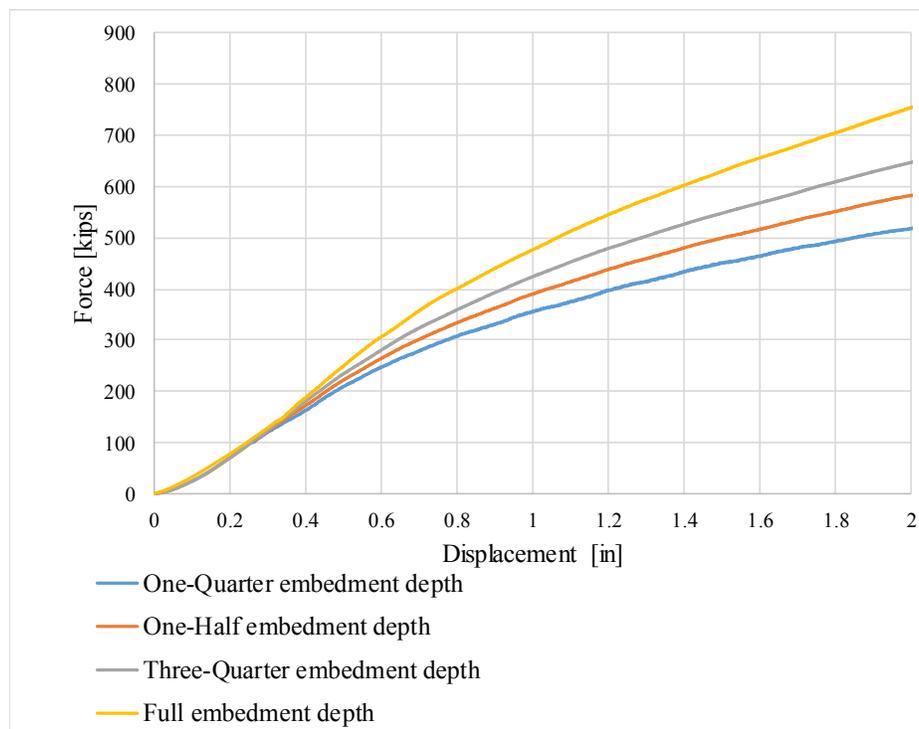
Figure 4.1 Force-displacement plots for loading Scenario 2 with horizontal distance between pile and SPW equal to 4 ft

111
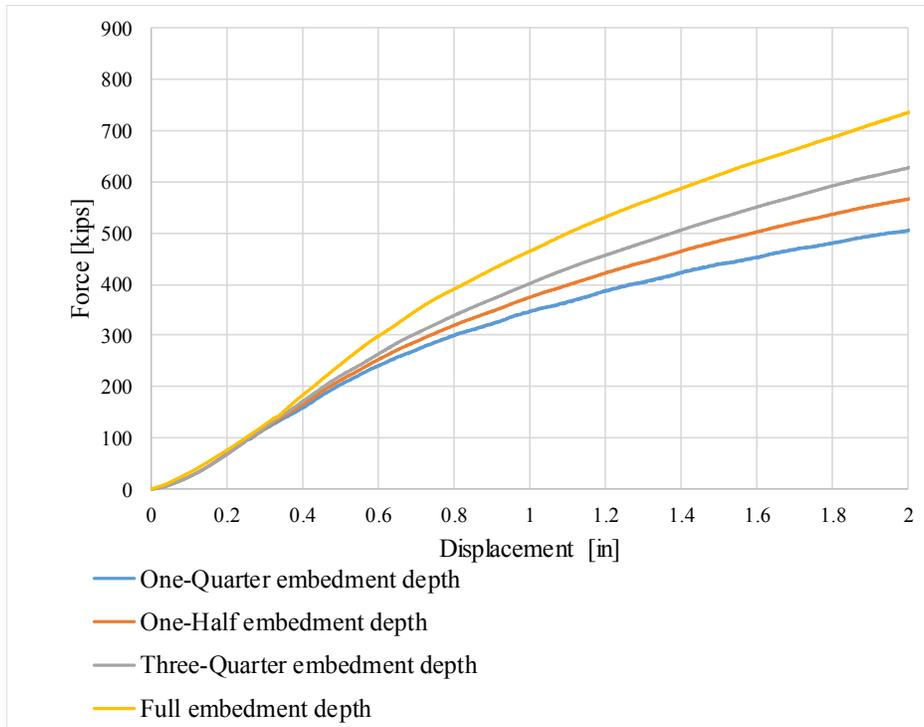
Figure 4.2 Force-displacement plots for loading Scenario 2 with horizontal distance between pile and SPW equal to 5 ft
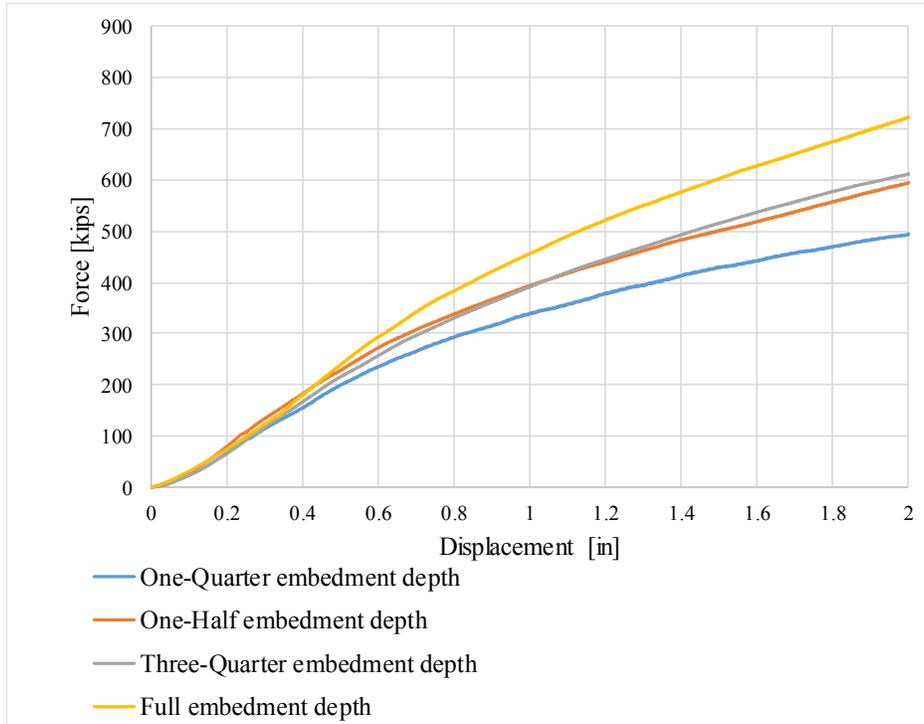
Figure 4.3 Force-displacement plots for loading Scenario 2 with horizontal distance between pile and SPW equal to 6 ft
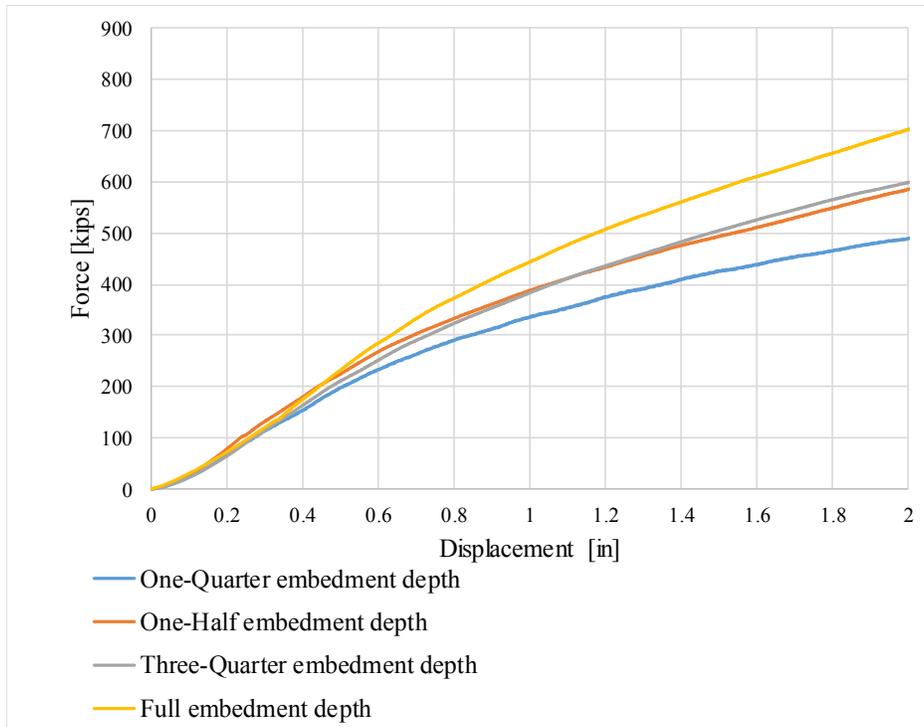
Figure 4.4 Force-displacement plots for loading Scenario 2 with horizontal distance between pile and SPW equal to 8 ft
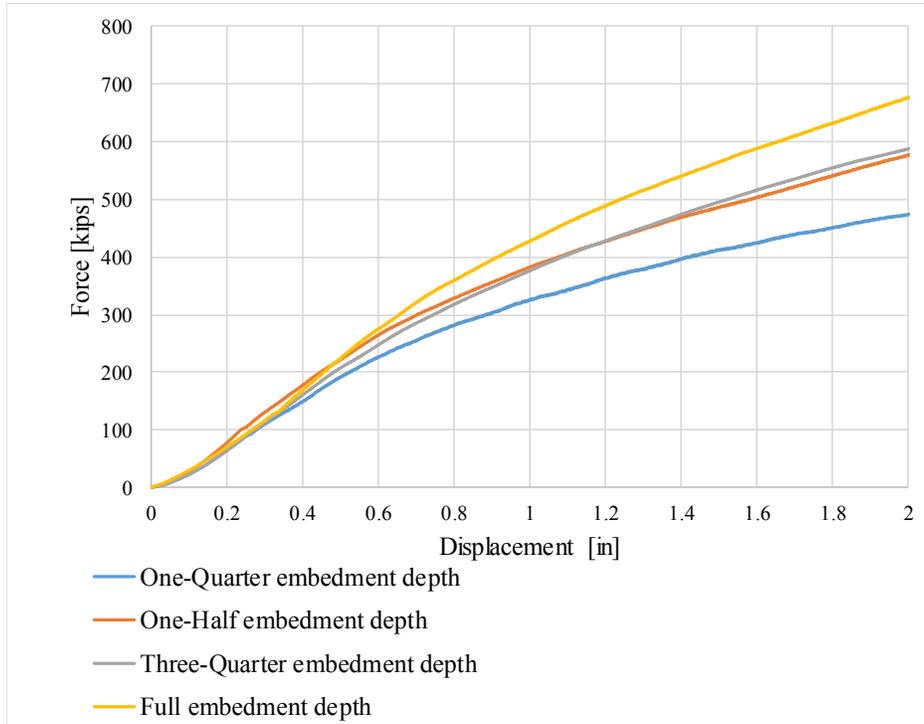
Figure 4.5 Force-displacement plots for loading Scenario 2 with horizontal distance between pile and SPW equal to 10 ft

In Fig. 4.6 through Fig. 4.10, the load-displacement behaviors are presented for Scenario 3. A reverse trend of Scenario 2 is observed for Scenario 3 where reduction in the pile capacities is evident. Recall that the SPW-pile load capacity drastically increases in Scenario 2 where we observe about maximum 40% difference in the ultimate capacity, depending on SPW embedment depths (Fig. 4.5). However, the rate of decrease in the predicted capacities exacerbates with SPW embedment depth; given the case of full SPW pre-embedment depth the largest reduction of the Davisson capacity is predicted. In comparison to Scenario 1, minimal changes in the ultimate capacities are predicted at given all HOD in a range of 4-10 ft when the SPW is pre-installed less than the half of the pile embedment length.
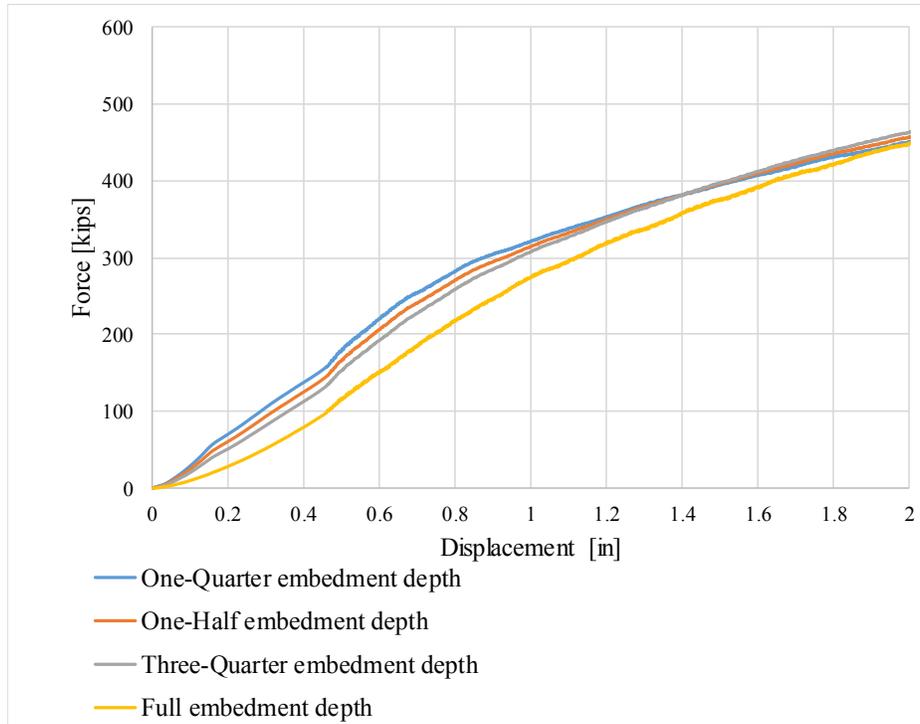
Figure 4.6 Force-displacement plots for loading Scenario 3 with horizontal distance between pile and SPW equal to 4 ft
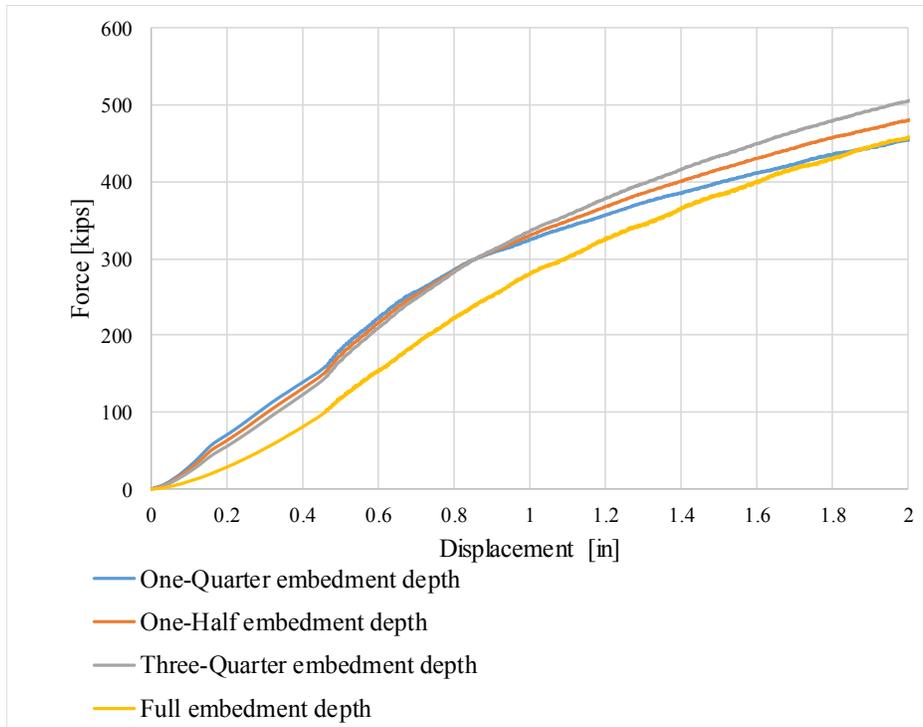
Figure 4.7 Force-displacement plots for loading Scenario 3 with horizontal distance between pile and SPW equal to 5 ft
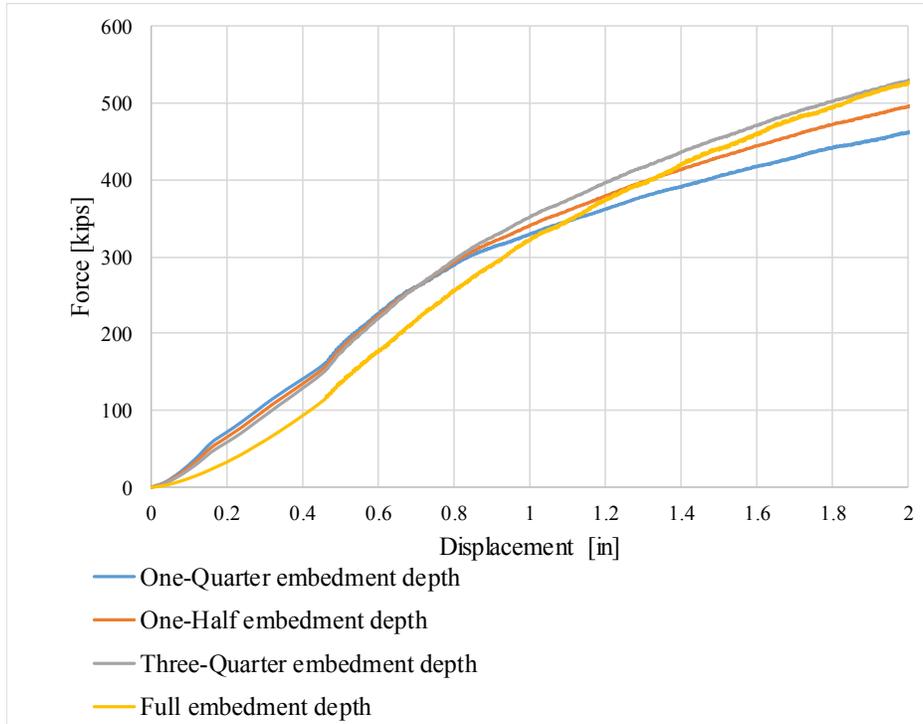
Figure 4.8 Force-displacement plots for loading Scenario 3 with horizontal distance between pile and SPW equal to 6 ft

115
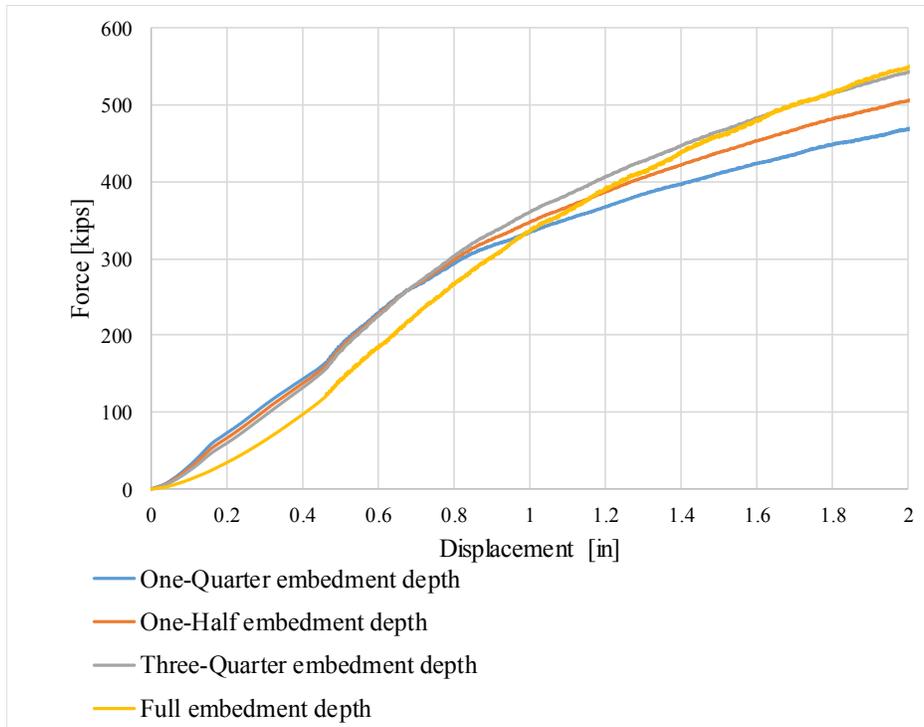
Figure 4.9 Force-displacement plots for loading Scenario 3 with horizontal distance between pile and SPW equal to 8 ft
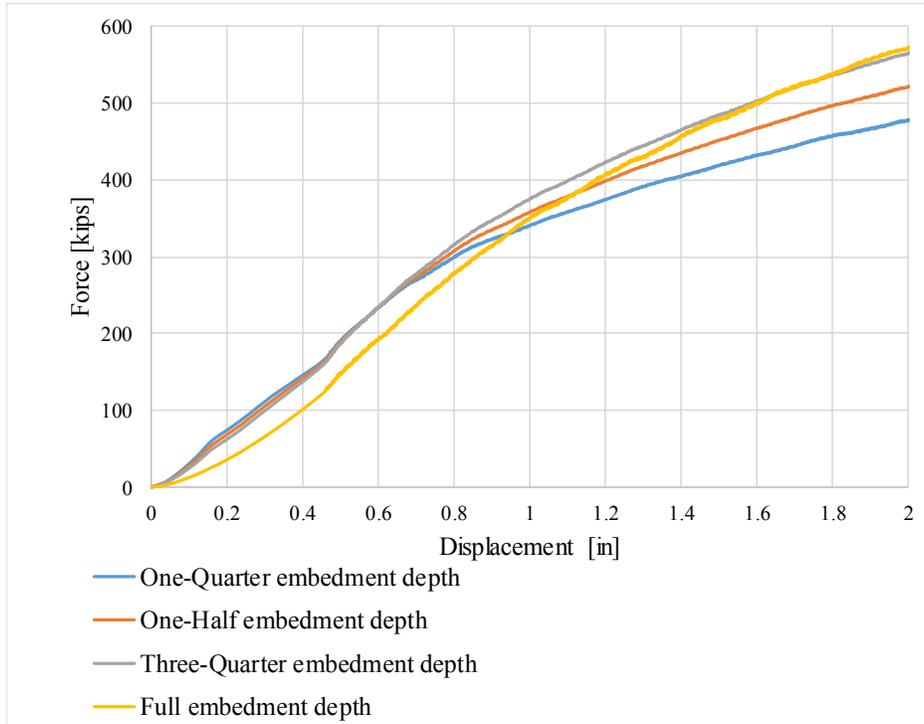
Figure 4.10 Force-displacement plots for loading Scenario 3 with horizontal distance between pile and SPW equal to 10 ft

4.2.2 Top-Down Loads when Controlling for Relative Embedment Depth

As shown in Fig. 4.11 through Fig. 4.14, the quasi-static top-down load-displacement behaviors of the SPW-pile system are presented as per variations of SPW pre-embedment depth relative to pile tip depth. Recall that the results of quasi-static centrifuge load tests under a full SPW pre-embedment condition have been demonstrated by means of FEM-DEM model calibration or otherwise; validity of the numerical predictions has been demonstrated by the prototype-scale load tests in controlled loading sequences. The observed performance of the SPW-pile foundation provides that the SPW pre-embedment depth is the controlling factor in determination of the pile capacities. Within a HOD range of 4-10 ft, numerical results indicate rather minimal variation in the quasi-static top-down load-displacement behaviors at a given SPW pre-embedment depth. In turn, a consistent trend can be found in which the pile load capacities increase as the SPW pre-embedment depth increases, i.e., ranging from Fig. 4.11 to Fig. 4.14. This can be attributed to the formation of larger influence zones as the SPW is pushed (pressed) down deeper which results in further increase in the total confinement forces.
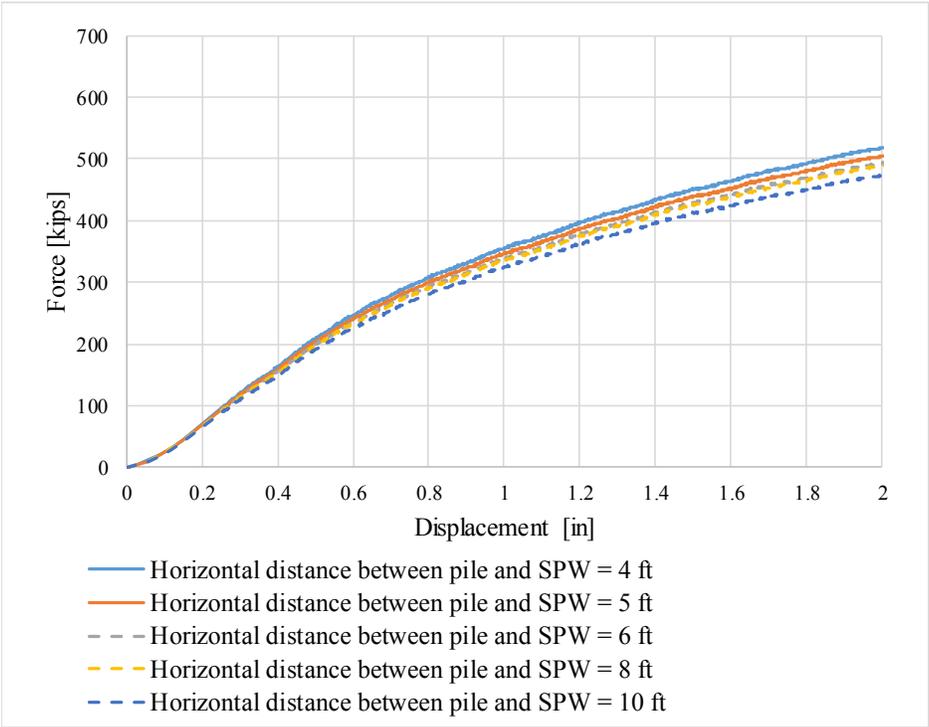
Figure 4.11 Force-displacement plots for loading Scenario 2 for one-quarter embedment depth of SPW relative to pile tip depth

117
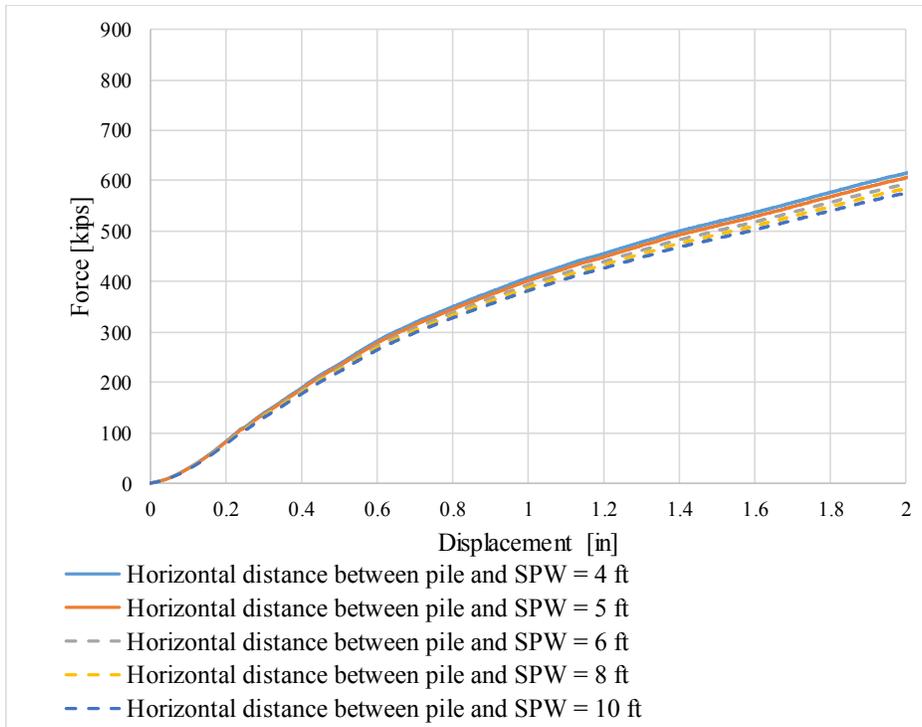
Figure 4.12 Force-displacement plots for loading Scenario 2 for one-half embedment depth of SPW relative to pile tip depth
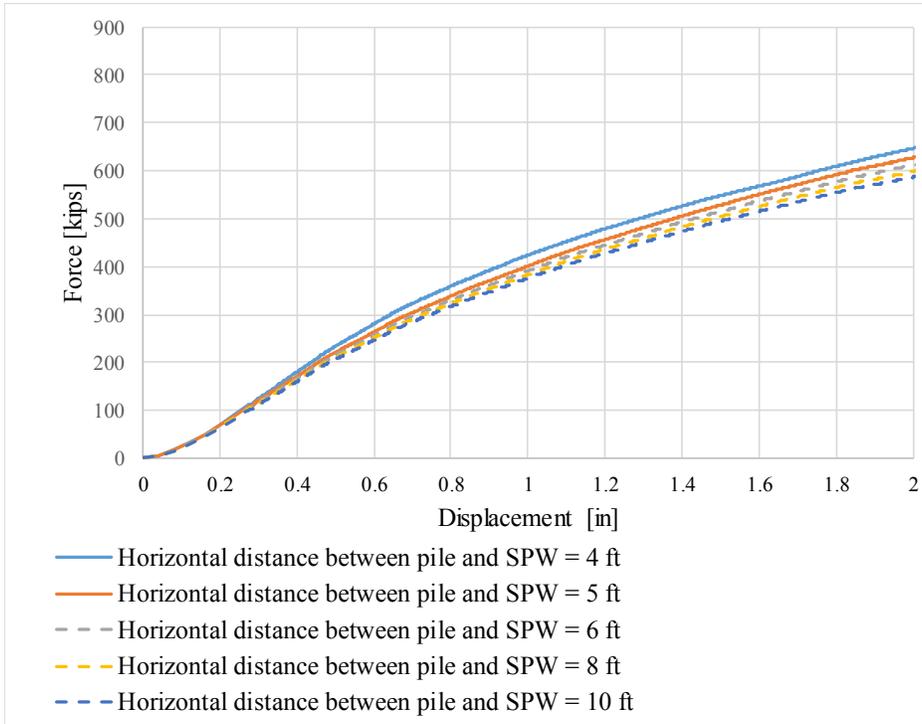
Figure 4.13 Force-displacement plots for loading Scenario 2 for three-quarter embedment depth of SPW relative to pile tip depth
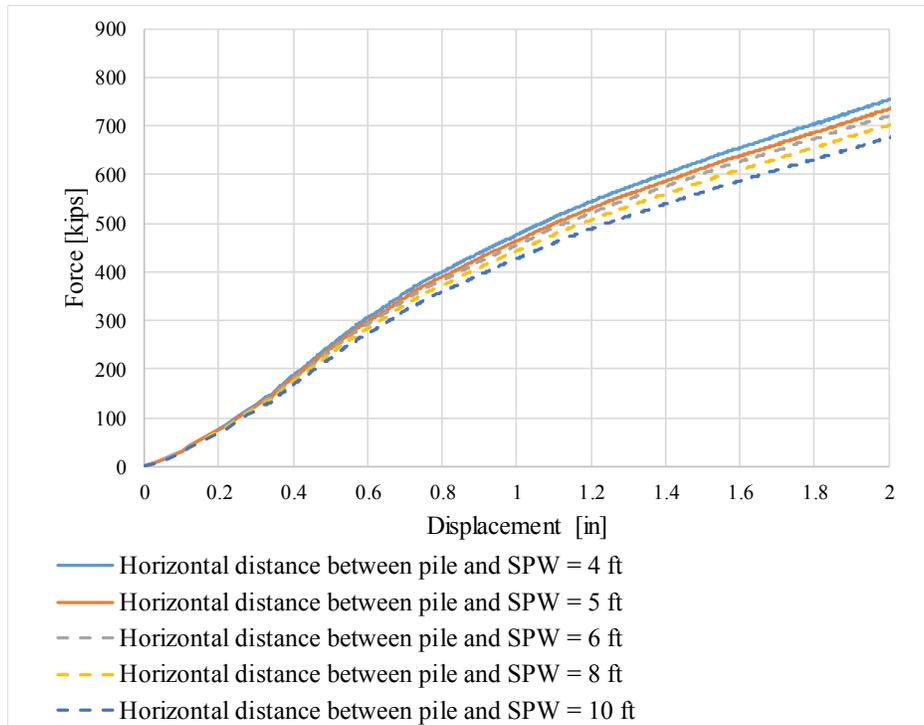
Figure 4.14 Force-displacement plots for loading Scenario 2 for full embedment depth of SPW relative to pile tip depth

In the following Fig. 4.15 through Fig. 4.18, the load-displacement behaviors of the pile foundation after the SPW removal, i.e., Scenario 3, are presented in terms of the ratio of SPW pre-embedment depth to the pile tip depth (i.e., 18 ft). Numerical results indicate that effective stress in the end bearing region is substantially influenced with SPW pre-embedment depth. When SPW is installed deeper in relation to the pre-determined pile embedment depth, we observe a significant increase in the effective stresses in vicinity of the pile tip region. However, as the SPW is removed vertically upward, side shear forces around the SPW wall causes disturbance in the dense configurations of granular structure compacted by pile driving. In addition, cavity formation near the moving SPW toe substantially relieves horizontal confining stresses that have been developed along the length of the pile. This phenomenon becomes more pronounced with closer horizontal offset distances. Eventually, the granular structure regains a stress equilibrium at a looser density state. Noticeably, the looser state directly affects the axial resistance (stiffness) of the pile foundation subjected to quasi-static top-down loads.
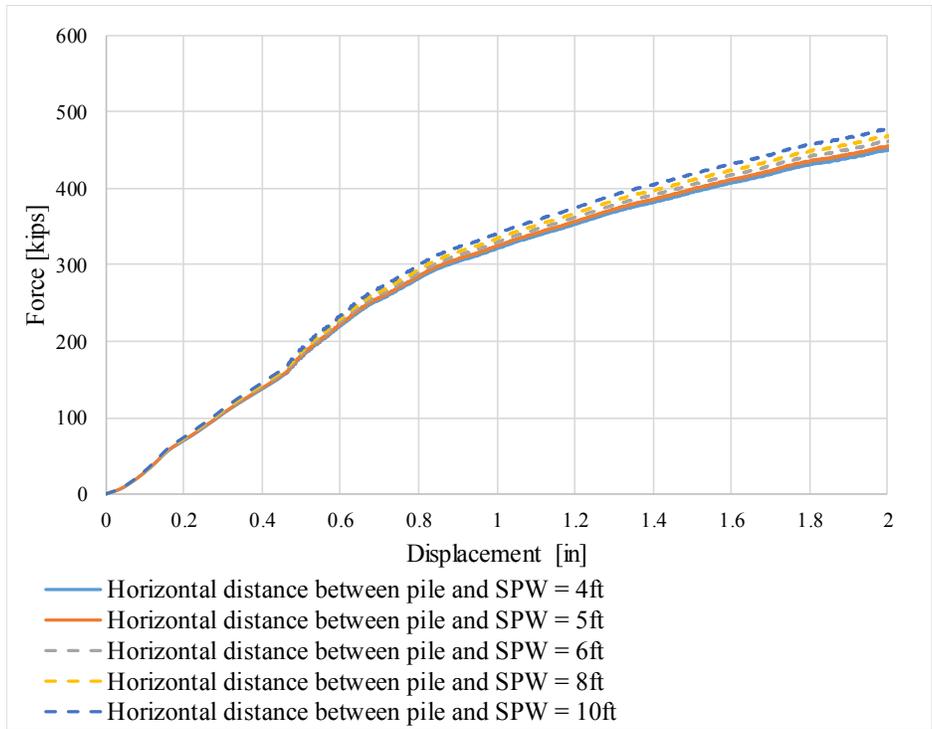
Figure 4.15 Force-displacement plots for loading Scenario 3 for one-quarter embedment depth of SPW relative to pile tip depth
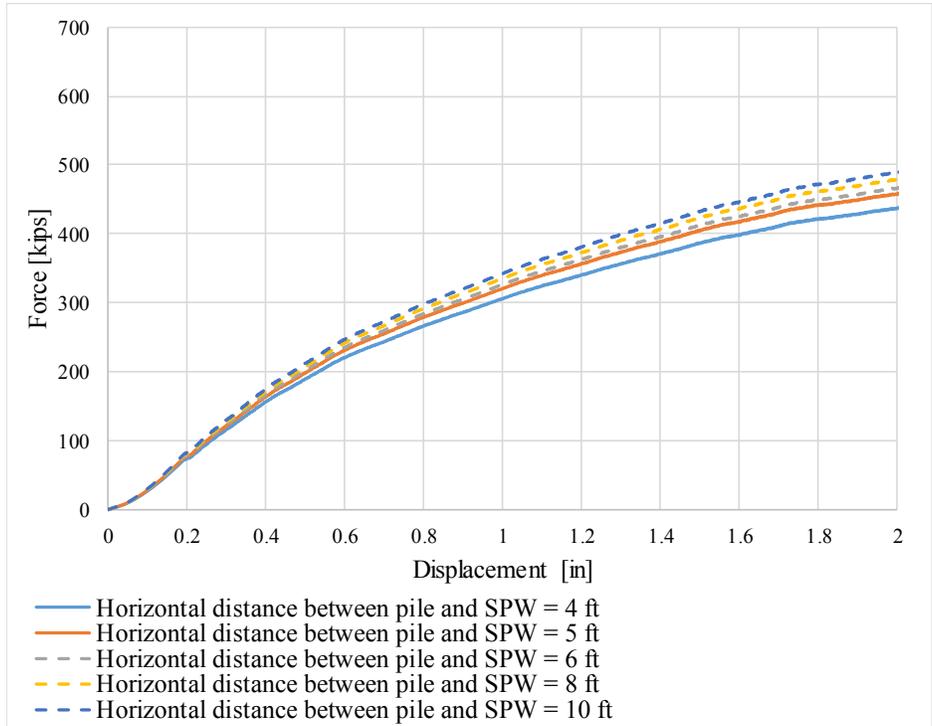
Figure 4.16 Force-displacement plots for loading Scenario 3 for one-half embedment depth of SPW relative to pile tip depth
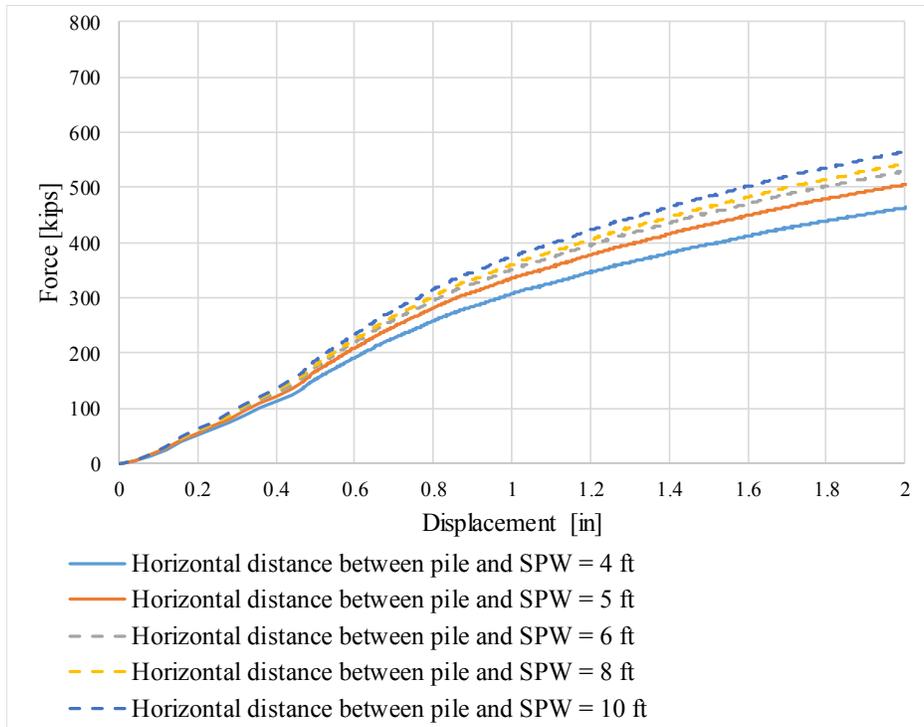
Figure 4.17 Force-displacement plots for loading Scenario 3 for three-quarter embedment depth of SPW relative to pile tip depth
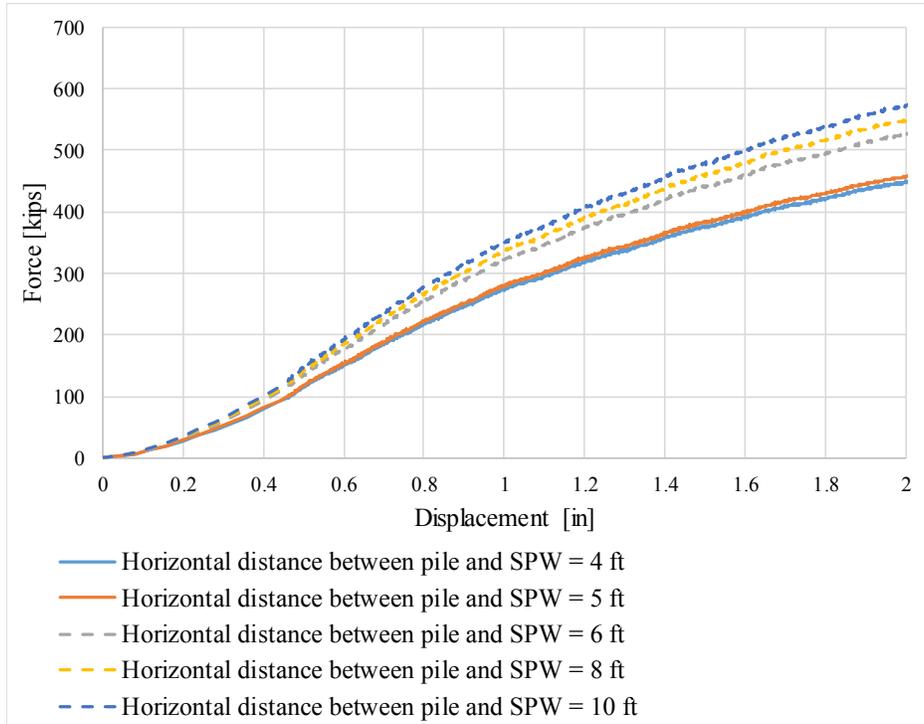
Figure 4.18 Force-displacement plots for loading Scenario 3 for full embedment depth of SPW relative to pile tip depth

In summary, the parametric study clearly shows that there exist predictable trends in comparisons between Scenario 2 and Scenario 1, and Scenario 3 and Scenario 1, which can be used to establish simplified design guidelines to account for the post-SPW-removal effects in the calculation of the pile capacities. A calculation procedure is discussed regarding the horizontal offset distance (HOD) between pile and SPW and the SPW embedment depths relative to pile tip depth in the following chapter.

CHAPTER 5
RECOMMENDATIONS OF PILE DESIGN

5.1 Overview

In this chapter, design considerations are presented with respect to the geometric parameters of the SPW-pile system. In particular, the predictions of pile capacities under Scenario 2 and Scenario 3 are made to account for the effect of the pre-installation and post removal of the SPW in comparison to the single pile system of Scenario 1. This way, engineers can estimate the pile capacities using multipliers as factors of geometric configurations of the SPW-pile foundation system under both scenarios.

5.2 Accounting for Relative Horizontal Offset

The load-displacement behaviors of the SPW-pile foundation (from Sec. 4.2.1) are represented in terms of Davisson and ultimate capacities. The differences between Scenario 1 and Scenario 2 are first presented in a graphical format for the horizontal offset distances between pile and SPW. Fig 5.1 and Fig. 5.2 illustrate percentage changes to Scenario 2 from Scenario 1, which the trend-line curves give graphical means to assess Davisson and ultimate pile capacities as per the horizontal offset distances between SPW and pile, and the ratios of SPW embedment depth to pile tip depth.
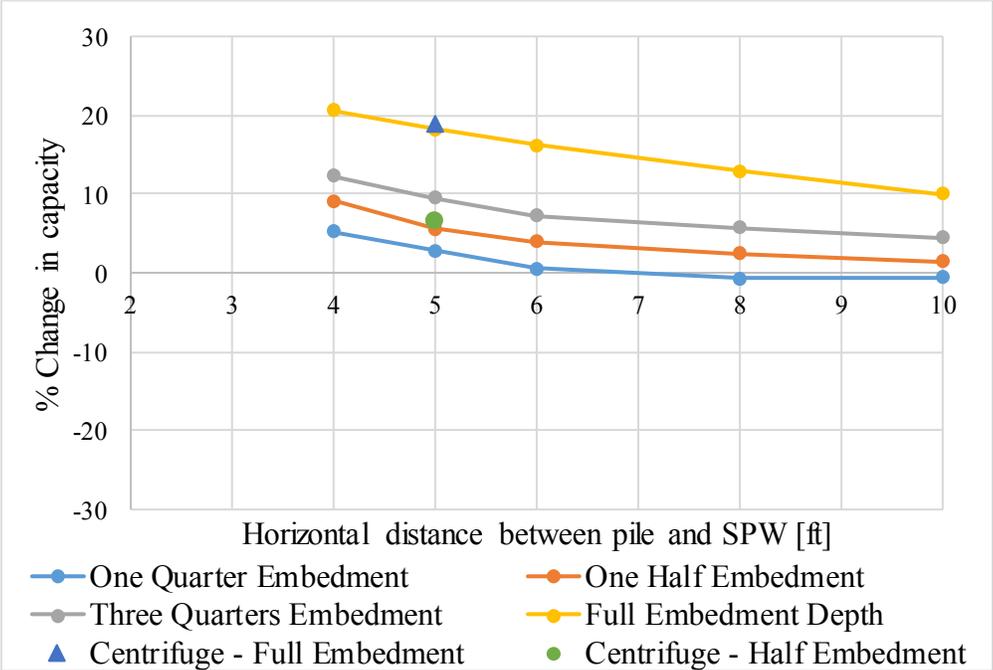
Figure 5.1 Variation of Davisson pile capacity for Scenario 2 with horizontal offset distances between pile and SPW. Recall that in Scenario 2, a sheet pile is pushed into the soil, followed by a pile driven in the vicinity of the sheet pile. At a steady state, quasi-static axial loading is applied to the top of the pile.
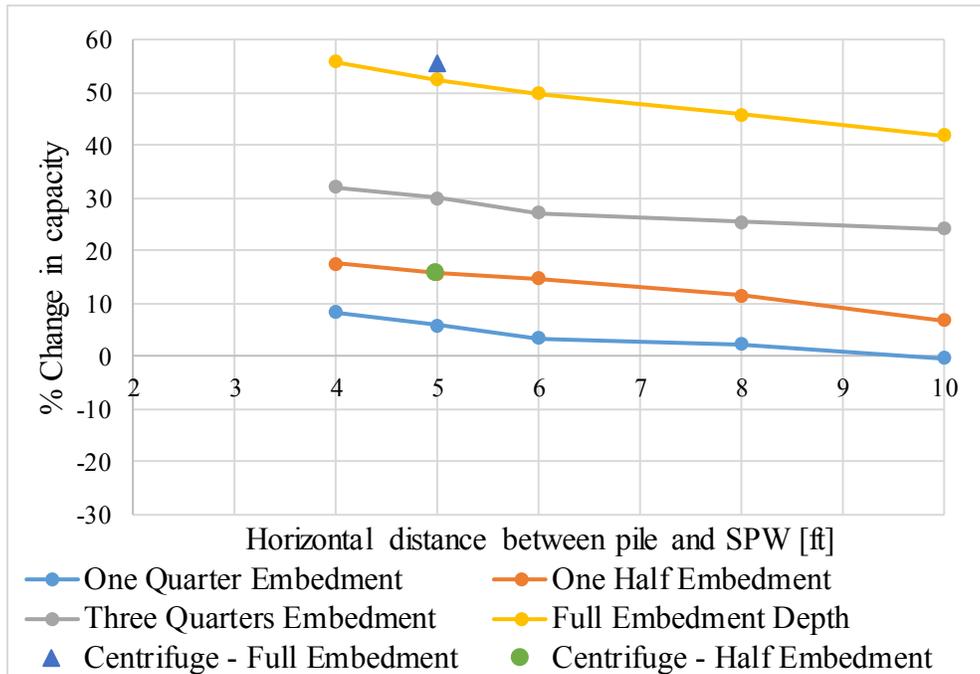
Figure 5.2 Variation of ultimate pile capacity for Scenario 2 with horizontal offset distances between pile and SPW. Recall that in Scenario 2, a sheet pile is pushed into the soil, followed by a pile driven in the vicinity of the sheet pile. At a steady state, quasi-static axial loading is applied to the top of the pile.

In addition, Fig. 5.3 and Fig. 5.4 illustrate the percentage changes of the pile capacities under Scenario 3 in comparison to Scenario 1. The trend-line curves give graphical means to assess Davisson and ultimate pile capacities as per the horizontal offset distances between SPW and pile per rations of SPW embedment depth to pile tip depth.
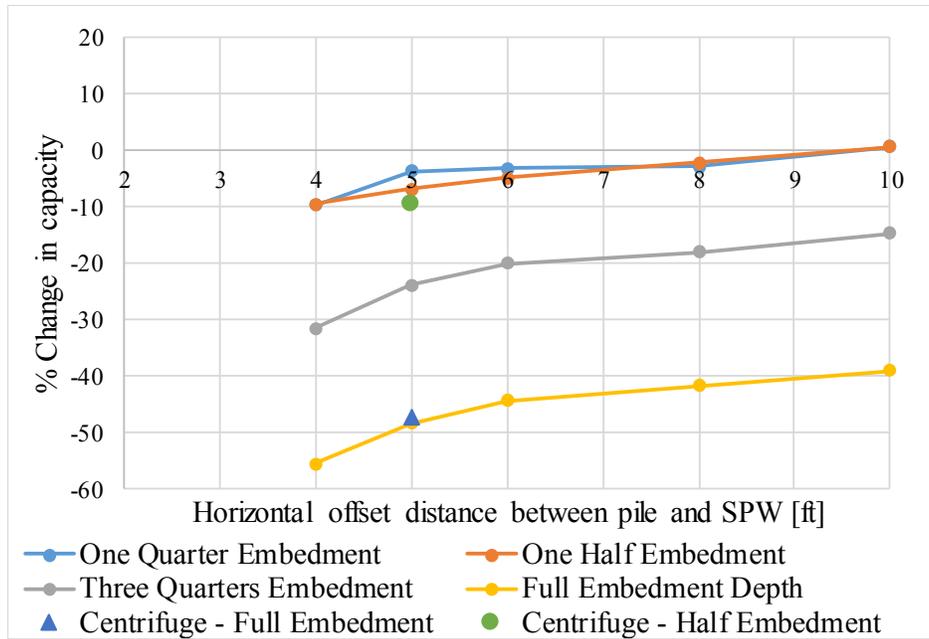
Figure 5.3 Variation of Davisson capacity for Scenario 3 with horizontal offset distances between pile and SPW. Recall that in Scenario 3, a sheet pile is driven into the soil, followed by the pile driven in vicinity of the SPW, then the SPW is vertically extracted. At a steady state, quasi-static axial loading is applied to the top of the pile.
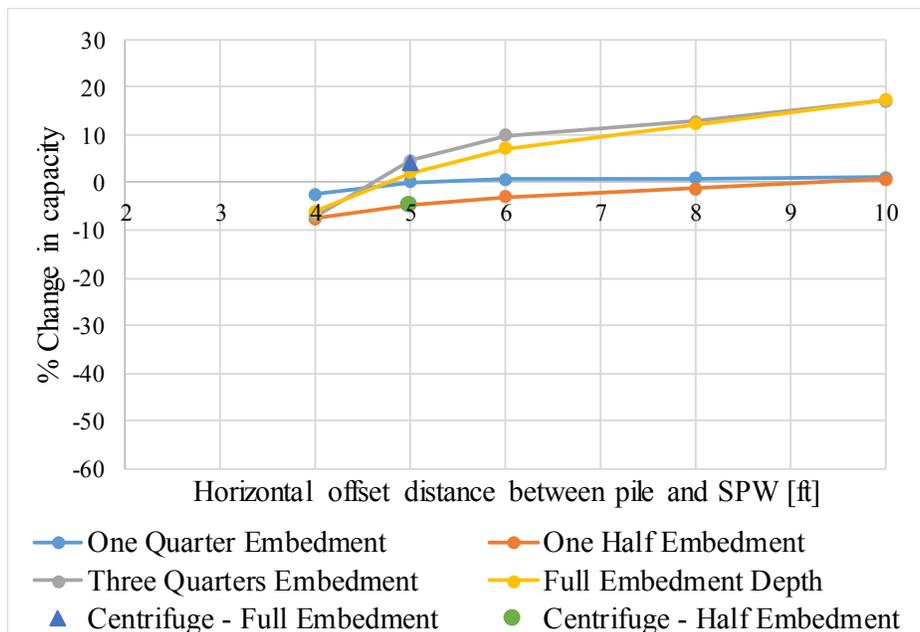
Figure 5.4 Variation of ultimate pile capacity for Scenario 3 with horizontal offset distances between pile and SPW. Recall that in Scenario 3, a sheet pile is driven into the soil, followed by the pile driven in vicinity of the SPW, then the SPW is vertically extracted. At a steady state, quasi-static axial loading is applied to the top of the pile.

5.3 Accounting for Relative Embedment Depth

As shown in Fig. 5.5 and Fig. 5.6, the increase in pile capacities under Scenario 2 are presented with respect to ratios of SPW embedment depth to pile embedment length. In relation to pile load capacity of the single pile foundation, Davisson and ultimate pile capacities for this scenario can be assessed in a straightforward manner for the percentage changes per incremental SPW pre-embedment depths.
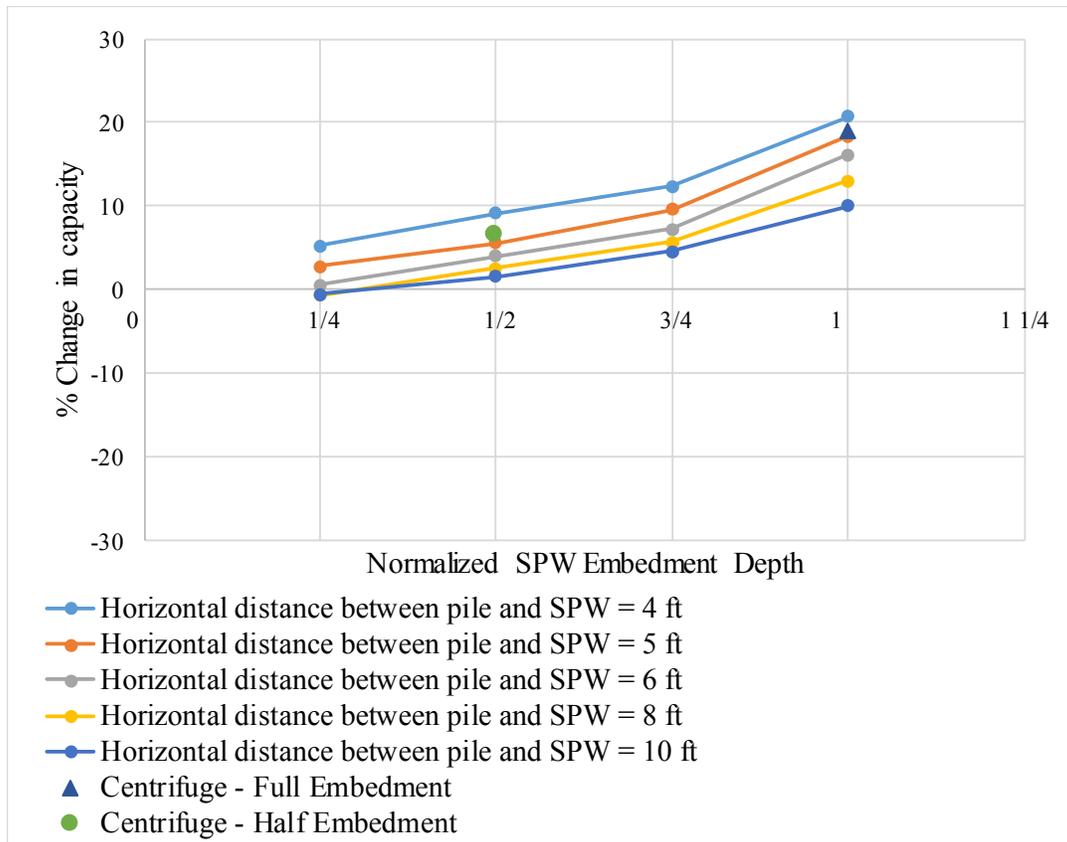
Figure 5.5 Variation of Davisson pile capacity for Scenario 2 as per ratios of SPW embedment depth to pile embedment length. Recall that in Scenario 2, a sheet pile is pushed into the soil, followed by a pile driven in the vicinity of the sheet pile. At a steady state, quasi-static axial loading is applied to the top of the pile.
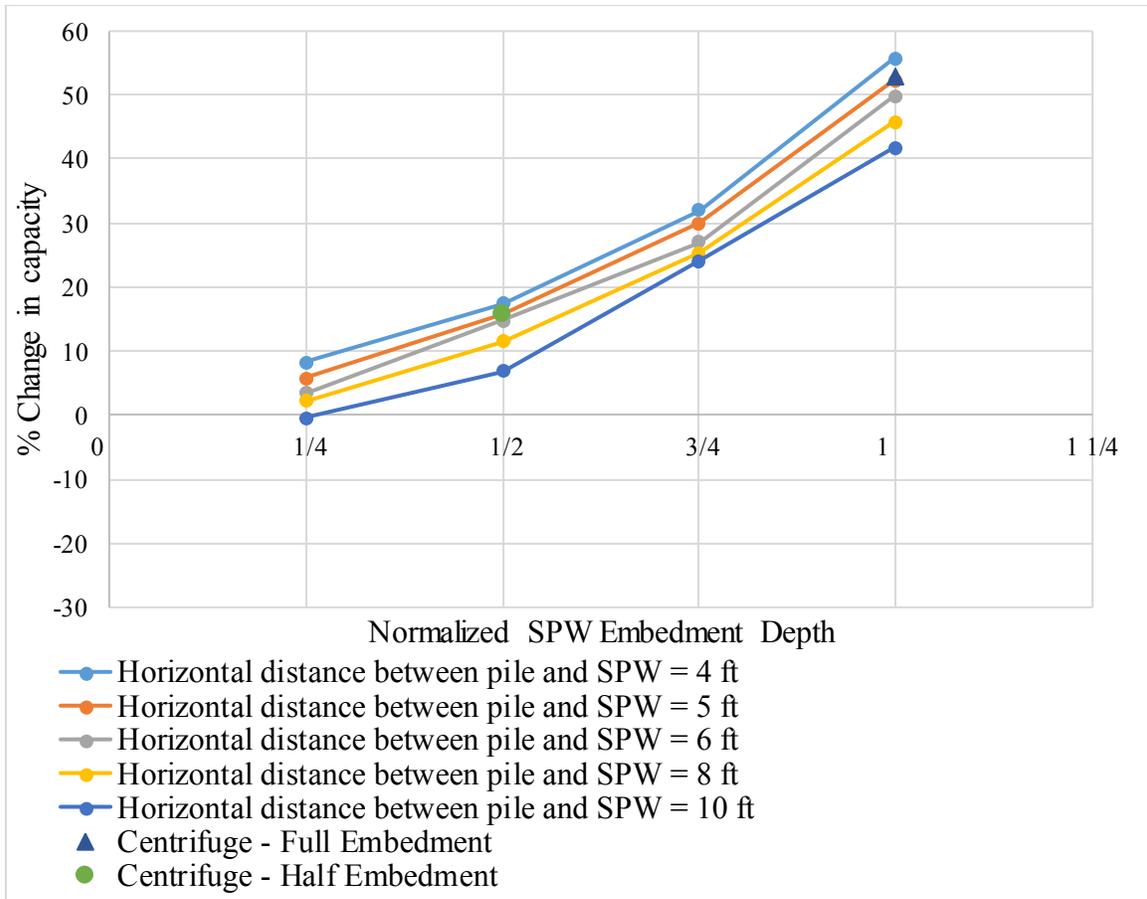
Figure 5.6 Variation of ultimate pile capacity for Scenario 2 as per ratios of SPW embedment depth to pile embedment length. Recall that in Scenario 2, a sheet pile is pushed into the soil, followed by a pile driven in the vicinity of the sheet pile. At a steady state, quasi-static axial loading is applied to the top of the pile.

In contrast, the Davisson capacity decreases upon the SPW removal as shown in Fig. 5.7. This trend is mainly due to decrease in the axial resistance of the pile foundation; for example, as seen in the difference between the two scenarios in the initial slope (and shape) of the load-displacement curve (Fig. 5.8). In turn, the reduction relative to the pile capacities of Scenario 1 can be interpreted as a function of the ratio of SPW embedment depth to pile embedment length, which are presented in Figs 5.7 and 5.9 for graphical tools to estimate the Davisson capacities of the pile foundation system after the removal of SPW.
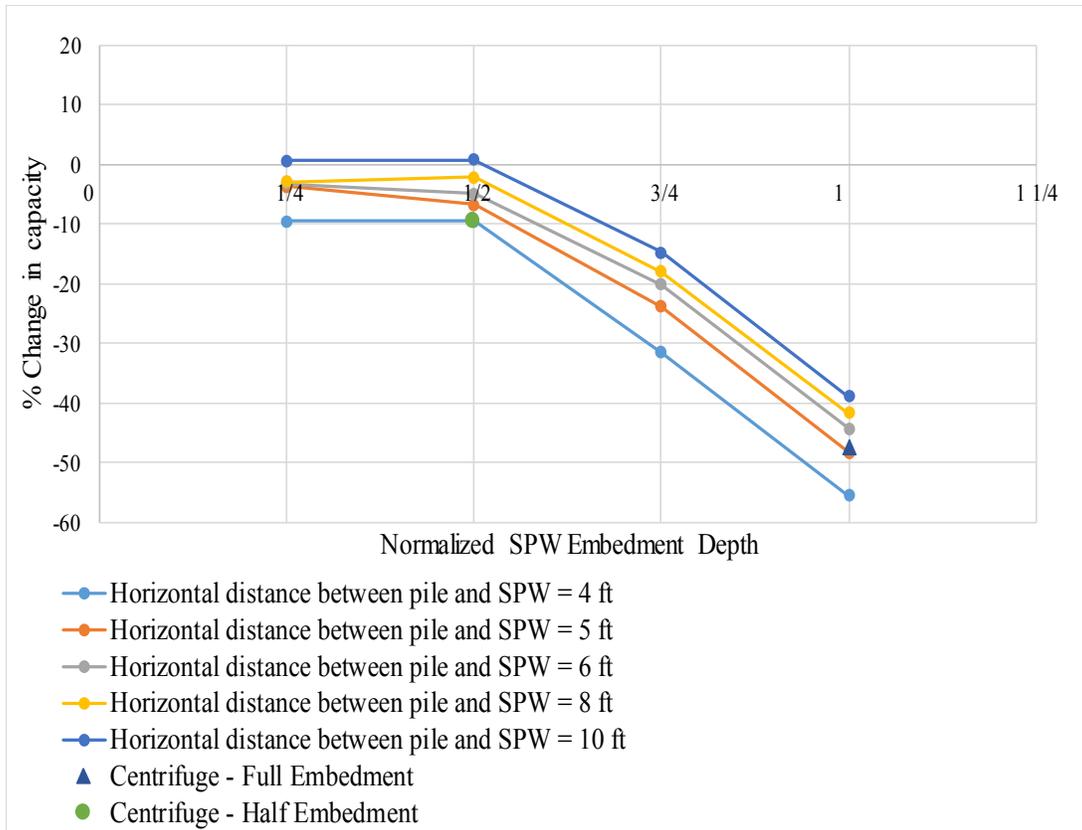
Figure 5.7 Variation of Davisson pile capacity for Scenario 3 as per ratios of SPW embedment depth to pile embedment length. Recall that in Scenario 3, a sheet pile is driven into the soil, followed by the pile driven in vicinity of the SPW, then the SPW is vertically extracted. At a steady state, quasi-static axial loading is applied to the top of the pile.
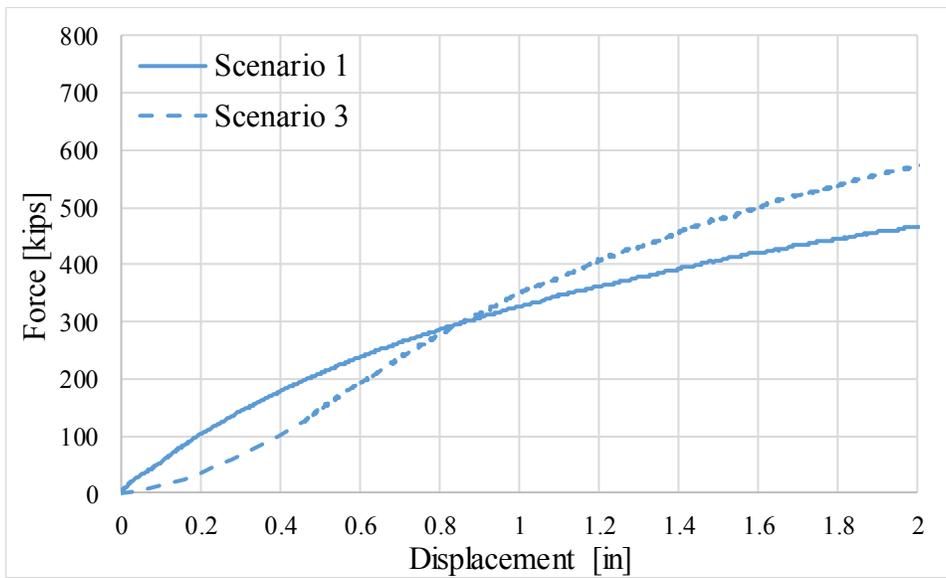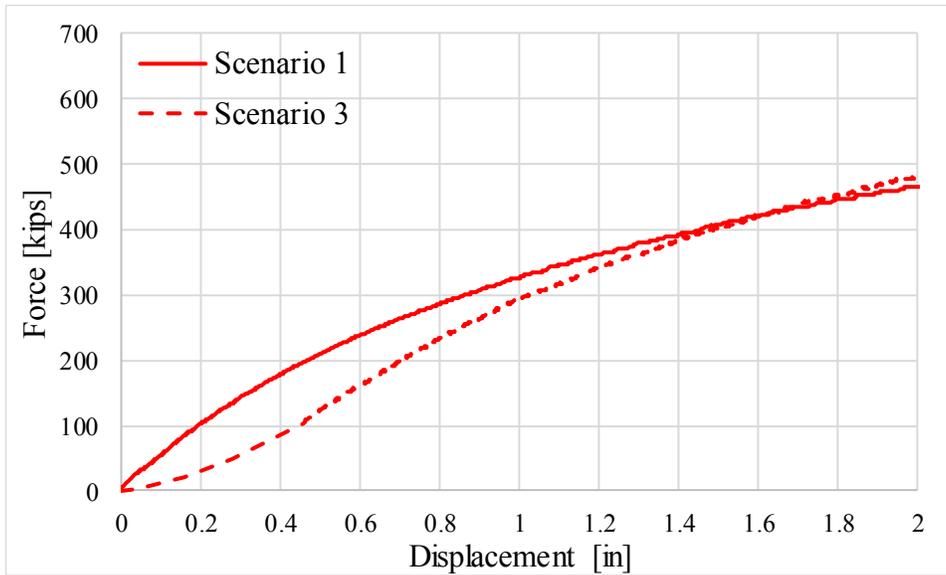
Figure 5.8 Scenario 1 and 3 top-down load-settlement behaviors at HOD of 5 ft (top; red curves) and 10 ft (bottom; blue curves) for the full SPW embedment case

The SPW removal process evidently appears to cause less disturbance in the end bearing region when HOD is larger than 6 ft (3B) (Fig. 5.9a). This results in a small net gain on the ultimate capacity even after the removal of SPW in comparison to Scenario 2 as shown in Fig. 5.9b. At HOD between 6 ft and 10 ft, the stress path in the end bearing region of Scenario 3 is evidently different from that of Scenario 1 which is illustrated in Fig. 5.10a. It is noted that the triangular points of the stress paths represent stress states (in the end bearing region) prior to the application of quasi-static top-down loads. Scenario 3 (only when HOD is greater than 6 ft) may attribute to

mobilization of slightly larger shear resistance along the path towards the p-q failure envelope, and result in apparent increase in the ultimate load. However, the maximum load-carrying capacity should be considered with caution. Given computational and time constraints, the parametric sensitivity study does not consider other factors (in association with construction methods of pile driving and/or vibratory SPW removal) in empirically supporting such increases in the ultimate load capacity. The investigators thus recommend a conservative design approach such that no increase in the ultimate capacity be taken, but at maximum 10% reduction be accounted for in the maximum load capacity accordingly to the cases of HOD and embedment ratios.

The SPW removal process evidently appears to cause less disturbance in the end bearing region when HOD is larger than 6 ft (Fig. 5.9a). This results in a small net gain on the ultimate capacity even after the removal of SPW as shown in Fig. 5.8. At HOD between 6 ft and 10 ft, the stress path in the end bearing region of Scenario 3 is evidently different from that of Scenario 1 which is illustrated in Fig. 5.10a. It is noted that the triangular points of the stress paths represent stress states (in the end bearing region) prior to the application of quasi-static top-down loads. Only when HOD is greater than 6 ft, Scenario 3 may attribute to mobilization of slightly larger shear resistance along the path towards the p-q failure envelope, and result in apparent increase in the ultimate load. However, the maximum load-carrying capacity should be considered with caution. Given computational and time constraints, the parametric sensitivity study does not consider other factors (in association with construction methods of pile driving and/or vibratory SPW removal) in empirically supporting such trends in the ultimate load capacity. The investigators thus recommend a conservative design approach such that no increase in the ultimate capacity be taken, but at maximum 10% reduction be accounted for in the ultimate load capacity accordingly to the cases of HOD and embedment ratios.
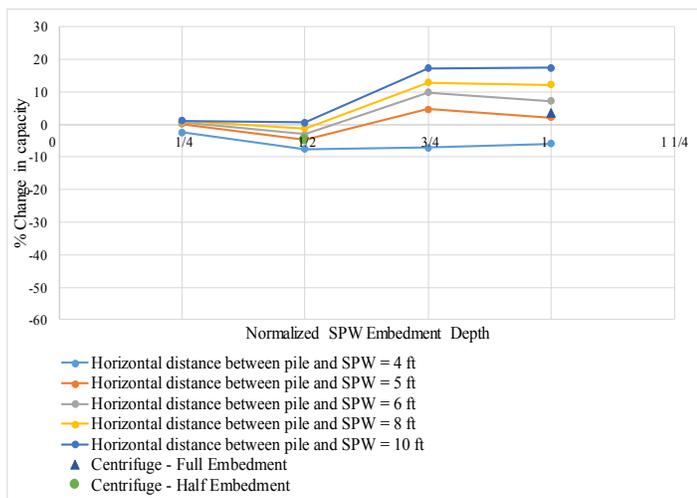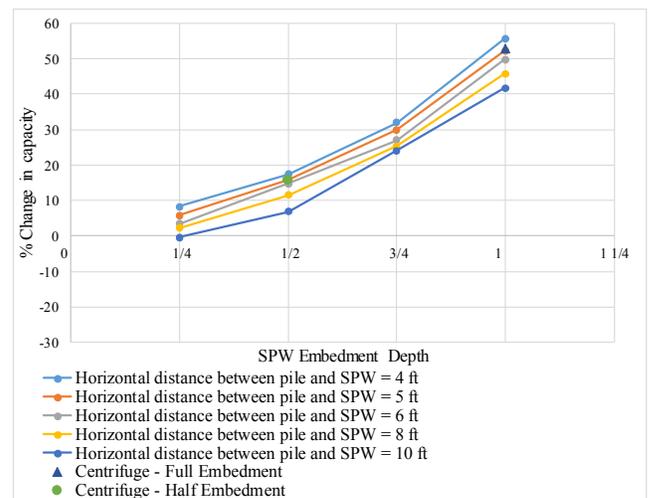
(a)   (b)

Figure 5.9 Variation of ultimate pile capacity for (a) Scenario 3 and (b) Scenario 2 as per ratios of SPW embedment depth to pile embedment length
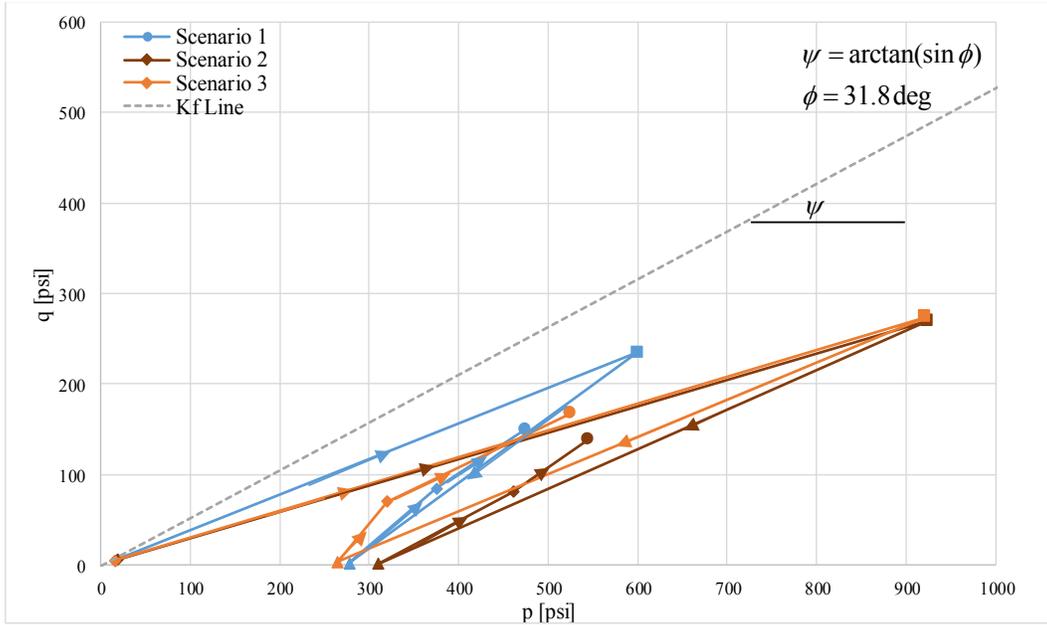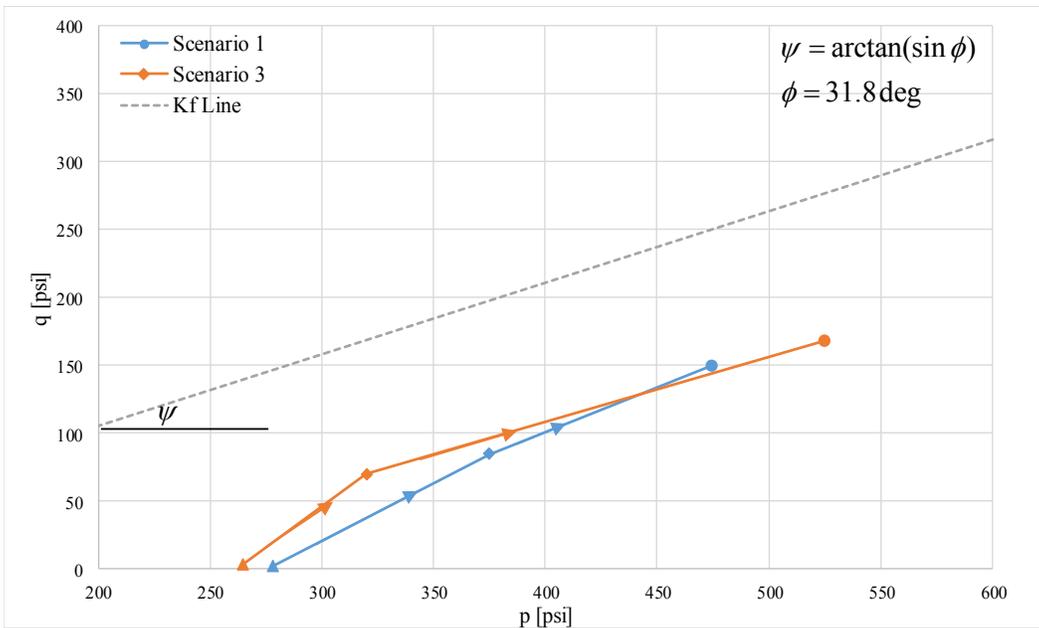
Figure 5.10 Stress paths of the end bearing region during Scenario 1 and Scenario 3 for the case of HOD of 10 ft and full SPW embedment depth: (a) Complete stress paths during the loading sequences; the solid squares are stress states at the end of pile driving: (b) Stress paths developed under the quasi-static top-down loading condition; the solid circles are stress states at the top settlement equal to 2 inches.

5.4 Recommended Use of Graphical Design Tools

The plots given in Figs. 5.5 through 5.7, and Fig. 5.9 are recommended to be used as straightforward graphical tools for making quick assessments of pile capacities upon pre-installation and post-removal of SPWs in close proximity to driven pile foundations. These plots also provide the construction engineer with basic guidance related to SPW behavior during installation and removal. An example is given below as a demonstration of using the design plots.

Let us consider a design problem in which a sheet pile wall (SPW) is installed to a depth of 25 ft in medium dense FL sand. The square pile with width of 24 inches is then driven to a depth of 40 ft at a horizontal offset distance of 6 ft from SPW. The Davisson and ultimate pile capacities of the single pile foundation are calculated, using the program FB-Deep, as 320 kips and 960 kips, respectively. The load capacities after the removal of SPW can be solved either using Fig. 5.3 or Fig. 5.7. In this example, we shall use Fig. 5.7 to calculate reduction factors to account for the effects of the SPW removal in the design load capacities.

The ratio of SPW embedment depth to the pile embedment length is 25 ft /40 ft = 0.625. The horizontal offset distance (HOD) between SPW and pile is given as 6 ft. From Fig. 5.7, the reduction percentage at HOD of 6 ft is interpolated between the reduction percentage values of the embedment-depth ratios of 0.5 and 0.75; $\dfrac{0.625 - 0.5}{0.75 - 0.5} \times (20\% - 5\%) + 5\% = 12.5\%$. Thus, reduced Davisson pile capacity (DC) is estimated as

$$\text{DC on removal of SPW} = 320 \text{ kips} - \frac{12.5}{100}(320 \text{ kips}) = 320 - 40 = 280 \text{ kips}$$

Therefore, it is recommended to drive the pile to a higher pile driving resistance that provides a desired "Davisson" capacity (i.e., 320 kips of the example) after SPW extraction. However, no reduction in the ultimate capacity is considered as per Fig. 5.9a. Similar calculations can be performed by using the graphs given in Figs. 5.3 and 5.4.

CHAPTER 6
CONCLUSIONS

The current research has been undertaken to provide robust design tools for geotechnical engineers who design the load capacities of displacement pile foundation in close proximity to sheetpile walls (SPW). Physical and numerical research tasks have been carried out for characterization of dynamic shear behaviors of Florida medium sand subjected to SPW per-installation and post-removal processes, pile driving by multiple impacts, and load/stress quantities throughout simulations of the construction phases (sequences) of pile-soil-SPW systems. Numerical modeling efforts are ongoing for simulation of breakage of soil particles during pile penetration.

This report focuses mainly on the numerical modeling of three scenarios involving both dynamic and quasi-static interactions between piles, soil, and SPWs: (1) Pile driven into sand, followed by pile top-down load test; (2) SPW driven into sand, followed by pile driven into sand, ending with pile top-down load test;, and (3) SPW driven into sand, followed by pile driven into sand, SPW removal, ending with pile top-down load test. A three-dimensional discrete element method has been used to numerically simulate SPW and pile penetration centrifuge tests in granular soil. In the test simulations, SPW is pushed into the granular medium at a constant rate. The resistance measured on the SPW tip is related to a particular soil classification and properties of Florida top soil in terms of elastic deformability and shear strength in macroscales. In turn, the particulate nature of granular soil is successfully simulated such that discrete soil masses move around the penetrating structural members and collectively produce macroscopic shear resistances in both quasi-static and dynamic loading regimes. Proper continuum-scale DEM models for granular materials in penetration analyses has been developed and bench-marked against prototype-scale centrifuge test results. The bench-marked models are then adopted in analysis and interpretation of in-situ construction scenarios. The study shows that the penetration makes the soil near the SPW tip undergo a significant changes of stresses in both magnitude and direction. The discrete (particulate) rearrangement at large deformation rates may arrive at a stress state in rate-dependent strength envelope obtained from conventional high-strain rate tests. As a result, shear dilatancy, rate-dependency, and particle crushing are the main features that future refinement of the DEM models may warrant for more realistic simulations of granular bulk behaviors in penetration analyses.

Centrifuge tests provide useful data in developing semi-empirical correlations between mesoscale granulate properties and dynamic resistance results. However, state-of-the-art techniques used in the available facility are limited by the sampling rates of data acquisition systems, particularly for capturing stress wave propagation, short-lived spikes in stress, and immediately resulting stress paths. The discrete element analyses overcome these sampling rate limitations and demonstrate that the actual deformation pattern associated with SPW installation and subsequent pile driving may well be simulated, and possibly different from that assumed in existing continuum mechanics or cavity-expansion theory; the pile dynamic resistance is affected by deformation properties such as effective shear modulus and intergranular friction coefficient that ultimately produce angle of dilation due to dynamic compaction. Therefore, the present DEM modeling method is reasonably successful in terms of practical application in in-situ scale foundation engineering.

6.1 Research Contributions

The present study includes development of advanced numerical models of pile and SPW driving into granular soil-bodies, where computed soil stresses and pile axial load-resistance show agreement with physical measurements from recently completed scaled-centrifuge testing (see the Task 4 report for additional details).

It was aimed to provide reliable numerical modeling and design of the system "sheet pile–driven pile–soil media". Thus, the main portion of the current research dealt with discrete element modeling of relatively large granular bodies under geostatic stress equilibrium being subjected to dynamic loading due to pile and SPW driving processes under three specific setups: (1) Pile driven into sand, followed by pile top-down load test; (2) SPW driven into sand, followed by pile driven into sand, ending with pile top-down load test;, and (3) SPW driven into sand, followed by pile driven into sand, SPW removal, ending with pile top-down load test. It is necessary to note the difference between the intervals of loading stages and their effects in pile displacement for the serviceability of structure operation. Pile displacements may be limited by a few millimeters or centimeters under more or less stable quasi-static service loading. During pile installation, the steps of dynamic loading are calibrated with incremental pile displacements measured in physical centrifuge tests. As such, prototype-scale physical modeling serves bench-marking for simulating the inertial resistance during the dynamic installation process.

As a first step in developing numerical models of the three above-defined scenarios, selected measurements from the recently completed (Task 4) physical scaled-centrifuge were selected and documented. This process was crucial to establishing specific, quantitative benchmarks for the simulations of pile and SPW driving. Subsequently, to help elucidate parameter value selection for constituent discrete spherical elements (DSEs) of granular assembly models, triaxial compression test data was identified and acquired from the literature. Then, a previously developed (combined discrete-finite element method, DEM-FEM) model of a triaxial compression was utilized to conduct triaxial compression test simulations. In bringing about agreement between the simulated (versus physical) laboratory test results, insights were gained over which range of parameters were to be investigated for those simulations involving pile-soil-SPW interactions.

The completed (physical) scaled-centrifuge tests provided benchmark measurements (e.g., geostatic stresses; pile skin-friction and end bearing forces) for assessment of the predictive qualities of corresponding numerical models. The simulation results show great resemblance to the measurements from the centrifuge test. This suggests that our three-dimensional DEM simulation framework, which considers the mesoscale contact model and involves a careful calibration based on triaxial tests, is capable of giving reasonable estimations on the magnitudes and trends of both the base and shaft resistances under all three considered loading scenarios. Further, the numerical models developed as part of Task 3 are capable of phenomenologically simulating a range of bulk shear responses of the granular media as part of a parametric study. Therefore, following acquisition of benchmark (physical) soil-stress and pile load-deformation relationships; development of boundary condition models; and, identification of DSE parameter ranges, simulations of the two aforementioned test scenarios were carried out. The models considered involved interactions between millions of DSEs, both among themselves and with structural (FE) objects. For each simulation, changes in soil-stresses were captured, along with (as the final stage of each simulation) pile load-deformation response to vertical (downward) quasi-

static pile head loading. Particularly, conceptual models for SPW vibration effect zone that have been reported by many researchers in the past are validated per explicit DEM simulations. Generation of body and surface waves during vibratory driving of SPW can be conceptualized in a simplified manner as shown in Figure 6.1. Along the shaft of the SPW, resistive shear forces are believed to induce vertically polarized shear waves in the surrounding ground. For vibratory driving, the wave front is thought to propagate almost cylindrically from the SPW shaft. Based on these observations in numerical data analysis, validity of a semi-empirical analysis model based on a hypothesis proposed by Massarsch (2000; cited in Guillemet 2013) is proven for which the vertical oscillation movement of the SPW shaft couples with a horizontal movement in granular soils, altering the geostatic stress states via mobilized granular interlocking, i.e., dilative angle of internal friction. Horizontal vibrations deem to be relatively small. However, during the removal of SPW, cavity formation in the tip region of, and drag force along the vertically-moving SPW shaft, are significant to disturb the granular structure. Substantial loss in granular contact forces results in relieving locked-in effective stresses. These phenomena have direct impacts on the end bearing of the displacement pile foundation. In particular, the reduction of Davisson capacity exacerbates with SPW embedment depth (relative to pile embedment length).
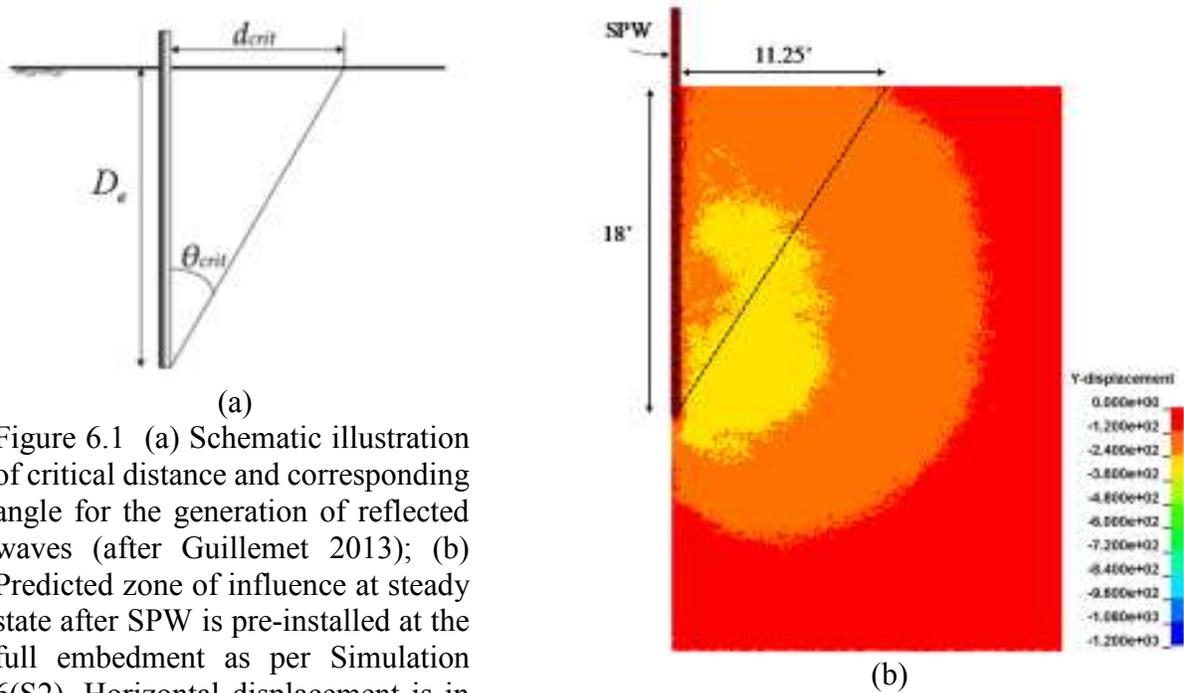

(a)

Figure 6.1 (a) Schematic illustration of critical distance and corresponding angle for the generation of reflected waves (after Guillemet 2013); (b) Predicted zone of influence at steady state after SPW is pre-installed at the full embedment as per Simulation 6(S2). Horizontal displacement is in unit of mm.

(b)

The prototype-scale experiments and laboratory testing also provided new information about the development of the dynamic resistance in the granular soil. The applied experimental techniques made it possible to control the loading history of soil resistance in sheet pile driving, and to consider the influence of particles' interlocking and inelastic collision. The obtained new mesoscale "intergranular normal contact force–displacement" and "intensity of tangential (interlock friction) force–displacement" may be useful to improve calculation models describing dynamic soil–structure interaction and, correspondingly, to refine design approaches in other types of deep foundation (e.g., retaining walls and quay wall) constructions. The DEM-FEM model may be applied to the stage of large-diameter steel pipe pile installation and also to operation period of the piled structures. An improved calculation model for the design of sheet pile walls can be developed and applied to cofferdam structures. The results obtained demonstrate new possibilities to clarify the stiffness parameters of SPW-pile-soil system regarding the development of loss of shear strength during the stage of SPW removal operation.

6.2 Recommendations

This section provides design recommendations on assessment of displacement-pile capacities in consideration for the removal of the sheet pile walls pre-installed in close proximity. The guidance is based on the present numerical analysis of the geometry of sheet pile-soil-pile system. Thus, the following is intended for preliminary design guidance for the geotechnical and structural engineers who may seek out essential information for the effects of SPW removal in pile design loads. It also provides the construction engineer with basic guidance related to sheet pile wall behavior during installation and removal.

Substantial reduction in Davisson capacity should be accounted for in the determination of serviceability criteria of the pile foundation after the removal of pre-installed SPW. Embedment depth of SPW in relation to the depth of the pile tip has direct impact on rates of the capacity reduction. For instance, axial stiffness of pile foundation may suffer up to 55% loss upon SPW removal if SPW was pre-installed for a full pile embedment length and in a horizontal offset of two times the pile width. No post-SPW-removal reduction in the Davisson capacity would be expected *if and only if* the horizontal offset distance between pre-installed SPW and pile locations is equal to at least five times the pile width, and the ratio of SPW embedment depth to pile tip depth is less than 0.5.

On the basis of the obtained numerical (and physical test) results, any disturbance in a compacted soil condition near the tip of displacement pile may cause a substantial loss in end bearing. It is reasonable to conclude that the Davisson capacity values of the displacement pile can be substantially affected by non-vibratory removal (pull-out) of the SPW in the cases of the embedment depth ratios greater than 0.5. Thus, top-down displacements should be calculated using the reduced axial stiffness for the serviceability design. Particularly, deep SPW installation during construction requires considerable reduction of Davisson capacity that can undermine superstructure support and cause excessive settlement. In the worst case of Figure 6.2, service load can be as little as 45% of the Scenario 1 values. By taking into account reduction of load capacity (in comparison with Scenario 1), there is a correction to be made, i.e., reduction factors of approximately 0.9-0.45, for the cases considered. By taking these changes in soil resistance values with respect to SPW embedment depths into account, the reduction factors provide a designer-friendly means of estimating service loads; for instance, the non-vibratory extraction of pre-

installed SPW would disturb and weaken the granular structure, reducing the capacity of driven pile per relative embedment depths and horizontal offset distances to the SPW.

Figure 6.2 Variation of Davisson capacity in Scenario 3 with respect to horizontal offset distance (feet) per SPW embedment depth normalized by pile tip depth

It is important to note that the embedment depth of the SPW in relation to the depth of the pile tip has severe influence on rates of capacity reduction, especially when SPW was pre-installed in close proximity, e.g., horizontal offset distance (HOD) of 4-6 ft. Practically, no post-SPW-removal reduction in the Davisson capacity could be expected if and only if the HOD between SPW and pile is equal to at least five times the pile width (5B), and the ratio of SPW embedment depth to pile embedment length is less than 0.5.

It is important to note that the embedment depth of the SPW in relation to the depth of the pile tip has severe influence on rates of capacity reduction, especially when SPW was pre-installed in close proximity, e.g., horizontal offset distance (HOD) of 4-6 ft. Practically, no post-SPW-removal reduction in the Davisson capacity could be expected *if and only if* the HOD between SPW and pile is equal to at least five times the pile width (5B), and the ratio of SPW embedment depth to pile embedment length is less than 0.5.

Ultimate bearing capacity is a complex function of a large number of unknown factors. These factors include method of pile driving, method of SPW installation, in-situ soil condition and the pile geometry. Due to practical and time constraints, it was not possible to simulate a variety of pile driving methods and the pile up-to-failure behavior. Thus, the ultimate capacity of the pile may warrant further investigation with respect to these factors. Though, at minimum 10% reduction in the ultimate load carrying capacity would be recommended for the case of the horizontal offset distances in a range of 4-5 ft, as shown in Figure 6.3.
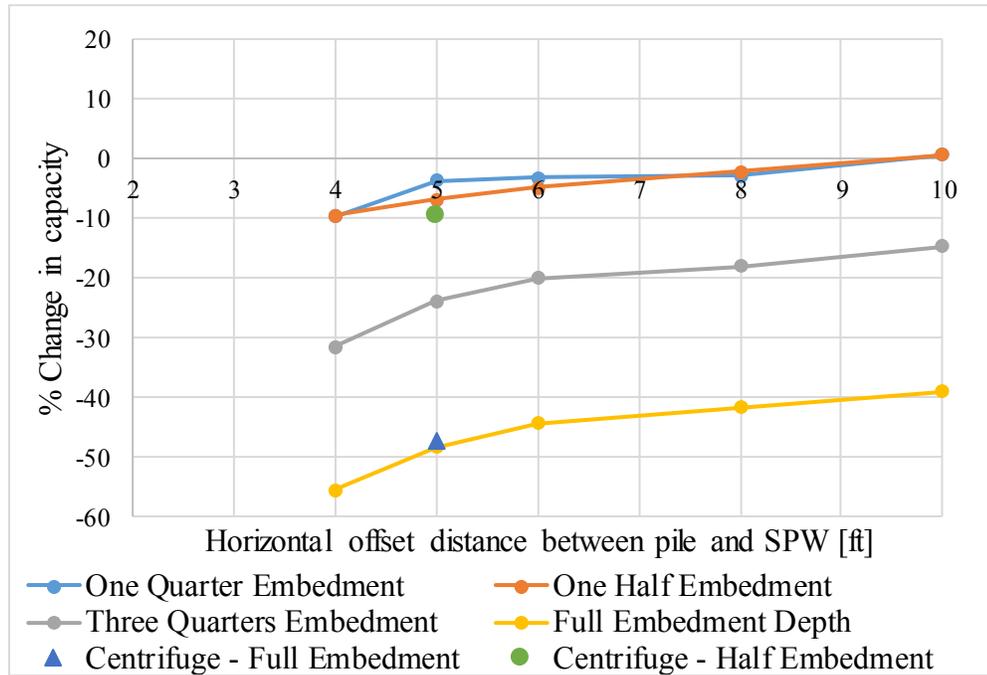
Figure 6.3 Variation of ultimate capacity in Scenario 3 with respect to horizontal offset distance (feet) and SPW embedment depth normalized by pile tip depth

REFERENCES

Athanasopoulos, G.A. and Pelekis, P.C. (2000). "Ground Vibrations from sheetpile driving in urban environment: measurements, analysis and effects on buildings and occupants. *Soil Dynamics and Earthquake Engineering*, 19(5), pp. 371-387.

Archard, J. F. (1957). "Elastic Deformation and the Laws of Friction," *Proceedings of the Royal Society of London A*, 243: pp.190-205

Attewell, P.B. and Farmer, I.W. (1973). "Attenuation of ground vibrations from pile driving." *Ground Engineering*, 3(7), pp. 26-29.

Bathurst, R. J. and Rothenburg, L. (1992). "Investigation of Micromechanical Features of Idealized Granular Assemblies using DEM," *Engineering Computations*, 9(2), pp. 199-210.

Butlanska, J., Arroyo, M., Gens, A., O'Sullivan, C. (2014). "Multi-scale Analysis of Cone Penetration Test (CPT) in a Virtual Calibration Chamber," Canadian Geotechnical Journal; 51(1), pp. 51–66.

Bhushan B. (2001). Introduction to Tribology. New York. John Wiley & Sons.

Cavarretta, I., Coop, M., O'Sullivan, C. (2010). "The Influence of Particle Characteristics on the Behavior of Coarse Grained Soil. *Géotechnique*; 60(6), pp. 413–423.

Chang, C S., Misra, A., Sundaram, S. S. (1991). "Properties of Granular Packings under low-Amplitude Cyclic Loading," *Soil Dynamics and Earthquake Engineering*, 10, pp. 201–211.

Craig, WH. (1985). "Modeling Pile Installation in Centrifuge Experiments." 11th International Conference on Soil Mechanics and Foundation Engineering. San Francisco, California, pp. 1101-1104.

D'Appolonia, D.J. (1971). "Effects of Foundation Construction on nearby Structures." Proc. of the 4th Panamerican Conf. on Soil Mechanics and Foundation Engineering, June 1971, San Juan, Puerto Rico. American Society of Civil Engineers, New York, NY, U.S.A. pp. 189-236.

Davidson, M. T., Chung, J. H., Teng, H., Han, Z., and Le, V. (2015). "Volume-Averaged Stress States for Idealized Granular Materials using Unbonded Discrete Spheres in LS-DYNA®," *10th European LS-DYNA Conference*, Würzburg Germany.

Deckner, F., Viking, K., and Hintze, S. (2012). "Ground vibrations due to pile and sheet pile driving – prediction models of today." Proc. of the 22nd European Young Geotechnical Engineers Conf., 26-29 August, Gothenburg, Sweden. pp. 107-112.

Denies, N. (2010). "Dynamic Behavior of Vibrated Sand – Sphere Penetration Experiments and Discrete Element Modeling of Vibro-fluidization." Doctoral Thesis, Université Catholique deLouvain, Louvain-la-Neuve, Belgium.

Dowding, C.H. (1996). "Construction Vibrations." Prentice Hall, Upper Saddle River, NJ, U.S.A. ISBN 0-13-299108-X. 610. pp.

Erlingsson, S. and Bodare, A. (1996). "Live load induced vibrations in Ullevi Stadium – dynamic soil analysis." *Soil Dynamics and Earthquake Engineering*, 15(3), pp. 171-188.

Fahey, M. (1992). "Shear Modulus of Cohesionless Soil: Variation with Stress and Strain Level," Canadian Geotechnical Journal; 29, pp. 157–161.

Field, W. G. (1963). "Towards the Statistical Description of Granular Mass", *Proceedings of the 4th Australian and New Zealand Conference on Soil Mechanics*, New Zealand Institution of Engineers, Wellington, pp. 143-148.

Fuglsang, L.D. and Ovesen, N.K. (1987). "The application of theory of modelling to centrifuge studies. Centrifuge in soil mechanics," Craig, W., James, Schofield, A. (eds), Balkema, Rotterdam, Netherlands pp. 119-138.

Garnier J., Gaudin C., Springman S. M., Culligan P. J., Goodings D. J., Konig D., Kutter, B., Phillips, R. And Randolph, M. F. (2007), "Catalogue of Scaling Laws and Similitude Questions in Geotechnical Centrifuge Modelling." *International Journal of Physical Modelling in Geotechnics*; 7, pp. 1-23.

German, R. M. (1989). Particle Packing Characteristics. Metal Powder Industry Federation, Princeton NJ.

Givoli, D. (1991). "Non-Reflecting Boundary Conditions", *Journal of Computational Physics*, 94(1), pp. 1-29.

Greenwood, J. A., and Williamson, J. B. P., (1966). "The Contact of Nominally Flat Surfaces," *Proceedings of the Royal Society London Series A*, 295, pp. 300-319.

Guillemet, C. (2013). "Vibratory Sheet Pile Driving: a Full Scale Field Study." Master Thesis. Civil and Architectural Engineering, Royal Institute of Technology.

Hanna, T. H. (1963). "Model studies of foundation groups in sand," *Géotechnique*, 13, pp. 334

Head, J.M. and Jardine, F.M. (1992). "Ground-borne vibrations arising from piling." CIRIA Technical Note 142. CIRIA, London, U.K. ISBN 0-86017-351-8.

Hertz, H. (1882). "On the Contact of Elastic Solids." in Miscellaneous Papers. London. Macmillan. 1896 pp. 146

Hintze, S. (1994). *Risk analysis in foundation engineering with application to piling in loose friction soils in urban situations*. Doctoral Thesis, Div. of Soil and Rock Mechanics, Royal Institute of Technology, Stockholm, Sweden. ISBN 991-884902-9. 153 pp.

Holscher, P., van Tol, A.F., and Huy, N.Q. (2012). " Rapid Pile Load Tests in the Geotechnical Centrifuge," *Soils and Foundations,* 52(6), pp. 1102–1117.

Hope, V.S. and Hiller, D.M. (2000). "The prediction of groundborne vibration from percussive piling." *Canadian Geotechnical Journal*, 37, pp. 700-711.

Iwanowski, T. and Berglars, B. (1986). "Experiences of Swedish and Norwegian Contractors on Vibratory Pile Driving." UPTEK 8628 R. Teknikum, Institute of Technology, Uppsala University, Sweden.

Iwasaki, T., Tatsuoka, F.,and Takagi, Y. (1978). "Shear Moduli of Sands under Cyclic Torsional Shear Loading," *Soils and Foundation,* 18, pp. 39-56.

Karajan, N., Han, Z., Teng, H., and Wang, J. (2014). "On the Parameter Estimation for the Discrete-Element Method in LS-DYNA." *13th International LS-DYNA Users Conference*, Michigan.

Kishida, H. (1967). "Ultimate bearing capacity of piles driven into loose sand." *Soils and Foundations,* 7(3), pp. 20-29

Kutter, BL. (1992). "Dynamic Centrifuge Modeling of Geotechnical Structures." *Transportation Research Record*, No. 1336, pp. 24-30.

Kutter, BL. (1995). "Recent advances in centrifuge modeling of seismic shaking." Third International Conference on Recent Advances in Geotechnical Earthquake Engineering and Soil Dynamics. Rolla, MO, pp. 927–942.

Jingbo, L. and Yandong, L. (1998). "A direct method for analysis of dynamic soil-structure interaction based on interface idea," Dynamic Soil-Structure Interaction Research in China and Switzerland, editors: Zhang C., and Wolf, J. P.

Langroudi, M.K., Sun, J., Sundaresan, S., Tardos, G.I. (2010). "Transmission of stresses in static and sheared granular beds: The influence of particle size, shearing rate, layer thickness and sensor size." *Powder Technology,* 203(1), pp. 23-32

LSTC. (2017). *LS-DYNA Keyword User's Manual, Volume I*. Livermore Software Technology Corporation, Livermore CA.

Lysmer, J. and Kuhlemeyer, R. L. (1969). "Finite dynamic model for infinite media," *ASCE Journal of the Engineering Mechanics Division*, 95(4), 859-877.

Mandal, A. and Maity, D. (2016). Study of local non-reflective boundary condition on soil domain," *Procedia Engineering,* 144(2016), pp. 1252-1259.

Massarsch, R. (2000). *Vibratorers användningsmöjligheter vid drivning av pålar och spont. Pålkommissionen*, Rapport 99, Linköping, Sweden. ISSN 0347-1047: cited in Guillemet, C. (2013). "Vibratory Sheet Pile Driving: a Full Scale Field Study." Master Thesis. Civil and Architectural Engineering, Royal Institute of Technology.

McDowell, R. G., and Bolton, D. M. (2000). "Effect of particle size distribution on pile tip resistance in calcareous sand in the geotechnical centrifuge." *Granular Matter*, 2(4), pp. 179-187.

McVay, M., Bloomquist, D., Vanderlinde, D., and Clausen, J. (1994). "Centrifuge Modeling of Laterally Loaded Pile Groups in Sands." *Geotechnical Testing Journal*, 17(2), 9.

McVay, M., Zhang, L., Molnit, T., and Lai, P. (1998). "Centrifuge Testing of Large Laterally Loaded Pile Groups in Sands." *Journal of Geotechnical and Geoenvironmental Engineering*, 124(10), pp. 1016-1026.

Meyerhof, G. G. (1959). "Compaction of sands and bearing capacity of piles." *Proc. American Society of Civil Engineers,* I.A.B.S.E. Stockholm, Sweden, p. 105

Meyerhof, G. G. (1960). "The design of franki piles with special reference to groups in sand." *Proc. Sympisium on Pile Foundations,* 85(SM6) pp. 1

Mindin, R.D. and Deresiewicz, H. (1953). "Elastic Spheres in Contact under Varying Oblique Forces," *ASME Journal of Applied Mechanics*, 20, pp. 327-344.

Mitchell, RJ. (1991). "Centrifuge Modelling as a Consulting Tool." *Canadian Geotechnical Journal*, 28, pp.162-167.

Nayak, P.R. (1971) "Random Process Model of Rough Surfaces," *ASME Journal of Lubrication Technology*, 93, 398-407.

O'Neill, M. (2001). "Side Resistance in Piles and Drilled Shafts." *J. Geotech, Geoenviron. Eng.* 127(1), pp. 3-16

Ovesen, N. K. (1981). "Centrifuge Tests to Determine the Uplift Capacity of Anchor Slabs in Sand. In: Proceedings of the 10th International Conference on Soil Mechanics and Foundation Engineering, Stockholm, Sweden, 1, pp. 717–722.

Richart, F.E. Jr., Woods, R.D., and Hall, J.R. Jr. (1970). "Vibrations of Soils of Foundations." Prentice Hall, Inc., Englewood Cliffs, New Jersey, U.S.A. 414 p.

Rothenburg, L. and Bathurst, R. J. (1989). "Analytical Study in Induced Anisotropy in Idealized Granular Material," *Géotechnique*; 49, pp. 601–614.

Santamarina, J. C. (2001). Soils and Waves. New York. John Wiley & Sons.

Santamarina, J., Goodings D. (1989). "Centrifuge Modeling: A Study of Similarity." *Geotechnical Testing Journal*; 12, pp. 163-166.

Schofield, A. N., (1981). "Dynamic and Earthquake Geotechnical Centrifuge Modelling." *International Conference on Recent Advances in Geotechnical Earthquake Engineering and Soil Dynamics*. Rolla, MO: Missouri University of Science and Technology; pp. 1081–100.

Semblat, J. F., Luong, M. P., Thomas, J.J. (1995) "Dropball Arrangement for Centrifuge Experiments," the 5th SECED Conference on European Seismic Design Practice, Chester, UK, pp.567-575, Balkema, Rotterdam, Netherlands.

Smith, w. O., Foote, P. D., Busang, P. F. (1929). "Packing of Homogeneous Spheres," *Physics Review,* 34, pp. 1271–1274.

Zhao, C. and Liu, T. (2003). "Non-reflecting artificial boundaries for transient scalar wave propagation in a two-dimensional infinite homogeneous layer," International Journal for Numerical Methods in Engineering, 58(10) pp. 1435-1456.